
JSCSEN 80(11)1339–1459(2015)

ISSN 1820-7421(Online)

Journal of the Serbian Chemical Society

Volume 80 :: 2015 :: 85 Years of the Journal

1930 Glasnik Hemिजkog Društva Kraljevine Jugoslavije

Journal of the Chemical Society of the Kingdom of Yugoslavia

1947 Glasnik hemijskog društva Beograd

Journal of the Chemical Society of Belgrade

1985 Journal of the Serbian Chemical Society

VOLUME 80

No 11

BELGRADE 2015

Available on line at



www.shd.org.rs/JSCS/

The full search of JSCS
is available through

DOAJ DIRECTORY OF
OPEN ACCESS
JOURNALS
www.doaj.org



Journal of the Serbian Chemical Society

JSCS-info@shd.org.rs • www.shd.org.rs/JSCS

J. Serb. Chem. Soc. Vol. 80, No. 11 (2015)

CONTENTS

Organic Chemistry

- D. M. Opsenica, J. Radivojević, I. Z. Matić, T. Štajner, S. Knežević-Ušaj, O. Djurković-Djaković and B. A. Šolaja: Tetraoxanes as inhibitors of apicomplexan parasites *Plasmodium falciparum* and *Toxoplasma gondii* growth and anti-cancer molecules.. 1339
D. Ashok, S. Ravi, B. V. Lakshmi and A. Ganesh: One-pot synthesis of carbazole based 3-hydroxy-4H-chromen-4-ones by a modified Algar–Flynn–Oyamada reaction and their antimicrobial activity 1361
Y.-W. Li and S.-T. Li: Facile synthesis and antifungal activity of dithiocarbamate derivatives bearing an amide moiety..... 1367

Biochemistry and Biotechnology

- B. Dojnov, M. Grujić and Z. Vujičić: Highly efficient production of *Aspergillus niger* amylase cocktail by solid-state fermentation using triticale grains as a well-balanced substrate 1375

Inorganic Chemistry

- D. Li, G.-Q. Zhong and Z.-X. Wu: Solid–solid synthesis, characterization and thermal decomposition of a homodinuclear cobalt(II) complex..... 1391

Theoretical Chemistry

- M. Gruden, S. Stepanović and M. Swart: Spin state relaxation of iron complexes: The case for OPBE and S12g..... 1399

Physical Chemistry

- C. Karunakaran, S. Karuthapandian and P. Vinayagamoorthy: Light-induced oxidative transformation of diphenylamine on ZrO₂. Synergism by ZnO and ZnS..... 1411

Thermodynamics

- G. R. Ivaniš, A. Ž. Tasić, I. R. Radović, B. D. Djordjević, S. P. Šerbanović and M. Lj. Kijevčanin: Modeling of density and calculations of derived volumetric properties for *n*-hexane, toluene and dichloromethane at pressures 0.1–60 MPa and temperatures 288.15–413.15 K 1423

Polymers

- H. Zeghioud, S. Lamouri, Y. Mahmoud and T. Hadj-Ali: Preparation and characterization of a new polyaniline salt with good conductivity and great solubility in dimethyl sulphoxide..... 1435

Materials

- M. Jabbarzadeh and A. R. Golkarian: The influence of interlayer interactions on the mechanical properties of polymeric nanocomposites..... 1449

Published by the Serbian Chemical Society
Karnegijeva 4/III, P.O. Box 36, 11120 Belgrade, Serbia
Printed by the Faculty of Technology and Metallurgy
Karnegijeva 4, P.O. Box 35-03, 11120 Belgrade, Serbia



Tetraoxanes as inhibitors of apicomplexan parasites *Plasmodium falciparum* and *Toxoplasma gondii* growth and anti-cancer molecules

DEJAN M. OPSENICA^{1**#}, JELENA RADIVOJEVIĆ², IVANA Z. MATIĆ³,
TIJANA ŠTAJNER⁴, SLAVICA KNEŽEVIĆ-UŠAJ⁵, OLGICA DJURKOVIĆ-DJAKOVIĆ⁴
and BOGDAN A. ŠOLAJA^{6#}

¹Institute of Chemistry, Technology, and Metallurgy, University of Belgrade, Njegoševa 12,
11000 Belgrade, Serbia, ²Institute of Molecular Genetics and Genetic Engineering, University
of Belgrade, Vojvode Stepe 444a, P. O. Box 23, 11010 Belgrade, Serbia, ³Institute for
Oncology and Radiology of Serbia, Pasterova 14, 11000 Belgrade, Serbia, ⁴National
Reference Laboratory for Toxoplasmosis, Institute for Medical Research, University of
Belgrade, Dr. Subotića 4, P. O. Box 102, 11129 Belgrade, Serbia, ⁵Institute for Pathology,
Medical Faculty, University of Novi Sad, Hajduk Veljkova 3, 21000 Novi Sad, Serbia and
⁶Faculty of Chemistry, University of Belgrade, Studentski trg 12–16, P. O. Box 51, 11158,
Belgrade, Serbia

(Received 30 April, revised and accepted 22 June 2015)

Abstract: New cyclohexylidene 1,2,4,5-tetraoxanes with polar guanidine and urea based groups were synthesized and evaluated for their antimalarial activity against chloroquine resistant and susceptible *Plasmodium falciparum* strains. The derivatives showed moderate, nM range antimalarial activities and low cytotoxicity. The *N*-phenylurea derivative **24** exhibited the best resistance indices ($RI_{W2} = 0.44$, $RI_{TM91C235} = 0.80$) and was not toxic against human normal peripheral blood mononuclear cells ($IC_{50} > 200 \mu\text{M}$). Seven derivatives were tested *in vitro* against four human cancer cell lines and they demonstrated high selectivity toward leukaemia K562 cells. One compound, derivative **21** with a primary amino group, was the first tetraoxane tested *in vivo* against *Toxoplasma gondii* as another apicomplexan parasite. Subcutaneous administration at a dose of $10 \text{ mg kg}^{-1} \text{ day}^{-1}$ for 8 days allowed the survival of 20 % of infected mice, thus demonstrating the high potential of tetraoxanes for the treatment of apicomplexan parasites.

Keywords: antimalarials; antiparasitic; peroxides; cancer; cytotoxicity.

* Corresponding author. E-mail: dopsen@chem.bg.ac.rs

Serbian Chemical Society member.

doi: 10.2298/JSC150430063O

INTRODUCTION

Apicomplexan protozoa are single-celled parasites, with significant medical, veterinary and economic effects worldwide. From the aspect of human medicine, two apicomplexan infections are of major health concern – malaria, caused by *Plasmodium spp.*, and toxoplasmosis, caused by *Toxoplasma gondii*.

A potentially devastating disease, malaria represents an enormous public health problem in the majority of developing countries, further emphasized by the fact that nearly half of the world population is exposed to the infection.¹ Malaria may be caused by five *Plasmodium* species, *P. falciparum*, *P. ovale*, *P. vivax*, *P. malariae* and *P. knowlesi*, of which *P. falciparum* that causes cerebral malaria is the major threat. On a cellular level, all *Plasmodium* parasites contain acidic food vacuoles (FV), where digestion of haemoglobin occurs and it is generally accepted that the FV are the site of action for a number of quinoline-like drugs. The haem obtained from haemoglobin degradation is toxic to the parasite and is transformed into insoluble haemozoin pigment, while the globin is hydrolysed into individual amino acids. Antimalarial drugs active within FV appear to kill the parasite either by producing toxic free radicals² or by blocking haemozoin formation, as in the case of the 4-amino-7-chloroquinolines (ACQs).³ The development of widespread drug-resistance to chloroquine (CQ), the most successful antimalarial drug, has resulted in severe health issues in malaria endemic regions. Although thorough investigation led to the realization that mutations in *P. falciparum* chloroquine resistant transporter (PfCRT), multidrug resistance protein 1 (PfMDR1) and multidrug resistance-associated protein (PfMRP) are responsible for the development of resistance of the malaria parasite against chloroquine and its analogues,⁴ additional analysis appears necessary.⁵ Therefore, significant focus has been placed on the synthesis of peroxide antimalarials active in FV⁶ or interfering in NADPH balance acting as leuco-methylene blue (LMB) and FADH₂ oxidisers,⁷ as well as on the development of new 4-amino-quinolines,⁸ acridines⁹ and other molecules that prevent haem polymerisation.¹⁰

T. gondii is an obligatory intracellular apicomplexan protozoan with worldwide distribution. Globally, it has been estimated that one in three persons is infected with *T. gondii*. In the United States, nearly 25 % of the adult population has been infected with this organism,¹¹ while most studies of European populations report 20–35 % seropositivity.¹² However, in South America, these rates can reach 50–75 %.¹³ Individuals with a compromised immune system, such as HIV-infected persons and transplant recipients, are particularly prone to severe *T. gondii* induced disease, mainly as a result of reactivation of a previously latent infection.¹⁴ When primary *T. gondii* infection occurs during pregnancy, it can be vertically transmitted, which may result in intrauterine death, birth defects, or to late sequelae, such as ocular disease and mental retardation.

As intracellular pathogens, *Plasmodium spp.* and *T. gondii* both rely on the invasion of host cells for survival and proliferation. Since both parasites belong to the same apicomplexan phylum, they have common metabolic pathways and thus may be susceptible to same drugs for prevention or treatment.^{15–17} However, there are a number of differences between the two pathogens. During the asexual reproduction stage, *P. falciparum* exclusively targets human erythrocytes, whereas *T. gondii* can infect any cell in most vertebrates.¹⁷ And, while malaria is transmitted only via the mosquito vector or blood exchange, infection with *T. gondii* occurs via ingestion of sporulated oocysts shed into the environment by infected cats, or by consuming bradyzoites in the form of tissue cysts from infected animals. Current therapies for *T. gondii* include drugs which inhibit folate metabolism, protein synthesis, or disrupt electron transport.^{18,19} For the inhibition of folate metabolism, a combination of diaminopyrimidine antimalarials, such as trimethoprim **1** or pyrimethamine **2** (Fig. 1), and sulfonamides, such as sulfadiazine **3** (Fig. 1) or sulfamethoxazole, is the recommended therapy. This combination acts synergistically not only against *T. gondii*, but also against various bacterial and other parasitic microorganisms. In patients sensitive to sulfonamides, protein synthesis inhibitors such as macrolide and lincosamide antibiotics are the second line of drugs. Another antimalarial, atovaquone, an inhibitor of mitochondrial electron-transport processes, is the drug of choice as third line therapy.²⁰ In all these treatments, drug resistance, high cost, limited efficacy, and side effects²¹ often result in discontinuation of therapy. Therefore, new agents with better activity and safety profiles and that are less expensive are

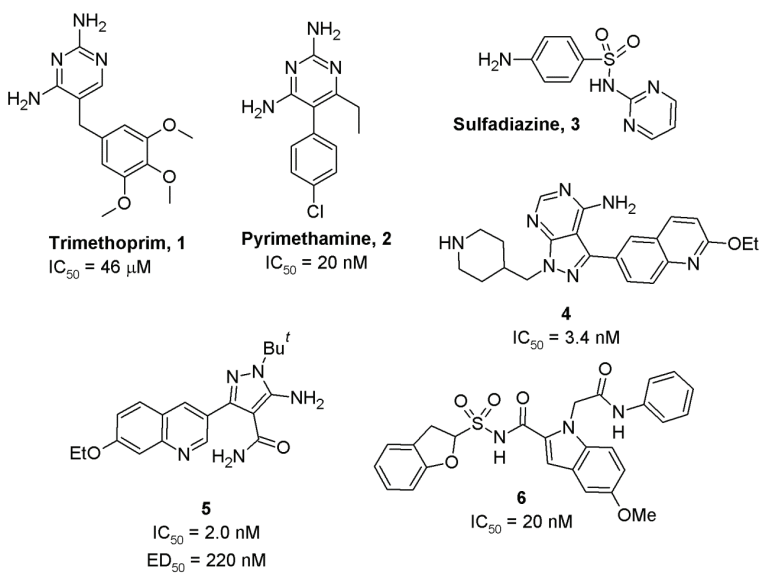


Fig. 1. Various inhibitors of the *T. gondii* parasite.

urgently needed.¹⁹ A variety of *T. gondii* inhibitors designed for different targets have been reported in the last few years, such as inhibitors of Ca-dependent protein kinase-1 (TgCDPK1),^{22,23} compounds which cause the disappearance of apicoplasts and plastid-like organelles,¹⁶ phosphodiesterase,¹⁷ purine nucleoside phosphorylase,¹⁸ and biosynthesis of pantothenic acid.²⁴ Of these, outstanding activities were exhibited by TgCDPK1 inhibitors **4** and **5**,^{22,23} and the inhibitor of the vitamin B5 biosynthetic pathway, derivative **6** (Fig. 1).²⁴

Outstanding examples of drugs active against both *Plasmodium spp.* and *T. gondii* parasites include artemisinin (**7**, ART, Fig. 2) and its semi-synthetic derivatives. It was established that their main mechanism of action is interfering in calcium homeostasis and triggering of micronema.^{25,26} ART and artemether **8** exhibited 100 times better *in vitro* activity against *T. gondii* than trimethoprim **1**, the current front-line drug.¹⁹ Other semi-synthetic artemisinin derivatives, including **9**,¹⁹ artemisone **10** or artemiside **11** have shown even better activities in the nM region (Fig. 2).²⁷ These derivatives inhibit multiple steps in the *T. gondii* cycle,^{19,28} and the absence of activity of deoxyartemisinine confirmed the peroxide group as the pharmacophore.²⁵ *In vivo* results are rare and incomplete,²³ and only few studies are reliable. Thus, artemisinin showed complete clearance of parasitaemia after a 5-day treatment with $1.3 \mu\text{g mL}^{-1} \text{ day}^{-1}$.²⁹ An 8-day administration of artemiside at $10 \text{ mg kg}^{-1} \text{ day}^{-1}$ 3 days after sulfadiazine treatment prolonged survival in 80 % of the mice, without toxic side-effects.²⁴

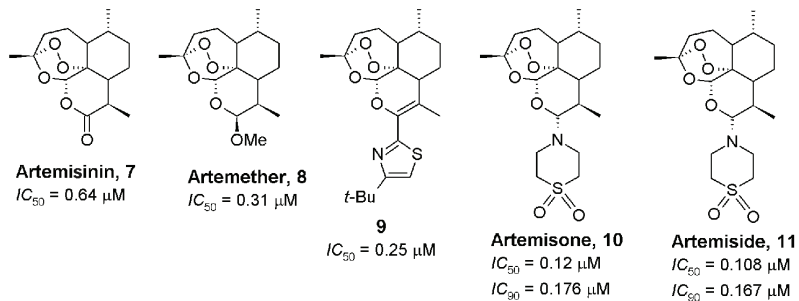


Fig. 2. Structures of artemisinin derivatives.

Artemisinin and its derivatives,³⁰ artemisone³¹ and other synthetic peroxides^{32,33} also exert potent *in vitro* and *in vivo* anticancer activities affecting diverse signalling pathways that regulate cell cycle, differentiation, apoptosis, invasion and angiogenesis in cancer cells.³⁰ Artemisinins can functionally be clearly distinguished from the synthetic peroxides, in spite of the fact that they all share a common peroxide pharmacophore, which suggests that these molecules have multiple modes of action.³³ Furthermore, it was found that synthetic and semi-synthetic peroxides exhibited specific activities against cancer cells. Thus, steroidal mixed tetraoxanes show highly specific activity toward UO31 renal

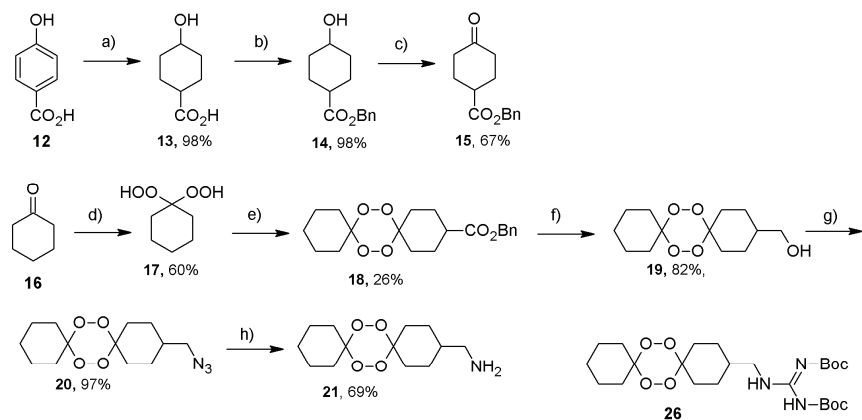
cancer cells,^{2b} and artesunate against non-small cell lung cancer and colorectal cancer.³⁴

The high antimalarial activities of dicyclohexylidene tetraoxanes that possess polar end groups attached to one of the cyclohexane units³⁵ encouraged us to explore the influence of modifications to the polar groups on their antimalarial and cytotoxic activities. For this, compound **21** was chosen since it showed the most promising *in vivo* activity against the malaria parasite.^{35c}

RESULTS AND DISCUSSIONS

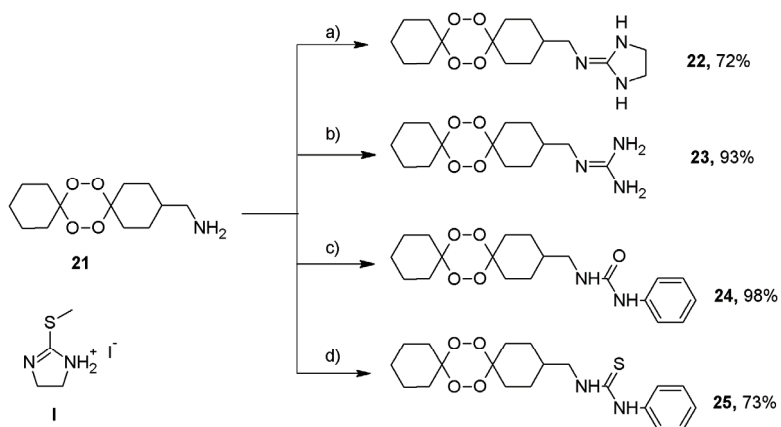
Synthesis

Synthesis of targeted derivatives is presented in Schemes 1 and 2. The key intermediary tetraoxane amine **21** was prepared according to a previously described procedure (Scheme 1).^{35c} In brief, cyclohexane was transformed into *gem*-dihydroperoxide **17** using 50 % H₂O₂ in the presence of Re₂O₇ as catalyst,³⁶ which was further coupled with benzyl 4-oxocyclohexanecarboxylate **15**^{35a,37} producing tetraoxane benzyl ester **18**. The presence of the benzyl-group enabled a more efficacious purification of the crude product using a Biotage SP chromatography system. Reduction with LiAlH₄ produced alcohol **19**, which was transformed *via* the corresponding azide **20** into amine **21**. Final derivatives **22–25** (Scheme 2) were obtained from **21** and corresponding coupling reactants, in high to excellent yield (72–98 %). All derivatives were fully characterized and their purity, as determined by HPLC, was ≥95 %, with the exception of compound **23** that was 79–81 % pure. Full details are given in the Experimental and the Supplementary material to this paper.



<i>IC</i> ₅₀ (D6) = 90.56 nM
<i>IC</i> ₅₀ (W2) = 54.70 nM
<i>IC</i> ₅₀ (TM91C235) = 116.0 nM
<i>IC</i> ₅₀ (TM90C2B) = 52.07 nM

Scheme 1. Reaction pathway for the synthesis of derivative **21**.



a) I, MeOH, TEA, 70 °C; b) S-methylthiourea sulphate, MeOH, TEA, 70 °C;
 c) phenyl isocyanate, CH₂Cl₂, r.t.; d) phenyl isothiocyanate, CH₂Cl₂, r.t.;

Scheme 2. Reaction pathway for the synthesis of derivatives **22–25**.

In the ¹H-NMR spectra, all derivatives showed a characteristic signal at around 3.0 ppm for the methylene groups bonded to the polar groups (imidazoline, guanidine, urea or thiourea), and characteristic signals for the introduced polar groups: singlet at 3.38 ppm for the ethylene group in **22** and multiplets in the region 7.50–6.80 ppm for the aromatic protons in **24** and **25**. In the ¹³C-NMR spectra, all derivatives showed signals for peroxy-acetal carbons in 107–108 ppm region and signals in the 45–50 ppm region for the methylene groups bonded to the polar groups. Additionally, a signal at 160 ppm for sp² carbon in polar groups in **22**, **23** and **24**, and a signal at 180 ppm for **25** were present. Furthermore, aromatic carbons from the phenyl-groups in **24** and **25** appeared in the 117–140 ppm region.

Antimalarial activity

Compounds were screened *in vitro* against four *P. falciparum* strains: D6 (CQ susceptible (CQS) strain), W2 (CQ resistant (CQR) strain), TM91C235 (CQ and MFQ resistant) and TM90C2B (atovaquone resistant), following well-established protocols.³⁸ In brief, the Malaria SYBR Green I based fluorescence (MSF) assay is a microtiter plate drug sensitivity assay that uses the presence of malarial DNA as a measure of parasitic proliferation in the presence of antimalarial drugs or experimental compounds. The intercalation of SYBR Green I dye, and its resulting fluorescence, is relative to parasite growth, and a compound that inhibits the growth of the parasite will result in lower fluorescence intensities.

The antimalarial activities are presented in Table I. Tetraoxane **21**^{35c} was also screened here in order to enable a more reliable comparison to be drawn

with the activities of the new derivatives. All derivatives, with the exception of **23**, showed low nanomolar activities against all four strains.

TABLE I. *In vitro* antimarial activities against *P. falciparum* strains and cytotoxicity (PBMC) of tetraoxanes **21–25**; n.t. – not tested

Compd.	<i>P. falciparum</i> , IC_{50} / nM				PBMC, IC_{50} / μM		RI^h	SI^i
	D6 ^a	W2 ^b	TM91C235 ^c	TM90C2B ^d	(-)PHA ^{e,f}	(+)PHA ^g		
21	13.99	7.26	10.81	7.03	185.61	182.22	0.52/ 0.77	13265/25560/ 17165/26388
22	92.75	72.86	208.54	85.89	166.10	168.70	0.79/ 2.25	1791/2280/ 796/1934
23	243.84	494.37	1489.80	n.t.	>200	>200	2.03/ 6.11	820/400/ 134/–
24	36.50	15.97	29.14	21.40	>200	>200	0.44/ 0.80	5480/12525/ 6863/9343
25	16.30	9.94	28.28	n.t.	32.74	32.01	0.61/ 1.73	2008/3295/ 1158/–
ART ^j	6.66	3.79	16.90	6.23	n.t.	n.t.	0.57/ 2.54	
CQ	7.63	462.99	198.70	181.08	n.t.	n.t.	60.70/ 26.05	
MQ	14.69	6.52	80.28	11.60	n.t.	n.t.	0.44/ 5.47	

^a*P. falciparum* African D6 strain; ^b*P. falciparum* Indochina W2 strain; ^c*P. falciparum* TM91C235 strain; ^d*P. falciparum* TM90C2B strain; ^enon-stimulated with PHA; ^fPHA = phytohaemagglutinin, ^gstimulated with PHA; ^hresistance index (RI) is defined as the ratio of the IC_{50} values for the CQR versus CQS strain, W2/D6 and TM91C235/D6, respectively; ⁱselectivity index (SI) is defined as the ratio of the IC_{50} values for PBMC (-)PHA/D6, PBMC (-)PHA/W2, PBMC (-)PHA/TM91C235 and PBMC (-)PHA/TM90C2B, respectively; ^javerage of greater than eight replicates, CQ = chloroquine, MQ = mefloquine

Simultaneously, all derivatives except **23** were more active against the chloroquine-resistant (CQR) W2 strain than against the chloroquine-susceptible (CQS) D6 strain, which could be seen from the favourable RI values. The derivatives were somewhat less active against the multi-drug resistant TM91C235 (CQR and MQR strain) in comparison with the activities exhibited toward the W2 strain. In addition, the corresponding RI values were less favourable, with the exceptions **21** and **25**. However, three of the five derivatives were 7.4–2.8 times more active than MQ against the TM91C235 strain – **21**, $IC_{50} = 10.81$ nM, **24**, $IC_{50} = 29.14$ nM and **25**, $IC_{50} = 28.28$ vs. MQ, $IC_{50} = 80.28$ nM. The most active derivative was **21** that showed exceptional activities against all the resistant strains. Even against the atovaquone resistant strain TM90C2B, this amine showed activities comparable with those of MQ. Removing the basic character of the terminal amino-group attenuates the anti-malarial activity, as seen in the case of compounds **21**, **24** and **25**. Transformation of the primary amino-group into *N*-phenyl urea or thiourea reduced the antimalarial activity. However, **25** pre-

served high activity against the W2 strain, with an IC_{50} of 9.94 nM, which is comparable to those of MQ and **21** with values of 6.52 nM and 7.26 nM, respectively. On the other hand, increasing basic character of the terminal group did not increase the activity unconditionally. Introduction of more basic groups, such as imidazolidine or guanidine, led to a sharp decrease in activity. This was even more striking with the guanidine derivative **23**, which was 17, 68 and 138 times less active than **21** against D6, W2 and TM91C235 strains, respectively. Such sharp decreases in activity caused by more basic groups is in accordance to the behaviour observed with trioxolanes.³⁹ Derivative **23** was also less active than **22**, which makes it the least active compound within this series. Derivatives **22** and **23** have same pK_a values (Table S-I of the Supplementary material to this paper), which are two orders of magnitude higher than the pK_a for **21**, and correlations between pK_a or $\log P$ values (Table S-I) with antimarial activity could not be established.⁴⁰ The derivatives were in general less active than ART against all four strains. Tetraoxane **21** was the only one with activities comparable with those of ART. However, two tetraoxanes **21** and **25** had better RI values compared to that of ART against multi-drug resistant strain TM91C235 – **21**, $RI = 0.77$ and **24**, $RI = 0.80$ vs. ART, $RI = 2.54$.

The toxicity of the compounds was estimated using human normal peripheral blood mononuclear cells (PBMC), non-stimulated (PBMC (-)PHA) and stimulated (PBMC (+) PHA) with PHA (Table I). In general, the PBMC assay for cytotoxicity estimation revealed that all compounds are well tolerated by normal immunocompetent cells, possessing $IC_{50} \geq 32 \mu\text{M}$. In addition, high selectivity indices (*SI*) were obtained for all compounds toward all *P. falciparum* strains. Derivative **21** had the best *SI* indices, which were in the range 13000–26000, depending on the strain. The second best *SI* was exhibited by the urea derivative **24**, which had the lowest cytotoxicity $>200 \mu\text{M}$ and moderate antimarial activities in the range 16–36 nM.

In vitro cytotoxic activity

Cytotoxic activities of the new tetraoxanes and the previous compounds **21** and **20**^{35c} were evaluated against four human cancer cell lines: cervix adenocarcinoma HeLa, melanoma Fem-x, breast adenocarcinoma MDA-MB-361 and chronic myelogenous leukaemia K562 cells.

The intensities of the cytotoxic activities are given in Table II and Fig. 3. First, it should be emphasized that the tested tetraoxanes showed the strongest cytotoxic activities against myelogenous leukaemia K562 cells. The highest cytotoxicity against K562 cells was exerted by derivatives **25** with an IC_{50} of 6.15 μM , **24** with 13.23 μM , and **18**, **20** and **22** with an IC_{50} of ca. 18.5 μM .

TABLE II. *In vitro*^a activities (IC_{50} / μM) of tetraoxanes against cancer cell lines (Fem-x, human melanoma cell line; HeLa, human cervical adenocarcinoma cell line; K562, myelogenous leukaemia cell line; MDA-MB-361, human breast adenocarcinoma cell line) and peripheral blood mononuclear cells (PBMC), non-stimulated or stimulated with PHA (phytohaemagglutinin)

Compd.	Fem-x	HeLa	K562	MDA-MB-361	PBMC (-)PHA	PBMC (+)PHA	$SI_{\text{Fem-x}}^{\text{a}}$	SI_{HeLa}	SI_{K562}	$SI_{\text{MDA-MB-361}}$
21	79.75	63.56	33.68	>100	185.61	182.22	2	3	6	2
18	31.86	27.01	18.84	73.92	>200	>200	6	7	11	3
20	98.82	37.67	18.43	94.7	>200	>200	2	5	11	2
22	43.84	34.56	18.38	80.29	166.10	168.70	4	5	9	2
23	>100	75.66	81.49	90.91	>200	>200	2	3	2	2
24	52.68	39.85	13.23	96.85	>200	>200	4	5	15	2
25	15.67	10.51	6.15	41.13	32.74	32.01	2	3	5	1
cis-Pt	8.10	7.89	5.64	>33.34	>66.67	>66.67	8	8	12	2

^aThe selectivity index (SI) is defined as the ratio of the IC_{50} for PBMC (-)PHA / cancer cell line

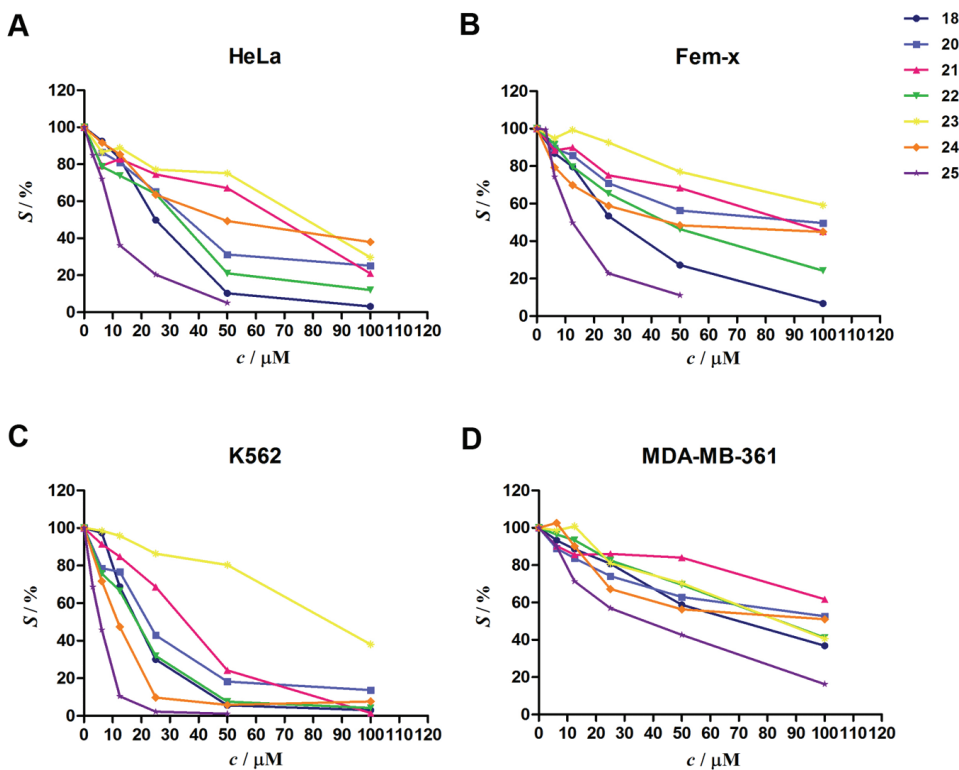


Fig. 3. Survival (S%) of: A) cervical adenocarcinoma HeLa, B) melanoma Fem-x, C) myelogenous leukaemia K562 and D) breast adenocarcinoma MDA-MB-361 cells grown for 72h in the presence of increasing concentrations of the investigated tetraoxanes, determined by MTT test.

Against cervix adenocarcinoma HeLa cells, compounds **18**, **20**, **22**, **24** and **25** exerted pronounced cytotoxic actions with IC_{50} values in the range of 10.51 and 39.85 μM . The highest cytotoxic effect was exhibited by derivative **25** with $IC_{50} = 10.51 \mu\text{M}$. Against melanoma Fem-x cells, compound **25** was the most active with an IC_{50} of 15.67 μM ; derivative **18** exerted pronounced cytotoxic effects with IC_{50} value of 31.86 μM . Compounds **22** and **24** exerted moderate cytotoxic action, while the cytotoxic effects of the other derivatives were lower, with derivative **23** being the least active, showing an IC_{50} value higher than 100 μM . All tested tetraoxanes exerted low cytotoxic actions against breast adenocarcinoma MDA-MB-361 cells with IC_{50} values $>73.92 \mu\text{M}$, except derivative **25** which had moderate activity against this cell line, with an IC_{50} value of 41.13 μM . Tetraoxane **23** with a guanidine group was the least active compound in this series, showing lowest activities towards all cell lines in comparison with other members of the series.

All tetraoxanes exerted selective concentration-dependent cytotoxic activity against specific malignant cell lines, which was especially high against myelogenous leukaemia K562 cells. It is noteworthy that the cytotoxic actions of compounds **21**, **18**, **22**, **24** and **25** were notably higher against K562, HeLa and Fem-x cells than against MDA-MB-361 breast cancer cells, indicating selectivity in their anticancer action against specific malignant cell types.

To further evaluate the anticancer potential of the tested tetraoxanes, their cytotoxic activities were examined against normal healthy peripheral blood mononuclear cells (PBMC), both resting and stimulated to proliferate by mitogen phytohaemagglutinin (PHA), Table II and Fig. 4. Each of the examined tetraoxanes exerted remarkably higher cytotoxic activities against K562, HeLa and Fem-x malignant cell lines than against both non-stimulated and stimulated PBMC, indicating a significant specificity in their anticancer action. The highest

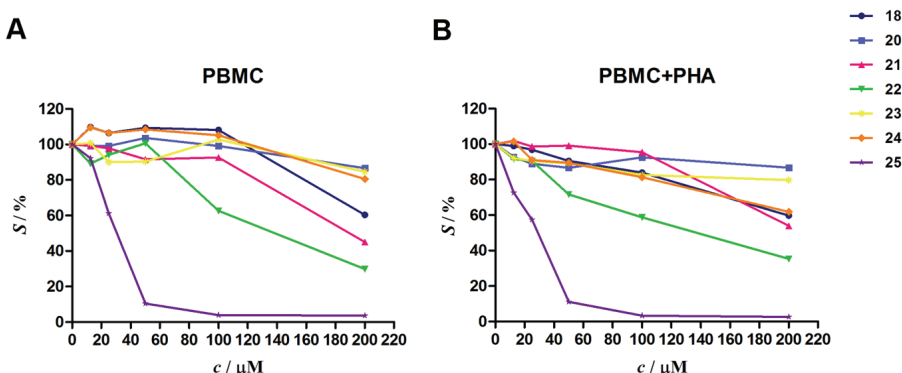


Fig. 4. Survival of (A) resting PBMC and (B) PBMC stimulated to proliferate by PHA grown for 72 h in the presence of increasing concentrations of the investigated tetraoxanes, determined by the MTT test.

selectivity in antitumor action was observed against myelogenous leukaemia K562 cells in comparison with normal healthy PBMC with tetraoxanes **18**, **20** and **24**, which showed the highest SI values, 11, 11 and 15 respectively. In addition, the tested tetraoxanes showed good selectivity as follows: **18** and **24** against cervix adenocarcinoma HeLa and melanoma Fem-x cells, **20** against HeLa cells, and **22** against K562, HeLa and Fem-x cells. Low selectivity in the anticancer action of the tested tetraoxanes was observed against breast adenocarcinoma MDA-MB-361 cells, which showed the lowest sensitivity to the cytotoxic action of these compounds.

In contrast to antimalarial activity, it could not be concluded that activities depend on the presence of a specific functional group. Rather, the activity was specific towards particular cell lines. However, in general, the obtained results showed that derivatives **21–23** with basic groups have lower activities. Derivatives were less active than cisplatin with the exception of derivative **25**. The thiourea derivative **25** was the most active tetraoxane in this series, with IC_{50} values in the range 41–6.0 μ M, which are the same as for cisplatin. However, the low *SI* of **25** for all tested cell lines makes this derivative less interesting, in spite of having good cytotoxic activities. Conversely, derivatives **18**, **20** and **24** had *SI* values for the K562 cell line in the same range as that for cisplatin, which makes them very interesting candidates for further examinations.

The mechanisms of cytotoxic action of **18**, **20** and **24** were examined by cell cycle analysis and morphological assessment of cell death modalities induced by these tetraoxanes using fluorescence microscopy. The tested compounds at IC_{50} concentrations induced time-dependent percentage increases of the target K562 cells in the subG1 phase, as could be seen in Fig. 5. It is noteworthy that compound **20** at the IC_{50} concentration caused the most remarkable increase in the percentage of K562 cells in the subG1 cell cycle phase after 48 h treatment. In addition, treatment with $2IC_{50}$ concentrations of three tetraoxanes resulted in an increase in the percentages of apoptotic subG1 K562 cells after 24 h exposure. After 48h, the percentages of subG1 K562 cells exposed to $2IC_{50}$ concentrations of **18**, **20** and **24** were approximately 12 times higher compared to the control cell sample, pointing to a strong proapoptotic activity of these compounds. Examination of changes in the morphological features confirmed that the tested tetraoxanes triggered apoptosis in K562 leukaemia cells after 24 h treatment. Typical hallmarks of apoptotic K562 cells induced by tetraoxanes, such as shrinkage of the nucleus, chromatin condensation and fragmentation of the nucleus in addition to orange-red stained cells in the final stages of apoptosis are presented in Fig. 6.

Prominent proapoptotic effects of tetraoxanes **18**, **20** and **24** in addition to high selectivity in their anticancer activity against myelogenous leukaemia K562 cells in comparison to normal immunocompetent PBMC, suggest significant anticancer potential of these compounds.

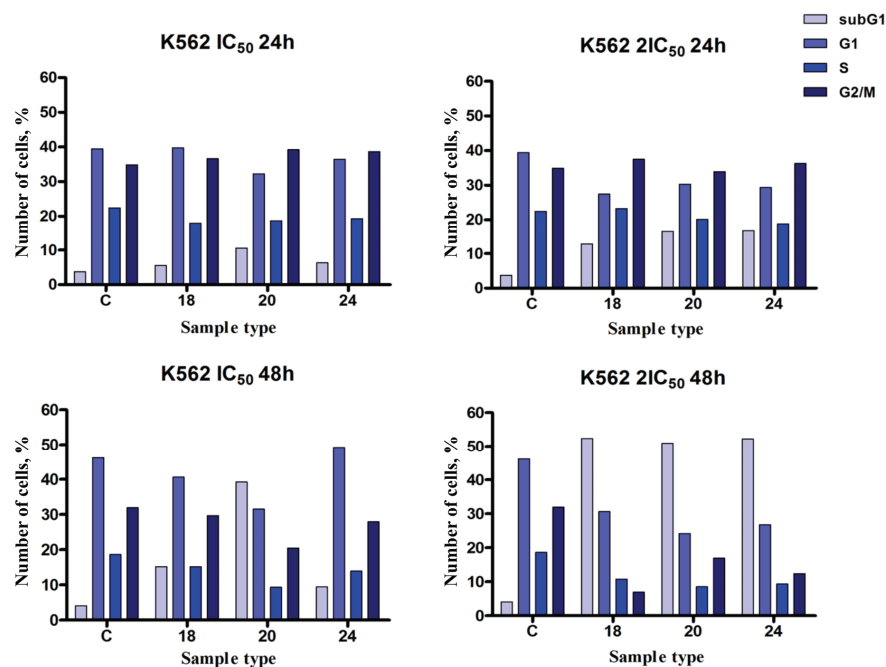


Fig. 5. Changes in the cell cycle phase distribution of K562 cells induced by the investigated tetraoxanes **18**, **20** and **24** (tested concentrations corresponded to IC_{50} and $2IC_{50}$ values).
C: control K562 cell sample.

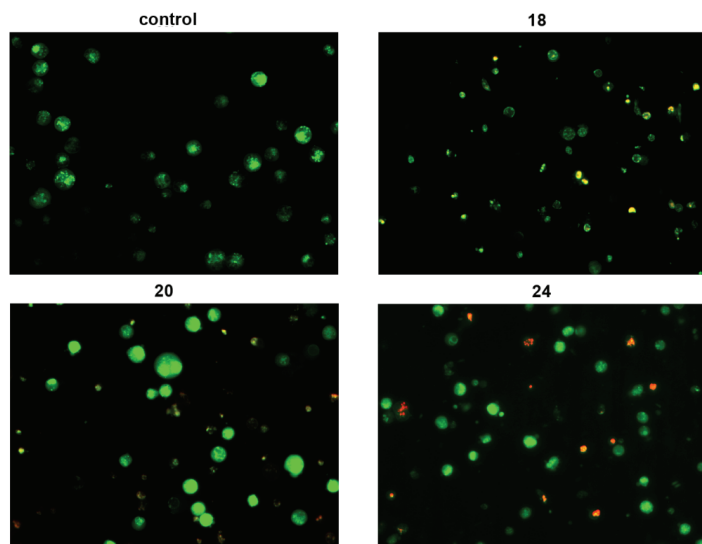


Fig. 6. Photomicrographs of acridine orange/ethidium bromide-stained control K562 cells and K562 cells treated with $2 \times IC_{50}$ concentrations of **18**, **20** and **24**, for 24 h.

*In vivo activity against *T. gondii**

Derivative **21** was chosen for examination of *in vivo* activity against *T. gondii*. The activity was examined in murine models of infection with tachyzoites of the highly virulent RH strain of *T. gondii* following a well-established protocol.⁴¹ The compound exhibited no visible toxicity as judged by the quality of fur, gait and general activity of the uninfected treated mice. The activity of **21** was compared to that of ART.

The results obtained in the treated animals are presented in Fig. 7. In the infection model where infection was established with 10^2 per mL, all untreated mice died between day 6 and day 9 p.i. (mean 8 days). Most importantly, treatment with both **21** and ART in $10 \text{ mg kg}^{-1} \text{ day}^{-1}$ doses allowed survival of 20 % of infected treated mice after 15 days (Fig. 7a). Compared with the control mice, treatment with both drugs significantly prolonged survival, but the effect of **21** was more pronounced ($P = 0.014$) than that of ART ($P = 0.0413$), whereas the effects of the two compounds were mutually comparable ($P = 0.9086$).

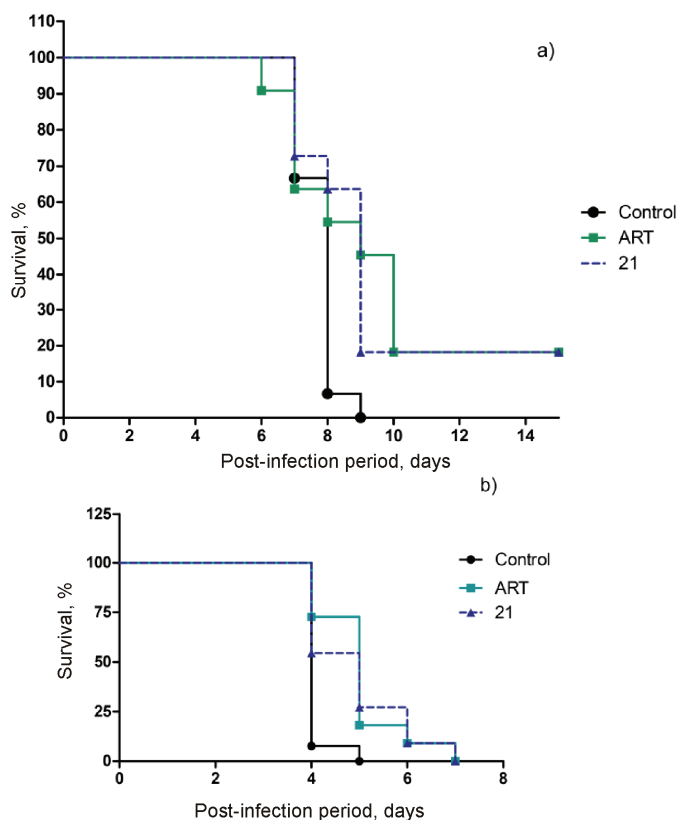


Fig. 7. Survival of infected mice after treatment with **21** or ART; parasite concentration:
a) 10^2 and b) 10^6 mL^{-1} .

In mice infected with 10^6 mL $^{-1}$, all untreated mice died within 5 days. Compared to these, treatment with either **21** or ART significantly prolonged survival ($P = 0.0092$ and $P = 0.0013$, respectively) but did not afford complete protection. The antitoxoplasmatic activity of the two compounds was similar ($P = 0.8358$).

Pathohistological analysis was performed on all surviving infected treated mice (four treated with **21** and two treated with ART), as well as on representative controls (non-infected treated mice), which were all sacrificed day 24 p.i. No pathological changes other than extramedullary haematopoiesis (characteristic of these mice) and mild lymphocyte infiltration of the liver were revealed in both **21** and ART-treated mice, except for the finding of focal myocarditis in one ART-treated infected mouse. These results indicate no significant macroscopic or microscopic toxicity of the tested compounds, and moreover, show the potential of derivative **21** to clear *T. gondii* infection.

EXPERIMENTAL

Chemistry

Melting points were determined on a Boetius PMHK or a Mel-Temp apparatus and were not corrected. Optical rotations were measured on a Rudolph Research analytical automatic polarimeter, Autopol IV in dichloromethane (DCM) or methanol (MeOH) as solvent. The IR spectra were recorded on a Perkin-Elmer FT-IR 1725X spectrophotometer. The ^1H - and ^{13}C -NMR spectra were recorded on a Varian Gemini-200 spectrometer (at 200 and 50 MHz, respectively), and on a Bruker Ultrashield Advance III spectrometer (at 500 and 125 MHz, respectively) employing the indicated solvents (Supplementary material) using TMS as the internal standard. Chemical shifts are expressed in ppm (δ) values and coupling constants (J) in Hz. The ESI-MS spectra were recorded on an Agilent Technologies 6210 Time-Of-Flight LC-MS instrument in the positive ion mode with $\text{CH}_3\text{CN}/\text{H}_2\text{O}$ 1/1 with 0.2 % HCOOH as the carrying solvent solution. The samples were dissolved in CH_3CN or MeOH (HPLC grade purity). The selected values were as follows: capillary voltage, 4 kV; gas temperature, 350 °C; drying gas, 12.1 min $^{-1}$; nebulizer pressure, 310 kPa and fragmentator voltage, 70 V. Elemental analyses were realized on the Vario EL III- C,H,N,S/O elemental analyzer (Elementar Analysensysteme GmbH, Hanau, Germany). Thin-layer chromatography (TLC) was performed on precoated Merck silica gel 60 F₂₅₄ and RP-18 F₂₅₄ plates. Column chromatography was performed on Lobar LichroPrep Si 60 (40–63 µm), or RP-18 (40–63 µm) columns coupled to a Waters RI 401 detector, and on Biotage SP1 system with a UV detector and FLASH 12+, FLASH 25+ or FLASH 40+ columns charged with KP-SIL (40–63 µm, pore diameter 60 Å), or KP-C18-HS (40–63 µm, pore diameter 90 Å) as adsorbent. Compounds **18** and **20–25** were analyzed for purity (HPLC) using an Agilent 1200 HPLC system equipped with Quat pump (G1311B), injector (G1329B) 1260 ALS, TCC 1260 (G1316A) and a 1260 Infinity refractive index detector (RID) was. HPLC analyses were performed in two diverse systems. Method A: Zorbax Eclipse Plus C18, 4.6 mm×150 mm, 1.8 µm, S.N. USWKY01594 was used as the stationary phase. The compounds were eluted using an isocratic protocol and eluent was made from water/MeOH, 30/70 (V/V). The compounds were dissolved in methanol; the final concentrations were 0.5 mg mL $^{-1}$. Method B: Poroshell 120 EC-C18, 4.6 mm×50 mm, 2.7 µm, S.N. USCFSU07797 was used as the stationary phase. The compounds were

eluted using an isocratic protocol and the eluent was made from water/MeOH, 30/70 (*V/V*). The compounds were dissolved in methanol; the final concentrations were 0.5 mg mL⁻¹.

Synthetic procedures

Benzyl 7,8,15,16-tetraoxadispiro[5.2.5.2]hexadecane-3-carboxylate (18). Into ice-cold (ice–water mixture) solution of *gem*-dihydroperoxide **17** (412.7 mg, 2.53 mmol) and ketone **15** (374.8 mg, 2.53 mmol) in CH₂Cl₂ (5 mL), under intensive stirring, precooled freshly prepared solution of conc. H₂SO₄/CH₃CN (1/10, *V/V*, 1.82 mL) was added dropwise. After one hour stirring at the same temperature, the reaction was quenched with water and the layers were separated. Water layer was extracted with CH₂Cl₂ (3×50 mL). The combined organic layers were washed with sat. NaHCO₃ (3×20 mL), brine (2×10 mL) and dried over anh. Na₂SO₄. The solvent was removed under reduce pressure and the product was isolated after column chromatography purification (dry-flash, SiO₂-column, eluent hexane/EtOAc, gradient 97/3 → 9/1). Yield: 241.9 mg (26 %), as an amorphous powder.

N-(7,8,15,16-Tetraoxadispiro[5.2.5.2]hexadec-3-ylmethyl)-4,5-dihydro-1*H*-imidazol-2-amine (22). A mixture of **21** (100.0 mg, 0.39 mmol), **I** (142.2 mg, 0.58 mmol) and Et₃N (0.5 mL) in methanol (3 mL) was stirred under an inert atmosphere (Ar) for 3 days at 70 °C. The solvent was evaporated, the residue dissolved in CH₂Cl₂, 10 % NaOH solution added and the mixture intensively shaken. The layers were separated, the organic layer was washed once with water, once with brine and dried over anh. Na₂SO₄. The solvent was removed under reduce pressure and the product isolated after column chromatography purification (Lobar, SiO₂-column A, eluent CH₂Cl₂/CH₃OH sat. NH₃ = 1/1). Yield: 91 mg (72 %).

1-(7,8,15,16-Tetraoxadispiro[5.2.5.2]hexadec-3-ylmethyl)guanidine (23). A mixture of **21** (100.0 mg, 0.39 mmol), *S*-methylthiourea sulphate (162.0 mg, 0.58 mmol) and Et₃N (0.5 mL) in methanol (3 mL) was stirred at 70 °C under an inert atmosphere (Ar) for 3 days. Into the warm solution, methanol was added (10 mL) and the warm mixture was filtered, the solvent removed under reduce pressure and product isolated after column chromatography purification (dry-flash, SiO₂-column, gradient CH₂Cl₂/MeOH, = 9/1 → 1/1) as a pale yellow oil that became solid with time. Yield: 108.6 mg (93 %).

1-Phenyl-3-(7,8,15,16-tetraoxadispiro[5.2.5.2]hexadec-3-ylmethyl)urea (24). A mixture of **21** (150.0 mg, 0.58 mmol) and phenyl-isocyanate (63.4 µL, 0.58 mL) in CH₂Cl₂ (10 mL), was stirred at r.t. under an inert atmosphere (Ar) for 45 min. The solvent was evaporated and product isolated after column chromatography purification (dry-flash, SiO₂-column, gradient hexane/EtOAc = 1/1 → EtOAc → EtOAc/MeOH = 7/3). Yield: 215 mg (98 %).

1-Phenyl-3-(7,8,15,16-tetraoxadispiro[5.2.5.2]hexadec-3-ylmethyl)thiourea (25). A mixture of **21** (78.2 mg, 0.30 mmol) and phenyl-iso thiocyanate (35.57 µL, 0.30 mL) in CH₂Cl₂ (15 mL) was stirred under an inert atmosphere at r.t. for 2 h. The solvent was removed under reduce pressure and the product isolated after column chromatography purification (dry-flash, SiO₂-column, gradient hexane/EtOAc = 9/1 → EtOAc). Yield: 87.3 mg (73 %).

In vitro antimalarial activity

The *in vitro* antimalarial drug susceptibility screen is a modification of the procedures first published by Desjardins *et al.*⁴² with modifications developed by Milhous *et al.*, the details of which are given in ref. 8b. All the synthesized aminoquinolines were screened *in vitro* against the *P. falciparum* strains CQ and MFQ, as well as the susceptible strain D6 (clone of the Sierra I/UNC isolate), the CQ resistant but MFQ susceptible strain W2 (clone of the Indochina I isolate), and the CQ and MFQ resistant strain TM91C235 (clone of the South-East Asian isolate), and TM90C2B (clone of the Thailand isolate).

Cytotoxic activity

Reagents. Stock solutions of investigated tetraoxanes were prepared in dimethyl sulfoxide (DMSO) at concentrations of 10 mM and subsequently diluted with complete nutrient medium (RPMI-1640 without phenol red) supplemented with 3 mmol L⁻¹ L-glutamine, 100 µg mL⁻¹ streptomycin, 100 IU mL⁻¹ penicillin, 10 % heat inactivated foetal bovine serum (FBS), and 25 mM HEPES, and adjusted to pH 7.2 with bicarbonate solution. RPMI-1640, FBS, HEPES, and L-glutamine were purchased from Sigma-Aldrich, St. Louis, MO, USA.

Cell cultures. Human cervical adenocarcinoma HeLa, human melanoma Fem-x and human breast adenocarcinoma MDA-MB-361 cells were cultured as a monolayer, while human chronic myelogenous leukaemia K562 cells were grown in a suspension in the complete nutrient medium, at 37 °C in a humidified air atmosphere with 5 % CO₂, as previously described.⁴³

Preparation of peripheral blood mononuclear cells (PBMC). PBMC were separated from whole heparinised blood (obtained from two healthy volunteers) by Histopaque®-1077 (Sigma-Aldrich) density gradient centrifugation. Interface cells, washed three times with Haemaccel (aqueous solution supplemented with 145 mM Na⁺, 5.1 mM K⁺, 6.2 mM Ca²⁺, 145 mM Cl⁻ and 35 g L⁻¹ gelatine polymers, pH 7.4), were counted and suspended in nutrient medium with 10 % FBS.⁴³

Treatment of human malignant cell lines. HeLa (2,000 cells per well), Fem-x (5,000 cells per well) and MDA-MB-361 cells (10,000 cells per well) were seeded into 96-well microtiter plates. Twenty hours later, after cell adherence, five different concentrations of the investigated compounds in complete nutrient medium were added to the cells (range 6.25–100 µM or 3.125–50 µM), except for the control cells to which nutrient medium only was added. K562 cells (5,000 cells per well) were seeded two hours before addition of the investigated compounds to obtain final concentrations within the above-mentioned range. All experiments were realised in triplicate. Cisplatin was used as a positive control.

Treatment of PBMC from healthy donors. PBMC cells were seeded at a density of 150,000 cells per well in nutrient medium only, or in the nutrient medium enriched with 5 µg mL⁻¹ of phytohaemagglutinin (PHA – INEP, Belgrade, Serbia) in 96-well microtiter plates. Two hours later, five different concentrations of the investigated tetraoxanes were added to the wells with non-stimulated and PHA-stimulated PBMC (in order to obtain five final concentrations within the range of 12.5–200 µM). All experiments were realised in triplicate. Cisplatin was used as a positive control.

Determination of cell survival. Cell survival 72 h after addition of the drug was determined by the MTT test according to the method of Mosmann⁴⁴ as modified by Ohno and Abe.⁴⁵ Briefly, 10 µL of MTT solution (3-(4,5-dimethylthiazol-2-yl)-2,5-diphenyltetrazolium bromide, 5 mg mL⁻¹ in phosphate buffered saline) was added to each well.⁴³ The samples were incubated for a further four hours at 37 °C in a humidified atmosphere with 5 % CO₂. Then, 100 µL of 10 % SDS solution was added to the wells. The absorbance was measured at 570 nm the next day. To obtain cell survival (*S* / %), the absorbance at 570 nm of a sample with cells grown in the presence of various concentrations of agent was divided by the absorbance of the control sample (the absorbance of cells grown only in nutrient medium), implying that the absorbance of the blank was always subtracted from the absorbance of a corresponding sample with target cells. The *IC*₅₀ concentration was defined as the concentration of an agent inhibiting cell survival by 50 %, compared to the corresponding control.

Cell cycle analysis. K562 cells were exposed to two different concentrations of the examined compounds **18**, **20** and **24** (corresponding to the *IC*₅₀ and 2*IC*₅₀ values determined

after 72 h treatment) for 24 and 48 h. After incubation, the target cells were collected, washed and fixed in 70 % ethanol on ice. The cell samples were stored at -20 °C for at least one week before staining. The cells were collected by centrifugation, washed, resuspended in PBS containing RNase A at a final concentration of 200 µg mL⁻¹ and incubated for 30 min at 37 °C. Subsequently, the propidium iodide solution was added to the cells at a final concentration of 40 µg mL⁻¹.⁴³

The phase distribution of the cell cycle was determined using a FACSCalibur flow cytometer (BD Biosciences, Franklin Lakes, NJ, USA). The data (10,000 events collected for each sample) were analysed using CELLQuest software (BD Biosciences).

Morphological evaluation of K562 cell death. To examine the mode of death of human chronic myelogenous leukaemia K562 cells induced by the investigated tetraoxanes, morphological analysis by microscopic examination of acridine orange/ethidium bromide-stained target cells was performed, as already described.⁴³ The K562 cells were seeded in 6-well plates (200,000 cells per well) in complete nutrient medium. After 2 h, the cells were treated with the investigated compounds for 24 h at concentrations corresponding to double the IC_{50} values obtained after 72 h treatments. After this period, the target cells were collected by centrifugation and stained with 20 µL of a mixture of acridine orange and ethidium bromide (3 µg mL⁻¹ AO and 10 µg mL⁻¹ EB in PBS) dyes, and visualized under a fluorescence microscope – Carl Zeiss PALM MicroBeam with Axio Observer.Z1 using AxioCam MRm (filters Alexa 488 and Alexa 568).

Anti-toxoplasmatic activity

Mice. Female Swiss Webster mice (Medical Military Academy Animal Research Facility, Belgrade, Serbia) weighing 18 to 20 g at the beginning of each experiment were used. The mice were housed six to a cage and offered drinking water *ad libitum*.

T. gondii. Tachyzoites of the virulent RH strain maintained through serial intraperitoneal (i.p.) passages were used. For the experimental infections, tachyzoites were harvested from mouse peritoneal fluids 72 h post infection and purified by centrifugation, cotton wool filtration, and needle extraction. The parasites were counted in a haemocytometer, and their numbers were adjusted to 2×10⁶ mL⁻¹ with saline. The suspensions were also serially 10-fold diluted, and 0.5-mL aliquots of 2×10² and 2×10⁶ mL⁻¹ dilutions were inoculated i.p. into fresh mice.

Infected non-treated mice served as infection controls. Mice were randomly assigned into experimental groups and treated with **21** or ART. Both drugs were administered at a dose of 0.2 mg per mouse per day (10 mg kg⁻¹ day⁻¹), subcutaneously (s.c.) for 8 consecutive days starting from the day of infection (day 0). Survival of the mice was monitored for another week after the end of treatment, meaning a total follow-up period of 15 days post infection (p.i.). To control for drug side effects (toxicity), separate groups of non-infected animals were given **21** (10 mg kg⁻¹ day⁻¹) and ART (10 mg kg⁻¹ day⁻¹) in the same manner and duration as in the experimental groups.

Statistical analysis

The rates of survival in particular treatment groups were estimated by the Kaplan–Meier product limit method and compared by the log-rank test. The level of statistical significance was 0.05.

CONCLUSIONS

Herein, the synthesis and biological activity of new cyclohexylidene mixed 1,2,4,5-tetraoxanes containing polar guanidine and urea based groups were reported. Four new tetraoxanes were tested *in vitro* against *P. falciparum* CQR and CQS strains. The derivatives showed moderate nanomolar antimarial activities, and differences in activities were clearly influenced by changes in the structures of the introduced polar groups. The *N*-phenylurea derivative **24** showed the best resistance indices ($RI_{W2} = 0.44$, $RI_{TM91C235} = 0.80$), the highest *SI* score against all four tested *P. falciparum* strains and the lowest toxicity against PBMC ($IC_{50} > 200 \mu\text{M}$). Seven tetraoxanes were tested *in vitro* against four human cancer cell lines and five of them showed pronounced cytotoxic effects against myelogenous leukaemia K562 cells in $6.15\text{--}18.84 \mu\text{M}$ concentrations with high SI_{K562} index. The amino-tetraoxane **21** was the first one evaluated for its anti *T. gondii* effect *in vivo*, in a murine model of acute toxoplasmosis. An 8-day treatment at a dose of $10 \text{ mg kg}^{-1} \text{ day}^{-1}$ allowed survival of 20 % of the infected mice. The obtained results clearly showed the activity of the investigated tetraoxanes against acute murine toxoplasmosis, suggesting the potential of synthetic organic peroxides in *T. gondii* treatment.

SUPPLEMENTARY MATERIAL

Calculated pK_a and $\log P$ values for derivatives **21**–**23**, synthetic procedures for derivatives **13**–**17** and **19**–**21** and analytical data for derivatives **13**–**25** and HPLC chromatograms for determination of the purity of tested compounds are available electronically from <http://www.shd.org.rs/JSCS/>, or from the corresponding author on request.

Acknowledgements. This work was supported by the Ministry of Education, Science and Technological Development of the Republic of Serbia (Grants 172008 and 175011).

ИЗВОД

ТЕТРАОКСАНИ КАО ИНХИБИТОРИ АПИКОМПЛЕКСНИХ ПАРАЗИТА *Plasmodium falciparum* И *Toxoplasma gondii* И АНТИ-КАНЦЕРСКИ МОЛЕКУЛИ

ДЕЈАН М. ОПСЕНИЦА¹, ЈЕЛЕНА РАДИВОЈЕВИЋ², ИВАНА З. МАТИЋ³, ТИЈАНА ШТАЈНЕР⁴,
СЛАВИЦА КНЕЖЕВИЋ-УШАЈ⁵, ОЛГИЦА ЂУРКОВИЋ-ЂАКОВИЋ⁴ И БОГДАН А. ШОЛАЈА⁶

¹Институут за хемију, технолохију и међалурерију, Универзитет у Београду, Његошева 12, 11000 Београд, ²Институут за молекуларну генетику и генетички инжењеринг, Универзитет у Београду, Војводе Степе 444а, бр. 23, 11010 Београд, ³Институут за онкологију и радиологију Србије, Пасјевова 14, 11000 Београд, ⁴Национална референтна лабораторија за шоксилазмуз, Институут за медицинска истраживања, Универзитет у Београду, гр Суботића 4, бр. 102, 11129 Београд, ⁵Институут за патологију, Медицински факултет, Универзитет у Новом Саду, Хајдук Вељкова 3, 21000 Нови Сад и ⁶Хемијски факултет, Универзитет у Београду, Студентски трг 12–16, бр. 51, 11158 Београд

Синтетисана је група нових циклохексилиденских 1,2,4,5-тетраоксана који имају гванидино и уреидо поларне групе и испитана је њихова антималијска активност према хлорокивин-резистентним и осетљивим сојевима *Plasmodium falciparum*. Деривати

показују умерене активности у nM опсегу и ниску цитотоксичност. Дериват *N*-фенил-уреа **24** има најбољи индекс резистенције ($RI_{W2} = 0,44$; $RI_{TM91C235} = 0,80$) и није токсичан према хуманим нормалним мононуклеарним ћелијама периферне крви ($IC_{50} > 200 \mu\text{M}$). Седам деривата је тестирано *in vitro* према четири хумане малигне ћелијске линије и показало је високу селективност према K562 ћелијама леукемије. Дериват **21** који има примарну амино групу је први тетраоксан тестиран *in vivo* према још једном паразиту из филума Apicomplexa, *Toxoplasma gondii*. Приликом супутног администрирања, дневна доза од 10 mg kg^{-1} омогућила је преживљавање 20 % инфицираних мишева, што показује висок потенцијал тетраоксана за терапију инфекција изазваних апикомплексним паразитима.

(Примљено 30. априла, ревидирано и прихваћено 22. јуна 2015)

REFERENCES

1. S. I. Hay, C. A. Guerra, A. J. Tatem, A. M. Noor, R. W. Snow, *Lancet*, **4** (2004) 327
2. a) D. M. Opsenica, B. A. Šolaja, *J. Serb. Chem. Soc.* **74** (2009) 1155, and references cited therein; b) I. Opsenica, N. Terzić, D. Opsenica, G. Angelovski, M. Lehnig, P. Eilbracht, B. Tinant, Z. Juranić, K. S. Smith, Z. S. Yang, D. S. Diaz, P. L. Smith, W. K. Milhous, D. Đoković, B. A. Šolaja, *J. Med. Chem.* **49** (2006) 3790
3. P. M. O'Neill, V. E. Barton, S. A. Ward, J. Chadwick, *4-Aminoquinoline: Chloroquine, Amodiaquine and Next-Generation Analogues*, in *Treatment and Prevention of Malaria: Antimalarial Drug Chemistry, Action and Use*, H. M. Staines, S. Krishna, Eds., Springer, Basel, 2012, p. 19
4. A. Ecker, A. M. Lehane, D. A. Fidock, *Molecular Markers of Plasmodium Resistance to Antimalarials*, in *Treatment and Prevention of Malaria: Antimalarial Drug Chemistry, Action and Use*, H. M. Staines, S. Krishna, Eds., Springer, Basel, 2012, p. 249
5. P. D. Roepe, *Biochemistry* **50** (2011) 163
6. a) D. M. Opsenica, B. A. Šolaja, *Second-Generation Peroxides: The OZs and Artemisone*, in *Treatment and Prevention of Malaria: Antimalarial Drug Chemistry, Action and Use*, H. M. Staines, S. Krishna, Eds., Springer, Basel, 2012, p. 211; b) R. D. Slack, A. M. Jacobine, G. H. Posner, *Med. Chem. Commun.* **3** (2012) 281; c) N. Kumar, R. Singh, D. S. Rawat, *Med. Res. Rev.* **32** (2012) 581; d) J. L. Vennerstrom, S. Arbe-Barnes, R. Brun, S. A. Charman, F. C. K. Chiu, J. Chollet, Y. Dong, A. Dorn, D. Hunziker, H. Matile, K. McIntosh, M. Padmanilayam, J. T. Santo, C. Scheurer, B. Scorneaux, Y. Tang, H. Urwyler, S. Wittlin, W. N. Charman, *Nature* **430** (2004) 900
7. a) R. K. Haynes, W.-C. Chan, H.-N. Wong, K.-Y. Li, W.-K. Wu, K.-M. Fan, H. H. Y. Sung, I. D. Williams, D. Prosperi, S. Melato, P. Coghi, D. Monti, *ChemMedChem* **5** (2010) 1282; b) R. K. Haynes, K.-W. Cheu, M. M.-K. Tang, M.-J. Chen, Z.-F. Guo, Z.-H. Guo, P. Coghi, D. Monti, *ChemMedChem* **6** (2011) 279
8. a) M. Videnović, D. M. Opsenica, J. C. Burnett, L. Gomba, J. E. Nuss, Ž. Selaković, J. Konstantinović, M. Krstić, S. Šegan, M. Zlatović, R. J. Sciotti, S. Bavari, B. A. Šolaja, *J. Med. Chem.* **57** (2014) 4134; b) I. M. Opsenica, M. Tot, L. Gomba, J. E. Nuss, R. J. Sciotti, S. Bavari, J. C. Burnett, B. A. Šolaja, *J. Med. Chem.* **56** (2013) 5860; c) I. M. Opsenica, K. K. Smith, L. Gerena, S. Gaica, B. A. Šolaja, *J. Serb. Chem. Soc.* **73** (2008) 1021
9. M. Tot, D. M. Opsenica, M. Mitić, J. C. Burnett, L. Gomba, S. Bavari, B. A. Šolaja, *J. Serb. Chem. Soc.* **78** (2013) 1847, and references cited therein
10. a) K. Kaur, M. Jain, R. P. Reddy, R. Jain, *Eur. J. Med. Chem.* **45** (2010) 3245; b) E. Milner, W. McCalmont, J. Bhonsle, D. Caridha, J. Cobar, S. Gardner, L. Gerena, D.

- Goodine, C. Lanteri, V. Melendez, N. Roncal, J. Sousa, P. Wipf, G. S. Dow, *Malaria J.* **9** (2010), doi:10.1186/1475-2875-9-51; c) C. A. Lanteri, J. D. Johnson, N. C. Waters, *Recent Pat. Antiinfect. Drug Discov.* **2** (2007) 95
11. J. G. Montoya, O. Liesenfeld, *Lancet* **363** (2004) 1965
 12. a) F. Berger, V. Goulet, Y. Le Strat, J. C. Desenclos, *Bull. Epidemiol. Hebd. (Paris)* **14** (2008) 117; b) B. Bobić, A. Nikolić, I. Klun, O. Djurković-Djaković, *Wien Klin. Wochenschr.* **123** (2011) Suppl. 1 and 2
 13. a) E. A. Figueiró-Filho, F. R. Senefonte, A. H. Lopes, O. O. de Moraes, V. G. Souza Júnior, T. L. Maia, G. Duarte, *Rev. Soc. Bras. Med. Trop.* **40** (2007) 181; b) B. Carme, F. Bissuel, D. Ajzenberg, R. Bouyne, C. Aznar, M. Demar, S. Bichat, D. Louvel, A. M. Bourbigot, C. Peneau, P. Neron, M. L. Darde, *J. Clin. Microbiol.* **40** (2002) 4037
 14. O. Djurković-Djaković, *Srp. Arh. Celok Lek.* **126** (1998) 197
 15. E. Moine, C. Denevault-Sabourin, F. Debierre-Grockiego, L. Silpa, O. Gorgette, J.-C. Barale, P. Jacquiet, F. Brossier, A. Gueiffier, I. Dimier-Poisson, C. Enguehard-Gueiffier, *Eur. J. Med. Chem.* **89** (2015) 386e400, doi 0.1016/j.ejmech.2014.10.057
 16. D. Kadri, A. K. Crater, H. Lee, V. R. Solomon, S. Ananvoranich, *Exp. Parasitol.* **145** (2014) 135
 17. B. L. Howard, K. L. Harvey, R. Stewart, M. F. Azevedo, B. S. Crabb, I. G. Jennings, P. R. Sanders, D. T. Manallack, P. E. Thompson, C. J. Tonkin, P. R. Gilson, *ACS Chem. Biol.* **10** (2015) 1145
 18. K. Dzitko, A. Paneth, T. Plech, J. Pawełczyk, L. Węglińska, P. Paneth, *Antimicrob. Agents Chemother.* **58** (2014) 7583
 19. C. P. Hencken, L. Jones-Brando, C. Bordon, R. Stohler, B. T. Mott, R. Yolken, G. H. Posner, L. E. Woodard, *J. Med. Chem.* **53** (2010) 3594
 20. A. E. Vercesi, C. O. Rodrigues, S. A. Uyemura, L. Zhong, S. N. J. Moreno, *J. Biol. Chem.* **273** (1998) 31040
 21. a) J. McAuley, K. M. Boyer, D. Patel, M. Mets, C. Swisher, N. Roizen, C. Wolters, L. Stein, M. Stein, W. Schey, J. Remington, P. Meier, D. Johnson, P. Heydeman, E. Holfels, S. Withers, D. Mack, C. Brown, D. Patton, R. McLeod, *Clin. Infect. Dis.* **18** (1994) 38; b) A. B. Foot, Y. J. Garin, P. Ribaud, A. Devergie, F. Derouin, E. Gluckman, *Bone Marrow Transpl.* **14** (1994) 241
 22. S. M. Johnson, R. C. Murphy, J. A. Geiger, A. E. DeRocher, Z. Zhang, K. K. Ojo, E. T. Larson, B. G. K. Perera, E. J. Dale, P. He, M. C. Reid, A. M. W. Fox, N. R. Mueller, E. A. Merritt, E. Fan, M. Parsons, W. C. Van Voorhis, D. J. Maly, *J. Med. Chem.* **55** (2012) 2416
 23. Z. Zhang, K. K. Ojo, R. S. R. Vidadala, W. Huang, J. A. Geiger, S. Scheele, R. Choi, M. C. Reid, K. R. Keyloun, K. Rivas, L. K. Siddaramaiah, K. M. Comess, K. P. Robinson, P. J. Merta, L. Kifle, W. G. J. Hol, M. Parsons, E. A. Merritt, D. J. Maly, C. L. M. J. Verlinde, W. C. Van Voorhis, E. Fan, *ACS Med. Chem. Lett.* **5** (2014) 40
 24. S. N. Mageed, F. Cunningham, A. W. Hung, H. L. Silvestre, S. Wen, T. L. Blundell, C. Abell, G. A. McConkey, *Antimicrob. Agents Chemother.* **58** (2014) 6345
 25. K. Nagamune, S. N. J. Moreno, L. D. Sibley, *Antimicrob. Agents Chemother.* **51** (2007) 3816
 26. K. Nagamune, W. L. Beatty, L. D. Sibley, *Eukaryot. Cell* **6** (2007) 2147
 27. I. R. Dunay, W. C. Chan, R. K. Haynes, L. D. Sibley, *Antimicrob. Agents Chemother.* **51** (2007) 2147
 28. J. G. D'Angelo, C. Bordón, G. H. Posner, R. Yolken, L. Jones-Brando, *J. Antimicrob. Chemother.* **63** (2009) 146

29. K. Ou-Yang, E. C. Krug, J. J. Marr, R. L. Berens, *Antimicrob. Agents Chemother.* **34** (1990) 1961
30. a) G. L. Firestone, S. N. Sundar, *Expert. Rev. Mol. Med.* **11** (2009) e32; b) M. P. Crespo-Ortiz, M. Q. Wei, *J. Biomed. Biotechnol.* **2012** (2012) 247597, and references cited therein
31. A. M. Gravett, W. M. Liu, S. Krishna, W.-C. Chan, R. K. Haynes, N. L. Wilson, A. G. Dalgleish, *Cancer Chemother. Pharmacol.* **67** (2011) 569
32. I. N. Cvjetić, Ž. P. Žižak, T. P. Stanojković, Z. D. Juranić, N. Terzić, I. M. Opsenica, D. M. Opsenica, I. O. Juranić, B. J. Drakulić, *Eur. J. Med. Chem.* **45** (2010) 4570
33. R. H. van Huijsdijnen, R. K. Guy, K. Chibale, R. K. Haynes, I. Peitz, G. Kelter, M. A. Phillips, J. L. Vannerstrom, Y. Yuthavong, T. N. C. Wells, *PLoS One* **8** (2013) e82962, doi:10.1371/journal.pone.0082962
34. Z. Y. Zhang, S. Q. Yu, L. Y. Miao, X. Y. Huang, X. P. Zhang, Y. P. Zhu, X. H. Xia, D. Q. Li, *Chin. J. Integr. Med.* **6** (2008) 134; b) S. Krishna, S. Ganapathi, I. C. Ster, M. E. M. Saeed, M. Cowan, C. Finlayson, H. Kovacsevics, H. Jansen, P. G. Kremsner, T. Efferth, D. A. Kumar, *EBioMedicine* **2** (2015) 82
35. a) I. Opsenica, N. Terzić, D. Opsenica, W. K. Milhous, B. Šolaja, *J. Serb. Chem. Soc.* **69** (2004) 919; b) I. Opsenica, D. Opsenica, M. Jadranin, K. Smith, W. K. Milhous, M. Stratakis, B. Šolaja, *J. Serb. Chem. Soc.* **72** (2007) 1181; c) I. Opsenica, D. Opsenica, K. S. Smith, W. K. Milhous, B. A. Šolaja, *J. Med. Chem.* **51** (2008) 2261
36. P. Ghorai, P. H. Dussault, *Org. Lett.* **10** (2008) 4577
37. a) S. D. Kuduk, R. K. Chang, R. M. Di Pardo, C. N. Di Marco, K. L. Murphy, R. W. Ransom, D. R. Reiss, C. Tang, T. Prueksaritanont, D. J. Pettibone, M. G. Bock, *Bioorg. Med. Chem. Lett.* **18** (2008) 5107; b) A. Bahadoor, A. C. Castro, L. K. Chan, F. G. Keaney, M. Nevalainen, V. Nevalainen, S. Peluso, D. A. Snyder, T. T. Tibbitts, WO 2011/140190 A1
38. W. K. Milhous, N. F. Weatherly, J. H. Bowdre, R. E. Desjardins, *Antimicrob. Agents Chemother.* **27** (1985) 525
39. Y. Tang, Y. Dong, S. Wittlin, S. A. Charman, J. Chollet, F. C. K. Chiu, W. N. Charman, H. Matile, H. Urwyler, A. Dorn, S. Bajpai, X. Wang, M. Padmanayam, J. M. Karle, R. Brun, J. L. Vannerstrom, *Bioorg. Med. Chem. Lett.* **17** (2007) 1260
40. For pK_a calculations, Epik, version 2.9, Schrödinger, LLC, New York, NY, 2014 and for log P calculations, QikProp, version 4.1, Schrödinger, LLC, New York, NY, 2014 were used.
41. O. Djurković-Djaković, T. Nikolić, F. Robert-Gangneux, B. Bobić, A. Nikolić, *Antimicrob. Agents Chemother.* **43** (1999) 2240
42. R. E. Desjardins, C. J. Canfield, D. E. Haynes, J. D. Chulay, *Antimicrob. Agents Chemother.* **16** (1979) 710
43. N. M. Krstić, I. Z. Matić, Z. D. Juranić, I. T. Novaković, D. M. Sladić, *J. Steroid. Biochem. Mol. Biol.* **143** (2014) 365
44. T. Mosmann, *J. Immunol. Methods* **65** (1983) 55
45. M. Ohno, T. Abe, *J. Immunol. Methods* **145** (1991) 199.



SUPPLEMENTARY MATERIAL TO
**Tetraoxanes as inhibitors of Apicomplexan parasites
Plasmodium falciparum and *Toxoplasma gondii* and
anti-cancer molecules**

DEJAN M. OPSENICA^{1*}, JELENA RADIVOJEVIĆ², IVANA Z. MATIĆ³,
TIJANA ŠTAJNER⁴, SLAVICA KNEŽEVIĆ-UŠAJ⁵, OLGICA DJURKOVIĆ-DJAKOVIĆ⁴
and BOGDAN A. ŠOLAJA^{6#}

¹Institute of Chemistry, Technology, and Metallurgy, University of Belgrade, Njegoševa 12,
11000 Belgrade, Serbia, ²Institute of Molecular Genetics and Genetic Engineering, University
of Belgrade, Vojvode Stepe 444a, P. O. Box 23, Belgrade, 11010, Serbia, ³Institute for
Oncology and Radiology of Serbia, Pasterova 14, 11000 Belgrade, Serbia, ⁴National
Reference Laboratory for Toxoplasmosis, Institute for Medical Research, University of
Belgrade, Dr. Subotića 4, P. O. Box 102, 11129 Belgrade, Serbia, ⁵Institute for Pathology,
Medical Faculty, University of Novi Sad, Hajduk Veljkova 3, 21000 Novi Sad, Serbia and
⁶Faculty of Chemistry, University of Belgrade, Studentski trg 12–16, P. O. Box 51, 11158,
Belgrade, Serbia

J. Serb. Chem. Soc. 80 (11) (2015) 1339–1359

TABLE S-I. Calculated pK_a and $\log P$ values for derivatives **21**, **22** and **23**; for the pK_a calculations, Epik, version 2.9, Schrödinger, LLC, New York, NY, 2014 and for the $\log P$ calculations, QikProp, version 4.1, Schrödinger, LLC, New York, NY, 2014 were used

Compound	21	22	23
pK_a	10.16	12.08	12.14
$\log P$	1.70	3.12	1.63

SYNTHESIS

4-Hydroxycyclohexanecarboxylic acid (13)¹

A mixture of 4-hydroxybenzoic acid (15.0 g, 108.6 mmol) and 5 % Rh-Al₂O₃ (1 g) in MeOH (100 mL) was shaken in a Parr-shaker under a hydrogen atmosphere (345 kPa) at r.t. After 24 h, the hydrogen was exchanged with Ar, the mixture filtered through celite and the solvent removed under reduced pressure. The product was obtained as a mixture of *cis/trans* isomers. Yield: 15.39 g (98 %).

Benzyl 4-hydroxycyclohexanecarboxylate (14)²

A mixture of **13** (10.0 g, 69.4 mmol) and anhydrous K₂CO₃ (19.1 g, 138.2 mmol) in DMF (18 mL) was warmed to 55 °C, benzyl chloride (10.48 mL, 90.8 mmol) was added in drops and stirring was continued at same temperature. After 12 h, the reaction mixture was

*Corresponding author. E-mail: dopsen@chem.bg.ac.rs

cooled to room temperature, water (25 mL) was added and the mixture was extracted with CH₂Cl₂ (4×30 mL). The combined organic layers were washed once with sat. NaHCO₃ (15 mL), once with brine (15 mL) and dried over anh. Na₂SO₄. The crude product (white powder, 49.28 g) was used without further purification in next reaction step. An analytical sample was obtained after column chromatography purification (flash, SP Biotage, SiO₂-column, flash 12+M, hexane/EtOAc = 6:4). The product was obtained as a *cis/trans* mixture with 2:1 ratio of axial:equatorial hydroxyl groups (¹H-NMR).

Benzyl 4-oxocyclohexanecarboxylate (15)^{2,3}

A mixture of alcohol **14** (25.0 g, 106.7 mmol) and PCC (34.44 g, 160.0 mmol) in CH₂Cl₂ (150 mL) was stirred at r.t for 2 h. The suspension was transferred onto a SiO₂ column and the product was collected after eluting with CH₂Cl₂ (600 mL). The solvent was removed under reduce pressure and the product was obtained after purification by column chromatography (flash, SP Biotage, SiO₂-column, 40+M, eluent hexane / EtOAc gradient 85/15 → 7/3) as a pale green–yellow oil. Yield: 9.57 g (67 %)

Cyclohexylidene bis[hydroperoxide] (17)

Into a mixture of cyclohexanone (980.0 mg, 10.0 mmol) and Re₂O₇ (242.2 mg, 0.5 mmol, 5 mol %) in CH₃CN (25 mL), a 50 % solution of H₂O₂ (1.12 mL, 40.0 mmol) was added and stirring was continued at r.t. for 1 h. The reaction mixture was transferred onto a SiO₂ column and eluted with EtOAc. Fractions containing the crude product were combined, washed once with brine and dried over anh. Na₂SO₄ at 0 °C. Solvent was removed under reduced pressure and product was isolated after column chromatography (Lobar, SiO₂-column C, eluent hexane/EtOAc = 7/3). Yield: 890.2 mg (60 %).

*7,8,15,16-Tetraoxadispiro[5.2.5.2]hexadec-3-ylmethanol (19)*⁴

A flame-dried, two-neck round bottom flask was charged, under Ar atmosphere, with LiAlH₄ (280.0 mg, 7.3 mmol) and dry THF (20 mL), and a solution of ester **18** (2.4 g, 4.55 mmol) in dry THF (20 mL) was added dropwise under intensive stirring, at r.t. After 2 h, the reaction was quenched with EtOAc, water was added and emulsion was transferred into a separatory funnel. Water layer was acidified (pH 2) with dilute HCl (1:1, V/V), the layers were separated and the water layer was extracted with EtOAc (3×20 mL). The combined organic layers were dried over anh. Na₂SO₄, the solvent was removed under reduce pressure and the product was isolated after column chromatography purification (dry-flash, SiO₂-column, eluent heptane/EtOAc = 8/2). Yield: 1.4 g (82 %).

*3-(Azidomethyl)-7,8,15,16-tetraoxadispiro[5.2.5.2]hexadecane (20)*⁴

Into a solution of **19** (1.38 g, 5.34 mmol) in dry Py (11 mL), methanesulphonyl chloride (495 µL, 6.4 mmol) was added at r.t. under intensive stirring. After 2 h, the reaction was quenched with water/EtOAc mixture, transferred into separatory funnel. The aqueous layer was acidified (pH 5) with dilute HCl (1:1, V/V), the layers were separated and the aqueous layer was extracted with EtOAc (4×25 mL). The combined organic layers were dried over anh. Na₂SO₄, filtered off and the solvent was removed under reduced pressure. The obtained crude product was used in next reaction step without further purification. A mixture of mesylate and Na₃ (3.47 g, 53.4 mmol) in DMF (20 mL) was stirred at 50 °C over 12 h, cooled to r.t. and poured into an EtOAc/water mixture. The layers were separated and the aqueous layer was extracted with EtOAc (4×25 mL). The combined organic layers were washed with brine (2×25 mL), dried over anh. Na₂SO₄, filtered off and the solvent was removed under reduced

pressure. The product was isolated after column chromatography purification (dry-flash, SiO₂-column, eluent heptane/EtOAc = 9/1). Yield: 1.45 g (97 %).

PHYSICAL, ANALYTICAL AND SPECTRAL DATA FOR THE ISOLATED COMPOUNDS

*4-Hydroxycyclohexanecarboxylic acid (13).*¹ Yield: 98 %; m.p.: 120–123 °C (lit. m.p.: 126–128 °C); IR (ATR, cm^{−1}): 3437s, 2934s, 2857m, 2601w, 1702s, 1443w, 1368w, 1312m, 1242w, 1203w, 1058m, 1026w, 949w, 913w, 736w, 587w; ¹H-NMR (200 MHz, CDCl₃, δ / ppm): 4.52 (2H, *bs*, OH), 3.98–3.84 (1H, *m*, He-COH), 3.72–3.54 (1H, *m*, Ha-COH), 2.54–2.16 (2H, *m*, Ha-CCO₂H), 2.14–1.86 (4H, *m*), 1.84–1.16 (12, *m*).

*Benzyl 4-hydroxycyclohexanecarboxylate (14).*² IR (ATR, cm^{−1}): 3405m, 3033w, 2938s, 2863w, 1732s, 1496w, 1454w, 1385m, 1311w, 1236m, 1169s, 1136w, 1070m, 1033m, 967m, 907w, 749m, 699m; ¹H-NMR (200 MHz, CDCl₃, δ / ppm): 7.40–7.30 (5H, *m*, Ar-H), 5.12 (*s*, Ar-CH₂), 3.95–3.85 (*m*, He-COH), 2.52–2.36 (*m*, Ha-CO₂Bn), 2.12–1.86 (3H, *m*), 1.80–1.52 (5H, *m*); ¹³C-NMR (50 MHz, CDCl₃, δ / ppm): 175.10, 136.14, 128.51, 128.11, 127.98, 66.77, 66.04, 41.26, 31.94, 23.58.

Benzyl-4-oxocyclohexanecarboxylate (15).^{2,3} Yield: 67 %; pale green-yellow oil; IR (ATR, cm^{−1}): 3033w, 2954m, 1710s, 1453m, 1384m, 1303m, 1210s, 1158s, 1028w, 1004m, 965w, 746s, 698s, 495w, 421w; ¹H-NMR (200 MHz, CDCl₃, δ / ppm): 7.36 (5H, *s*, Ph), 5.16 (2H, *s*, Ar-CH₂), 2.90–2.70 (1H, *m*, Ha-CO₂Bn), 2.56–1.92 (8H, *m*); ¹³C-NMR (50 MHz, CDCl₃, δ / ppm): 210.02, 173.94, 135.72, 128.62, 128.36, 128.13, 66.49, 40.62, 39.62, 28.42.

Cyclohexylidene bis[hydroperoxide] (17). Yield: 60 %; colourless oil; IR (film, cm^{−1}): 3419s, 2946s, 2863s, 1712m, 1634w, 1454s, 1391s, 1278m, 1161m, 1098m, 1064s, 947m, 927m, 849m. IR (CCl₄, cm^{−1}): 3424s, 2948s, 2865s, 1746m, 1722m, 1452s, 1393s, 1349m, 1162s, 951s, 922m; ¹H-NMR (200 MHz, CDCl₃, δ / ppm): 9.60 (*bs*, 2×HOO), 2.0–1.8 (4H, *m*), 1.6–1.4 (6H, *m*); ¹³C-NMR (50 MHz, CDCl₃, δ / ppm): 110.94, 29.41, 25.18, 22.31.

Benzyl 7,8,15,16-tetraoxadispiro[5.2.5.2]hexadecane-3-carboxylate (18). Yield: 26 %; amorphous powder; m.p.: 70–73 °C; Anal. Calcd. for C₂₀H₂₆O₆: C, 66.28; H, 7.23 %. Found: C, 65.82; H, 6.96 %; IR (ATR, cm^{−1}): 3033w, 2939s, 2863m, 1734s, 1496w, 1449s, 1357m, 1274m, 1254m, 1169m, 1066s, 947w, 925w, 750w, 699w; ¹H-NMR (200 MHz, CDCl₃, δ / ppm): 7.31 (5H, *bs*, Ph), 5.12 (2H, *s*, Ar-CH₂), 2.89 (1H, *bs*), 2.60–2.10 (3H, *m*), 2.10–1.30 (15H, *m*); ¹³C-NMR (50 MHz, CDCl₃, δ / ppm): 174.37, 135.96, 128.56, 128.20, 128.04, 108.39, 107.22, 66.20, 41.57, 31.76, 30.35, 28.02, 25.27, 24.54, 23.80, 22.62, 21.92; (+)ESI-HRMS (*m/z*): Calcd. for [M+Na]⁺: 385.16216. Found: 385.16216; HPLC purity: Method A: *RT* 3.141 min, area 96.25 %; Method B: *RT* 1.372 min, area 96.82 %.

*7,8,15,16-Tetraoxadispiro[5.2.5.2]hexadec-3-ylmethanol (19).*⁴ Yield: 82 %; colourless foam; m.p.: 116–118 °C; Anal. Calcd. for C₁₃H₂₂O₅: C, 60.45; H, 8.58 %. Found: C, 60.47; H, 8.18 %; IR (KBr, cm⁻¹): 3320m, 3009w, 2940s, 2861s, 1443m, 1360w, 1339w, 1310w, 1273w, 1250w, 1159w, 1094w, 1068m, 1045m, 984w, 941w, 918m, 897w, 881w, 850w; ¹H-NMR (500 MHz, CDCl₃, δ / ppm): 3.5 (d, J = 6.2 Hz, CH₂—OH), 3.12 (1H, bs), 2.45–2.15 (2H, m), 1.85–1.70 (3H, m), 1.70–1.35 (12H, m), 1.35–1.20 (2H, m); ¹³C-NMR (125 MHz, CDCl₃, δ / ppm): 108.29, 108.16, 67.41, 39.44, 31.80, 30.90, 29.52, 28.53, 25.35, 24.95, 24.45, 22.17, 21.88; (+)ESI-HRMS (m/z): Calcd. for [M+NH₄]⁺: 276.18055. Found: 276.18041.

*3-(Azidomethyl)-7,8,15,16-tetraoxadispiro[5.2.5.2]hexadecane (20).*⁴ Yield: 97%; colourless foam; m.p.: 86–87 °C; IR (KBr, cm⁻¹): 2993w, 2946m, 2868w, 2096s, 1714w, 1445m, 1358w, 1338w, 1292m, 1258m, 1213w, 1183w, 1183w, 1155w, 1137w, 1091w, 1067w, 1047m, 1016w, 952w, 915m, 883w, 850w, 817w; ¹H-NMR (200 MHz, CDCl₃, δ / ppm): 3.18 (2H, d, J = 6.2 Hz, CH₂), 3.14 (1H, bs), 2.27 (2H, bs), 1.80–1.26 (16H, m); ¹³C-NMR (50 MHz, CDCl₃, δ / ppm): 108.39, 107.73, 56.74, 37.04, 31.65, 30.81, 29.48, 28.46, 25.29, 22.05. HPLC purity: Method A: RT 3.140 min, area 96.998 %; Method B: RT 1.371 min, area 96.81 %.

*1-(7,8,15,16-Tetraoxadispiro[5.2.5.2]hexadec-3-yl)methanamine (21).*⁴ Yield: 69 %; pale yellow amorphous powder; m.p.: 75–77 °C.; IR (KBr, cm⁻¹): 3378m, 3340m, 3010w, 2941s, 2862s, 1720w, 1443m, 1362w, 1341w, 1275w, 1253w, 1160w, 1096w, 1069m, 1049m, 984w, 942w, 919m, 896w, 851w, 824w; ¹H-NMR (200 MHz, CDCl₃, δ / ppm): 3.11 (1H, bs) 2.58 (2H, d, J = 6.0 Hz, CH₂—NH₂), 2.26 (2H, bs), 1.90–1.11 (18H, m); ¹³C-NMR (50 MHz, CDCl₃, δ / ppm): 108.26, 47.58, 40.20, 31.68, 31.0, 29.52, 28.73, 25.78, 25.31, 21.96; HPLC purity: Method A: RT 3.139, area 97.24 %; method B: RT 1.369 min, area 96.93 %.

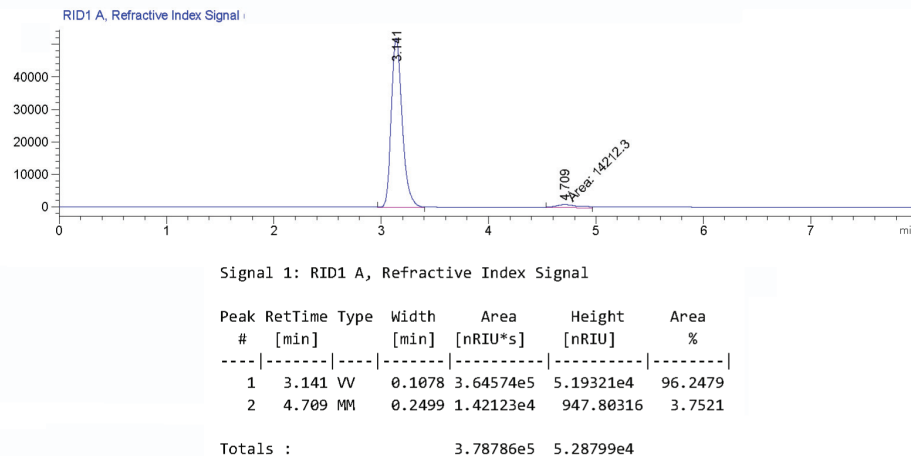
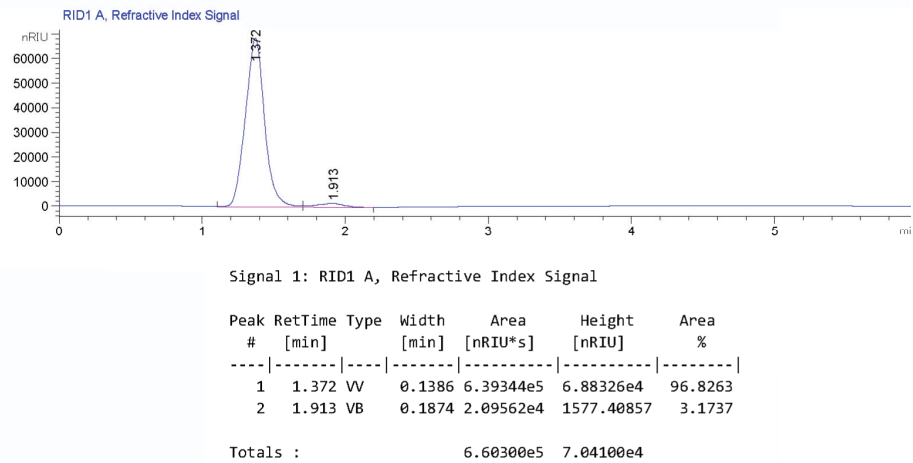
*N-(7,8,15,16-Tetraoxadispiro[5.2.5.2]hexadec-3-ylmethyl)-4,5-dihydro-1*H*-imidazol-2-amine (22).* Yield: 72 %; amorphous powder; m.p.: 153–156 °C; Anal. Calcd. for C₁₆H₂₇N₃O₄: C, 59.06; H, 8.36; N, 12.91 %. Found: C, 59.43; H, 8.71; N, 12.61 %; IR (ATR, cm⁻¹): 2939s, 2862m, 1693s, 1636m, 1551m, 1446m, 1366m, 1252m, 1157w, 1068m, 952w, 844w, 804w, 714w; ¹H-NMR (500 MHz, T = 340.2 K, DMSO-d₆, δ / ppm): 3.38 (4H, s, N—CH₂CH₂—N), 2.98 (2H, d, J = 6.6 Hz, CH₂—N), 1.86 (3H, bs), 1.70–1.40 (9H, m), 1.28–1.23 (1H, m), 1.18–1.06 (2H, m); ¹³C-NMR (125 MHz, δ / ppm): 160.38, 107.09, 46.83, 45.81, 35.91, 28.67, 28.29, 24.87, 24.10, 21.06; (+)ESI-HRMS (m/z): Calcd. for [M+H⁺]: 325.20016. Found: 326.20896; HPLC purity: Method A: RT 3.139 min, area 95.88 %; Method B: RT 1.367 min, area 96.77 %.

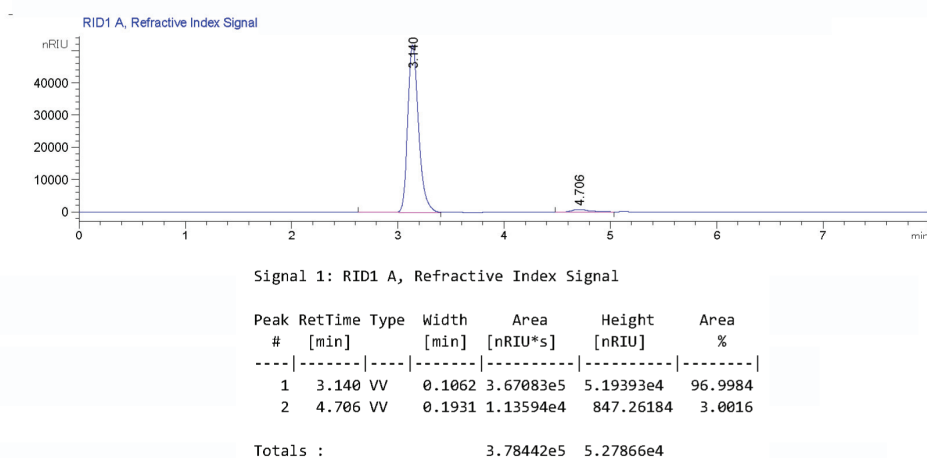
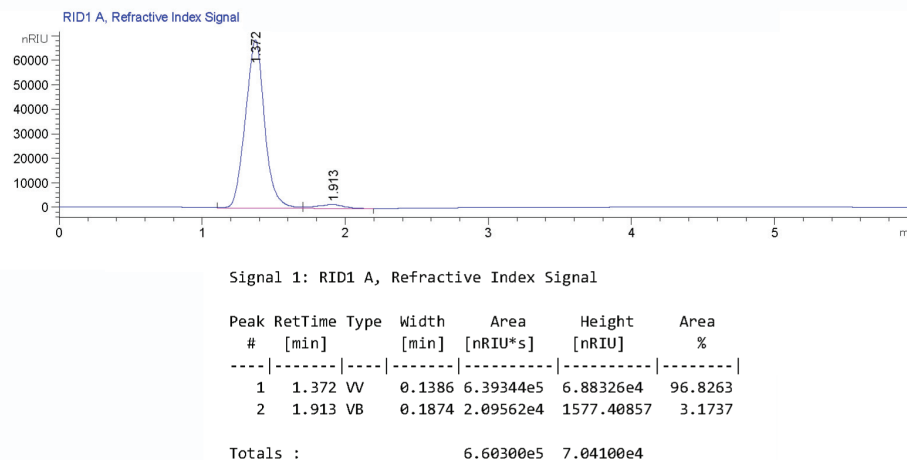
1-(7,8,15,16-Tetraoxadispiro[5.2.5.2]hexadec-3-ylmethyl)guanidine (23). Yield: 93 %: pale yellow oil, becomes solid with time; m.p.: 36 °C; Anal. Calcd. for C₁₄H₂₅N₃O₄: C, 56.17; H, 8.42; N, 14.04 %. Found: C, 55.87; H, 8.02; N,

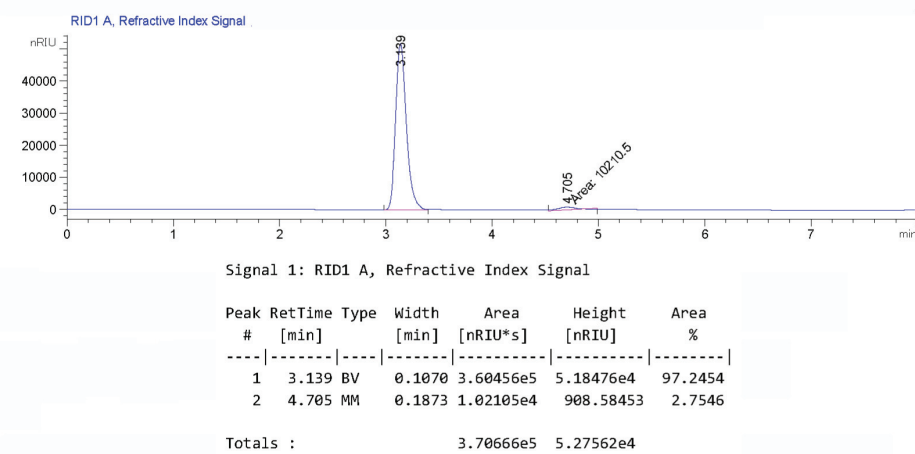
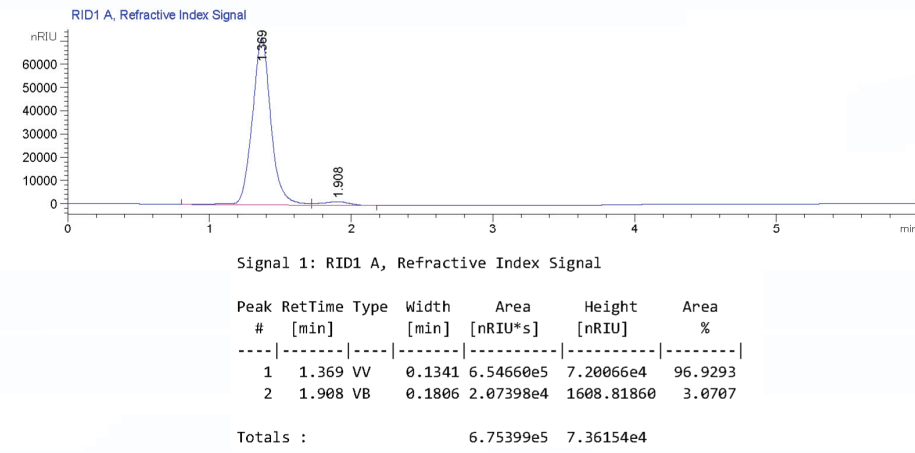
13.74 %; IR (ATR, cm^{-1}): 3360s, 2943m, 2865w, 1674s, 1579s, 1415m, 1254m, 1061w, 1010m, 766w, 651w, 618w; $^1\text{H-NMR}$ (500 MHz, DMSO- d_6 , δ / ppm): 5.29 (bs, 2 \times NH₂), 2.95 (2H, d, J = 6.9 Hz, CH₂-N), 1.75–1.39 (13H, m), 1.33–1.10 (6H, m); $^{13}\text{C-NMR}$ (125 MHz, 340.1 K, DMSO- d_6 , δ / ppm): 157.76, 107.44, 107.38, 45.02, 35.62, 30.16, 28.56, 24.86, 24.38, 21.31; (+)ESI-HRMS (m/z): Calcd. for [M+H]⁺: 299.18451. Found: 300.19232; HPLC purity: Method A: RT, 3.133 min, area 78.69 %; Method B: RT, 1.071 min, area 80.69 %.

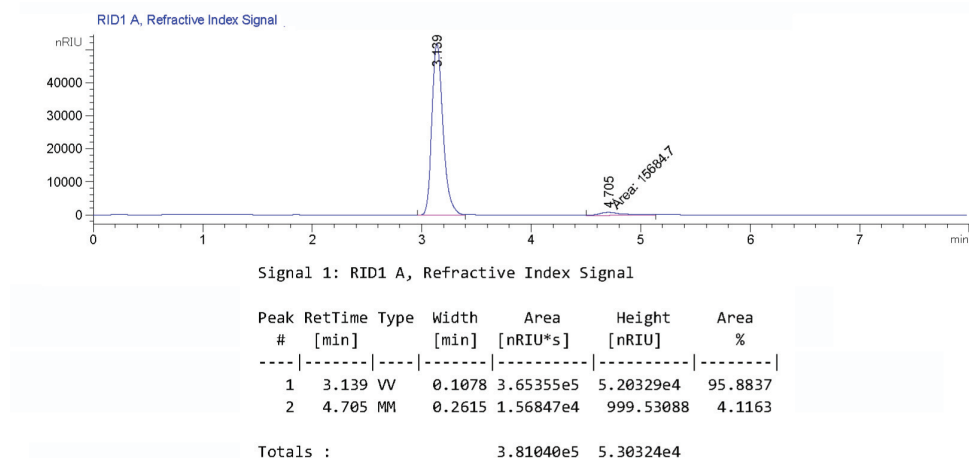
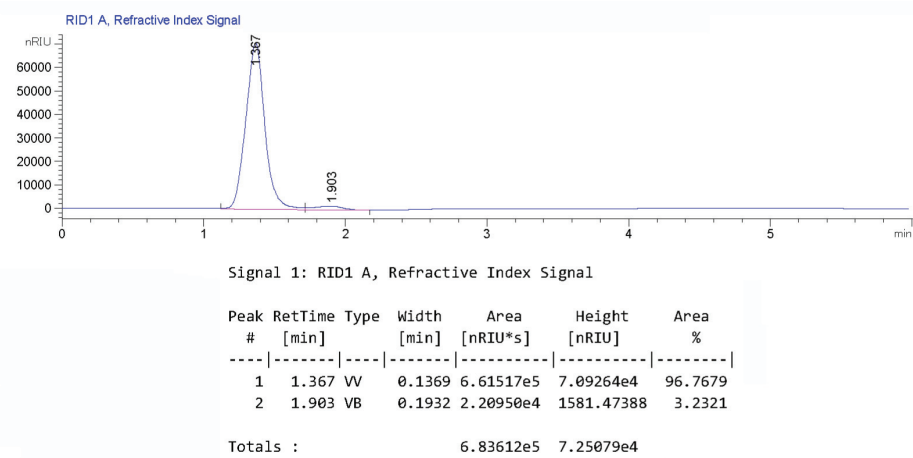
1-Phenyl-3-(7,8,15,16-tetraoxadispiro[5.2.5.2]hexadec-3-ylmethyl)urea (24). Yield: 215 98 %; colourless foam; softening temp.: 188–191 °C; Anal. Calcd. for C₂₀H₂₈N₂O₅×0.5H₂O: C, 62.32; H, 7.58; N, 7.27 %. Found: C, 62.63; H, 7.71; N, 7.56 %; IR (ATR, cm^{-1}): 3389m, 3304m, 3182w, 3150w, 3042w, 2934m, 2861m, 2363m, 1647s, 1601s, 1559s, 1499m, 1442m, 1357w, 1314m, 1248s, 1156w, 1055w, 952w, 927w, 757m, 728w, 698m; $^1\text{H-NMR}$ (500 MHz, DMSO- d_6 , δ / ppm): 8.37 (1H, s, NH-Ph), 7.50–7.42 (2H, m, Ar-H), 7.25–7.15 (2H, m, Ar-H), 6.90–6.85 (1H, m, Ar-H), 6.10 (1H, bs, HN), 3.17 (d, J = 5.25 Hz, CH₂-NH), 3.05–2.95 (2H, m), 2.30–2.10 (1H, m), 1.75–1.0 (16H, m); $^{13}\text{C-NMR}$ (125 MHz, DMSO- d_6 , δ / ppm): 155.23, 140.53, 128.61, 120.90, 117.51, 107.81, 107.71, 43.93, 36.73, 31.11, 30.29, 28.99, 28.06, 27.93, 25.68, 25.11, 24.66, 21.83, 21.42; (+)ESI-HRMS (m/z): Calcd. for [M+H]⁺: 376.19982. Found: 377.20742; HPLC purity: Method A: RT 3.141 min, area 96.56 %; Method B: RT 1.368 min, area 96.97 %.

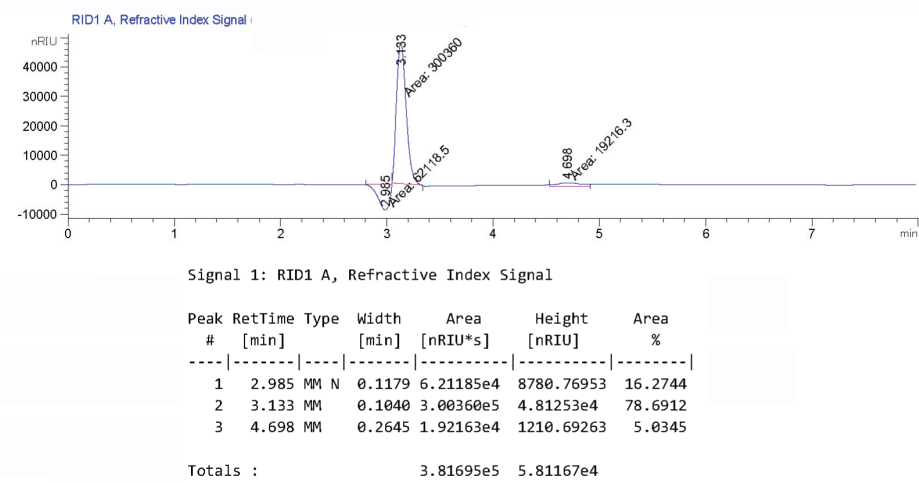
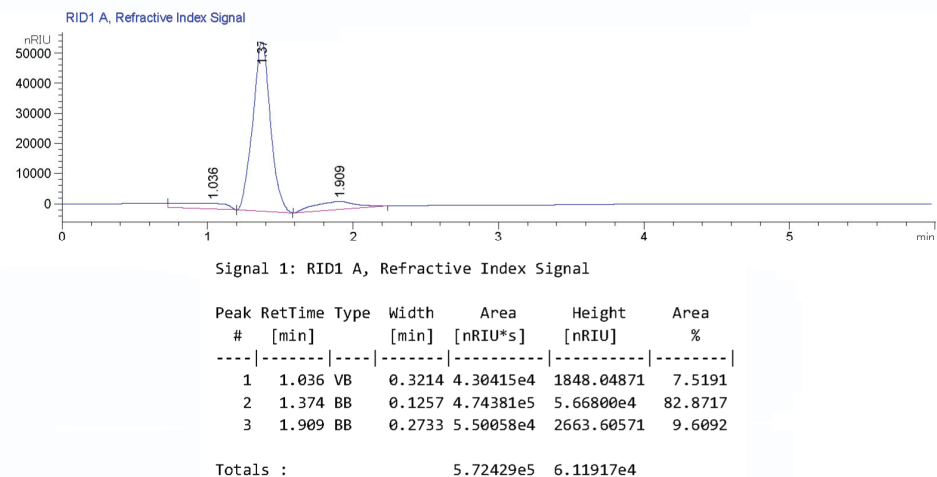
1-Phenyl-3-(7,8,15,16-tetraoxadispiro[5.2.5.2]hexadec-3-ylmethyl)thiourea (25). Yield: 73 %; colourless foam; m.p.: 143–147°C; Anal. Calcd. for C₂₀H₂₈N₂O₄S: C, 61.20; H, 7.19; N, 7.14; S, 8.17 %. Found: C, 60.88; H, 7.27; N, 7.02; S, 8.39 %; IR (KBr, cm^{-1}): 3326m, 3240m, 2948m, 2920m, 2885w, 2858w, 1736w, 1593m, 1550s, 1513s, 1447m, 1390w, 1345m, 1313m, 1256m, 1233m, 1190m, 1069s, 983w, 947w, 917w, 886w, 750w, 695w; $^1\text{H-NMR}$ (500 MHz, CDCl₃, δ / ppm): 7.81 (1H, s, Ph-NH), 7.49–7.43 (2H, m, Ar-H), 7.38–7.30 (2H, m, Ar-H), 7.25–7.19 (1H, m, Ar-H), 6.13–6.06 (1H, m, NH-C=S), 3.54 (2H, bs, CH₂-NH), 3.08 (1H, bs), 2.26 (2H, bs), 1.89–1.40 (14H, m), 1.32–1.18 (2H, m). $^{13}\text{C-NMR}$ (125 MHz, CDCl₃, δ / ppm): 180.99, 135.92, 130.34, 127.54, 125.35, 108.31, 107.80, 50.43, 36.25, 31.68, 30.81, 29.53, 28.41, 26.21, 25.54, 25.32, 22.09. (+)ESI-HRMS (m/z): Calcd. for [M+Na]⁺: 415.16620. Found: 415.16570; HPLC purity: Method A: RT 3.138 min, area 96.34 %; Method B: RT, 1.374 min, area 96.40 %.

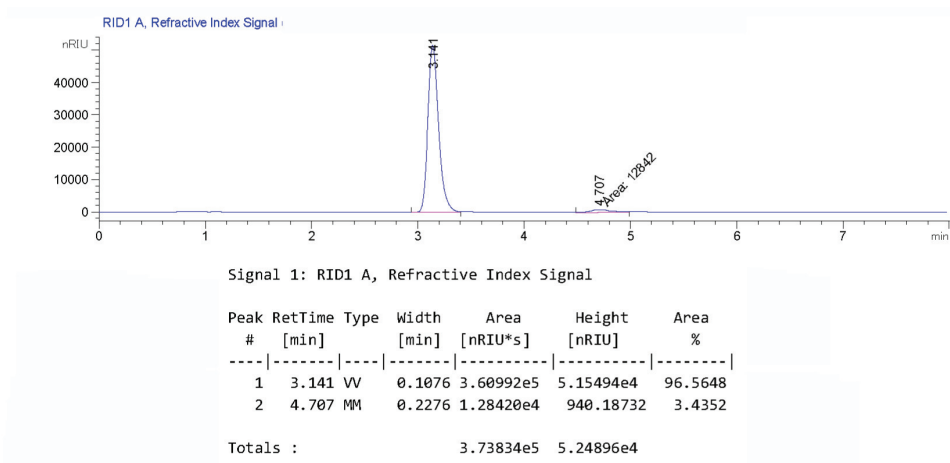
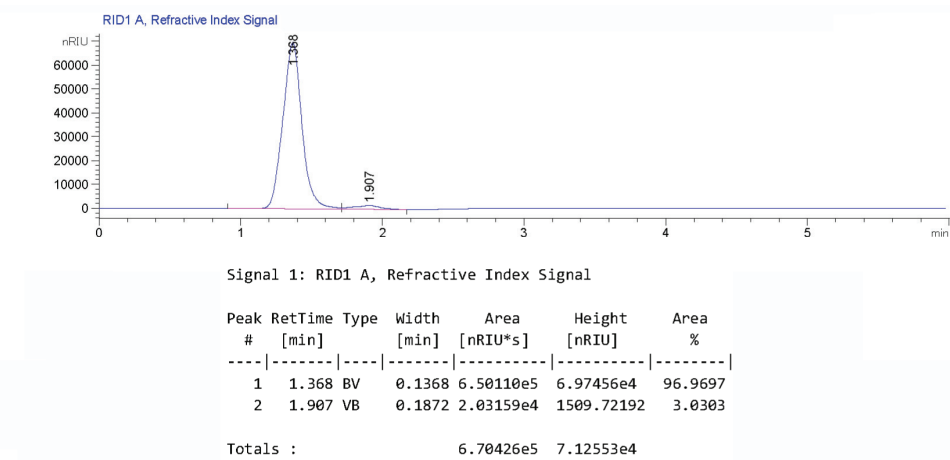
PURITY CONTROL HPLC CHROMATOGRAMS FOR **18, 20–25**Fig. S-1. HPLC chromatogram for **18** obtained using method A.Fig. S-2. HPLC chromatogram for **18** obtained using method B.

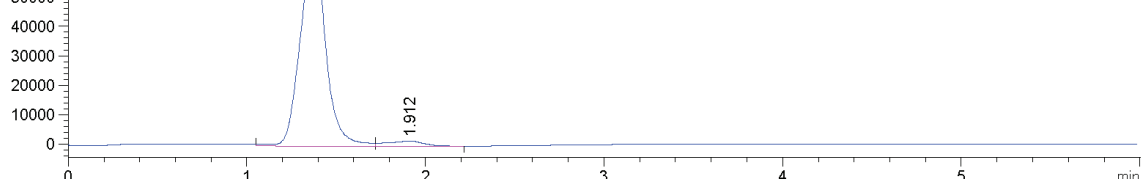
Fig. S-3. HPLC chromatogram for **20** obtained using method A.Fig. S-4. HPLC chromatogram for **20** obtained using method B.

Fig. S-5. HPLC chromatogram for **21** obtained using method A.Fig. S-6. HPLC chromatogram for **21** obtained using method B.

Fig. S-7. HPLC chromatogram for **22** obtained using method A.Fig. S-8. HPLC chromatogram for **22** obtained using method B.

Fig. S-9. HPLC chromatogram for **23** obtained using method A.Fig. S-10. HPLC chromatogram for **23** obtained using method B.

Fig. S-11. HPLC chromatogram for **24** obtained using method A.Fig. S-12. HPLC chromatogram for **24** obtained using method B.



```
=====
Fraction Information
=====
```

```
No Fractions found.
=====
```

```
=====
Area Percent Report
=====
```

```
Sorted By : Signal
Multiplier : 1.0000
Dilution : 1.0000
Use Multiplier & Dilution Factor with ISTDs
```

Signal 1: RID1 A, Refractive Index Signal

Peak #	RetTime [min]	Type	Width [min]	Area [nRIU*s]	Height [nRIU]	Area %
1	1.374	VV	0.1390	6.78876e5	7.14253e4	96.4019
2	1.912	VB	0.2010	2.53385e4	1731.30737	3.5981

Totals : 7.04215e5 7.31566e4

1.
2.

```
=====
*** End of Report ***
=====
```

3.
4.



One-pot synthesis of carbazole based 3-hydroxy-4H-chromen-4-ones by a modified Algar–Flynn–Oyamada reaction and their antimicrobial activity

DONGAMANTI ASHOK*, SIDDA RAVI, BOMMIDI VIJAYA LAKSHMI
and ARRAM GANESH

Department of Chemistry, Osmania University, Hyderabad - 500 007, India

(Received 3 December 2014, revised 30 March, accepted 10 June 2015)

Abstract: A new series of 2-(9-ethyl-9*H*-carbazol-3-yl)-3-hydroxy-4*H*-chromen-4-ones were synthesized from substituted 2-hydroxyacetophenones and 9-ethyl-9*H*-carbazole-3-carbaldehyde using NaOH and H₂O₂ by a modified Algar–Flynn–Oyamada reaction. In this method, the flavonols were synthesized in good yields (70–82 %) without isolating chalcones. The structures of the compounds were established based on ¹H-NMR, ¹³C-NMR, FT-IR and mass spectral and analytical data. All the compounds were evaluated for their antimicrobial activity against bacteria, such as *Staphylococcus aureus*, *Bacillus subtilis*, *Escherichia coli* and *Klebsiella pneumoniae*, as well as fungi, such as *Aspergillus flavus* and *Fusarium oxysporum*.

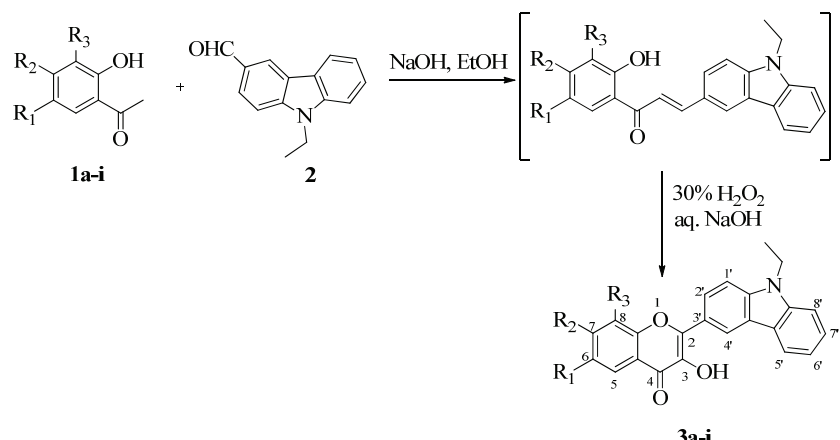
Keywords: 2-(9-ethyl-9*H*-carbazol-3-yl)-3-hydroxy-4*H*-chromen-4-ones; modified Algar–Flynn–Oyamada reaction; antimicrobial activity.

INTRODUCTION

Flavonoids constitute an important class of secondary metabolites that are widely distributed in plants. Their widespread distribution in nature, their structural variability, relatively low toxicity and antioxidant activities have increased interest in flavonoids. Furthermore, flavonoids possess multimodal biological activities, such as anticancer,¹ antihypertensive,² anti-inflammatory,³ antibacterial⁴ and antifungal⁵ activities. Chromones are interesting structural scaffolds and have been assigned as privileged structures for drug discovery. Substituted chromones were reported to show potential anticancer,⁶ antihistamine⁷ and antagonistic⁸ activities against leukotriene D4. On the other hand, carbazole derivatives are an important class of heterocyclic compounds that are known to possess important biological properties, such as antibacterial, antifungal,⁹ antitumor,¹⁰ antioxidant¹¹ and antidiabetic¹² properties.

* Corresponding author. E-mail: ashokdou@gmail.com
doi: 10.2298/JSC141203051A

In the light of biological importance of the chromone and carbazole scaffolds and in continuation of the ongoing search for biologically active heterocyclic molecules,¹³ herein, the one pot synthesis of 2-(9-ethyl-9*H*-carbazol-3-yl)-3-hydroxy-4*H*-chromen-4-ones using a modified Algar–Flynn–Oyamada reaction (Scheme 1) and the antimicrobial properties of the obtained derivatives are reported.



Scheme 1. Synthetic route for the preparation of carbazole based 3-hydroxy-4*H*-chromen-4-ones (**3a-i**).

RESULTS AND DISCUSSION

The original Algar–Flynn–Oyamada reaction¹⁴ is a two step process for the synthesis of 3-hydroxy chromenones. In the first step, 2-hydroxy chalcones are formed, which on subsequent cyclisation in the second step in the presence of alkaline hydrogen peroxide yields the corresponding flavonols, whereas the modified Algar–Flynn–Oyamada reaction¹⁵ is a one step process for the synthesis of flavonols from 2-hydroxyacetophenone and aromatic aldehydes in the presence of alkaline hydrogen peroxide (Table I). In this modified version there is no need to isolate the intermediate chalcones. As a model case, 2-hydroxyacetophenone **1a** was condensed with 9-ethyl-9*H*-carbazole-3-carbaldehyde **2** at room temperature using alkali and subsequently treated with alkaline hydrogen peroxide at room temperature to yield the flavonol derivative. It was identified as 2-(9-ethyl-9*H*-carbazol-3-yl)-3-hydroxy-4*H*-chromen-4-one **3a** by IR, ¹H-NMR, ¹³C-NMR and mass spectral data, which ruled out the formation of corresponding aurones and some other benzofuran derivatives, which were reported to form as by-products in Algar–Flynn–Oyamada reaction. In the ¹H-NMR spectra of **3a**, the OH proton appeared at δ 7.08 ppm as broad singlet and H_{4'} proton appeared as a doublet at δ 9.03 ppm. In the ¹³C-NMR spectra of **3a**, the carbonyl carbon appeared at δ 173.0 ppm and the N-CH₂ carbon resonated at δ 37.7 ppm. The ESI mass spectra of **3a** showed a molecular ion peak at m/z = 356 [M+H]⁺.

TABLE I. Physical data of the synthesized compounds **3a–i**

Compd.	M.p., °C	R ₁	R ₂	R ₃	Time, h	Yield, % ^a
3a	134–136	H	H	H	6	72
3b	128–130	F	H	H	7	78
3c	178–180	Cl	H	H	5	82
3d	190–192	Br	H	H	8	76
3e	140–142	CH ₃	H	H	6	80
3f	206–208	Cl	CH ₃	H	6	82
3g	212–214	Cl	H	Cl	7	80
3h	148–150	H	OCH ₃	H	7	76
3i	172–174	H	OC ₂ H ₅	H	8	70

^aIsolated yield*Antibacterial activity*

The newly synthesized compounds **3a–i** were screened *in vitro* for their antibacterial activity against two Gram-positive bacterial strains (*Staphylococcus aureus* (ATCC 6538), *Bacillus subtilis* (ATCC 6633)) and two Gram-negative bacterial strains (*Escherichia coli* (ATCC 25922), *Klebsiella pneumoniae* (ATCC 13883)) at two different concentrations 20 and 40 µg mL⁻¹. The zone of inhibition was measured in mm and ciprofloxacin was used as a standard antibacterial substance, under similar conditions for comparison. All the synthesized compounds showed good activity against the tested microorganisms (Table II). Among all, compounds **3a**, **3h** and **3i** showed maximal zones of inhibition against the tested bacterial strains. It could be concluded that 3-hydroxy chromenones with electron releasing groups, such as methoxy, ethoxy and unsubstituted compounds, showed the maximum activity. Furthermore, the antibacterial results observed for other substitutions on the phenyl ring were very similar

TABLE II. Antimicrobial activities (zones of inhibition in mm) of the synthesized compounds **3a–i**

Compd.	Concentration, µg mL ⁻¹											
	<i>S. aureus</i>		<i>B. subtilis</i>		<i>E. coli</i>		<i>K. pneumoniae</i>		<i>A. flavus</i>		<i>F. oxysporum</i>	
	20	40	20	40	20	40	20	40	50	50		
3a	16	28	14	26	14	30	13	26	10	12		
3b	11	22	6	14	05	12	7	15	5	10		
3c	12	24	9	18	08	17	8	15	6	5		
3d	11	20	9	17	10	17	9	19	6	4		
3e	10	22	7	16	7	7	5	10	9	8		
3f	11	21	9	18	9	10	7	15	11	4		
3g	13	23	10	21	7	15	9	19	8	12		
3h	16	29	16	29	17	32	24	35	13	16		
3i	18	30	17	30	19	33	25	36	15	19		
Ciprofloxacin	15	28	16	30	18	35	23	35	—	—		
Amphotericin-B	—	—	—	—	—	—	—	—	12	15		

to each other. It was also concluded that changing the halogen substituent from F to Cl and Br does not provide any significant changes in antibacterial activity.

Antifungal activity

The antifungal activities of the synthesized compounds **3a–i** were tested against two pathogenic fungi, *Aspergillus flavus* (ATCC-9643) and *Fusarium oxysporum* (ATCC-48112), at a concentration of 50 µg mL⁻¹ and the results were compared with those of the standard, amphotericin-B. All the compounds showed good activity against the tested fungal strains (Table II). Among all the compounds, **3a**, **3h** and **3i** showed maximal zones of inhibition against the tested fungal strains. Thus, electron releasing groups on 3-hydroxy chromenone, *i.e.*, methoxy and ethoxy substitutions and the unsubstituted compound showed the highest antifungal activities, followed by the halogen substituted compounds.

EXPERIMENTAL

Materials

All the employed materials were obtained commercially, mostly from Sigma–Aldrich, and used without further purification.

Equipment

The melting points were determined in open capillaries and are uncorrected. The purity of the compounds was checked by TLC on silica gel 60 F₂₅₄ (Merck). The ¹H-NMR and ¹³C-NMR spectra were recorded on a Bruker Avance II 400 spectrometer using TMS as an internal standard. The IR spectra were recorded in KBr on a Shimadzu FTIR 8400S spectrophotometer. The mass spectra were recorded on a Shimadzu LCMS 2020 mass spectrometer. The elemental microanalysis was realised on a Perkin Elmer CHN-2400 analyzer.

The physical, analytical and spectral data of compounds **3a–i** are given in the Supplementary material to this paper.

General procedure for the synthesis of 2-(9-ethyl-9H-carbazol-3-yl)-3-hydroxy-4H-chromen-4-ones

To a well stirred solution of 2-hydroxyacetophenone **1a–i** (1 mmol) and 9-ethyl-9H-carbazole-3-carbaldehyde **2** (1 mmol) in EtOH (20 mL) was added NaOH (4 mmol in 10 mL of EtOH) at room temperature. The reaction mixture was further stirred for 4–5 h. After consumption of reactants (as indicated by TLC), the reaction mixture was dissolved in aqueous NaOH (5 mmol in 5 mL), 3 mL of 30 % H₂O₂ was added dropwise and the stirring was continued for 2–3 h. After completion of reaction (monitored by TLC), the resulting light yellow reaction mixture was poured onto crushed ice and neutralized with dilute HCl. The thus-obtained light yellow solid was filtered, washed with water and dried. The crude product was purified by column chromatography on silica gel using hexane:ethyl acetate (7:3) as eluent to afford the desired products **3a–i**. The respective yields are given in Table I.

Biological assay

Synthesized compounds were screened for their antibacterial activities against pathogenic bacteria, *i.e.*, *S. aureus*, *B. subtilis*, *E. coli* and *K. pneumoniae* and their antifungal activity against *A. flavus* and *F. oxysporum*.

The test organisms were cultured on agar slants, incubated for 24 h at 37 ± 0.5 °C and 24–48 h at 27 ± 0.2 °C for the bacteria and fungi, respectively, to obtain freshly prepared cultures. The synthesized compounds were evaluated for antibacterial activity and antifungal activity against these freshly prepared strains of test organisms by the agar diffusion method and the poison plate technique, respectively. Muller–Hinton agar (MHA) and potato dextrose agar (PDA) were used as nutrient media for bacterial and fungal strains, respectively. The broth cultures were diluted with sterilized saline to bring the final size of the inoculum to approximately 10^5 – 10^6 CFU mL⁻¹. The compounds were diluted in acetone, dimethyl sulphoxide (DMSO) and diethyl ether for biological assays. Of the three solvents, diethyl ether is found to be the best. The bacterial cultures were placed on the media and incubated at 37 °C for 24 h along with the diluted compounds introduced through discs (diameter 5 mm) dipped and placed over the nutrient media. The discs of ciprofloxacin (20–40 µg) and amphotericin-B (50 µg) were also incorporated into the medium for comparison. The same procedure was employed for determining the antifungal activity except that the culture strains of fungi were maintained on PDA and spores were transferred into PDA medium and the plates were incubated at 27 ± 0.2 °C for 24–48 h. Inhibition of growth of the test organisms (bacterial and fungal) in presence of the test material and the standards was measured with the help of a standard scale. The values of the inhibition zones are reported in Table II.

CONCLUSIONS

In conclusion, an easy, facile and one-pot route for the synthesis of 2-(9-ethyl-9*H*-carbazol-3-yl)-3-hydroxy-4*H*-chromen-4-ones in good yields is reported. In this method, there is no need to isolate the intermediate chalcones, which tremendously reduces the man power, time and cost and also improves the overall yields. The antimicrobial assay of these compounds revealed that compounds **3a**, **3h** and **3i** showed maximal zones of inhibition against the tested microorganisms compared with the standards.

SUPPLEMENTARY MATERIAL

Physical, analytical and spectral data of compounds **3a**–**i** are available electronically from <http://www.shd.org.rs/JSCS/>, or from the corresponding author on request.

Acknowledgements. The authors are thankful to the Head of Department of Chemistry for providing the laboratory facilities and the Director of Central Facilities for Research and Development (CFRD), Osmania University, India, for providing the IR and NMR spectral analysis. Financial support for SR from CSIR, New Delhi, is gratefully acknowledged.

ИЗВОД

СИНТЕЗА КАРБАЗОЛСКИХ ДЕРИВАТА 3-ХИДРОКСИ-4*H*-ХРОМЕН-4-ОНА
МОДИФИКОВАНОМ АЛГАР-ФЛИН-ОЈИМАДИНОМ РЕАКЦИЈОМ И ИСПИТИВАЊЕ
ЊИХОВЕ АНТИМИКРОБНЕ АКТИВНОСТИ

DONGAMANTI ASHOK, SIDDA RAVI, BOMMIDI VIJAYA LAKSHMI и ARRAM GANESH

Department of Chemistry, Osmania University, Hyderabad - 500 007, India

Синтетисана је серија деривата 2-(9-етил-9*H*-карбазол-3-ил)-3-хидрокси-4*H*-хромен-4-она полазећи од супституисаних 2-хидрокси-ацетофенона и 9-етил-9*H*-карбазол-3-карбалдехида помоћу NaOH и H₂O₂ у модификованој Алгар-Флин-Ојамадином реакцији. Овим поступком синтетисани су флавоноли, без изоловања халкона, у добром

приносу (70–82 %). Структуре једињења утврђене су $^1\text{H-NMR}$ и $^{13}\text{C-NMR}$ техникама, FT-IR спектроскопијом, масеном спектрометријом и елементалном анализом. Испитана је антимикробна активност добијених једињења према бактеријама *Staphylococcus aureus*, *Bacillus subtilis*, *Escherichia coli* и *Klebsiella pneumoniae* као и према гљивицама *Aspergillus flavus* и *Fusarium oxysporum*.

(Примљено 3. децембра 2014, ревидирано 30. марта, прихваћено 10. јуна 2015)

REFERENCES

1. E. Genoux, E. Nicolle, A. Boumendjel, *Curr. Org. Chem.* **15** (2011) 2608
2. Z. P. Xiao, Z. Y. Peng, M. J. Peng, W. B. Yan, Y. Z. Ouyang, H. L. Zhu, *Mini-Rev. Med. Chem.* **11** (2011) 169
3. H. P. Kim, K. H. Son, H. Chang, S. S. Kang, *Nat. Prod. Sci.* **2** (1996) 1
4. A. Mishra, A. K. Sharma, S. Kumar, A. K. Saxena, A. K. Pandey, *BioMed Res. Int.* **10** (2013) 915
5. M. Friedman, *J. Agric. Food Chem.* **62** (2014) 6025
6. M. Grazul, A. Kufelnicki, M. Wozniczka, I. P. Lorenz, P. Mayer, A. Jozwiak, M. Czyz, E. Budzisz, *Polyhedron* **31** (2012) 150
7. E. O. Meltzer, *Allergy Asthma Proc.* **26** (2005) 445
8. M. Q. Zhang, Y. Wada, F. Sato, H. Timmerman, *J. Med. Chem.* **38** (1995) 2472
9. R. Velmurugan, A. V. Vijayasankar, M. Sekar, *Indian J. Chem., B* **52** (2013) 414
10. T. Indumathi, A. Muthusankar, P. Shanmughavel, K. Prasad, J. Rajendra, *Med. Chem. Commun.* **4** (2013) 450
11. B. P. Bandgar, L. K. Adsul, S. V. Lonikar, H. V. Chavan, S. N. Shringare, S. A. Patil, S. S. Jalde, B. A. Koti, N. A. Dhole, R. N. Gacche, *J. Enzyme Inhib. Med. Chem.* **28** (2013) 593
12. U. Ramachandran, R. Kumar, A. Mital, P. R. Rao, K. Srinivasan, C. S. Dey, A. Ishrath, H. P. S. Chawla, C. L. Kaul, *Indian Pat. Appl.* 2008, IN 2003DE01268 A20080509
13. a) D. Ashok, D. Mohan Gandhi, G. Srinivas, A. Vikas Kumar, *Med. Chem. Res.* **23** (2014), 3005; b) D. Ashok, B. Vijaya Lakshmi, S. Ravi, A. Ganesh, *Med. Chem. Res.* **84** (2015) 2234
14. A. C. Jain, S. M. Gupta, A. Sharma, *Bull. Chem. Soc. Jpn.* **56** (1983) 1267
15. D. H. Girish, P. K. Ashish, H. R. Atish, H. T. Rajesh, S. B. Satish, J. P. Mahendra, M. K. Vandana, *Med. Chem. Res.* **23** (2014) 461.



SUPPLEMENTARY MATERIAL TO

One-pot synthesis of carbazole based 3-hydroxy-4H-chromen-4-ones by a modified Algar–Flynn–Oyamada reaction and their antimicrobial activity

DONGAMANTI ASHOK*, SIDDA RAVI, BOMMIDI VIJAYA LAKSHMI
and ARRAM GANESH

Department of Chemistry, Osmania University, Hyderabad - 500 007, India

J. Serb. Chem. Soc. 80 (11) (2015) 1361–1366

PHYSICAL, ANALYTICAL AND SPECTRAL DATA FOR COMPOUNDS **3a–i**

2-(9-Ethyl-9H-carbazol-3-yl)-3-hydroxy-4H-chromen-4-one (3a). Anal. Calcd. for C₂₃H₁₇NO₃: C, 77.73; H, 4.82; N, 3.94 %. Found: C, 77.78; H, 4.86; N, 3.97 %. IR (KBr, cm⁻¹): 3446 (–OH), 1632 (C=O); ¹H-NMR (400 MHz, CDCl₃, δ / ppm): 1.48 (3H, t, J = 7.27 Hz, CH₃), 4.42 (2H, q, J = 7.27 Hz, N–CH₂), 7.08 (1H, brs, OH), 7.29–7.33 (1H, m, Ar-H), 7.41–7.54 (4H, m, Ar-H), 7.66–7.74 (2H, m, Ar-H), 8.24–8.29 (2H, m, Ar-H), 8.42 (1H, dd, J = 1.7, 8.7 Hz, Ar-H), 9.03 (1H, d, J = 1.5 Hz, Ar-H); ¹³C-NMR (100 MHz, CDCl₃, δ / ppm): 13.8, 37.7, 108.4, 108.8, 114.6, 118.2, 119.6, 120.7, 120.8, 121.7, 123.1, 124.3, 125.3, 125.5, 126.2, 133.1, 137.6, 140.5, 140.8, 146.7, 155.3, 173.0; ESI-MS (m/z): 356 ([M+H]⁺, 100 %).

2-(9-Ethyl-9H-carbazol-3-yl)-6-fluoro-3-hydroxy-4H-chromen-4-one (3b). Anal. Calcd. for C₂₃H₁₆FNO₃: C, 73.99; H, 4.32; N, 3.75 %. Found: C, 74.05; H, 4.36; N, 3.79 %. IR (KBr, cm⁻¹): 3441 (–OH), 1631 (C=O); ¹H-NMR (400 MHz, CDCl₃, δ / ppm): 1.49 (3H, t, J = 7.25 Hz, CH₃), 4.43 (2H, q, J = 7.20 Hz, N–CH₂), 7.00 (1H, brs, OH), 7.30–7.33 (1H, m, Ar-H), 7.42–7.45 (2H, m, Ar-H), 7.52–7.55 (2H, m, Ar-H), 7.90 (1H, dd, J = 4.0, 9.2 Hz, Ar-H), 8.22 (2H, d, J = 7.7 Hz, Ar-H), 8.41 (1H, dd, J = 1.7, 8.7 Hz, Ar-H), 9.02 (1H, d, J = 1.5 Hz, Ar-H); ¹³C-NMR (100 MHz, CDCl₃, δ / ppm): 13.8, 37.8, 108.5, 108.9, 109.7, 119.7, 120.2, 120.4, 120.8, 121.7, 121.8, 123.1, 123.2, 125.5, 126.3, 137.3, 140.5, 147.2, 151.6, 157.8, 160.2, 172.3; ESI-MS (m/z): 374 ([M+H]⁺, 100 %).

6-Chloro-2-(9-ethyl-9H-carbazol-3-yl)-3-hydroxy-4H-chromen-4-one (3c). Anal. Calcd. for C₂₃H₁₆ClNO₃: C, 70.86; H, 4.14; N, 3.59 %. Found: C, 70.91; H, 4.19; N, 3.63 %. IR (KBr, cm⁻¹): 3442 (–OH), 1630 (C=O); ¹H-NMR (400

*Corresponding author. E-mail: ashokdou@gmail.com

MHz, CDCl₃, δ / ppm): 1.48 (3H, *t*, *J* = 7.20 Hz, CH₃), 4.42 (2H, *q*, *J* = 7.02 Hz, N-CH₂), 7.02 (1H, *brs*, OH), 7.29–7.33 (1H, *m*, Ar-H), 7.45–7.62 (5H, *m*, Ar-H), 8.21 (2H, *d*, *J* = 7.5 Hz, Ar-H), 8.39 (1H, *d*, *J* = 8.5 Hz, Ar-H), 9.00 (1H, *d*, *J* = 1.2 Hz, Ar-H); ¹³C-NMR (100 MHz, CDCl₃, δ / ppm): 13.8, 37.8, 108.5, 108.9, 119.7, 119.9, 120.7, 120.8, 121.2, 121.7, 123.0, 123.2, 124.6, 125.5, 126.4, 130.4, 133.4, 137.7, 140.5, 140.9, 147.2, 153.6, 171.8; ESI-MS (*m/z*): 390 ([M+H]⁺, 100 %).

6-Bromo-2-(9-ethyl-9H-carbazol-3-yl)-3-hydroxy-4H-chromen-4-one (3d).

Anal. Calcd. for C₂₃H₁₆BrNO₃: C, 63.61; H, 3.71; N, 3.23 %. Found: C, 63.65; H, 3.75; N, 3.27 %; IR (KBr, cm⁻¹): 3440 (–OH), 1632 (C=O); ¹H-NMR (400 MHz, CDCl₃, δ / ppm): 1.48 (3H, *t*, *J* = 7.20 Hz, CH₃), 4.42 (2H, *q*, *J* = 7.20 Hz, N-CH₂), 6.99 (1H, *brs*, OH), 7.30–7.34 (1H, *m*, Ar-H), 7.50–7.56 (4H, *m*, Ar-H), 7.64 (1H, *s*, Ar-H), 8.22 (2H, *d*, *J* = 7.5 Hz, Ar-H), 8.40 (1H, *d*, *J* = 8.5 Hz, Ar-H), 9.01 (1H, *s*, Ar-H); ¹³C-NMR (100 MHz, CDCl₃, δ / ppm): 13.8, 37.8, 108.5, 108.9, 109.1, 119.7, 119.9, 120.3, 120.7, 120.8, 121.2, 123.0, 123.1, 124.6, 125.6, 126.4, 126.7, 130.2, 133.4, 137.7, 140.5, 140.9, 147.4, 151.0, 153.6, 171.9; ESI-MS (*m/z*): 434 ([M+H]⁺, 100 %).

2-(9-Ethyl-9H-carbazol-3-yl)-3-hydroxy-6-methyl-4H-chromen-4-one (3e).

Anal. Calcd. for C₂₄H₁₉NO₃: C, 78.03; H, 5.18; N, 3.79 %. Found: C, 71.41; H, 4.51; N, 3.51 %; IR (KBr, cm⁻¹): 3444 (–OH), 1628 (C=O); ¹H-NMR (400 MHz, CDCl₃, δ / ppm): 1.47 (3H, *t*, *J* = 7.02 Hz, CH₃), 2.48 (3H, *s*, Ar-CH₃), 4.40 (2H, *q*, *J* = 7.02 Hz, N-CH₂), 7.09 (1H, *brs*, OH), 7.28–7.32 (1H, *m*, Ar-H), 7.43–7.56 (5H, *m*, Ar-H), 8.04 (1H, *s*, Ar-H), 8.21 (1H, *d*, *J* = 7.7 Hz, Ar-H), 8.40 (1H, *dd*, *J* = 1.7, 8.7 Hz, Ar-H), 9.01 (1H, *d*, *J* = 1.5 Hz, Ar-H); ¹³C-NMR (100 MHz, CDCl₃, δ / ppm): 13.8, 29.6, 37.9, 108.4, 108.6, 108.8, 109.1, 117.9, 119.6, 120.3, 120.7, 120.8, 123.0, 123.1, 123.2, 124.0, 124.5, 125.6, 126.2, 126.7, 127.2, 128.5, 134.6, 140.5, 140.7, 143.6, 160.4, 172.7. ESI-MS (*m/z*): 370 ([M+H]⁺, 100 %).

6-Chloro-2-(9-ethyl-9H-carbazol-3-yl)-3-hydroxy-7-methyl-4H-chromen-4-one (3f). Anal. Calcd. for C₂₄H₁₈ClNO₃: C, 71.38; H, 4.49; N, 3.47 %. Found: C, 71.41; H, 4.51; N, 3.51 %; IR (KBr, cm⁻¹): 3445 (–OH), 1632 (C=O); ¹H-NMR (400 MHz, CDCl₃, δ / ppm): 1.48 (3H, *t*, *J* = 7.02 Hz, CH₃), 2.55 (3H, *s*, Ar-CH₃), 4.43 (2H, *q*, *J* = 7.02 Hz, N-CH₂), 7.21 (1H, *s*, OH), 7.29–7.33 (1H, *m*, Ar-H), 7.45–7.57 (4H, *m*, *J* = 4.0, 9.2 Hz, Ar-H), 8.15–8.23 (2H, *m*, Ar-H), 8.40 (1H, *d*, *J* = 8.7 Hz, Ar-H), 8.99 (1H, *d*, *J* = 1.5 Hz, Ar-H); ¹³C-NMR (100 MHz, CDCl₃, δ / ppm): 13.8, 29.7, 37.9, 108.7, 109.0, 109.1, 116.1, 119.9, 120.3, 120.5, 120.7, 120.8, 122.1, 123.1, 123.2, 124.0, 125.5, 126.5, 126.7, 126.8, 127.2, 128.5, 129.1, 140.7, 141.8, 143.6, 145.0, 147.7, 162.0, 172.3; ESI-MS (*m/z*): 404 ([M+H]⁺, 100 %).

6,8-Dichloro-2-(9-ethyl-9H-carbazol-3-yl)-3-hydroxy-4H-chromen-4-one (3g).

Anal. Calcd. for C₂₃H₁₅Cl₂NO₃: C, 65.11; H, 3.56; N, 3.30 %. Found: C,

65.15; H, 3.61; N, 3.35 %; IR (KBr, cm^{-1}): 3445 ($-\text{OH}$), 1629 (C=O); $^1\text{H-NMR}$ (400 MHz, CDCl_3 , δ / ppm): 1.50 (3H, *t*, J = 7.02 Hz, CH_3), 4.43 (2H, *q*, J = 7.02 Hz, N- CH_2), 6.31 (1H, *brs*, OH), 7.33–7.66 (6H, *m*, Ar-H), 8.03 (1H, *d*, J = 7.8 Hz, Ar-H), 8.18 (1H, *d*, J = 7.8 Hz, Ar-H), 8.63 (1H, *s*, Ar-H); $^{13}\text{C-NMR}$ (100 MHz, CDCl_3 , δ / ppm): 13.8, 37.9, 108.4, 108.6, 109.1, 119.1, 119.8, 120.3, 120.6, 120.8, 120.9, 123.0, 123.2, 123.3, 124.2, 125.6, 126.2, 126.5, 126.7, 127.2, 128.3, 128.8, 135.9, 140.7, 143.7, 155.4, 155.7, 171.9; ESI-MS (*m/z*): 424 ([M+H]⁺, 100 %).

2-(9-Ethyl-9H-carbazol-3-yl)-3-hydroxy-7-methoxy-4H-chromen-4-one (3h). Anal. Calcd. for $\text{C}_{24}\text{H}_{19}\text{NO}_4$: C, 74.79; H, 4.97; N, 3.63 %. Found: C, 74.85; H, 5.01; N, 3.67 %; IR (KBr, cm^{-1}): 3440 ($-\text{OH}$), 1625 (C=O); $^1\text{H-NMR}$ (400 MHz, CDCl_3 , δ / ppm): 1.48 (3H, *t*, J = 7.27 Hz, CH_3), 3.97 (3H, *s*, O- CH_3), 4.42 (2H, *q*, J = 7.27 Hz, N- CH_2), 6.99–7.07 (3H, *m*, OH & Ar-H), 7.29–7.32 (1H, *m*, Ar-H), 7.45–7.54 (3H, *m*, Ar-H), 8.16 (1H, *d*, Ar-H), 8.23 (1H, *d*, J = 7.7 Hz, Ar-H), 8.40 (1H, *dd*, J = 1.5, 8.7 Hz, Ar-H), 8.98 (1H, *d*, J = 1.25 Hz, Ar-H); $^{13}\text{C-NMR}$ (100 MHz, CDCl_3 , δ / ppm): 13.8, 37.7, 55.8, 99.8, 108.4, 108.8, 114.6, 114.7, 119.5, 120.3, 120.7, 121.8, 123.0, 123.1, 125.4, 126.2, 126.6, 137.2, 140.4, 140.6, 146.1, 157.2, 163.9, 172.5. ESI-MS (*m/z*): 386 ([M+H]⁺, 100 %).

7-Ethoxy-2-(9-ethyl-9H-carbazol-3-yl)-3-hydroxy-4H-chromen-4-one (3i). Anal. Calcd. for $\text{C}_{25}\text{H}_{21}\text{NO}_4$: C, 75.17; H, 5.30; N, 3.51 %. Found: C, 75.21; H, 5.35; N, 3.54 %; IR (KBr, cm^{-1}): 3442 ($-\text{OH}$), 1628 (C=O); $^1\text{H-NMR}$ (400 MHz, CDCl_3 , δ / ppm): 1.45–1.48 (6H, *m*, 2× CH_3), 4.12 (2H, *q*, J = 7.02 Hz, O- CH_2), 4.42 (2H, *q*, J = 7.02 Hz, N- CH_2), 6.98–7.06 (3H, *m*, OH & Ar-H), 7.28–7.31 (1H, *m*, Ar-H), 7.42–7.52 (3H, *m*, Ar-H), 8.13 (1H, *d*, Ar-H), 8.21 (1H, *d*, J = 7.4 Hz, Ar-H), 8.38 (1H, *dd*, J = 1.6, 8.6 Hz, Ar-H), 8.96 (1H, *d*, J = 1.4 Hz, Ar-H); $^{13}\text{C-NMR}$ (100 MHz, CDCl_3 , δ / ppm): 13.8, 14.5, 37.8, 62.8, 99.9, 108.2, 109.4, 114.6, 114.7, 119.5, 120.2, 120.7, 121.9, 122.6, 123.0, 125.4, 126.2, 126.6, 137.6, 140.1, 140.3, 144.7, 157.0, 162.7, 172.3; ESI-MS (*m/z*): 400 ([M+H]⁺, 100 %).



Facile synthesis and antifungal activity of dithiocarbamate derivatives bearing an amide moiety

YU-WEN LI* and SHU-TAO LI

School of Chemistry and Pharmacy, Qingdao Agricultural University, Qingdao, P. R. China

(Received 14 January, accepted 24 May 2015)

Abstract: Two series of novel dithiocarbamate derivatives bearing an amide moiety, **3a–i** and **4a–i**, were synthesized by a facile method, and the structures of the derivatives were confirmed by elemental analysis and $^1\text{H-NMR}$, $^{13}\text{C-NMR}$ and high-resolution mass spectrometry (HRMS). Their antifungal activity against five phytopathogenic fungi were evaluated, and the results showed that most of the target compounds displayed low antifungal activity *in vitro* against *Gibberella zaeae*, *Cytospora* sp., *Colletotrichum gloeosporioides*, *Alternaria solani*, and *Fusarium solani* at a concentration of 100 mg L⁻¹. However, two compounds, **4f** and **4g**, exhibited significant activity against *A. solani* and *C. gloeosporioides*, respectively.

Keywords: antifungal activity; dithiocarbamate derivatives; amide moiety; synthesis.

INTRODUCTION

Plant disease arising from phytopathogenic fungi is one of the major causes of severe losses in agriculture and horticulture crop production worldwide, and poses a threat to global food security.¹ In the past years, fungicides have contributed enormously to reduce crop loss caused by phytopathogenic fungi. However, the main problem associated with the application of fungicides is the emergence of fungicide resistance. Therefore, it is necessary to develop efficient fungicides with novel structures to obviate this resistance.

Due to their multiple biological profiles, carboxylic acid amide compounds have found application not only in medicinal chemistry but also in pesticide chemistry, *i.e.*, as insecticides,^{2–4} fungicides,⁵ herbicides⁶ and plant growth regulators.⁷ Dithiocarbamate derivatives, on the other hand, have played important roles in medicinal and pesticide chemistry because of their diverse activities.^{8–11} In pesticide chemistry, dithiocarbamate derivatives have also served as fungicides.¹² An important strategy for drug discovery has emerged that consists of

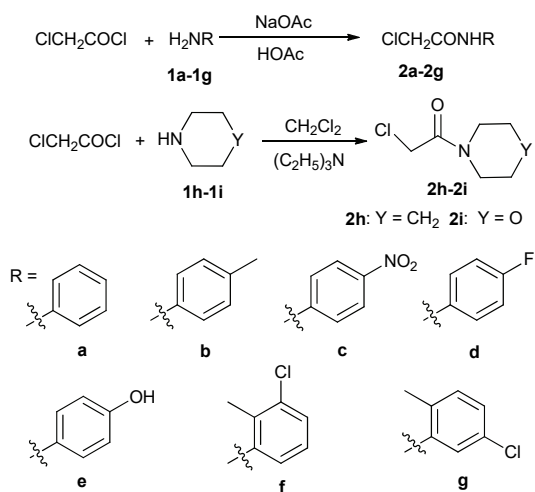
*Corresponding author. E-mail: ywli@qau.edu.cn
doi: 10.2298/JSC150114047L

hybridizing two bioactive molecules or pharmacophores to generate a novel class of molecules with a potentially stronger bioactivity profile.^{13,14} Thus, inspired by the biological importance of carboxylic acid amides and dithiocarbamates as fungicides in the pesticide field, herein, the synthesis of novel carboxylic acid amide-dithiocarbamate hybrids **3a–i** and **4a–i** and their antifungal activities are reported.

RESULTS AND DISCUSSION

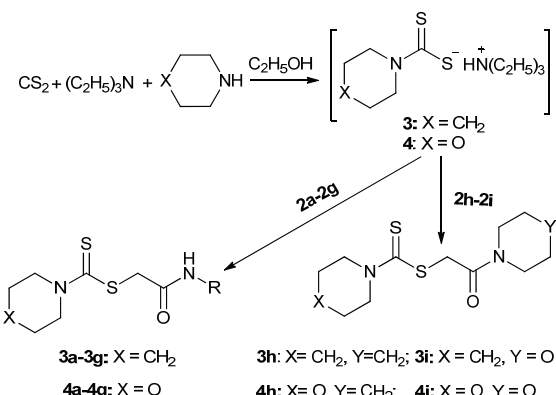
Chemistry

In this study, the starting materials, 2-chloroacetamides **2a–i**, were prepared according to the literature¹⁵ with some modifications (Scheme 1). The intermediates **2a–g** were synthesized by treatment of 2-chloroacetyl chloride with **1a–g**, respectively, in a mixture of acetic acid and a saturated solution of sodium acetate. However, this procedure was unsuitable for the synthesis of intermediates **2h** and **2i** due to difficulties encountered in the separation and purification of the liquid **2h** and **2i** from the liquid mixture of HOAc and NaOAc. Thus, intermediates **2h** and **2i** were synthesized by reaction of 2-chloroacetyl chloride with **1h** and **1i**, respectively, in the presence of triethylamine as acid-scavenger and dichloromethane as solvent. With intermediates **2a–i** available, the target compounds **3a–i** and **4a–i** were synthesized. However, conventional synthesis of dithiocarbamates involves costly and toxic chemical reagents, such as thiophosgene.¹⁶ Current strategies could partially alleviate the expense and toxicity for the synthesis by several one-pot syntheses *via* the reaction of carbon disulfide with amine and alkyl halides or acrylates.¹⁷ Still, several drawbacks of these one-pot procedures remained inevitable, such as the use of strong bases, high reac-



Scheme 1. Synthesis of intermediates **2a–i**.

tion temperatures, long reaction time, and harmful organic solvents.¹⁸ To circumvent the drawbacks associated with the previous procedures for the preparation of dithiocarbamates, the target compounds **3a–i** and **4a–i** were prepared according to Scheme 2.



Scheme 2. Synthesis of target compounds **3a–i** and **4a–i**.

As illustrated in Scheme 2, the synthesis method was improved such that the reactions of carbon disulfide, triethylamine and piperidine or morpholine were realized at 0 °C to obtain intermediates **3** and **4**, respectively, as white solids. To the thus-obtained intermediates **3** and **4**, absolute ethanol was added *in situ*, leading to the respective suspensions of **3** and **4** in absolute ethanol. Subsequently, reaction of the suspended **3** and **4** in ethanol with the intermediates **2a–i** at 50 °C led to the generation of the target compounds **3a–i** and **4a–i**, respectively. Upon completion of the reaction, **3a–i** and **4a–i** were *in situ* precipitated by cooling the corresponding reaction mixture down to 0 °C and collected by filtration. Since more or less **3a–i** or **4a–i** remained in the mother liquor, more sequential steps were indispensable to recover the residual **3a–i** and **4a–i** from their corresponding mother liquor. Firstly, evaporation of the mother liquor to dryness afforded a solid mixture containing the side-product triethylamine hydrochloride and residual **3a–i** and **4a–i**, respectively. Furthermore, given that triethylamine hydrochloride is not soluble in ether solvents while **3a–i** and **4a–i** are, the addition of 2-methyltetrahydrofuran to the thus-obtained solid mixtures left a white precipitate of triethylamine hydrochloride, a useful reagent in drug synthesis,¹⁹ that was removed by filtration. The filtrates were then concentrated under reduced pressure to give the respective residuals **3a–i** and **4a–i**. Finally, recrystallization of the residuals **3a–i** and **4a–i** from 95 % ethanol led to the desired target compounds. The notable advantages of the present procedure over previous ones are that it is easy to conduct in terms of generation, separation, and purification of the target compounds **3a–i** and **4a–i** and is readily performed in one pot with only

one solvent by modulating the temperature in the range from 50 to 0 °C. In addition, taking the recovered **3a–i** and **4a–i** into account, the overall yields of the products were almost quantitative.

Antifungal activity: in vitro screening of compounds **3a–3i** and **4a–4i**

All the newly synthesized target compounds **3a–i** and **4a–i** were evaluated *in vitro* for their antifungal activity against five phytopathogenic fungi, *i.e.*, *Gibberella zaeae*, *Cytospora* sp., *Colletotrichum gloeosporioides*, *Alternaria solani* and *Fusarium solani* at concentration of 100 mg L⁻¹. As summarized in Table I, most target compounds displayed low antifungal activities against these five phytopathogenic fungi at the indicated concentration with exception of compounds **4f** and **4g**. Compound **4f** displayed 77.26 % inhibition of *A. solani*, while compound **4g** exhibited 74.87 % inhibition of *C. gloeosporioides* at a concentration of 100 mg L⁻¹. To understand further the role of different groups of the compounds in conferring the antifungal activity, it is necessary to compare their structures. Structurally, compounds **3a–i** and **4a–i** are derived from same scaffold but with different substituents, leading to the difference in the antifungal activity. Generally, compounds **4a–4i** were superior to the corresponding compounds **3a–i** in terms of their antifungal activity, suggesting that the presence of morpholinyl group in **4a–i** conferred better antifungal activity than the corresponding piper-

TABLE I. Fungicidal activities of the target compounds **3a–i** and **4a–i** at a concentration of 100 mg L⁻¹; Hy – hymexazol

Compound	Antifungal activity (Inhibition rate, %)				
	<i>G. zaeae</i>	<i>A. solani</i>	<i>C. gloeosporioides</i>	<i>Cytospora</i> sp.	<i>F. solani</i>
3a	33.41	24.52	20.25	5	26.75
3b	30.32	23.48	24.97	42.13	24.46
3c	34.42	21.47	14.81	36.29	34.79
3d	39.52	41.23	38.65	39.49	36.13
3e	21.78	30.14	23.41	31.73	35.47
3f	43.97	46.13	40.94	49.78	41.64
3g	40.27	43.94	39.08	46.66	39.35
3h	19.24	23.56	34.75	28.91	14.34
3i	27.88	29.76	30.51	32.14	30.09
4a	41.77	36.72	38.13	32.43	38.19
4b	46.18	39.76	30.67	51.09	32.08
4c	40.07	28.94	34.96	46.81	40.11
4d	47.14	45.97	47.08	52.13	43.93
4e	23.93	35.46	26.43	33.19	39.86
4f	58.11	77.26	59.04	57.89	53.98
4g	62.93	51.67	74.87	60.09	56.89
4h	30.08	32.77	47.69	38.06	45.77
4i	31.18	35.26	43.22	39.18	34.17
Hy	90.56	82.15	53.78	46.69	79.23

idinyl group in compounds **3a–i**. More interestingly, compounds **4f** and **4g**, bearing two substituents on the benzene ring, displayed significantly higher antifungal activities relative to the compounds with a single substituent on the benzene ring. In addition, the compounds with fluorine substituent on the benzene ring regardless of the substituent on the carbamic moiety, such as **3d** and **4d**, showed higher antifungal activities (although not dramatic) compared to other corresponding compounds without fluorine substituent on the benzene ring. Although most of the target compounds display low inhibition rate against mycelia growth of these five tested fungi at concentration of 100 mg/L, target compounds **4f–g** could be potential lead structures for further discovery of novel antifungal agrochemicals.

EXPERIMENTAL

Chemistry

All the employed chemicals were obtained from Qingdao Justness Reagent Company (China) and used without further purification. The melting points were measured using a WRS-1B digital melting point apparatus. The ¹H-NMR spectra were recorded on a Bruker DRX-400 Advance spectrometer at 400 MHz using TMS as an internal standard.

The physical, analytical and spectral data of the synthesized compounds are given in the Supplementary material to this paper.

General procedure for the synthesis of compounds 2a–g

A substituted aniline (34.3 mmol) was added to 12.5 mL of a saturated solution of sodium acetate, followed by 12.5 mL acetic acid. The suspension was cooled to 0 °C, and 2-chloroacetyl chloride (34.4 mmol, 2.75 ml) was added dropwise to the suspension at ≤5 °C. During the addition of 2-chloroacetyl chloride, the suspension dissipated and the mixture clarified. Before the addition of 2-chloroacetyl chloride was complete, a white precipitate began to form. Upon completion of the addition, the heterogeneous mixture was brought to 25 °C and stirred at room temperature for 2 h. The white precipitate was filtered, washed with distilled water (2×5 mL) and dried under vacuum to afford the crude product. Recrystallization of crude **2a–g** from absolute ethanol gave the desired **2a–g**, respectively. The physical, analytic and spectral data of **2a–g** are summarized in the Supplementary material to this paper.

General procedure for synthesis of compounds 2h and 2i

To a stirred solution of triethylamine (17.2 mmol, 2.5 mL) and 17.2 mmol piperidine **1h** (or morpholine **1i**) in 10 mL CH₂Cl₂, 2-chloroacetyl chloride (17.2 mmol, 1.38 mL) was added dropwise at 0 °C. Upon completion of the dropwise addition, the solution was brought to room temperature and stirred for 2 h. Subsequently, the resulting solution was diluted with 20 mL CH₂Cl₂ and successively washed with 20 mL water and 20 mL brine. The CH₂Cl₂ layer was separated and concentrated under reduced pressure to give crude **1h** (or **1i**) which was further purified by chromatography to afford the desired **1h** (or **1i**) as a yellowish oil. The physical, analytical and spectral data of **2h** and **2i** are summarized in the Supplementary material to this paper.

General procedure for the synthesis of compounds 3a–i and 4a–i

To a solution of triethylamine (17.2 mmol, 1.5 mL) and 17.2 mmol piperidine **1h** (or morpholine **1i**), carbon disulfide (18.9 m mol, 1.2 mL) was added dropwise at 0 °C to form a white solid **3** (or **4**). Upon completion of the addition, 15 mL absolute ethanol was added to form a slurry of the white solid **3** (or **4**), to which 17.2 mmol respective intermediate **2a–i** was added. The mixture was heated to 50 °C to afford a clear solution. The clear solution was kept stirring at 50 °C for 3 h and then cooled to 0 °C. The cooled solution was kept for 2 h at 0 °C and the precipitate of **3a–i** (or **4a–i**) was collected by filtration and the corresponding filtrate was evaporated to dryness leading to a solid mixture of triethylamine hydrochloride and residual **3a–i** (or **4a–i**). Then, the addition of 2-methyltetrahydrofuran to the thus obtained solid mixture led to triethylamine hydrochloride by filtration. The corresponding filtrate was concentrated under vacuum to give the residual **3a–i** (or **4a–i**). Recrystallization of thus obtained residual **3a–i** (or **4a–i**) from 95 % ethanol led to the desired **3a–i** (or **4a–i**). Taking the recovered **3a–i** and **4a–i** into account, the overall yield of **3a–i** and **4a–i** was almost quantitative. The physical, analytical and spectral data for **3a–i** and **4a–i** are summarized in the Supplementary material to this paper.

Antifungal activity

Antifungal activities of target compounds **3a–i** and **4a–i** were evaluated *in vitro* against five phytopathogenic fungi (*Gibberella zeae*, *Cytospora* sp., *Colletotrichum gloeosporioides*, *Alternaria solani* and *Fusarium solani*) using the mycelium growth rate method.^{20,21} All the fungi were provided by the Qingdao Agricultural University. The strains were retrieved from the storage tube and cultured for 2 weeks at 25 °C on potato dextrose agar (PDA).

The antifungal activity was assessed as follows: PDA medium was prepared in flasks and sterilized. The target compounds **3a–i** and **4a–i** were dissolved in acetone prior to mixing with molten agar at 55 °C, and the concentration of the target compounds **3a–i** and **4a–i** were 100 mg L⁻¹. The PDA medium was then poured into sterilized Petri dishes. The five fungi were incubated in PDA at 25 °C for 7 days to obtain new mycelium for the fungicidal assays, and a mycelia disk of 4 mm in diameter cut from culture medium was picked up with a sterilized inoculation needle and inoculated in the centre of the PDA Petri dishes. The inoculated Petri dishes were incubated at 25 °C for 3–4 days. Acetone was used as the control, and the commercially available agricultural fungicide hymexazol served as the positive control. Each compound was measured in three replicates, and each colony diameter of the three replicates was measured 4 times by the cross bracketing method. The inhibition rate (IR) was calculated according to the following formula:

$$IR(\%) = 100 \frac{C - T}{C - 4}$$

where *C* is the average diameter of mycelia in the blank test and *T* is the average diameter of mycelia on PDA treated with the target compounds.

CONCLUSIONS

In summary, a series of dithiocarbamates bearing an amide moiety **3a–i** and **4a–i** were synthesized in almost quantitative yield by a facile and convenient procedure. Especially, the synthesis, separation, and purification by recrystallization could be conducted in one-pot and in same medium by regulating the temperature from 50 to 0 °C. The results of the bioassay indicated that most target compounds

displayed low activities against *G. zae*, *Cytospora* sp., *C. gloeosporioides*, *A. solani* and *F. solani* at a concentration of 100 mg L⁻¹. However, the compounds **4f** and **4g** gave significant inhibition rates against *A. solani* and *C. gloeosporioides*, respectively, at a concentration of 100 mg L⁻¹. Generally, the antifungal activities of compounds **4a–i**, which have a morpholinyl substituent, are superior to the corresponding compounds **3a–i** with the piperidinyl substituent. Additionally, the number of substituents on benzene ring influenced the antifungal activity as evidenced by the fact that the compounds bearing two substituents on the benzene ring, such as **3f** and **3g** and **4f** and **4g**, displayed better antifungal activities than the compounds with a single substituent on the benzene ring. Although most of the target compounds displayed low inhibition rates against mycelia growth of the five tested fungi at concentrations of 100 mg L⁻¹, the target compounds **4f** and **4g** could be potentially leading structures for further discovery of novel antifungal agrochemicals.

SUPPLEMENTARY MATERIAL

Physical, analytical and spectral data of the synthesized compounds are available electronically from <http://www.shd.org.rs/JSCS/>, or from the corresponding author on request.

Acknowledgement. This work was financially supported by the Natural Science Foundation of Shandong Province (ZR2011BL003).

ИЗВОД
ЈЕДНОСТАВНА СИНТЕЗА АМИДНИХ ДЕРИВАТА ДИТИОКАРБАМАТА И ЊИХОВА
АНТИФУНГАЛНА АКТИВНОСТ

YU-WEN LI и SHU-TAO LI

School of Chemistry and Pharmacy, Qingdao Agricultural University, Qingdao, P. R. China

Синтетисана је серија нових деривата дитиокарбамата који садрже амидну групу, **3a–i** и **4a–i**, применом олакшаног поступка и добијеним дериватима је структура потврђена ¹H-NMR, ¹³C-NMR спектроскопијом, елементалном анализом и масеном спектрометријом високе резолуције (HRMS). Испитана је антифунгална активност према пет фитопатогених гљива. Резултати су показали да већина деривата показује *in vitro* активност према *Gibberella zae*, *Cytospora* sp., *Colletotrichum gloeosporioides*, *Alternaria solani* и *Fusarium solani* при концентрацији 100 mg L⁻¹. Једињења **4f** и **4g** показују значајну активност према *A. solani* и *C. gloeosporioides*, редом.

(Примљено 14. јануара, прихваћено 24. маја 2015)

REFERENCES

1. S. Savary, P. S. Teng, L. Willocquet, F. W. Nutter, *Annu. Rev. Phytopathol.* **44** (2006) 89
2. J. C. Yang, J. B. Zhang, B. S. Chai, C. L. Liu, *Chin. J. Pestic. Sci.* **47** (2008) 6
3. X. T. Xu, F. Leng, W. G. Duan, G. S. Lin, Q. J. Mo, W. K. Wang, *Chem. Bulletin* **75** (2012) 463 (in Chinese)
4. G. P. Lahm, T. M. Stevenson, T. P. Selby, J. H. Freudenberger, D. Cordova, L. Flexner, C. A. Bellin, C. M. Dubas, B. K. Smith, J. G. Hollingshaus, C. E. Clark, E. A. Benner, *Bioorg. Med. Chem. Lett.* **17** (2007) 6274

5. J. Liu, H. P. Xie, B. A. Song, D. Y. Hu, S. Yang, L. H. Jin, W. Xue, J. Wu, W. M. Xu, *Chin. J. Org. Chem.* **30** (2010) 1347
6. Q. J. Ge, L. Z. Chen, X. H. Du, *Chin. J. Org. Chem.* **31** (2011) 1510
7. J. H. Choi, N. Abe, H. Tanaka, K. Fushimi, Y. Nishina, A. Morita, Y. Kirhwa, R. Motohashi, D. Hashizume, H. Koshino, H. Kawagishi, *J. Agric. Food Chem.* **58** (2010) 9956
8. F. Carta, C. T. Supuran, *Chem. Commun.* **48** (2012) 1870
9. F. Carta, M. Aggarwal, A. Maresca, R. McKenna, E. Masini, C. T. Spuran, *J. Med. Chem.* **55** (2012) 1730
10. K. Bacharaju, S. R. Jambula, S. Sivan, S. J. Tangeda, V. Manga, *Bioorg. Med. Chem. Lett.* **22** (2012) 3277
11. X. J. Wang, H. W. Xu, L. L. Guo, X. Guo, C. X. Zheng, H. M. Liu, *Bioorg. Med. Chem. Lett.* **21** (2011) 3074
12. C. Len, A. S. Boulogne-Merlot, D. Postel, G. Ronco, P. Villa, C. Goubert, E. Jeufraut, B. Mathon, H. Simon, *J. Agric. Food Chem.* **44** (1996) 2856
13. A. C. Pierce, G. Rao, G. W. Bemis, *J. Med. Chem.* **47** (2004) 2768
14. A. K. Ghose, T. Herbertz, D. A. Pippin, J. M. Salvino, J. P. Mallamo, *J. Med. Chem.* **51** (2008) 5149
15. L. Miao, L. Xu, K. W. Narducy, M. L. Trudell, *Org. Process Res. Dev.* **13** (2009) 820
16. J. T. R. Burker, B. S. Bajwa, A. E. Jacobsen, K. C. Rice, R. A. Streaty, W. A. Klee, *J. Med. Chem.* **27** (1984) 1570
17. S. R. Guo, Y. Q. Yuan, C. N. Zhang, *Chin. J. Org. Chem.* **32** (2012) 907
18. J. Garin, E. Melendez, F. L. Merchan, T. Tejero, S. Uriel, J. Ayestaran, *Synthesis* (1991) 147
19. S. Y. Jang, S. B. Kim, S. Yun, H. K. Kim, K. H. Suh, WO133040 (2007)
20. X. J. Li, Q. Zhang, A. L. Zhang, J. M. Gao, *J. Agric. Food Chem.* **60** (2012) 3424
21. X. J. Li, X. W. Shi, Q. Shuai, J. M. Gao, A. L. Zhang, *Nat. Prod. Commun.* **6** (2011) 1129.



SUPPLEMENTARY MATERIAL TO
Facile synthesis and antifungal activity of dithiocarbamate derivatives bearing an amide moiety

YU-WEN LI* and SHU-TAO LI

School of Chemistry and Pharmacy, Qingdao Agricultural University, Qingdao, P. R. China

J. Serb. Chem. Soc. 80 (11) (2015) 1367–1374

2-Chloro-N-phenylacetamide (2a). Yield: 90.1 %; white solid; m.p.: 148.8–150 °C; Anal. Calcd. for C₈H₈ClNO: C, 56.65; H, 4.75; Cl, 20.90; N, 8.26 %. Found: C, 56.63; H, 4.72; Cl, 20.87; N, 8.29 %; ¹H-NMR (400 MHz, CDCl₃, δ / ppm): 4.20 (2H, s, ClCH₂CO), 7.18 (1H, t, J = 7.2 Hz, Ar-H), 7.35–7.39 (2H, m, Ar-H), 7.55–7.57 (2H, m, Ar-H), 8.27 (1H, bs, CONH); ESI-HRMS (m/z): Calcd. for C₈H₉ONCl [M+H]⁺: 170.0373. Found: 170.0367.

2-Chloro-N-p-tolylacetamide (2b): Yield: 87.3 %; white solid; m.p.: 168.5–169 °C; Anal. Calcd. for C₉H₁₀ClNO: C, 58.86; H, 5.49; Cl, 19.31; N, 7.63 %. Found: C, 58.88; H, 5.51; Cl, 19.29; N, 7.60 %; ¹H-NMR (400 MHz, CDCl₃, δ / ppm): 2.33 (3H, s, CH₃), 4.19 (2H, s, ClCH₂CO), 7.16 (2H, d, J = 8.4 Hz, Ar-H), 7.43 (2H, d, J = 8.4 Hz, Ar-H), 8.21 (1H, bs, CONH); ESI-HRMS (m/z): Calcd. for C₉H₁₁ONCl [M+H]⁺: 184.0529. Found: 184.0524.

2-Chloro-N-(4-nitrophenyl)acetamide (2c). Yield: 79 %; yellowish solid; m.p.: 185.2–186 °C; Anal. Calcd. for C₈H₇CIN₂O₃: C, 44.77; H, 3.29; Cl, 16.52; N, 13.05 %. Found: C, 44.74; H, 3.27; Cl, 16.49; N, 13.07 %; ¹H-NMR (400 MHz, CDCl₃, δ / ppm): 4.25 (2H, s, ClCH₂CO), 7.78 (2H, d, J = 9.2 Hz, Ar-H), 8.27 (2H, d, J = 9.2 Hz, Ar-H), 8.52 (1H, bs, CONH).

2-Chloro-N-(4-fluorophenyl)acetamide (2d). Yield: 93 %; white solid; m.p.: 146.6–147.2 °C; Anal. Calcd. for C₈H₇ClFNO: C, 51.22; H, 3.76; Cl, 18.90; F, 10.13; N, 7.47 %. Found: C, 51.20; H, 3.74; Cl, 18.91; F, 10.11; N, 7.49 %; ¹H-NMR (400 MHz, CDCl₃, δ / ppm): 4.20 (2H, s, ClCH₂CO), 7.04–7.08 (2H, m, Ar-H), 7.50–7.54 (2H, m, Ar-H), 8.26 (1H, bs, CONH); ESI-HRMS (m/z): Calcd. for C₈H₈ONClF [M+H]: 188.0278. Found: 188.0273.

2-Chloro-N-(4-hydroxyphenyl)acetamide (2e). Yield: 83 %; white solid; m.p.: 148.2–149 °C (lit.¹ 142–144 °C).

*Corresponding author. E-mail: ywli@qau.edu.cn

2-Chloro-N-(3-chloro-2-methylphenyl)acetamide (2f). Yield: 78 %; white solid; m.p.: 138.5–139 °C; Anal. Calcd. for C₉H₉Cl₂NO: C, 49.57; H, 4.16; Cl, 32.51; N, 6.42 %. Found: C, 49.59; H, 4.13; Cl, 32.49; N, 6.45 %; ¹H-NMR (400 MHz, CDCl₃, δ / ppm): 2.35 (3H, s, CH₃), 4.26 (2H, s, ClCH₂CO), 7.18 (1H, t, J = 8.0 Hz, Ar-H), 7.26–7.27 (1H, m, Ar-H), 7.73 (1H, d, J = 7.6 Hz, Ar-H), 8.28 (1H, bs, CONH); ESI-HRMS (m/z): Calcd. for C₉H₁₀ONCl₂ [M+H]⁺: 218.0139. Found: 218.0134.

2-Chloro-N-(5-chloro-2-methylphenyl)acetamide (2g). Yield: 75 %, white solid; m.p.: 142.1–142.5 °C; Anal. Calcd. for C₉H₉Cl₂NO: C, 49.57; H, 4.16; Cl, 32.51; N, 6.42 %. Found: C, 49.54; H, 4.18; Cl, 32.53; N, 6.39 %; ¹H-NMR (400 MHz, CDCl₃, δ / ppm): 2.28 (3H, s, CH₃), 4.25 (2H, s, ClCH₂CO), 7.09 (1H, dd, J = 8.4 Hz and 2.0 Hz, Ar-H), 7.14 (1H, d, J = 8.4 Hz, Ar-H), 8.05 (1H, s, Ar-H), 8.27 (1H, bs, CONH); ESI-HRMS (m/z): Calcd. for C₉H₁₀ONCl₂ [M+H]⁺: 218.0139. Found: 218.0133.

2-Chloro-1-(piperidin-1-yl)ethanone (2h). Yield: 81 %; yellowish oil; Anal. Calcd. for C₇H₁₂ClNO: C, 52.02; H, 7.48; Cl, 21.93; N, 8.67 %. Found: C, 51.99; H, 7.49; Cl, 21.91; N, 8.69 %; ¹H-NMR (400 MHz, CDCl₃, δ / ppm): 1.56–1.59 (2H, m, CH₂), 1.61–1.69 (4H, m, 2×CH₂), 3.46 (2H, t, J = 5.6 Hz, CH₂), 3.75 (2H, t, J = 5.6 Hz, CH₂), 4.09 (2H, s, ClCH₂CO); ESI-HRMS (m/z): Calcd. for C₇H₁₃ONCl [M+H]⁺: 162.0686. Found: 168.0680.

2-Chloro-1-morpholinoethanone (2i). Yield: 79 %; yellowish oil; Anal. Calcd. for C₆H₁₀ClNO₂: C, 44.05; H, 6.16; Cl, 21.67; N, 8.56 %. Found: C, 44.07; H, 6.14; Cl, 21.65; N, 8.59 %; ¹H-NMR (400 MHz, CDCl₃, δ / ppm): 3.54 (2H, t, J = 5.2 Hz, CH₂), 3.64 (2H, t, J = 4.8 Hz, CH₂), 3.70–3.75 (4H, m, 2×CH₂), 4.09 (2H, s, ClCH₂CO); ESI-HRMS (m/z): Calcd. for C₆H₁₁O₂NCl [M+H]⁺: 164.0478. Found: 164.0473.

2-Oxo-2-(phenylamino)ethyl piperidine-1-carbodithioate (3a). Yield: 92 %; white solid; m.p.: 146–147 °C; Anal. Calcd. for C₁₄H₁₈N₂OS₂: C, 57.11; H, 6.16; N, 9.51; S, 21.78 %. Found: C, 57.14; H, 6.14; N, 9.48; S, 21.79 %; ¹H-NMR (400 MHz, CDCl₃, δ / ppm): 1.73 (6H, bs, 3×CH₂), 3.91 (2H, bs, CH₂), 4.25 (2H, s, ClCH₂CO), 4.32 (2H, bs, CH₂), 7.08 (1H, t, J = 7.6 Hz, Ar-H), 7.29 (2H, t, J = 7.6 Hz, Ar-H), 7.53 (2H, d, J = 7.6 Hz, Ar-H), 9.23 (1H, bs, CONH); ¹³C-NMR (100 MHz, CDCl₃, δ / ppm): 24.1, 25.5, 26.1, 40.4, 52.0, 54.4, 119.8, 124.2, 128.9, 138.1, 167.3, 194.4; ESI-HRMS (m/z): Calcd. for C₁₄H₁₈ON₂S₂Na [M+Na]: 317.0758. Found: 317.0749.

2-Oxo-2-(p-tolylamino)ethyl piperidine-1-carbodithioate (3b). Yield: 95 %; white solid; m.p.: 142.9–143.8 °C; Anal. Calcd. for C₁₅H₂₀N₂OS₂: C, 58.41; H, 6.54; N, 9.08; S, 20.79 %; Found: C, 58.44; H, 6.56; N, 9.07; S, 20.81 %; ¹H-NMR (400 MHz, CDCl₃, δ / ppm): 1.73 (6H, bs, 3×CH₂), 2.29 (3H, s, CH₃), 3.91 (2H, bs, CH₂), 4.23 (2H, s, ClCH₂CO), 4.32 (2H, bs, CH₂), 7.09 (2H, d, J = 8.4 Hz, Ar-H), 7.40 (2H, d, J = 8.4 Hz, Ar-H), 9.11 (1H, bs, CONH); ¹³C-NMR (100

MHz, CDCl₃, δ / ppm): 20.9, 24.1, 25.5, 26.1, 40.4, 52.0, 54.3, 119.8, 129.4, 133.7, 135.5, 167.1, 194.5; ESI-HRMS (*m/z*): Calcd. for C₁₅H₂₀ON₂S₂Na [M+Na]: 331.0915. Found: 331.0897.

2-((4-Nitrophenyl)amino)-2-oxoethyl piperidine-1-carbodithioate (3c). Yield: 91 %; yellowish solid; m.p.: 180.9–181.2 °C; Anal. Calcd. for C₁₄H₁₇N₃OS₂: C, 49.54; H, 5.05; N, 12.38; S, 18.89 %. Found: C, 49.52; H, 5.03; N, 12.36; S, 18.91 %; ¹H-NMR (400 MHz, CDCl₃, δ / ppm): 1.76 (6H, *bs*, 3×CH₂), 3.93 (2H, *d*, *J* = 5.2 Hz, CH₂), 4.27 (2H, *s*, ClCH₂CO), 4.34 (2H, *bs*, CH₂), 7.69 (2H, *dd*, *J* = 7.2 and 2.0 Hz, Ar-H), 8.19 (2H, *dd*, *J* = 7.6 and 2.0 Hz, Ar-H), 9.91 (1H, *bs*, CONH); ¹³C-NMR (100 MHz, CDCl₃, δ / ppm): 23.9, 25.6, 26.1, 40.3, 52.3, 54.6, 119.2, 125.0, 143.4, 144.0, 167.9, 194.1; ESI-HRMS (*m/z*): Calcd. for C₁₄H₁₇N₃O₃S₂Na [M+Na]: 362.0609. Found: 362.0618.

2-((4-Fluorophenyl)amino)-2-oxoethyl piperidine-1-carbodithioate (3d). Yield: 96 %; white solid; m.p.: 180–181 °C; Anal. Calcd. for C₁₄H₁₇FN₂OS₂: C, 53.82; H, 5.48; F, 6.08; N, 8.97; S, 20.53 %. Found: C, 53.80; H, 5.46; F, 6.09; N, 8.95; S, 20.55 %; ¹H-NMR (400 MHz, CDCl₃, δ / ppm): 1.74 (6H, *bs*, 3×CH₂), 3.92 (2H, *d*, *J* = 4.8 Hz, CH₂), 4.23 (2H, *s*, ClCH₂CO), 4.32 (2H, *bs*, CH₂), 6.96–7.02 (2H, *m*, Ar-H), 7.46–7.51 (2H, *m*, Ar-H), 9.26 (1H, *bs*, CONH); ¹³C-NMR (100 MHz, CDCl₃, δ / ppm): 24.1, 25.5, 26.1, 40.2, 52.1, 54.4, 115.5 (2C, *d*, ²J_{CF} = 22 Hz, Ar-C), 121.4 (2C, *d*, ³J_{CF} = 7.0 Hz, Ar-C), 134.1 (1C, *d*, ⁴J_{CF} = 3.0 Hz, Ar-C), 159.3 (1C, *d*, ¹J_{CF} = 241 Hz, Ar-C), 167.2, 194.4; ESI-HRMS (*m/z*): Calcd. for C₁₄H₁₇FN₂OS₂Na [M+Na]: 335.0664. Found: 335.0658.

2-((4-Hydroxyphenyl)amino)-2-oxoethyl piperidine-1-carbodithioate (3e). Yield: 92 %; white solid; m.p.: 181–182.1 °C; Anal. Calcd. for C₁₄H₁₈N₂O₂S₂: C, 54.17; H, 5.84; N, 9.02; S, 20.66 %. Found: C, 54.19; H, 5.81; N, 8.99; S, 20.68 %; ¹H-NMR (400 MHz, CDCl₃, δ / ppm): 1.74 (6H, *bs*, 3×CH₂), 3.91 (2H, *bs*, CH₂), 4.23 (2H, *s*, ClCH₂CO), 4.31 (2H, *bs*, CH₂), 5.45 (1H, *bs*, OH), 6.77 (2H, *dd*, *J* = 6.8 and 2.0 Hz, Ar-H), 7.35 (2H, *dd*, *J* = 6.8 and 2.0 Hz, Ar-H), 9.07 (1H, *bs*, CONH); ¹³C-NMR (100 MHz, CDCl₃, δ / ppm): 24.1, 25.5, 26.1, 40.2, 52.0, 54.3, 115.6, 121.9, 122.1, 130.8, 152.8, 167.4, 194.4; ESI-HRMS (*m/z*): Calcd. for C₁₄H₁₈N₂O₂S₂Na [M+Na]: 333.0707. Found: 333.0710.

2-((3-Chloro-2-methylphenyl)amino)-2-oxoethyl piperidine-1-carbodithioate (3f). Yield: 93 %; white solid; m.p.: 157–158.1 °C; Anal. Calcd. for C₁₅H₁₉ClN₂OS₂: C, 52.54; H, 5.58; Cl, 10.34; N, 8.17; S, 18.70 %. Found: C, 52.56; H, 5.60; Cl, 10.32; N, 8.19; S, 18.68 %; ¹H-NMR (400 MHz, CDCl₃, δ / ppm): 1.74 (6H, *bs*, 3×CH₂), 2.32 (3H, *s*, CH₃), 3.94 (2H, *bs*, CH₂), 4.32 (4H, *s*, ClCH₂CO and CH₂), 7.09–7.27 (2H, *m*, Ar-H), 7.76 (1H, *d*, *J* = 7.6 Hz, Ar-H), 8.83 (1H, *bs*, CONH); ¹³C-NMR (100 MHz, CDCl₃, δ / ppm): 15.0, 24.1, 25.6, 26.2, 40.3, 52.1, 54.5, 121.7, 125.9, 126.8, 127.9, 134.8, 137.2, 167.7, 194.0;

ESI-HRMS (*m/z*): Calcd. for C₁₅H₁₉ClN₂OS₂Na[M+Na]: 365.0525. Found: 365.0521.

2-((5-Chloro-2-methylphenyl)amino)-2-oxoethyl piperidine-1-carbodithioate (3g). Yield: 91 %; white solid: m.p.: 172–174 °C; Anal. Calcd. for C₁₅H₁₉ClN₂OS₂: C, 52.54; H, 5.58; Cl, 10.34; N, 8.17; S, 18.70 %. Found: C, 52.52; H, 5.56; Cl, 10.37; N, 8.15; S, 18.72 %; ¹H-NMR (400 MHz, CDCl₃, δ / ppm): 1.74 (6H, *bs*, 3×CH₂), 2.24 (3H, *s*, CH₃), 3.93 (2H, *d*, *J* = 5.2 Hz, CH₂), 4.31 (4H, *bs*, ClCH₂CO and CH₂), 6.98–7.07 (2H, *m*, Ar-H), 8.06 (1H, *d*, *J* = 2.4 Hz, Ar-H), 8.81 (1H, *bs*, CONH); ¹³C-NMR (100 MHz, CDCl₃, δ / ppm): 18.1, 24.1, 25.6, 26.1, 40.4, 52.0, 54.57, 121.9, 124.5, 126.6, 131.2, 131.9, 137.2, 167.5, 194.0; ESI-HRMS (*m/z*): Calcd. for C₁₅H₁₉ClN₂OS₂Na [M+Na]: 365.0525. Found: 365.0516.

2-Oxo-2-(piperidin-1-yl)ethyl piperidine-1-carbodithioate (3h). Yield: 90 %; white solid; m.p.: 145–146 °C; Anal. Calcd. for C₁₃H₂₂N₂OS₂: C, 54.51; H, 7.74; N, 9.78; S, 22.39 %. Found: C, 54.52; H, 7.76; N, 9.75; S, 22.37 %; ¹H-NMR (400 MHz, CDCl₃, δ / ppm): 1.56 (2H, *t*, *J* = 4.8 Hz, CH₂), 1.65 (4H, *bs*, 2×CH₂), 1.66–1.71 (6H, *m*, 3×CH₂), 3.54–3.59 (4H, *m*, 2×CH₂), 3.94 (2H, *bs*, CH₂), 4.28 (2H, *bs*, CH₂), 4.32 (2H, *s*, CH₂CO); ¹³C-NMR (100 MHz, CDCl₃, δ / ppm): 24.2, 24.5, 25.5, 26.5, 41.2, 43.4, 47.3, 51.5, 53.2, 165.6, 194.3; ESI-HRMS (*m/z*): Calcd. for C₁₃H₂₂N₂OS₂Na [M+Na]: 309.1071. Found: 309.1095.

2-Morpholino-2-oxoethyl piperidine-1-carbodithioate (3i). Yield: 90.5 %; white solid; m.p.: 137–138 °C; Anal. Calcd. for C₁₂H₂₀N₂O₂S₂: C, 49.97; H, 6.99; N, 9.71; S, 22.23 %. Found: C, 49.99; H, 7.02; N, 9.73; S, 22.20 %; ¹H-NMR (400 MHz, CDCl₃, δ / ppm): 1.69 (6H, *t*, *J* = 5.2 Hz, 3×CH₂), 3.65–3.75 (8H, *m*, 4×CH₂), 3.93 (2H, *bs*, CH₂), 4.27 (2H, *bs*, CH₂), 4.30 (2H, *s*, CH₂CO); ¹³C-NMR (100 MHz, CDCl₃, δ / ppm): 24.2, 40.1, 42.6, 46.7, 66.7, 66.8, 166.3, 193.9; ESI-HRMS (*m/z*): Calcd. for C₁₂H₂₀N₂O₂S₂Na [M+Na]: 311.0864. Found: 311.0852.

2-Oxo-2-(phenylamino)ethyl morpholine-4-carbodithioate (4a). Yield: 93 %; white solid; m.p.: 176.4–176.9 °C; Anal. Calcd. for C₁₃H₁₆N₂O₂S₂: C, 52.68; H, 5.44; N, 9.45; S, 21.64 %. Found: C, 52.70; H, 5.47; N, 9.43; S, 21.61 %; ¹H-NMR (400 MHz, CDCl₃, δ / ppm): 3.80 (4H, *d*, *J* = 6.0 Hz, 2×CH₂), 3.98 (2H, *bs*, CH₂), 4.26 (2H, *s*, CH₂CO), 4.38 (2H, *bs*, CH₂), 7.09 (1H, *t*, *J* = 7.6 Hz, Ar-H), 7.26–7.33 (2H, *m*, Ar-H), 7.52 (2H, *d*, *J* = 8.4 Hz, Ar-H), 9.01 (1H, *bs*, CONH); ¹³C-NMR (100 MHz, CDCl₃, δ / ppm): 40.2, 50.9, 52.5, 65.9, 66.5, 119.8, 124.3, 128.9, 137.9, 166.7, 196.5; ESI-HRMS (*m/z*): Calcd. for C₁₃H₁₆N₂O₂S₂Na [M+Na]: 319.0551. Found: 319.0539.

2-Oxo-2-(p-tolylamino)ethyl morpholine-4-carbodithioate (4b). Yield: 94 %; white solid; m.p.: 157.1–158.6 °C; Anal. Calcd. for C₁₄H₁₈N₂O₂S₂: C, 54.17; H, 5.84; N, 9.02; S, 20.66 %. Found: C, 54.19; H, 5.87; N, 8.99; S, 20.64 %; ¹H-NMR (400 MHz, CDCl₃, δ / ppm): 2.30 (3H, *s*, CH₃), 3.79 (4H, *bs*, 2×CH₂),

3.98 (2H, *bs*, CH₂), 4.24 (2H, *s*, CH₂CO), 4.38 (2H, *bs*, CH₂), 7.11 (2H, *d*, *J* = 8.0 Hz, Ar-H), 7.39 (2H, *d*, *J* = 8.4 Hz, Ar-H), 8.89 (1H, *bs*, CONH); ¹³C-NMR (100 MHz, CDCl₃, δ / ppm): 20.9, 40.2, 50.9, 52.6, 65.9, 66.4, 119.8, 129.4, 133.9, 135.3, 166.6, 196.5; ESI-HRMS (*m/z*): Calcd. for C₁₄H₁₈N₂O₂S₂Na [M+Na]: 333.0707. Found: 333.0716.

2-((4-Nitrophenyl)amino)-2-oxoethyl morpholine-4-carbodithioate (4c). Yield: 93.2 %; yellowish solid; m.p.: 180.9–190.6 °C; Anal. Calcd. for C₁₃H₁₅N₃O₄S₂: C, 45.73; H, 4.43; N, 12.31; S, 18.78 %. Found: C, 45.71; H, 4.45; N, 12.29; S, 18.76 %. ¹H-NMR (400 MHz, CDCl₃, δ / ppm): 3.79 (2H, *bs*, CH₂), 3.84 (2H, *bs*, CH₂), 3.98 (2H, *bs*, CH₂), 4.28 (2H, *s*, CH₂CO), 4.39 (2H, *bs*, CH₂), 7.68 (2H, *dd*, *J* = 7.2 and 2.0 Hz, Ar-H), 8.19 (2H, *dd*, *J* = 7.2 and 2.0 Hz, Ar-H), 9.66 (1H, *bs*, CONH); ¹³C-NMR (100 MHz, CDCl₃, δ / ppm): 23.9, 25.6, 26.9, 40.2, 52.3, 54.6, 119.2, 125.0, 143.4, 144.0, 168.9, 194.1; ESI-HRMS (*m/z*): Calcd. for C₁₃H₁₅N₃O₄S₂Na [M+Na]: 364.0402. Found: 364.0426.

2-((4-Fluorophenyl)amino)-2-oxoethyl morpholine-4-carbodithioate (4d). Yield: 94.3 %; white solid; m.p.: 159.6–161.2 °C; Anal. Calcd. for C₁₃H₁₅FN₂O₂S₂: C, 49.66; H, 4.81; F, 6.04; N, 8.91; S, 20.40 %. Found: C, 49.64; H, 4.79; F, 6.07; N, 8.89; S, 20.37 %. ¹H-NMR (400 MHz, CDCl₃, δ / ppm): 3.80 (4H, *bs*, 2×CH₂), 3.98 (2H, *bs*, CH₂), 4.24 (2H, *s*, CH₂CO), 4.38 (2H, *bs*, CH₂), 6.98–7.02 (2H, *m*, Ar-H), 7.46–7.49 (2H, *m*, Ar-H), 9.03 (1H, *bs*, CONH); ¹³C-NMR (100 MHz, CDCl₃, δ / ppm): 24.1, 25.5, 26.1, 40.2, 52.1, 54.4, 115.6 (2C, *d*, ²J_{CF} = 22 Hz, Ar-C), 121.4 (2C, *d*, ³J_{CF} = 7.0 Hz, Ar-C), 134.1 (1C, *d*, ⁴J_{CF} = 3.0 Hz, Ar-C), 159.3 (1C, *d*, ¹J_{CF} = 241 Hz, Ar-C), 167.2, 194.4; ESI-HRMS (*m/z*): Calcd. for C₁₃H₁₅FN₂O₂S₂Na [M+Na]: 337.0457. Found: 337.0439.

2-((4-Hydroxyphenyl)amino)-2-oxoethyl morpholine-4-carbodithioate (4e). Yield: 90.2 %; white solid; m.p.: 213–214.2 °C; Anal. Calcd. for C₁₃H₁₆N₂O₃S₂: C, 49.98; H, 5.16; N, 8.97; S, 20.53. Found: C, 49.96; H, 5.19; N, 8.99; S, 20.51 %. ¹H-NMR (400 MHz, CDCl₃, δ / ppm): 3.76 (4H, *bs*, 2×CH₂), 3.94 (2H, *bs*, CH₂), 4.26 (2H, *s*, ClCH₂CO), 4.34 (2H, *bs*, CH₂), 5.41 (1H, *bs*, OH), 6.79 (2H, *dd*, *J* = 6.8 and 2.0 Hz, Ar-H), 7.39 (2H, *dd*, *J* = 6.8 and 2.0 Hz, Ar-H), 9.12 (1H, *bs*, CONH); ¹³C-NMR (100 MHz, CDCl₃, δ / ppm): 24.1, 25.5, 26.1, 40.2, 52.0, 54.3, 115.6, 121.9, 122.1, 130.8, 152.8, 167.4, 194.4; ESI-HRMS (*m/z*): Calcd. for C₁₃H₁₆N₂O₃S₂Na [M+Na]: 335.0500. Found: 335.0527.

2-((3-Chloro-2-methylphenyl)amino)-2-oxoethyl morpholine-4-carbodithioate (4f). Yield: 92.7 %; white solid; m.p.: 158.9–159.5 °C; Anal. Calcd. for C₁₄H₁₇ClN₂O₂S₂: C, 48.76; H, 4.97; Cl, 10.28; N, 8.12; S, 18.59 %. Found: C, 48.78; H, 4.99; Cl, 10.31; N, 8.09; S, 18.57 %. ¹H-NMR (400 MHz, CDCl₃, δ / ppm): 2.32 (3H, *s*, CH₃), 3.80 (4H, *bs*, 2×CH₂), 3.99 (2H, *bs*, CH₂), 4.32 (2H, *s*, ClCH₂CO), 4.38 (2H, *bs*, CH₂), 7.10–7.19 (2H, *m*, Ar-H), 7.75 (1H, *d*, *J* = 7.6 Hz, Ar-H), 8.67 (1H, *bs*, CONH); ¹³C-NMR (100 MHz, CDCl₃, δ / ppm): 15.0,

24.1, 25.6, 26.2, 40.3, 52.1, 54.5, 121.7, 125.9, 126.8, 127.9, 134.8, 137.2, 167.7, 194.0; ESI-HRMS (*m/z*): Calcd. for C₁₄H₁₇ClN₂O₂S₂Na [M+Na]: 367.0318. Found: 367.0341.

2-((5-Chloro-2-methylphenyl)amino)-2-oxoethyl morpholine-4-carbodithioate (4g). Yield: 91.4 %; white solid; m.p.: 152.3–153.5 °C; Anal. Calcd. for C₁₄H₁₇ClN₂O₂S₂: C, 48.76; H, 4.97; Cl, 10.28; N, 8.12; S, 18.59 %. Found: C, 48.74; H, 4.94; Cl, 10.26; N, 8.15; S, 18.62 %; ¹H-NMR (400 MHz, CDCl₃, δ / ppm): 2.23 (3H, *s*, CH₃), 3.79 (4H, *bs*, 2×CH₂), 3.99 (2H, *bs*, CH₂), 4.31 (2H, *s*, ClCH₂CO), 4.37 (2H, *bs*, CH₂), 6.99–7.08 (2H, *m*, Ar-H), 8.05 (1H, *d*, *J* = 2.0 Hz, Ar-H), 8.65 (1H, *bs*, CONH); ¹³C-NMR (100 MHz, CDCl₃, δ / ppm): 18.1, 24.1, 25.6, 26.1, 40.4, 52.0, 54.5, 121.9, 124.5, 126.6, 131.2, 131.9, 137.2, 167.5, 194.0; ESI-HRMS (*m/z*) Calcd. for C₁₄H₁₇ClN₂O₂S₂Na [M+Na]: 367.0318. Found: 367.0339.

2-Oxo-2-(piperidin-1-yl)ethyl morpholine-4-carbodithioate (4h). Yield: 90.4 %; white solid; m.p.: 123–124.5 °C; Anal. Calcd. for C₁₂H₂₀N₂O₂S₂: C, 49.97; H, 6.99; N, 9.71; S, 22.23 %. Found: C, 49.96; H, 6.98; N, 9.69; S, 22.25 %; ¹H-NMR (400 MHz, CDCl₃, δ / ppm): 1.57 (2H, *t*, *J* = 5.2 Hz, CH₂), 1.66 (4H, *t*, *J* = 2.4 Hz, 2×CH₂), 3.55–3.59 (4H, *m*, 2×CH₂), 3.77 (4H, *t*, *J* = 4.8 Hz, 2×CH₂), 4.01 (2H, *bs*, CH₂), 4.34 (4H, *bs*, CH₂CO and CH₂); ¹³C-NMR (100 MHz, CDCl₃, δ / ppm): 24.2, 40.1, 42.6, 46.7, 66.7, 66.8, 166.3, 193.9; ESI-HRMS (*m/z*): Calcd. for C₁₂H₂₀N₂O₂S₂Na [M+Na]: 311.0862. Found: 311.0875.

2-Morpholino-2-oxoethyl morpholine-4-carbodithioate (4i). Yield: 92.7 %; white solid; m.p.: 125.2–126.5 °C; Anal. Calcd. for C₁₁H₁₈N₂O₃S₂: C, 45.49; H, 6.25; N, 9.65; S, 22.08 %. Found: C, 45.46; H, 6.23; N, 9.67; S, 22.05 %; ¹H-NMR (400 MHz, CDCl₃, δ / ppm): 3.65–3.79 (12H, *m*, 6×CH₂), 4.01 (2H, *bs*, CH₂), 4.31 (4H, *bs*, CH₂CO and CH₂); ¹³C-NMR (100 MHz, CDCl₃, δ / ppm): 24.2, 40.1, 42.6, 46.7, 66.7, 66.8, 166.3, 193.9; ESI-HRMS (*m/z*): Calcd. for C₁₁H₁₈N₂O₃S₂Na [M+Na]: 313.0657. Found: 313.0642.

REFERENCES

1. L. Miao, L. Xu, K. W. Narducy, M. L. Trudell, *Org. Process Res. Dev.* **13** (2009) 820.



Highly efficient production of *Aspergillus niger* amylase cocktail by solid-state fermentation using triticale grains as a well-balanced substrate

BILJANA DOJNOV^{1*}, MARICA GRUJIĆ² and ZORAN VUJČIĆ²

¹Department of Chemistry, Institute of Chemistry, Technology and Metallurgy, University of Belgrade, Njegoševa 12, Belgrade, Serbia and ²Department of Biochemistry, Faculty of Chemistry, University of Belgrade, Studentski trg 12–16, Belgrade, Serbia

(Received 17 March, revised 12 May, accepted 18 May 2015)

Abstract: Triticale (x *Triticosecale*, Wittmack), an important industrial crop, with high grain yield, containing high amounts of starch, proteins and also major and minor mineral elements, is not yet sufficiently utilized. The simultaneous production of α -amylase and glucoamylase isoforms by *Aspergillus niger* on triticale grains, without any nutritive supplements, was developed, optimized and scaled up 10 fold for the first time. The specific combination of the examined effects led to the production of a novel glucoamylase isoform. Reduction of particle size, increase in oxygen availability and substrate height lead to an increase of 30 % in the production of amylases. Reduction of the relative humidity from 65 to 30 % increased glucoamylase production 2 fold and α -amylase production by 30%. The peak production of α -amylase (158 U g⁻¹) and glucoamylase (170 U g⁻¹) were obtained in Erlenmeyer flasks and in scaled-up trays. The obtained *A. niger* amylase cocktail was more efficient in raw starch hydrolysis from wheat flour, 29 % more efficient in glucose formation and 10 % more efficient in total reducing sugar formation, than the commercially available amylase cocktail SAN Super 240L, which is widely used in industry.

Keywords: α -amylase; glucoamylase; fungi; enzyme production; solid-state fermentation, raw starch.

INTRODUCTION

Solid-state fermentation (SSF) is widely used for fungal amylase production. It has many advantages over submerged fermentation (SmF), such as lower cost, higher efficiency, reduced catabolic repression, easier maintenance, easier scale-up, etc.^{1–3} Production of important industrial enzymes requires testing of various types of substrates and optimization of the fermentation conditions.

* Corresponding author. E-mail: bdojnov@chem.bg.ac.rs
doi: 10.2298/JSC150317041D

Natural materials, mostly wheat, are in use as substrates for the production of industrial enzymes and bioethanol, especially in Europe.^{4,5} Triticale (x *Triticosecale*, Wittmak) is an important industrial crop that is not yet sufficiently utilized. Cultivation of triticale has many benefits when compared to other crops, such as high biomass and grain yield in a wide range of soils (it is particularly resistant to low pH) and climatic conditions, with yields from 3 to 6 t ha⁻¹ depending on the geographic region.⁶ It is also cultivated in Serbia and gives high yields,⁷ especially in the region near Valjevo. Triticale contains high amounts of starch (about 60 %) and proteins (from 12 to 15 %).⁸ It also contains higher amounts of the major mineral elements (K, P and Mg) and nutritionally important minor elements (Na, Mn, Fe, Cu and Zn) than wheat.⁹ It could be a good choice as a substrate for fungal amylase production for several reasons: it is cheaper than other crops, not part of the human diet, and the obtained fermentation waste could be used as well balanced animal fodder. The use of triticale as substrate for *A. niger* amylase production, without any additional supplements, is described for the first time herein.

Glucoamylase and α -amylase are likely to be produced concomitantly in fungal fermentations.^{10–12} This fact is often ignored and *A. niger* was shown to be a producer of solely glucoamylase.^{13–15} In fungal enzyme production, the most efficient combination of the genetic properties of the fungus and substrate composition should be applied under optimal cultivation conditions. It would be far more efficient to use *A. niger* for the simultaneous production of both α -amylase and glucoamylase and to optimize the fermentation process in terms of enhancement of the production of both enzymes. Conventional techniques for raw starch hydrolysis involve two phases: liquefaction and saccharification. The first step (gelatinization and liquefaction) requires a high temperature (over 100 °C) at pH 6.5, as well as bacterial thermostable α -amylases.¹⁶ Fungal α -amylase or glucoamylase are used in the final phase (saccharification) depending on desired products – maltose or glucose.¹⁶ Saccharification requires a temperature of 55 °C at pH 5.5 in order to obtain maltose syrups, or 60 °C at pH 4.5 for glucose syrups.¹⁷ Implementation of different reaction conditions and several types of amylase makes starch hydrolysis difficult and expensive. An amylase cocktail (containing α -amylase and glucoamylase) could be used for starch hydrolysis in only one hydrolysis step, which would reduce the costs and/or time required for complete starch hydrolysis. Significant cost reduction could be achieved by avoidance of pH changes during starch hydrolysis, which are necessary in conventional methods. Cost reduction could also be achieved by saccharification using “*in situ*” produced enzymes, which avoids transportation expense, and which is trending in the development of bioethanol processing nowadays.

The aim of this work was to develop and optimize the simultaneous production of highly efficient *A. niger* α -amylase and glucoamylase using triticale

grains as substrate for SSF without any additional supplements; and to test the efficiency of the obtained enzyme cocktail in raw starch hydrolysis. Moreover, tests were performed with wheat flour as the starting material for raw starch hydrolysis.

EXPERIMENTAL

Reagents

All employed reagents and solvents were of the highest available purity and purchased from Merck (Darmstadt, Germany) and Sigma–Aldrich (St. Louis, MO, USA). Triticale (*x Triticosecale* sp.) “Odisej” line was obtained from the Institute of Field and Vegetable Crops, Novi Sad, Serbia. SAN Super 240L was received from Novozyme as a gift. Raw starch from wheat and wheat flour were produced in “Fidelinka”, Subotica, Serbia.

Microorganisms

The *A. niger* ATCC 10864 strain was cultivated on potato dextrose agar (PDA) at 28 °C for 7 days to obtain mature spores. A spore suspension was prepared in 0.1 % Tween 80 solution at a concentration of 5.9×10^5 spores mL⁻¹.

Optimization of SSF

Triticale, of three different particle sizes, was used for SSF. Equal quantities of triticale and water were mixed in a 250-mL Erlenmeyer flask, incubated at 60 °C for 3 h,¹⁸ and autoclaved. The spore suspension was spread on substrates in 1:0.19 ratio, w/V. SSF was performed at 28 °C for 120 h. The initial external relative humidity (RH) was 65 or 30 % during fermentation. The fermentations were terminated at 24, 29, 33, 57, 81, 96, 105 and 120 h.

The influence of particle size on α-amylase and glucoamylase production

Triticale grains were coarsely ground in a Mulinex mill, whereby obtaining mixture of particles with different sizes (30 % 1 mm, 28 % 2–3 mm, 18 % 4 mm, 20 % 5–6 mm, 4 % 7 mm) was obtained. Three solid-state supports were each made of 16 g of coarse ground triticale (mixture of particles with different sizes) and 16 g of water. Another set of three solid-state supports was prepared, each mixed with 8 g of coarse ground triticale, 8 g of whole grain triticale and 16 g of water (combined grains). A third set of three solid-state supports was prepared each with 16 g of whole triticale grains (size 8 mm) and 16 g of water. Fermentations were performed in Erlenmeyer flasks (250 mL) closed off with microbiological cotton wool caps at 28 °C, RH 30 % for 96 h.

The influence of aeration on α-amylase and glucoamylase production during SSF

Each SSF in these experiments was performed on 16 g of coarse ground triticale grains mixed with 16 g of water. Oxygen availability was varied using Erlenmeyer flasks covered either with microbiological cotton wool caps, or with metal microbiological caps. Both SSFs were realized in duplicate at 28 °C and RH 30 %.

The influence of relative humidity (RH) on α-amylase and glucoamylase production during SSF

Each SSF in these experiments was performed on 16 g of coarse ground triticale grains mixed with 16 g of water. The first SSF was realized at an initial external RH 30 % and the second was performed at an initial external RH of 65 %. The RH was measured using a humidity meter. Humidity was kept constant on RH 65 % using mist maker immersed in sterile distilled water. Both SSFs were performed in duplicate at 28 °C in Erlenmeyer flasks with metal microbiological caps.

The influence of substrate height on α -amylase and glucoamylase production during SSF

Three different quantities of coarse ground triticale grains (16, 32 and 48 g) were used in SSF to examine the influence of the substrate height on amylase production. Equal quantities of triticale grains and water were mixed in Erlenmeyer flasks of identical size and shape. SSF on different quantities of triticale grains was realized in duplicate at 28 °C and at an initial external RH of 65 %, using 250 mL Erlenmeyer flasks with metal microbiological caps.

Scale up

Coarse ground triticale grains (up to 160 g) were placed in trays (dimensions 20.5 cm×14.0 cm× 6.0 cm) and soaked with equal volume of water (160 mL). The trays were incubated at 60 °C for 3 h,¹⁸ and autoclaved. Spore suspension was spread on the substrates in 1:0.19 ratio, *w/V*. SSF was performed in duplicate at 28 °C for 120 h. The initial external RH was 30 % during fermentation. SSF appearance on the tray is shown in Fig. 1.



Fig. 1. SSF appearance on the tray after 36 h.

Enzyme extraction after SSF

Fermentation was terminated by the addition of a cold buffer solution (50 mM acetate buffer pH 4.5, 0.1 % Tween 80) in a 1:5 ratio (*w/V*) and homogenized with an Ikaturrax homogenizer in 3 cycles of 15 s. Extraction was performed at room temperature for 1 h. The obtained mixture was centrifuged at 5000 g for 15 min. The crude fermentation extracts were released from small sugars, which could interfere with the assays, by gel filtration on 2 mL Sephadex G25 columns. Acetate buffer pH 5.0 was used for the elution of proteins from the crude fermentation extracts. The eluted fractions were concentrated by ultrafiltration and then used for further analysis.

Amylase activity assay

The amylase activity was assayed at pH 5.0 according to the dinitrosalicylic acid (DNS) procedure¹⁹ using 1.0 % (*w/V*) soluble starch as substrate at 35 °C for 30 min. Maltose was used as a standard. Each data point represents the mean of three independent assays (standard errors of measurement (SEM) were less than 5 % of the means). One unit of α -amylase activity, U mL⁻¹, was defined as the amount of enzyme required to produce 1 μ mol of maltose in 1 min at 35 °C. The specific amylase activity, U g⁻¹, was calculated as the amylase units per 1 g of dry substrate in SSF (triticale).

Glucoamylase activity assay

The glucoamylase activity was assayed at pH 5.0 using 1.0 % (*w/V*) soluble starch as substrate at 35°C for 30 min. Glucose (the final product of the reaction) was detected in the reaction mixture by coupled reaction with glucose oxidase and horseradish peroxidase (HRPO, Trinder reagent, Pointe Scientific, USA). Samples (10 μ L) were mixed with Trinder reagents (1 mL),²⁰ incubated for 30 min and the absorbance was measured at 520 nm, according to the manufacturer's instructions. Each data point represents the mean of three

independent assays (the *SEM* values were less than 5 % of the means). One unit of glucoamylase activity, U mL⁻¹, was defined as the amount of enzyme required to produce 1 µmol of glucose in 1 min at 35 °C. The specific glucoamylase activity, U g⁻¹, was calculated as the amylase units per 1 g of dry substrate in the SSF (triticale).

Zymographic detection of α-amylase and glucoamylase

α-Amylase and glucoamylase were detected simultaneously on a zymogram.²¹ After electrophoresis (EF) separation of the crude fermentation extracts on native 10 % polyacrylamide (PAA, 30 % T, 2.7 % C) gel, the gel was printed simultaneously on a PAA gel with copolymerized β-limit dextrin (0.8 %) and on a nitrocellulose membrane (NC). α-Amylase was detected in the PAA gel with copolymerized β-limit dextrans after staining with iodine solution. The α-amylase activity appeared as clear bands on a purple background. In the native EF PAA gel after printing, both amylases were detected as clear bands on blue background using soluble starch as the substrate, and iodine solution for staining. Glucoamylases were detected on NC membrane using starch and a reaction mixture for glucose detection (Trinder's reagent and 4-Cl-1-naphthol as substrate). The NC was incubated in buffered substrate solution (1.0 % (w/V) starch, 50 mM acetate pH 5.0, 2.0 mM NaCl and 0.1 mM CaCl₂) and reaction mixture for glucose detection in a 9:1 ratio, after 30 min at 30 °C. A specific reaction leading to an insoluble purple product occurred on the NC membrane in the bands corresponding to glucoamylase. Positions and relative activities (representations) of the obtained bands were quantified using a GelAnalyzer 2010.

Hydrolysis of raw starch by the amylase cocktail

Raw starch from wheat and wheat flour (per 30 mL of 2 % mixtures in acetate buffer, pH 5.0) were soaked at 65 °C. Thereafter, equal quantities (in enzyme units, 106.3 U mL⁻¹ reaction mixtures) of commercial glucoamylase product (SAN Super 240L) or *A. niger* amylase cocktail were added to both substrates. Hydrolysis was performed at 50 °C overnight with agitation. Starch mixtures were analyzed for presence of starch, dextrans, reducing sugars and glucose prior to and after hydrolysis. The concentrations of starch and dextrin were determined by the iodine dextrin color method (IDC method), measuring the absorbance at 590 nm and 540 nm, respectively.²² Reducing sugars were determined by the DNS method, while the glucose concentration was measured using Trinder's reagents.

RESULTS AND DISCUSSION

Optimization of SSF

α-Amylase and glucoamylase activity is expressed in U/g of dry substrate that could be compared to each other in optimization processes. Each point on the graphs is a mean of the enzyme activities obtained from two independent fermentations ± *SEM*.

Use of triticale as substrate for amylase production in SSF was justified, since it resulted in peak amylase concentrations higher than amylase concentrations obtained by SSF on wheat flour, without additional supplements.²³ Moreover, it is in range of the amylase produced on rice waste materials without additional supplements.²⁴ These results indicate that triticale could be taken into consideration when choosing a substrate for amylase production. Triticale is an

accessible, cheap natural substrate, and the remaining biomass could be used as fodder. Simultaneously, SSF is an environmental friendly method.

The influence of particle size on α -amylase and glucoamylase production. Production levels of α -amylase and glucoamylase by *A. niger* on three forms (sizes) of triticale grains, *i.e.*, coarsely ground grains (particles of different sizes: 30 % 1 mm, 28 % 2–3 mm, 18 % 4 mm, 20 % 5–6 mm, 4 % 7 mm, combined grains – 50 % of whole grains (8 mm) and 50 % of coarsely ground grains, and whole grains (8 mm), are shown in Fig. 2. The highest α -amylase and glucoamylase activities were obtained on coarsely ground grains, 133.02 and 91.71 U g⁻¹, respectively. The activities were 30 % higher than those obtained on whole triticale grains, Fig. 2.

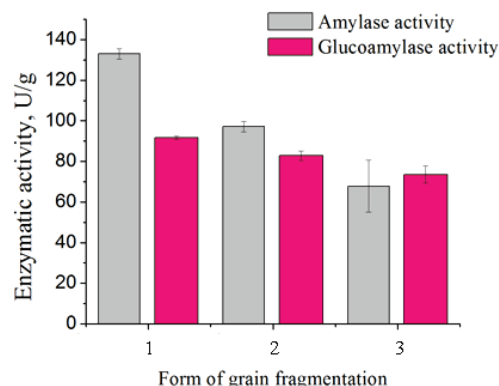


Fig. 2. Impact of particle size on amylase production by SSF using 16 g, in 96 h, RH 30 % in Erlenmeyer flasks with cotton cups. 1 – Coarse ground triticale, 2 – combined grains and 3 – whole grains.

Particle size is an important factor affecting enzyme production by SSF and it should be optimized.²⁵ Coarse ground triticale grains were of the most suitable particle size because they ensure better accessibility of fungi to the substrate inside the particles since the height of the penetrating hyphae layer is lower and, consequently, the restrictions for the diffusion of nutrients and products are reduced. Moreover, smaller particle sizes involve higher specific surface areas and, consequently, larger areas of external mycelium with better oxygenation. These were previously shown to be a critical factor affecting enzyme production.^{25,26} On the other hand, larger particles (whole grains) provide a limited surface for *A. niger* attack, which is known to be a limiting factor for enzyme production in SSF.²⁷ Smaller particles of triticale – bran, give homogenous and impervious substrate for fungal SSF because low particle size involves particle aggregations that reduce the interparticular space and thus, the volume and removal of the air phase; therefore they have not been tested here. The use of coarse ground triticale grains also increased the availability of starch and starch hydrolysis products (dextrans chains and maltose) formed during incubation of triticale at 60 °C for 3 h.¹⁸ This further increases the production of amylase cocktail. It is

known that maltose and even some dextrans are major inducers of amylase production in *A. niger*.^{28–30}

The influence of aeration on α -amylase and glucoamylase production during SSF. The use of cotton wool microbiological caps (higher oxygen) resulted in better fungal growth and higher production of α -amylase and glucoamylase than the use of metal microbiological caps (lower oxygen), Fig. 3. Sporulation of *A. niger* was delayed when SSF was performed in an Erlenmeyer with a metal microbiological cap.

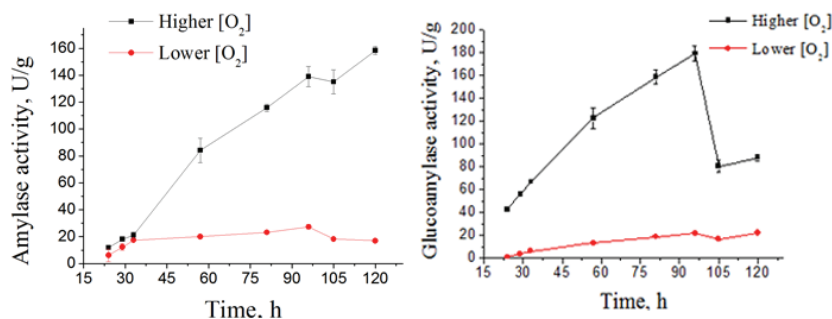


Fig. 3. Impact of aeration on amylase production in SSF with cotton wool caps and metal caps on 16 g of coarse ground triticale, on RH 30 %.

Use of cotton wool microbiological caps results in better fungal growth and higher production of α -amylase and glucoamylase than the use of metal microbiological caps. Prolonged production of α -amylase to the highest level in SSF under higher oxygen availability compared with the decreased production in SSF under lower oxygen availability seems to be more coherent with the fact that more aerated conditions generally accelerate the culture of aerobic microorganisms. The use of cotton wool caps provides for better aeration, higher oxygen consumption and CO_2 evaporation, thereby facilitating enhanced removal of metabolic heat. All these factors are important for the process of enzyme production in SSF.³ Fungal growth and amylase production under low oxygen concentrations were also reduced in *A. oryzae*.²⁶ Sporulation of *A. niger* was delayed when SSF was performed in an Erlenmeyer flask with a metal microbiological cap, maybe due to the slower evaporation of water under these terms.

As part of further investigations of the influence of individual factors on the production of amylases, metal microbiological caps were nevertheless used because the results showed that the SEM was lower than the SEM obtained when cotton wool microbiological caps were used.

Influence of humidity on α -amylase and glucoamylase production during SSF. *A. niger* production of α -amylase and glucoamylase during SSF on 16 g of coarse ground triticale grains at RH 65 % and RH 30 % was compared, Fig. 4.

The production of both α -amylase and glucoamylase was higher at RH 30 % but neither was in correlation with *A. niger* growth. SSF under conditions of high RH is followed by extensive biomass growth but lower production of amylases. The sporulation of *A. niger* was accelerated under conditions of lower RH, which could be associated with higher production of both enzymes.

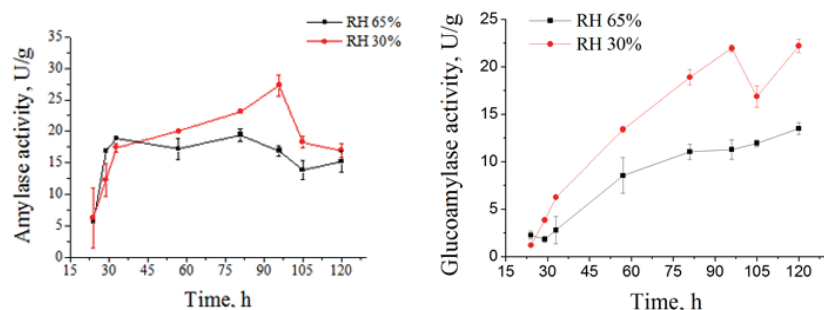


Fig. 4. Impact of RH on amylase production in SSF at RH 30 % and at RH 65 % on 16 g of coarse ground triticale in Erlenmeyer flasks with metal cups.

Fungal SSF can occur in the RH range from 20 to 80 % with the optimal RH depending on the type of substrate and the microorganism.²⁵ Maintenance of the optimal RH is important because it determines the water activity, which decreases during the fermentation part of the hydrolytic process in substrate and also because of increasing temperature in the system.²⁵ Reduction of bed porosity causes slower transport of oxygen at high RH values. Additionally, a low water content in SSF increases the concentration of nutritive elements in the substrate,²⁸ which could have contributed to higher production of *A. niger* amylases during SSF at the low RH value. The obtained results were not in correlation with results previously published on *A. niger*.³¹ However, it is difficult to observe the impact of RH independent of other factors affecting enzyme production in SSF.³² Acceleration of sporulation at the lower RH was due to a higher dryness of the substrate, which implies a higher oxygenation of the mycelium that would explain the better amylase production.

The influence of substrate heights on α -amylase and glucoamylase production during SSF. The impact of the substrate height was examined by using different quantities of coarse ground triticale grains, Fig. 5. Fungal growth was enhanced on higher quantities of substrate. The highest α -amylase activity was detected on 32 g of triticale grains (medium substrate height) during SSF, Fig. 5. Glucoamylase production was in correlation with fungal growth and was the highest on 48 g of triticale grains (highest substrate height), Fig. 5.

A higher substrate height increases the total surface area that may affect the slower evaporation of water from the lower layers of the substrate, thus main-

taining a better water activity, which would enhance fungal growth and amylases production. This may explain the higher amylase production when *A. niger* was cultivated on higher substrate heights.

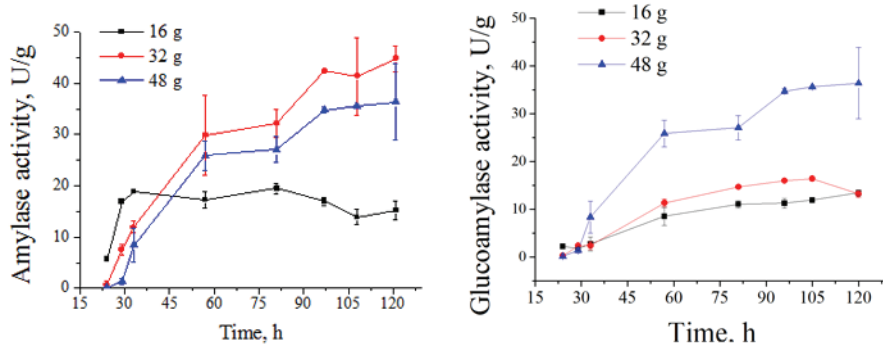


Fig. 5. Impact of substrate height on amylase production in SSF on 16, 32 and 48 g of coarse ground triticale grains in Erlenmeyer flasks with metal cups on RH 65 %.

Production of α -amylase and glucoamylase isoforms during SSF under different conditions

Great differences in the production of amylase isoforms after 57 h were observed under different fermentation conditions of SSF. Therefore, the extracts were analyzed by simultaneous zymographic detection of α -amylase and glucoamylase, Figs. 6–8, and the obtained results were further quantified using a Gel-Analyzer 2010, Table I.

Using 16 g of coarse ground triticale grains and 16 g of water as substrate, and microbiological cotton wool caps for the Erlenmeyer flasks with RH 30 % during SSF ensured the best fermentation conditions for the production of an amylase cocktail according to the zymogram and the relative activity determined

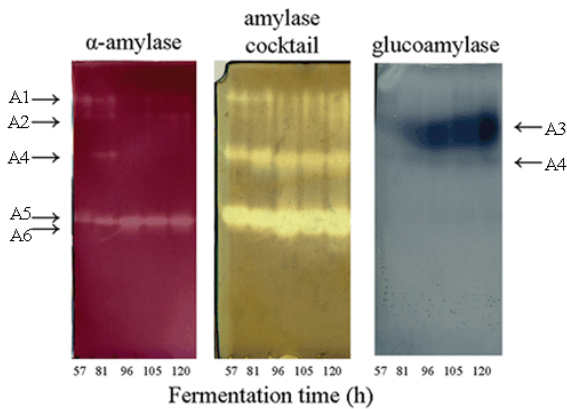


Fig. 6. Zymographic detection of amylase cocktail during different SSF conditions in 57, 81, 96, 105 and 120 h on 16 g of triticale grains, RH 30 % and higher aeration. Arrows indicate the positions of α -amylase (left) and glucoamylase (right) isoforms, labeled with A1–A6 (amylase isoform).

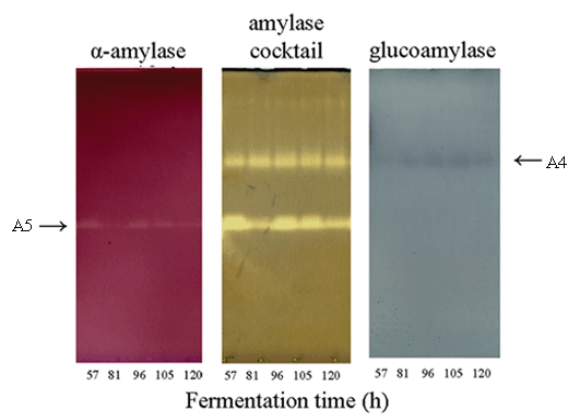


Fig. 7. Zymographic detection of amylase cocktail during different SSF conditions in 57, 81, 96, 105 and 120 h on 16 g of triticale grains, RH 65 % and lower aeration. Arrows indicate the positions of α -amylase (left) and glucoamylase (right) isoforms, labeled with A1-A6 (amylase isoform).

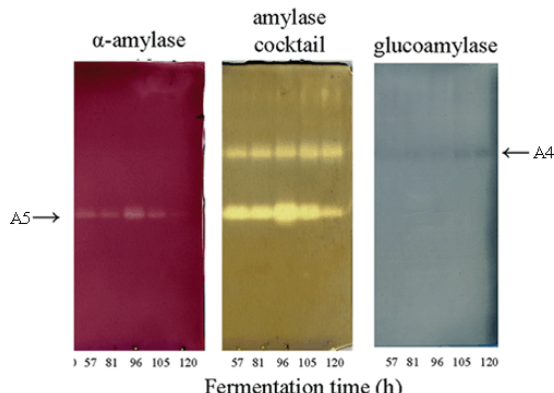


Fig. 8. Zymographic detection of amylase cocktail during different SSF conditions in 57, 81, 96, 105 and 120 h on 48 g of triticale grains, RH 65 % and lower oxygen availability. Arrows indicate the positions of α -amylase (left) and glucoamylase (right) isoforms, labeled with A1-A6 (amylase isoform).

by the GelAnalyzer, Figs. 6–8 and Table I. The highest numbers of α -amylase (5) and glucoamylase (2) isoforms were detected when performing SSF under these conditions, as can be seen on the specific zymograms (for α -amylase and glucoamylase) and on the zymogram for both amylases. A novel glucoamylase isoform A3, detected only under the SSF conditions described above, favors the use of more aerated conditions, Figs. 6–8. In addition, under these conditions *A. niger* produced the highest number of α -amylase isoforms (up to 4) – A1, A2, A5 and A6, while in the other fermentations, only one major isoform A5 could be found. The intensity – relative activity of the individual α -amylase isoforms differed during the fermentation, Fig. 6 and Table I, column a. The maximal activity of α -amylase was detected at 120 h by the A5 isoform on 16 g of triticale, RH 30 % and higher oxygen availability (Table I, column a), and also at 96 h by the A5 isoform under two other fermentation conditions, i.e., with 16 g and with 48 g of triticale, RH 65 % and lower oxygen availability (Table I, columns a and b). Under higher oxygen availability (Table I column a), there were no significant differences between the α -amylase production at 96 h (98.81 %) and at 120 h

(100 %), while the production was significantly smaller after 96 h of fermentation under lower oxygen availability (Table I, columns a and b). The maximal activity of glucoamylase was detected at 120 h of fermentation under all compared conditions, but the isoforms were different, Table I.

TABLE I. The relative activity of individual amylases isoforms (%) in amylase cocktails during SSF under different conditions. The most intense isoform per zymogram of the individual enzyme (in each column) is labeled as 100 % activity. Positions of every individual number in table are in correlation with *Rf* values obtained in the zymogram shown in Figs. 6–8. a) 16 g of triticale grains, RH 30 % and higher oxygen availability. b) 16 g of triticale grains, RH 65 % and lower oxygen availability. c) 48 g of triticale grains, RH 65 % and lower oxygen availability. A1–A6 - amylase isoforms according to the zymographic detection in Figs. 6–8. 1 – α -amylase, 2 – amylase cocktail, 3 – glucoamylase

Fermentation time, h	Amylase isoform	a)			b)			c)		
		1	2	3	1	2	3	1	2	3
57	A1	39.75	11.15	—	—	—	—	—	—	—
	A2	2.62	1.24	—	—	—	—	—	—	—
	A3	—	—	—	—	—	—	—	—	—
	A4	—	28.41	—	—	26.03	18.18	—	50.90	19.85
	A5	42.21	99.83	—	48.14	64.39	—	49.62	96.66	—
	A6	—	—	—	—	—	—	—	—	—
81	A1	10.10	3.56	—	—	—	—	—	—	—
	A2	1.91	0.40	27.89	—	—	—	—	—	—
	A3	—	—	—	—	—	—	—	—	—
	A4	3.66	53.49	0.55	—	38.03	94.32	—	60.23	43.13
	A5	17.17	100.00	—	37.84	64.76	—	21.67	100.00	—
	A6	—	—	—	—	—	—	—	—	—
96	A1	—	—	—	—	—	—	—	—	—
	A2	—	11.58	37.79	—	—	—	—	—	—
	A3	—	—	—	—	—	—	—	—	—
	A4	—	42.11	—	—	44.67	60.23	—	46.51	32.06
	A5	98.81	16.25	—	100.00	100.00	—	100.00	93.41	—
	A6	—	2.89	—	—	—	—	—	—	—
105	A1	—	—	—	—	—	—	—	—	—
	A2	—	—	—	—	—	—	—	—	—
	A3	—	11.11	77.27	—	—	—	—	—	—
	A4	—	43.79	0.75	—	42.49	54.55	—	43.31	61.45
	A5	87.84	7.86	—	48.65	70.52	—	48.33	89.17	—
	A6	—	6.98	—	—	—	—	—	—	—
120	A1	—	4.43	—	—	1.12	—	—	12.08	—
	A2	—	1.98	—	—	—	—	—	—	—
	A3	—	53.19	100.00	—	—	—	—	—	—
	A4	—	5.51	0.17	—	42.42	100.00	—	67.91	100.00
	A5	100.00	10.88	—	7.43	38.36	—	8.33	62.48	—
	A6	—	1.07	—	—	—	—	—	—	—

From the results of specific zymographic techniques, obtained for optimization of amylase cocktail production, it could be concluded that particle size, initial external *RH* and oxygen availability have a highly influential impact on α -amylase and glucoamylase production by *A. niger* in SSF using triticale as the substrate. The intensity of the major α -amylase isoform (A5) was contrary to the intensity of the major glucoamylase isoform (A4) on all zymograms.

Amylase cocktail production during SSF under selected conditions

The level of production of both amylases was analyzed each hour by spectrophotometric assays and by zymography during SSF under selected conditions, *i.e.*, on 16 g of triticale grains, at *RH* 30 % and with high oxygen availability, Figs. 9 and 10. Curves representing the production of the two amylases were parallel, while glucoamylase activity was higher, Fig. 8A. Peak production of glucoamylase was achieved at 96 h of SSF (170 U g^{-1}). After 96 h, the production of glucoamylase started to decrease, while the production of α -amylase continues to rise up at 120 h (158 U g^{-1}).

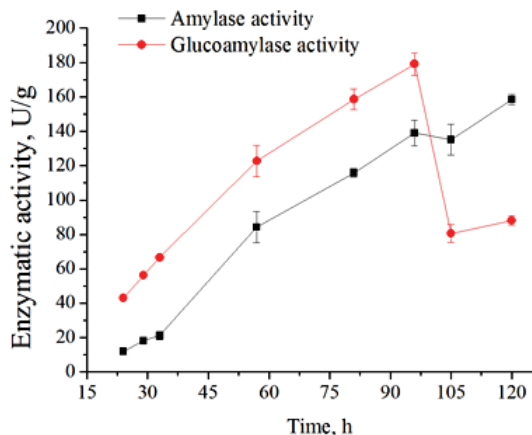


Fig. 9. α -Amylase and glucoamylase activity after SSF with 16 g of triticale grains, at *RH* 30 % and with high aeration.

A. niger started to produce the major α -amylase isoform (A5) during the first days of fermentation (24, 29 and 33 h). The production α -amylase isoforms with lower mobility (A1 and A2) commenced at 57 h at the same time when production of the major α -amylase (A5) started to decrease, Fig. 10. α -Amylase production increased from 96 h to 120 h, as shown by enzymatic assay and zymography, Fig. 10. *A. niger* started to produce glucoamylase (A3 and A4) at 81 h of fermentation, Fig. 10. Selected conditions enable obtaining amylase cocktail with maximal activity of both amylases in 120 h of fermentation, which could test for raw starch hydrolysis.

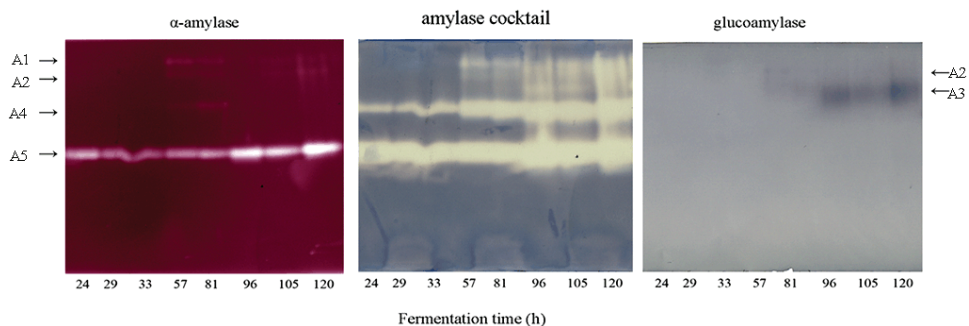


Fig. 10. Zymographic detection of α -amylase and glucoamylase after SSF with 16 g of triticale grains, at RH 30 % and with high oxygen availability. Arrows indicate the positions of α -amylase (right) and glucoamylase (left) isoforms labeled with A1-A6 (amylase isoform).

α -Amylase and glucoamylase occur together in many fermentation processes and it has been shown that they have a one-gene precursor,^{12,13} but here for the first time, it was demonstrated that they could be co-produced simultaneously in one SSF. This new approach to the fermentation process facilitates peak production of both enzymes or specific α -amylase or glucoamylase isoforms, and in addition enables modeling of the process to obtain a specific amylase cocktail, depending on the industry requirements.

Scale-up of amylase cocktail production

When the selected conditions for SSF were employed in large-scale production, very similar levels of α -amylase and glucoamylase, calculated on dry substrate, were obtained. The obtained crude extract (769 mL) contained α -amylase 31.02 U mL⁻¹, *i.e.*, 149.1 U g⁻¹ of dry substrate (coarse ground triticale grains) and glucoamylase 18.14 U mL⁻¹, *i.e.*, 87.2 U g⁻¹ of dry substrate (coarse ground triticale grains).

Scaling up of this SSF enabled larger amount of amylase cocktail to be produced. The very similar levels of amylase cocktails (expressed in U g⁻¹ of triticale) obtained in the scale-up experiments further confirmed the employment of the selected SSF conditions and justified the usage of triticale as a favorable substrate for the production of amylase cocktails.

Hydrolysis of raw starch by the amylase cocktails

The *A. niger* amylase cocktail was more efficient than a commercial enzyme product in hydrolysis of wheat flour, *i.e.*, it was 29 % more efficient in glucose formation and 10 % more efficient in the formation of total reducing sugars, Table II, a). The hydrolysis of starch isolated from wheat was similar between the *A. niger* amylase cocktail and the commercial cocktail, Table II, b). In terms of the formation of glucose, SAN Super 240L was more efficient by 8 %, while

in the formation of total reducing sugars, the *A. niger* amylase cocktail was more efficient by 5 %.

TABLE II. Comparison of the hydrolysis of raw starch and wheat by *A. niger* amylase cocktail and by a commercial enzyme product. a) Soaked wheat flour as substrate for hydrolysis; b) raw soaked starch from wheat as substrate for hydrolysis

State	Starch mg mL ⁻¹	Dextrin mg mL ⁻¹	Reducing sugars mM	Glucose mM
a) Wheat flour				
Prior to hydrolysis	1.64	9.22	5.37	11.04
After hydrolysis with SAN Super 240L, Novozyme	0.42	0.00	90.43	146.18
After hydrolysis with the <i>A. niger</i> amylase cocktail obtained in this work	0.45	0.00	100.28	206.12
b) Raw soaked wheat starch				
Prior to hydrolysis	1.59	8.51	0.00	11.04
After hydrolysis with SAN Super 240L, Novozyme	0.01	0.00	94.46	231.36
After hydrolysis with the <i>A. niger</i> amylase cocktail obtained in this work	0.01	0.00	99.38	213.48

Yields of the hydrolysis considering the amount of starch to be hydrolyzed, when wheat flour was the substrate were 74.39 % with the commercial cocktail and 72.56 % with the *A. niger* amylase cocktail obtained in this work. Hydrolysis of raw starch was more efficient, 99.37 % with both amylase cocktails (commercial and the present cocktail).

Hydrolysis of raw starch by amylase enzymes from *A. niger* was the subject of several papers and it showed high efficiency.^{12,33,34} In addition, amylase extracts obtained by SSF from *Aspergillus sp.* were previously used for raw starch hydrolysis with wheat flour as the initial substrate.^{23,35} The results mentioned above are not mutually comparable or comparable with the results obtained in this study because of individual calculations of efficiency and of the degrees of hydrolysis. In addition, the efficiencies were not compared to those of commercially available enzymes. Almost complete hydrolysis of raw starch (99.37 %) was attained by the *A. niger* amylase cocktail produced in this work when the yield of the hydrolysis was calculated based on the amount of available starch. It was the same result comparing with the commercial amylase cocktail and was much better compared with other *Aspergillus* amylase cocktails (69 % to 86 % depending on starch origin).³³

CONCLUSIONS

Triticale grains without the addition of any nutritive components could be used as the sole substrate for fungal production of important enzyme complexes under SSF conditions that could be industrially applicable. Based on triticale

properties as a nutritive rich substrate, competitive and superior amylase cocktails were obtained. The demonstrated higher efficiency of the obtained *A. niger* amylase cocktail in wheat flour hydrolysis indicates a possibility for implementation in starch industries. The use of the obtained amylase cocktail could unify the phases in the starch hydrolysis process, which would significantly reduce the costs of starch hydrolysis.

Acknowledgements. This study was supported by a grant from the Ministry of Education, Science and Technological Development of the Republic of Serbia (Project Grant No. 172048). We are grateful to Jasna Bojčevski for the correction of the English language, as well as for useful suggestions on the writing of the article.

ИЗВОД

ЕФИКАСНА ПРОИЗВОДЊА АМИЛАЗНОГ КОКТЕЛА ИЗ *Aspergillus niger* МЕТОДОМ ФЕРМЕНТАЦИЈЕ НА ЧВРСТОЈ ПОДЛОЗИ КОРИСТЕЋИ ТРИТИКАЛЕ КАО ДОБРО ИЗБАЛАНСИРАНИ ХРАНЉИВИ СУПСТРАТ

БИЉАНА ДОЈНОВ¹, МАРИЦА ГРУЈИЋ² И ЗОРАН ВУЧИЋ²

¹Центар за хемију, Институт за хемију, технологију и металургију Универзитета у Београду,
Новиашева 12, Београд и ²Катедра за биохемију, Хемијски факултет, Универзитет у Београду,
Слуденички шар 12–16, Београд

Тритикале (X *Triticosecale*, Wittmack) је важана индустријска житарица, високог приноса, и садржи велике количине скроба, протеина и макро- и микроелемената, а која још увек није довољно искоришћена. Метода истовремене производње α -амилазних и глукозамилазних изоформи из *Aspergillus niger*, користећи само зрна тритикала као подлогу без додатка других нутритивних елемената, развијена је, оптимизована и подигнута на већу скалу (10 пута) по први пут у овом раду. Специфична комбинација испитиваних фактора ферментације је довела до производње потпуно нове глукозамилазне изоформе. Смањење величине честица, повећање доступности кисеоника и висине стуба супстрата су довели до повећања производње амилазе до 30 %. Смањење релативне влажности са 65 на 30 % је повећало производњу глукозамилазе 2 пута и α -амилазе за 30 %. Максимална производња α -амилазе је била 158 U g⁻¹, а глукозамилазе 170 U g⁻¹, што је потврђено и на мањој и на већој скали. Добијени амилазни коктел из *A. niger* је био ефикаснији у хидролизи сировог скроба из пшеничног брашна од комерцијално доступног амилазног коктела, SAN Super 240L, који се најчешће користи у индустрији, и то 29 % ефикаснији у добијању глукозе и 10 % ефикаснији у добијању укупних редуктујућих шећера.

(Примљено 17. марта, ревидирано 12. маја, прихваћено 18. маја 2015)

REFERENCES

1. M. P. Nandakumar, M. S. Thakur, K. S. M. S. Raghavarao, N. P. Ghildyal, *Lett. Appl. Microbiol.* **29** (1999) 380
2. S. R. Couto, M. A. Sanroman, *J. Food Eng.* **76** (2006) 291
3. A. Pandey, C. R. Soccol, C. Larroche, *Current developments in solid state fermentations*. Springer, New Delhi, 2008
4. M. Hoogschagen, Y. Zhu, H. van As, J. Tramper, A. Rinzema, *Biotechnol. Lett.* **23** (2001) 1183

5. R. te Biesebeke, G. Ruijter, Y. S. P. Rahardjo, M. J. Hoogschagen, M. Heerikhuisen, A. Levin, K. G. A. van Driel, M. A. I. Schutyser, J. Dijksterhuis, Y. Zhu, F. J. Weber, W. M. de Vos, K. A. M. J. J. van den Hondel, A. Rinzema, P. J. Punt, *FEMS Yeast Res.* **2** (2002) 245
6. D. F. Salmon, M. Mergoum, H. Gómez Macpherson, in *Triticale improvement and production*, M. Mergoum, H. Gomez-Macpherson, Eds., FAO, Rome, 2004, p. 27
7. A. Pejić, *Agrosvet* **17** (2007) 6 (in Serbian)
8. R. J. Pena, *Food uses of triticale*, in *Triticale improvement and production*, M. Mergoum, H. Gomez-Macpherson, Eds. FAO, Rome, 2004, p. 37
9. K. Lorenz, F. W. Reuter, C. Sizer, *Cereal Chem.* **51** (1974) 376
10. H. Gasdorf, P. Athasampunna, V. Dan, D. Hensley, K. Smiley, *Carbohydr. Res.* **42** (1975) 147
11. A. Yuhki, T. Watanabe, K. Matsuda, *Starch* **29** (1977) 265
12. A. K. Dubey, C. Suresh, R. Kavitha, N. G. Karanth, S. Umesh-Kumar, *FEBS Lett.* **471** (2000) 251
13. P. Selvakumar, L. Ashakumary, A. Pandey, *Bioresour. Technol.* **65** (1998) 83
14. H. Pedersen, M. Beyer, J. Nielsen, *Appl. Microbiol. Biot.* **53** (2000) 272
15. Q. H. Wang, X. Q. Wang, X. M. Wang, H. Z. Ma, *Process Biochem. (Oxford, U.K.)* **43** (2008) 280
16. M. J. E. C. van der Maarel, B. van der Veen, J. C. M. Uitdehaag, H. Leemhuis, L. Dijkhuizen, *J. Biotechnol.* **94** (2002) 137
17. W. Crabb, D. Mitchinson, *Trends Biotechnol.* **15** (1997) 349
18. D. Pejin, Lj. Mojović, V. Vučurović, J. Pejin, S. Denčić, M. Rakin, *Fuel* **88** (2009) 1625
19. P. Bernfeld, in *Methods in enzymology*, Vol. I, P. De Murray, Ed., Deutcher Acad. Press, San Diego, CA, 1955, p. 149
20. I. Pointe Scientific, *Liquid Glucose (Oxidase) Reagent Set*. Pointe Scientific, Brussels, 2009
21. B. Dojnov, Z. Vujić, *Anal. Biochem.* **421** (2012) 802
22. D. E. Briggs, *J. Ind. Brew.* **67** (1961) 4
23. R. Wang, L. C. Godoy, S. M. Shaarani, M. Melikoglu, A. Koutinas, C. Webb, *Enzyme Microb. Technol.* **44** (2009) 223
24. H. Anto; U. B. Trivedi; K. C. Patel, *Bioresour. Technol.* **97** (2006), 1161.
25. J. Rodriguez-Leon, C. Soccol, A. Pandey, D. Rodriguez, in *Current developments in solid state fermentations*, A. Pandey, C. R. Soccol, C. Larroche, Eds., Springer, New Delhi, 2008, p. 26
26. Y. S. P. Rahardjo, J. Tramper, A. Rinzema, *Biotechnol. Adv.* **24** (2006) 161
27. A. Pandey, P. Selvakumar, C. R. Soccol, P. Nigam, *Curr. Sci. India* **77** (1999) 149
28. T. E. Bertolin, W. Schmidell, A. Maiorano, J. Casara, A. V. Z. Costa, Z. *Naturforsch.* **58** (2003) 708
29. R. Gupta, P. Gigras, H. Mohapatra, V. K. Goswami, B. Chauhan, *Process Biochem. (Oxford, U.K.)* **38** (2003) 1599
30. T. Sugimoto, H. Shoji, *Biotechnol. Lett.* **34** (2012) 347
31. A. Sharannappa, K. S. Wani, P. Patil, *Int. J. Adv. Biotechnol. Res.* **2** (2011) 473
32. Z. Hamidi-Esfahani, S. A. Shojaosadati, A. Rinzema, *Biochem. Eng. J.* **21** (2004) 265
33. J. Abe, F. Bergmann, K. Obata, S. Hizukuri, *Appl. Microbiol. Biotechnol.* **27** (1988) 4
34. A. M. Omemu, I. Akpan, M. O. Bankole, O. D. Teniola, *Afr. J. Biotechnol.* **4** (2005) 19
35. M. A. F. Farid, H. M. A. H. Shata, *Iran. J. Biotechnol.* **9** (2011) 267.



Solid–solid synthesis, characterization and thermal decomposition of a homodinuclear cobalt(II) complex

DI LI, GUO-QING ZHONG* and ZHI-XIAN WU

School of Material Science and Engineering, Southwest University of Science and Technology, Mianyang 621010, China

(Received 24 February, revised 25 May, accepted 6 June 2015)

Abstract: The homodinuclear cobalt(II) complex $[\text{Co}_2(\text{dipic})_2(\text{H}_2\text{O})_5] \cdot 2\text{H}_2\text{O}$ was synthesized using pyridine-2,6-dicarboxylic acid (H_2dipic) and cobalt(II) acetate as raw materials by room temperature solid–solid reaction. The complex was characterized by elemental analyses, single crystal X-ray diffraction, X-ray powder diffraction, Fourier transform infrared spectroscopy, UV spectroscopy, thermogravimetry and differential scanning calorimetry. Its crystal structure belongs to monoclinic system and space group $P2(1)/c$. There are two types of six-coordinated Co(II) ions, one Co(II) is coordinated by four carboxyl O atoms and two pyridine N atoms from two dipic²⁻ anions, and another Co(II) is coordinated by five O atoms from five H_2O molecules and one bridged carboxyl O atom from the dipic²⁻ anion. The possible pyrolysis reactions in the thermal decomposition processes of the complex, the experimental and calculated percentage mass loss are also given.

Keywords: cobalt(II) complex; pyridine-2,6-dicarboxylic acid; room temperature solid–solid reaction; crystal structure; thermal analysis.

INTRODUCTION

In the past several years, coordination frameworks with transition metal and organic functional ligands have been rapidly developing. However, it still remains one of the most active areas in chemistry and materials science, not only due to their highly fascinating structures and topologically diverse architectures, but also because they have potential applications in gas storage, molecular separations, drug delivery, heterogeneous catalysis, ion exchange, nonlinear optics, and other biomedical applications.^{1–5} The complexes of pyridinecarboxylic acids and their derivatives were successfully used as model systems for the design of new metallo-pharmaceutical compounds.⁶ Investigations on metalloproteins

* Corresponding author. E-mail: zqq316@163.com
doi: 10.2298/JSC150224050L

revealed that the carboxylate group plays an important role for structural folding and proton transfer *via* hydrogen bonding interactions in proteins.⁷

Pyridine-2,6-dicarboxylic acid (abbreviated as H₂dipic) can partly or fully deprotonate, the three coordination sites can undergo chelate or bridge coordination to form diverse structures.^{8–10} Furthermore, H₂dipic is usually found in the decomposition products of vitamins, coenzymes and alkaloids, which also have potential pharmacological activity.^{10,11} Cobalt is an essential trace element for humans and animals, which has potential applications in medicine and bio-inorganic chemistry, such as blood pressure regulation and proper thyroid function.^{12,13}

The method of room temperature solid–solid reaction is a simple and convenient method for the preparation of complexes. This method is energy-saving and environmentally friendly. In this article, cobalt acetate and the biologically functional ligand H₂dipic were chosen to synthesize a homodinuclear complex, using the room temperature solid–solid reaction method.

EXPERIMENTAL

Materials and physical measurements

H₂dipic was purchased from Alfa Aesar, while cobalt acetate was obtained from Merck. All chemicals were of analytical reagent grade and used without further purification.

Elemental analysis data were obtained using a Vario EL CUBE elemental analyzer, and cobalt was determined using a Thermo X-II inductively coupled plasma mass spectrometer. The XRD pattern was recorded on a D/max-II X-ray diffractometer in the diffraction angle range of 3–80°. The IR spectra were recorded from KBr pellets in the range of 400–4000 cm⁻¹ on a Perkin-Elmer Spectrum One spectrometer. The thermal analysis was realized using a SDT Q600 thermogravimetric analyzer, and the measurement was recorded from 30 to 800 °C at a heating rate of 10 °C min⁻¹ under air flow of 50 mL min⁻¹. The UV spectra in aqueous solution (1.0×10⁻⁴ mol L⁻¹) were recorded on a Shimadzu UV-2450 spectrophotometer.

Synthesis of complex

A mixture of H₂dipic (0.84 g, 5 mmol) and cobalt acetate (1.25 g, 5 mmol) was carefully ground in an agate mortar at room temperature, whereby a strong irritant gas was released. The released gas was tested with moist pH paper, and the result indicated that the gas was slightly acid due to the release of acetic acid during the reaction process. When the evolution of the irritant gas ceased, the reaction was complete. The reaction was conducted by grinding at room temperature for 4–5 h, and the mixture turned into loose pink powder. After obtaining the XRD data, the powder was dissolved in a small amount of distilled water and the solution was filtered and concentrated. When the concentrated solution was kept at room temperature for about 24 h, red–brown block-shaped crystals were obtained. Yield: 84 %; Anal. Calcd. for Co₂C₁₄H₂₀O₁₅N₂: C, 29.28; H, 3.51; N, 4.88; Co, 20.53 %. Found: C, 29.12; H, 3.65; N, 4.71; Co, 20.68 %.

X-Ray crystal structure determination

X-Ray diffraction data for a single crystal of the complex were collected at 293(2) K on a Bruker SMART APEX II CCD diffractometer equipped with graphite monochromated MoK_α radiation using the ω and φ scan mode. A crystal with dimensions 0.40 mm×0.38

mm×0.34 mm was mounted on a glass fiber. The structures were solved by direct methods and refined by full-matrix least squares on F^2 using the SHELXTL program package.¹⁴ All of the non-hydrogen atoms were refined with anisotropic displacement parameters and all of the hydrogen atoms were found objectively from difference Fourier syntheses. The crystallographic data for the complex are given in Table S-I of the Supplementary material to this paper, the selected bond distances and angles are listed in Table S-II, hydrogen bond lengths and angles are given in Table S-III of the Supplementary material, and the crystallographic data are deposited with the Cambridge Crystallographic Data Centre under deposition number CCDC 1028718.

RESULTS AND DISCUSSION

X-Ray crystal structure analysis

A view of the key fragments of the structure and the atom numbering of the complex are shown in Fig. 1. The complex crystallizes in the monoclinic system and space group $P2(1)/c$ with cell parameters of $a = 8.3680 \text{ \AA}$, $b = 27.2976 \text{ \AA}$, $c = 9.5826 \text{ \AA}$ and $\beta = 98.276^\circ$. The asymmetrical unit consists of the neutral complex $[\text{Co}_2(\text{dipic})_2(\text{H}_2\text{O})_5]$ and two lattice water molecules. The unit of the neutral complex is composed of two Co(II) ions, two dipic²⁻ anions and five coordinated water molecules. There are two different coordination environments that form two octahedral cobalt cations, one dipic²⁻ anion ligand utilizes the carboxyl bridged coordination mode to link Co1 and Co2. The Co1 contains a bridged carboxyl oxygen atom (O2) from one dipic²⁻ anion and five oxygen atoms (O9, O10, O11, O12 and O13) from water molecules. The Co1 bridges the carboxyl oxygen (O2) of dipic²⁻, and is surrounded by water molecules, forming an octahedral geometry. The Co2 exhibits a distorted octahedral coordination with two dipic²⁻, which has two anionic tridentate chelating modes. Therefore, its molecular structure could be written as $[(\text{H}_2\text{O})_5\text{Co}(\mu\text{-OCO-dipic})\text{Co}(\text{dipic})]\cdot 2\text{H}_2\text{O}$. The molecular structure shown in Fig. S-1 of the Supplementary material to this paper may indicate weak face-to-face $\pi-\pi$ stacking interactions, because the distances

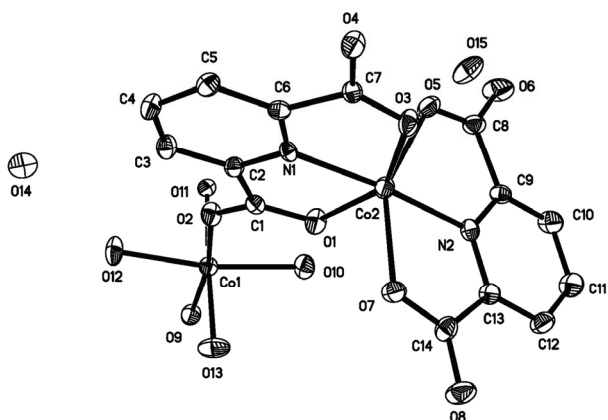


Fig. 1. Molecular structure of the title complex.

between the pyridine rings of situated in neighboring mirror planes are 3.703 and 3.791 Å.¹⁵

Crystal packing diagram of the title complex is presented in Fig. 2, which shows that the molecule of the complex is held together by intermolecular hydrogen bonds. There are three types of hydrogen bonds in the complex, the hydrogen bonds between coordinated water molecules and the O atoms of carbonyl groups, the coordinated water and lattice water molecules, and the O atoms of carboxylate groups with the lattice water molecules. The adjacent asymmetrical molecular units are interconnected through the hydrogen bond interactions between the coordinated water molecules (O13 and O9) and the carboxylic oxygen atoms (O5 and O6) of the dipic²⁻ ligand forming an extended 1D supramolecular chain. The chains of the 1D supramolecular chain are further combined with each other by means of hydrogen bond interactions between the lattice water or coordinated water molecules and other carboxylic oxygen atoms of the dipic²⁻ ligand, giving rise to the final extended 3D supramolecular network.

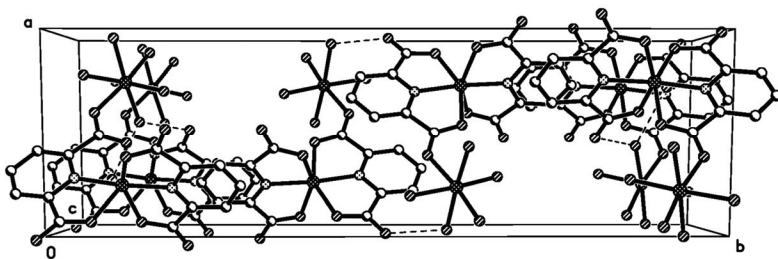


Fig. 2. Crystal packing diagram of the title complex.

X-Ray powder diffraction

The XRD pattern of the complex is shown in Fig. S-2a of the Supplementary material, from which it could be seen that the main diffraction peaks appeared at 2θ 14.60, 16.45 and 26.38°. The index was calculated from the XRD database on the computer program by the least squares method,¹⁶ and the results are shown in Table S-IV of the Supplementary material. The calculated spacing d_{hkl} is consistent with the experimental ones, and the maximum relative deviation between the experimental and calculated spacing d_{hkl} was less than 0.15 %. This indicates that the obtained powder was a single-phase compound. The crystal structure of the complex belongs to monoclinic system with the cell parameters $a = 8.397$ Å, $b = 27.409$ Å, $c = 9.609$ Å and $\beta = 98.22^\circ$. The results of indexes to the XRD data are consistent with the results of the single crystal structure. The experimental XRD pattern agrees well with the simulated pattern generated based on the single crystal analysis for the complex (Fig. S-2b of the Supplementary material).

FT-IR and UV spectra

The FT-IR spectrum of the complex is shown in Fig. S-3 of the Supplementary material. An intense broad absorption band in the region of 3200–3500 cm⁻¹, which can be assigned to stretching vibration of water molecules, could be seen.¹⁷ The presence of carboxyl groups was evidenced by the occurrence of strong absorption bands at 1618 cm⁻¹, attributed to $\nu_{as}(\text{COO}^-)$, and at 1395 cm⁻¹, attributed to $\nu_s(\text{COO}^-)$. The difference ($\Delta\nu = 223 \text{ cm}^{-1}$) between $\nu_{as}(\text{COO}^-)$ and $\nu_s(\text{COO}^-)$ suggests monodentate or bridged coordination mode of the carboxylate group to Co(II).¹⁸ The bands at 1576 and 1430 cm⁻¹ were assigned to $\nu(\text{C}=\text{N})$ and $\nu(\text{C}=\text{C})$, respectively. In addition, the bands at 594 and 544 cm⁻¹ are attributed to $\nu(\text{Cu}-\text{N})$ and $\nu(\text{Cu}-\text{O})$, respectively.

UV spectra of the ligand and the complex (Fig. S-4 of the Supplementary material) have only one absorption band, which was attributed to a $\pi-\pi^*$ transition of the ligand. Compared with those of the ligand (273 nm), the maximum absorption peak of the complex was shifted to 265 nm. The coordination bonds formed stabilize the structure, which led to the blue shift of the absorption peak.

Thermal analysis

Studying the thermal decomposition process of complexes is helpful to understanding of the coordination structure and the mechanism of thermal decomposition.^{19,20} The TG–DSC curves of the complex are shown in Fig. S-5 of the Supplementary material. The possible pyrolysis reaction, and the experimental and calculated mass losses in the thermal decomposition process are summarized in Table S-V of the Supplementary material. The first mass loss occurs about 102 °C, corresponding to the release of two crystalline water molecules, then the composition of the complex corresponds to be [Co₂(dipic)₂(H₂O)₅]. The second step in the mass loss of 14.61 % (calcd. 15.69 %) occurred at 150 °C, which shows the loss of five coordinated water molecules. The residue of [Co₂(dipic)₂] was stable between 180 to 320 °C. Thereafter, the exothermic peak at 469 °C corresponded to the decomposition of the ligand. In this step, two pyridine free radicals and two CO₂ molecules were lost, and the decomposition products were cobalt oxalate and Co atoms.¹² The cobalt oxalate decomposed at between 470 to 600 °C, and the result shows that the thermal decomposed product of cobalt oxalate is metallic cobalt²¹ at about 576 °C. Due to the oxidation of cobalt, a mass increase was observed (found 5.28 %, calcd. 5.57 %) in the TG curve. The final residue was CoO.

CONCLUSIONS

The homodinuclear complex [Co₂(dipic)₂(H₂O)₅]·2H₂O was synthesized by room temperature solid–solid reaction, and characterized by EA, single crystal X-ray diffraction, XRD, FT-IR, UV and TG–DSC. The crystal structure of the

complex belongs to monoclinic system and space group $P2(1)/c$. The two Co(II) ions are both six-coordinated, and the octahedral Co(II) cations show different coordination environments. The dipic²⁻ ligands utilize the carboxyl bridged coordination mode to link the two Co(II) ions. The 3D supramolecular architecture of the complex is constructed by means of hydrogen bond interactions between water molecules and carboxyl oxygen atoms of the ligands. The thermal decomposition processes of the complex include dehydration and pyrolysis of the ligand, and the residue is cobalt oxide.

SUPPLEMENTARY MATERIAL

The crystal data, bond lengths and angles, the results of indexes to XRD data, thermal decomposition data, XRD patterns, FT-IR and UV spectra, and TG-DSC curves of the complex are available electronically from <http://www.shd.org.rs/JSCS/>, or from the corresponding author on request. The crystallographic data are deposited with the Cambridge Crystallographic Data Centre under deposition number CCDC 1028718.

Acknowledgements. This work was supported by the National Natural Science Foundation of China (No. 21201142) and the Scientific Research Funds of Sichuan Provincial Education Department (No. 10ZA016).

ИЗВОД
СИНТЕЗА У ЧВРСТОМ СТАЊУ, КАРАКТЕРИЗАЦИЈА И ТЕРМИЧКО РАЗЛАГАЊЕ
ХОМОДИНУКЛЕАРНОГ КОБАЛТ(II)-КОМПЛЕКСА

DI LI, GUO-QING ZHONG and ZHI-XIAN WU

*School of Material Science and Engineering, Southwest University of Science and Technology, Mianyang
621010, China*

Полазећи од пиридин-2,6-дикарбоксилне киселине и кобалт(II)-ацетата у чврстом стању на собној температури синтетисан је хомодинуклеарни $[Co_2(dipic)_2(H_2O)_5] \cdot 2H_2O$ комплекс. Комплекс је окарактерисан помоћу елементарне микроанализе, методом дифракције X-зрака са кристала и праха, Фуријеровом трансформационом инфрацрвеној и електронском апсорpcionом спектроскопском методом, као и на основу термогравиметријских и диференцијалних калориметријских метода. Нађено је да комплекс представља моноклинични кристални систем са просторном групом $P2(1)/c$. У структури комплекса постоје два хексакоординована Co(II) јона. Један Co(II) јон је координован за четири карбоксилна атома кисеоника и два атома азота из dipic²⁻, док је други јон овог метала координован за пет молекула воде и један dipic²⁻ преко моста. Приказане су могуће реакције пиролизе и термичког разлагања комплекса, док су експериментално одређене масе продуката ових реакција.

(Примљено 24. фебруара, ревидирано 25. маја, прихваћено 6. јуна 2015)

REFERENCES

- M. Mirzaei, H. Eshtiagh-Hosseini, A. Hassanpoor, V. Barba, *J. Serb. Chem. Soc.* **77** (2012) 67
- G. H. Cui, C. H. He, C. H. Jiao, J. C. Geng, V. A. Blatov, *CrystEngComm* **14** (2012) 4210
- D. Sun, G. G. Luo, N. Zhang, R. B. Huang, L. S. Zheng, *Chem. Commun.* **47** (2011) 1461
- Z. G. Kong, S. N. Guo, Y. X. Zhao, D. Song, *J. Serb. Chem. Soc.* **79** (2014) 669

5. C. Y. Wang, Z. M. Wilseck, R. L. La Duca, *Inorg. Chem.* **50** (2011) 8997
6. H. Sakurai, Y. Koyima, Y. Yoshikawa, K. Kawabe, H. Yasui, *Coord. Chem. Rev.* **226** (2002) 187
7. J. Singh, P. Singh, *Bioinorg. Chem. Appl.* **2012** (2012), Article ID 104549
8. R. Gupta, S. Sanotra, H. N. Sheikh, B. L. Kalsotra, V. K. Gupta, Rajnikant, *J. Coord. Chem.* **65** (2012) 3917
9. K. Y. Choi, H. Ryu, Y. M. Lim, N. D. Sung, U. S. Shin, M. Suh, *Inorg. Chem. Commun.* **6** (2003) 412
10. D. Li, G. Q. Zhong, *Bioinorg. Chem. Appl.* **2014** (2014), Article ID 461605
11. H. Ilkimen, C. Yenikaya, M. Sari, M. Bulbul, E. Tunca, H. Dal, *J. Enzyme Inhib. Med. Chem.* **29** (2014) 353
12. D. Li, G. Q. Zhong, *Sci. World J.* **2014** (2014), Article ID 641608
13. A. B. Yılmaz, M. K. Sangün, D. Yağlıoğlu, C. Turan, *Food Chem.* **123** (2010) 410
14. G. M. Sheldrick, *Acta Crystallogr., A* **64** (2008) 112
15. C. Janiak, *J. Chem. Soc., Dalton Trans.* **21** (2000) 3885
16. G. Q. Zhong, Y. C. Guo, Y. R. Chen, S. R. Luan, X. S. Zang, *Acta Chim. Sin.* **59** (2001) 1599
17. S. Saha, D. Brahman, B. Sinha, *J. Serb. Chem. Soc.* **80** (2015) 35
18. G. Q. Zhong, J. Shen, Q. Y. Jiang, K. B. Yu, *Chin. J. Chem.* **29** (2011) 2650
19. G. Q. Zhong, J. Shen, Q. Y. Jiang, Y. Q. Jia, M. J. Chen, Z. P. Zhang, *J. Therm. Anal. Calorim.* **92** (2008) 607
20. V. N. Patange, B. R. Arbad, *J. Serb. Chem. Soc.* **76** (2011) 1237
21. B. Małecka, E. Drożdż-Cieśla, A. Małecki, *J. Therm. Anal. Calorim.* **68** (2002) 819.



SUPPLEMENTARY MATERIAL TO
Solid–solid synthesis, characterization and thermal decomposition of a homodinuclear cobalt(II) complex

DI LI, GUO-QING ZHONG* and ZHI-XIAN WU

School of Material Science and Engineering, Southwest University of Science and Technology, Mianyang 621010, China

J. Serb. Chem. Soc. 80 (11) (2015) 1391–1397

TABLE S-I. Crystal data and structure refinement parameters for the title complex

Empirical formula	Co ₂ C ₁₄ H ₂₀ O ₁₅ N ₂	Temperature, K	293(2)
Formula weight	574.18	Wavelength, Å	0.71073
Crystal system	Monoclinic	θ range, °	2.57–25.02
Space group	P2(1)/c	Limiting indices	-9≤h≤9, -32≤k≤27, -11≤l≤8
a, Å	8.3680(5)	Reflections collected/unique	8367/3807 [R(int) = 0.0649]
b, Å	27.2976(14)	Completeness to theta = 25.02	99.9 %
c, Å	9.5826(4)	Absorption correction	Semi-empirical from equivalents
B, °	98.276(5)	Max. and min. transmission	0.6105 and 0.5652
V, Å ³	2166.12(19)	Refinement method	Full-matrix least-squares on F ²
Z	4	Data / restraints / parameters	3807 / 0 / 298
D _c , g cm ⁻³	1.761	Goodness-of-fit on F ²	1.031
μ (Cu K _α), mm ⁻¹	1.610	Final R indices [I>2σ(I)]	R ₁ = 0.0519, wR ₂ = 0.0867
F(000)	1168	R indices (all data)	R ₁ = 0.0915, wR ₂ = 0.1086
Crystal size, mm	0.40×0.38×0.34	Δρ _{max} and Δρ _{min} , e Å ⁻³	0.488 and -0.492

*Corresponding author. E-mail: zqq316@163.com

TABLE S-II. Selected bond lengths and angles for the title complex

Bond	Distance, Å	Bond	Angle, °	Bond	Angle, °
Co1–O12	2.051(3)	O12–Co1–O13	96.40(16)	N2–Co2–N1	172.19(16)
Co1–O13	2.051(4)	O12–Co1–O2	79.84(13)	N2–Co2–O5	76.77(16)
Co1–O2	2.075(3)	O13–Co1–O2	86.93(14)	N1–Co2–O5	105.03(15)
Co1–O10	2.076(3)	O12–Co1–O10	169.57(14)	N2–Co2–O7	75.72(15)
Co1–O9	2.080(3)	O13–Co1–O10	88.33(15)	N1–Co2–O7	103.67(15)
Co1–O11	2.172(3)	O2–Co1–O10	91.18(14)	O5–Co2–O7	150.48(14)
Co2–N1	2.012(4)	O12–Co1–O9	91.00(13)	N2–Co2–O3	112.15(15)
Co2–N2	2.012(4)	O13–Co1–O9	91.79(14)	N1–Co2–O3	75.64(14)
Co2–O5	2.110(4)	O2–Co1–O9	170.53(13)	O5–Co2–O3	85.96(14)
Co2–O7	2.175(4)	O10–Co1–O9	98.17(14)	O7–Co2–O3	94.63(14)
Co2–O3	2.178(3)	O12–Co1–O11	86.32(15)	N2–Co2–O1	96.13(14)
Co2–O1	2.215(3)	O13–Co1–O11	176.65(14)	N1–Co2–O1	76.15(14)
O1–C1	1.263(5)	O2–Co1–O11	95.49(13)	O5–Co2–O1	96.80(14)
O2–C1	1.252(5)	O10–Co1–O11	89.31(13)	O7–Co2–O1	96.56(13)
		O9–Co1–O11	86.19(13)	O3–Co2–O1	151.39(13)

TABLE S-III. Hydrogen bond lengths and bond angles for the title complex

D–H	<i>d</i> (D–H), Å	<i>d</i> (H···A), Å	<i>d</i> (D···A), Å	\angle DHA, °	A symmetry operation
O9–H9C	0.850	1.919	2.764	172.28	O3 ($x-1, y, z-1$)
O9–H9D	0.850	1.808	2.652	171.56	O15 ($x, y, z-1$)
O10–H10C	0.850	1.985	2.831	173.26	O1
O10–H10C	0.850	2.470	2.965	117.97	O2
O10–H10D	0.850	1.848	2.695	173.45	O8 ($x-1, y, z-1$)
O11–H11C	0.850	1.831	2.675	171.39	O4 ($-x+1, -y+1, z+1$)
O11–H11D	0.850	1.939	2.782	171.32	O7 ($x-1, y, z$)
O12–H12C	0.850	1.801	2.635	166.60	O4 ($x-1, y, z-1$)
O12–H12D	0.850	2.127	2.936	167.46	O14
O13–H13C	0.850	1.886	2.726	169.72	O6 ($x, y, z-1$)
O13–H13D	0.850	1.982	2.823	170.12	O14 ($-x+1, -y+1, -z$)
O14–H14C	0.850	2.232	3.060	164.82	O5 ($-x+1, -y+1, -z+1$)
O14–H14D	0.850	2.103	2.933	165.10	O11 ($-x, -y+1, -z$)
O15–H10C	0.850	1.918	2.764	173.53	O6
O15–H10D	0.850	1.929	2.775	173.95	O8 ($x-1, -y+3/2, z+1/2$)

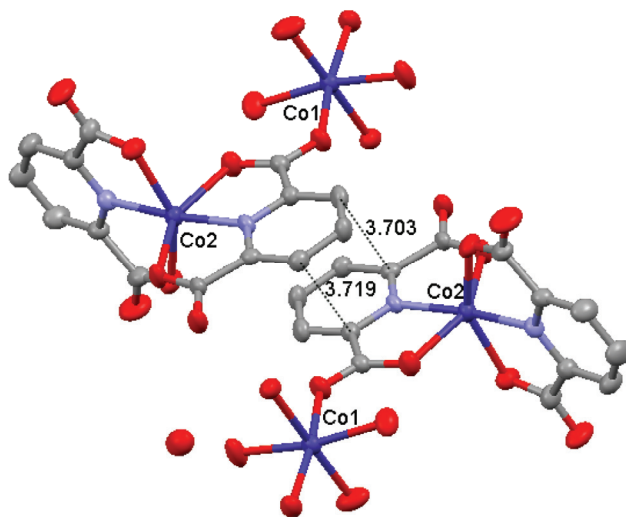
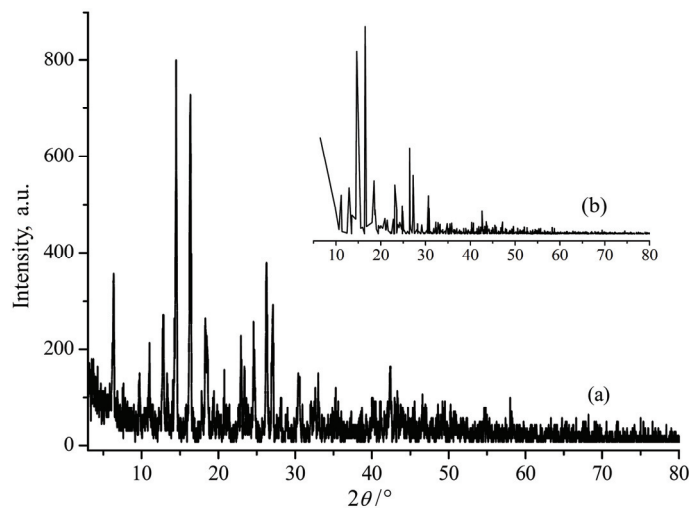
Fig. S-1. Weak spatial π - π stacking interactions of the title complex.

Fig. S-2. XRD patterns for the title complex (a) generated from the experimental data and (b) simulated from the single crystal X-ray data.

TABLE S-IV. Experimental data and calculated results for powder X-ray diffraction pattern of the title complex (monoclinic: $a = 8.397 \text{ \AA}$, $b = 27.409 \text{ \AA}$, $c = 9.609 \text{ \AA}$ and $\beta = 98.22^\circ$)

No.	$2\theta, {}^\circ$	h	k	l	$d_{\text{exp}}, \text{\AA}$	$d_{\text{cal}}, \text{\AA}$	I/I_0	No.	$2\theta, {}^\circ$	h	k	l	$d_{\text{exp}}, \text{\AA}$	$d_{\text{cal}}, \text{\AA}$	I/I_0
1	6.44	0	2	0	13.710	13.705	37.7	9	18.43	1	4	-1	4.811	4.810	34.0
2	9.84	0	1	1	8.980	8.985	13.2	10	18.65	0	0	-2	4.755	4.755	19.1
3	11.12	1	1	0	7.950	7.953	18.6	11	19.44	0	6	0	4.563	4.568	9.5
4	12.92	0	4	0	6.845	6.852	38.3	12	20.88	1	5	-1	4.250	4.256	9.6
5	13.48	1	1	-1	6.565	6.559	8.5	13	21.39	2	0	0	4.151	4.155	6.3

TABLE S-IV. Continued

No.	$2\theta, {}^\circ$	h	k	l	$d_{\text{exp}}, \text{\AA}$	$d_{\text{cal}}, \text{\AA}$	I/I_0	No.	$2\theta, {}^\circ$	h	k	l	$d_{\text{exp}}, \text{\AA}$	$d_{\text{cal}}, \text{\AA}$	I/I_0
6	14.60	1	2	-1	6.061	6.059	100	14	23.04	1	1	2	3.857	3.856	22.0
7	16.45	1	2	1	5.386	5.386	97.4	15	23.51	2	3	0	3.782	3.783	14.6
8	17.97	1	3	1	4.933	4.931	7.2	16	24.17	2	3	-1	3.680	3.683	6.3
17	24.74	0	5	2	3.596	3.592	17.4	26	40.14	1	4	-4	2.245	2.246	9.8
18	26.38	2	0	-2	3.376	3.377	56.0	27	41.83	3	8	0	2.158	2.154	6.2
19	27.17	2	2	-2	3.279	3.279	37.6	28	42.45	2	8	-3	2.128	2.128	13.1
20	30.52	1	7	-2	2.927	2.927	16.0	29	47.06	3	2	-4	1.929	1.928	6.3
21	32.23	1	9	-1	2.775	2.776	6.1	30	50.39	4	6	1	1.809	1.810	7.1
22	32.67	0	5	3	2.739	2.744	8.3	31	57.94	4	4	3	1.590	1.589	6.0
23	33.12	1	3	3	2.703	2.703	8.6	32	65.18	5	4	-4	1.430	1.432	6.4
24	38.36	2	7	2	2.345	2.345	7.4	33	76.94	2	1	7	1.238	1.239	7.5
25	38.87	3	5	-2	2.315	2.318	6.7								

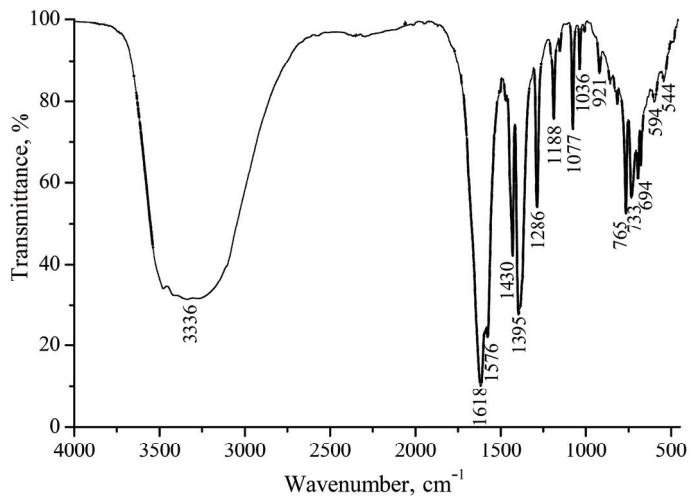


Fig. S-3. FT-IR spectrum of the title complex.

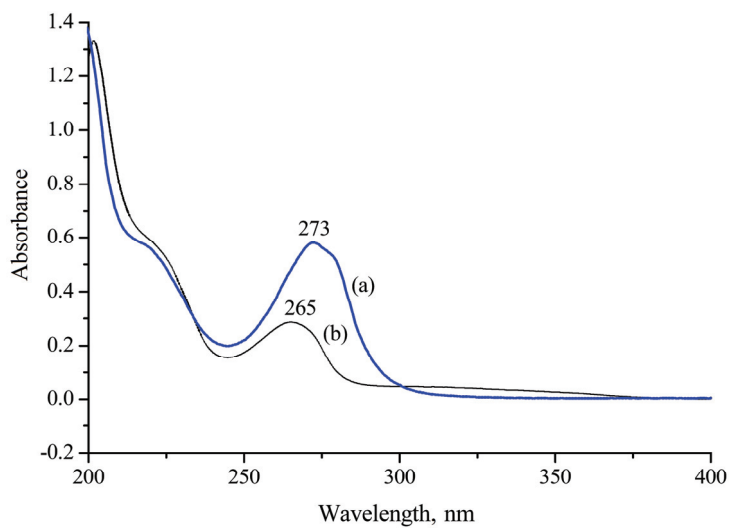


Fig. S-4. UV spectra of (a) the ligand and (b) the title complex.

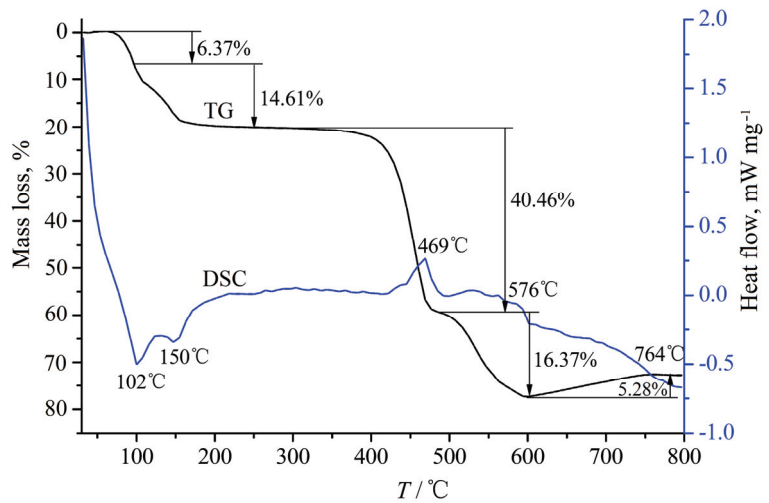


Fig. S-5. TG-DSC curves of the title complex obtained under a air atmosphere.

TABLE S-V. Thermal decomposition data of the title complex

Reaction	T_{DSC} , °C	Mass loss, %	
		m_{exp}	m_{theor}
[Co ₂ (C ₇ H ₃ O ₄ N) ₂ (H ₂ O) ₅]·2H ₂ O			
↓ -2H ₂ O	102 (endo.)	6.37	6.28
[Co ₂ (C ₇ H ₃ O ₄ N) ₂ (H ₂ O) ₅]			
↓ -5H ₂ O	150 (endo.)	14.61	15.69
[Co ₂ (C ₇ H ₃ O ₄ N) ₂]			
↓ -2C ₅ H ₃ N, -2CO ₂	469 (exo.)	40.46	42.17
CoC ₂ O ₄ + Co			
↓ -2CO ₂	576 (exo.)	16.37	15.33
2Co			
↓ +O ₂	764 (exo.)	5.28 ^a	5.57 ^a
2CoO		27.47 ^b	26.10 ^c

^aThe increased mass percentage; ^bthe experimental mass percentage of the residue in the sample, ^cthe calculated mass percentage of the residue in the sample



Spin state relaxation of iron complexes: The case for OPBE and S12g

MAJA GRUDEN¹, STEPAN STEPANOVIĆ^{2#} and MARCEL SWART^{3,4*}

¹Faculty of Chemistry, University of Belgrade, Studentski trg 12–16, 11001 Belgrade, Serbia,
²Center for Chemistry, ICTM, University of Belgrade, Njegoševa 12, 11001 Belgrade, Serbia,

³Institut de Química Computacional i Catalisi (IQCC) and Departament de Química,
Universitat de Girona, Campus Montilivi, Facultat de Ciències, 17071 Girona, Spain and

⁴Institució Catalana de Recerca i Estudis Avançats (ICREA), Pg. Lluís Companys 23,
08010 Barcelona, Spain

(Received 11 June, revised 14 July, accepted 15 July 2015)

Abstract: The structures of nine iron complexes that show a diversity of experimentally observed spin ground states were optimized and analyzed using the Density Functional Theory (DFT). An extensive validation study of the new S12g functional was performed, with a discussion concerning the influence of the environment, geometry and its overall performance based on a comparison with the well-proven OPBE functional. The OPBE and S12g functionals gave the correct spin ground state for all investigated iron complexes. Since S12g performs remarkably well, it could be considered a reliable tool for studying the energetics of the spin state in complicated transition metal systems.

Keywords: density functional theory; Fe(II) and Fe(III) coordination compounds; validation study; spin states.

INTRODUCTION

Spin is an intrinsic and inherent property of atoms and molecules.¹ Most transition metal ions with partially filled d-shells can exhibit different kinds of spin multiplicity in the ground state, *i.e.*, can lead to different spin states. Depending on the oxidation number, iron complexes usually have either 5 or 6 d-electrons that can be distributed in an octahedral environment in at least two different ways: with a maximum number of unpaired electrons, leading to the high spin (HS) state, or with maximally paired electrons – giving the low spin (LS) state. Other possibilities of the distribution of electrons represent an intermediate (IS) spin state. Since HS, IS and LS complexes usually display quite different

* Corresponding author. E-mail: marcel.swart@icrea.cat

Serbian Chemical Society member.

doi: 10.2298/JSC150611068G

structural, spectral and magnetic properties, and often reactivity, it is of the utmost importance to have both experimental and theoretical methods to determine correctly the spin ground state of a system. However, both experiment and theory have difficulties and problems, and many studies have been devoted to this issue in the last decade.^{2–5}

From a broad palette of quantum mechanical methods, the density functional theory (DFT)^{6–8} has emerged into the mainstream, mainly because it gives a good compromise between accuracy of the results and computational efficiency.^{9–11} However, although the DFT, in principle, gives an exact energy, a universal functional is still unknown, leading to density functional approximations (DFAs). These DFAs are parameterized for different properties and, noteworthy, spin-state energies were not included in the development for most of nowadays available DFAs.¹² It has been shown that the accuracy of the results not only strongly depends on the choice of the DFAs, but also on the basis set that is used.^{1,3,13,14} Early pure functionals, such as LDA,^{15–17} BP86,^{18,19} BLYP,^{19,20} and PW91,^{21,22} have a tendency to favor LS states,¹⁴ while hybrid functionals, such as B3LYP,^{23,24} PBE0²⁵ and M06,^{26,27} systematically favor HS states.¹⁴ For the reliable prediction of the correct spin ground state from a number of close lying states, OPBE¹⁴ has emerged to be one of the best functionals for the task.²⁸ Recently, Swart constructed a new density functional that combines the best of OPBE (spin states, reaction barriers) with the best of PBE (weak interactions) into the S12g⁵ DFA.

Previously, the relative spin state energies of seven iron complexes (**1–7**, Fig. 1) on OLYP^{20,29} optimized geometries (**1–3**) and on crystal structures (**4–7**) with a variety of DFAs were reported, which already showed the good performance of OPBE for vertical spin state splittings.¹⁴

Herein, a detailed DFT study on OPBE optimized geometries of iron complexes (**1–7**) with experimentally established spin ground states, ranging from singlet to sextet, is reported together with an extension to include two iron porphyrinato complexes (**8** and **9**, Fig. 1) that were reported to have different electronic ground states in spite of their similarity.^{30–32}

Furthermore, a comprehensive validation study of the S12g DFA,⁵ together with an examination of the influence of the chemical environment, was performed on all the investigated complexes.

METHODOLOGY

All DFT calculations were performed with the Amsterdam Density Functional (ADF) suite of program.^{33,34} MOs were expanded in an uncontracted set of Slater type orbitals (STOs) of triple- ζ quality containing diffuse functions (TZP)³⁵ and one set of polarization functions. Core electrons (1s for 2nd period and 1s2s2p for 3rd–4th period) were not treated explicitly during the geometry optimizations (frozen core approximation), as the core was shown to have a negligible effect on the obtained geometries.³⁶ An auxiliary set of s, p, d, f,

and g STOs was used to fit the molecular density and to represent the Coulomb and exchange potentials accurately for each self-consistent field (SCF) cycle.

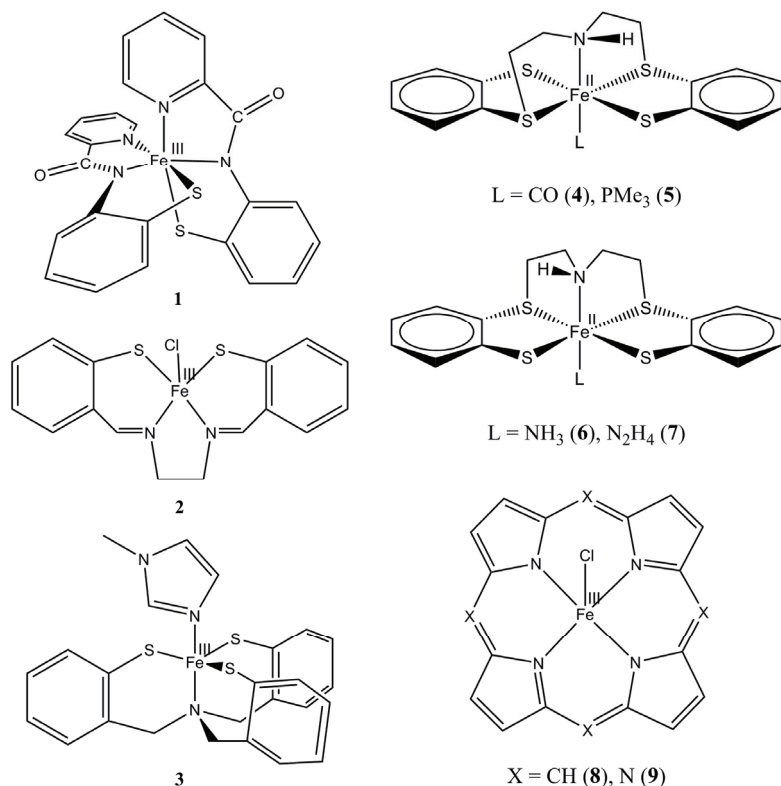


Fig. 1. Fe(PyPepS)₂ **1** (PyPepSH₂ = *N*-(2-mercaptophenyl)-2'-pyridinecarboxamide); Fe(tsalen)Cl **2** (tsalen = 2,2'-(1,2-ethanediyl)bis(nitrilomethylidyne)]bis[benzenethiolato]; Fe(N(CH₂-*o*-C₆H₄S)₃)(1-Me-imidazole) **3**; (Fe(NH)S₄)L **4** (L=CO), **5** (PMe₃), **6** (NH₃), **7** (N₂H₄)(NH)S₄ = bis(2-((2-mercaptophenyl)thio)ethyl)amine); iron porphyrin chloride (**8**, FePCL) and iron porphyrazine chloride (**9**, FePzCl).

Energies and gradients were calculated using the OPBE and S12g functionals in the gas phase and with COSMO (methanol as a solvent)³⁷⁻³⁹ in the dielectric continuum model for a solvent environment. The geometries were optimized with the QUILD program⁴⁰ using adapted delocalized coordinates⁴¹ until the maximum gradient component was less than 10⁻⁴ a.u. Subsequent single point calculations that utilize all electron basis set were performed on all optimized geometries, with OPBE and S12g.

RESULTS AND DISCUSSION

The total set of molecules consists of both Fe(III) (**1-3**, **8** and **9**) and Fe(II) (**4-7**) complexes, and show a diversity of experimentally observed spin ground states. A thorough examination with the OPBE and S12g functionals in the gas phase and the COSMO solvent environment was performed. The discussion is

commenced by focusing on the influence of structure relaxation on the spin states of Fe(III)-complexes **1–3**.⁴² Experimentally, Fe-(PyPepS)₂ (**1**, PyPepSH₂ = *N*-(2-mercaptophenyl)-2-pyridinecarboxamide) has a LS doublet ground state,⁴³ Fe(tsalen)Cl (**2**, tsalen = 2,2'-[1,2-ethanediylbis(nitrilomethylidyne)]bis[benzenethiolato] 2,2'-[1,2-ethanediylbis(nitrilomethylidyne)]bis[benzenethiolato]) an intermediate spin (IS), quartet ground state⁴⁴ and Fe(N(CH₂-*o*-C₆H₄S)₃)(1-Me-imidazole, **3**) a HS sextet ground state.⁴⁵ Then, the Fe(II)-complexes ((Fe(NH)S₄)L, (NH)S₄ = bis(2-((2-mercaptophenyl)thio)ethyl)amine, L = CO (**4**), PMe₃ (**5**), NH₃ (**6**) and N₂H₄ (**7**)) are discussed. Compounds **4** and **5** have a LS (singlet) state and compounds **6** and **7**, reportedly, a HS (quintet) ground state.^{46–48} Furthermore, focus is placed on Fe^{III}(porphyrinato)Cl, FeP_{Cl} (**8**) and, Fe^{III}(porphyrazinato)Cl, FePzCl (**9**), which have a sextet and a quartet ground state, respectively.

*Structure relaxation and spin state energies of Fe(III) compounds **1–3***

The optimization of the three Fe(III) molecules (**1–3**) led in all cases to the expected structural changes for the different spin states (Tables S-I–S-III of the Supplementary material to this paper). Comparison of the optimized structures of **1–3** indicated the existence of an expansion of the ligand sphere. Going from the doublet to the quartet state, first the equatorial ligands moved away from iron while the axial ligands stayed almost at the same position. In the sextet state, the equatorial ligands remained virtually at the same position, but the axial ligands (had to) moved out.

Comparing the vertical spin state energies, calculated on the experimental structure,¹⁴ with results from the optimized (“relaxed”) geometries, Table I, it is evident that the energy gap between different spin states decreased. In the case of compound **1**, the doublet state remained the spin ground state with the quartet state (from 22.5 kcal·mol⁻¹ “vertical” to 17.5 kcal·mol⁻¹ “relaxed”) and the sextet state (from 33.9 kcal·mol⁻¹ “vertical” to 10.2 kcal·mol⁻¹ “relaxed”) in closer energetic proximity after geometry optimization. Molecule **2** has the quartet ground state, and here, the relative energies of the doublet and sextet states were reduced after structure relaxation. The same trends apply for the sextet ground state of complex **3**. For all complexes, after spin state relaxation, both OPBE and its recently developed successor S12g gave the correct spin ground state. Spin contamination was small for these complexes, and therefore, will not be discussed further.

The choice of exchange-correlation functional had an obvious influence on the geometry, with a tendency of S12g to give somewhat longer bond lengths than OPBE (Tables S-I–S-III). It should be noted that S12g gave structural parameters that were in excellent agreement with experimental values. Unlike the

* 1 kcal = 4184 J

choice of functional, the influence of solvation on the geometrical parameters during the structural relaxation was not very significant, and it depended slightly on the system under consideration. In most cases, optimizations with COSMO gave slightly longer bonds, but without significant consequences for the spin-state splittings, Table I.

TABLE I. Spin state energies (kcal mol⁻¹) for Fe(III) molecules **1–3** using TZP basis set, with OPBE and S12g functionals, in vacuum and COSMO

Geo. ^a	SP ^b	Fe-(PyPepS) ₂ 1			Fe(tsalen)Cl 2			Fe(N(CH ₂ - <i>o</i> -C ₆ H ₄ S) ₃)(1MIm ^b) 3		
		Doublet	Quartet	Sextet	Doublet	Quartet	Sextet	Doublet	Quartet	Sextet
OPBE	OPBE	0	17.1	10.2	6.5	0	3.9	6.6	7.9	0
	OPBE	0	19.4	13.0	9.3	0	6.9	7.9	7.4	0
	cosmo									
	S12g	0	15.8	8.7	7.6	0	3.8	6.8	7.2	0
	S12g	0	18.2	11.6	10.2	0	6.4	8.2	6.8	0
OPBE	OPBE	0	18.8	13.1	5.2	0	2.9	6.2	7.5	0
	cosmo	OPBE	0	17.4	10.2	9.7	0	7.7	8.0	7.2
	cosmo									
	S12g	0	18.4	13.3	6.0	0	3.0	6.5	6.8	0
	S12g	0	17.1	10.6	10.2	0	7.4	8.3	6.5	0
S12g	OPBE	0	18.3	10.5	7.4	0	6.2	7.6	8.1	0
	OPBE	0	22.7	14.7	10	0	9.2	8.6	7.1	0
	cosmo									
	S12g	0	15.4	8.7	7.5	0	6.6	6.5	7.0	0
	S12g	0	19.9	13.1	9.9	0	9.3	7.7	6.1	0
S12g	OPBE	0	17.5	10.6	7.0	0	4.7	7.5	8.4	0
	OPBE	0	20.5	14.9	11.2	0	6.7	8.8	7.2	0
	cosmo									
	S12g	0	15.7	9.2	6.6	0	4.7	6.1	6.8	0
	S12g	0	18.8	13.7	10.4	0	6.5	7.6	5.9	0
cosmo	cosmo									

^aGeometry optimization with frozen core electrons; ^bsubsequent single point calculations with all-electron basis sets

Structure relaxation and spin state energies of compounds **4–7**

The spin state dependent structure relaxation for the Fe(II) compounds results in similar differences in Fe–ligand distances as for the Fe(III) compounds (Tables S-IV–S-VII). In the case of compounds **4–7**, the Fe–N, Fe–S and Fe–C distances were slightly elongated in comparison to the distances in the Fe(III) complexes due to the additional *d*-electron in the Fe(II) systems.

The spin ground states of the Fe(II) complexes **4** and **5** were correctly predicted using both the OPBE and S12g levels of theory (see Table II): the singlet state was the lowest in energy for both molecules, in agreement with expe-

TABLE II. Spin state energies (kcal mol⁻¹) for labile (*trans*) complexes **4** and **5** using TZP basis, with OPBE and S12g functionals, in vacuum and COSMO

Geo. ^a	SP ^b	<i>trans</i> -(Fe(NH)S ₄)CO 4			<i>trans</i> -(Fe(NH)S ₄)PMe ₃ 5		
		Singlet	Triplet	Quintet	Singlet	Triplet	Quintet
OPBE	OPBE	0	23.4	34.8	0	16.3	20.1
	OPBE cosmo	0	24.5	36.6	0	17.3	18.6
	S12g	0	19.1	28.0	0	14.5	17.7
	S12g cosmo	0	20.2	29.7	0	15.4	16.3
OPBE cosmo	OPBE	0	23.5	35.3	0	16.4	20.4
	OPBE cosmo	0	24.5	36.5	0	17.3	18.3
	S12g	0	19.4	29.1	0	15.1	19.1
	S12g cosmo	0	20.3	30.3	0	15.9	17.1
S12g	OPBE	0	23.4	34.2	0	19.6	19.4
	OPBE cosmo	0	24.3	36.4	0	20.3	19.2
	S12g	0	18.7	29.3	0	15.6	16.8
	S12g cosmo	0	19.6	31.4	0	16.3	16.6
S12g cosmo	OPBE	0	24.6	35.0	0	19.9	19.2
	OPBE cosmo	0	24.8	36.5	0	20.6	18.2
	S12g	0	20.4	30.8	0	15.8	17.1
	S12g cosmo	0	20.5	32.2	0	16.4	16.2

^aGeometry optimization with frozen core electrons; ^bsubsequent single point calculations with all-electron basis sets

rimental data. For compound **4**, the triplet and quintet states were significantly higher in energy. The energy differences between the different states were smaller for compound **5**. Similar to the Fe(III) complexes, spin contamination was small and will not be discussed any further. Similar to compounds **4** and **5**, after spin state structure relaxation, an LS ground state for iron complexes **6** and **7** was found, with IS and HS higher in energy. Unfortunately, the experimental determination of the spin states of compounds **6** and **7** were inconclusive, since anomalous high μ_{eff} values of 10–13 μ_{B} were measured that may indicate impurities, *e.g.*, by metallic iron, or oligomer formation. For compound **7** in solution, an HS state was observed,⁴⁸ but a compound similar to **7** showed a diamagnetic LS Fe center.⁴⁹ Moreover, indications of dimer formation of the ligand-free [(Fe(NH)S₄)] complex were observed.^{47,48} Since different forms of the (Fe(NH)S₄)L complex in these studies were obtained, both forms for compounds **4–7**, *i.e.*, with the “*trans*” and “*meso*” form (see Fig. 2) had to be checked. For both forms of each of compounds **4–7**, an LS ground state was found, albeit with smaller spin-state splitting for compounds **6** and **7**. These findings could be traced back to the strength of the iron–ligand bond, which seems to be much weaker for compounds **6/7** than for compounds **4/5**. The weakly bound NH₃ and N₂H₄ ligands are easily exchanged with CH₃OH, solvent (THF) or CO.⁴⁸ These experimental data corroborate the present computed ligand-binding energies, which indicate strong and favorable binding of CO and P(Me)₃ to form the singlet ground state, but less favorable binding of the other ligands or spin states

(see Table S-VIII of the Supplementary material). Interestingly, the monomeric Fe(NH)S₄ complex without a ligand was predicted to have a triplet spin ground state in the *trans* form, with the other spin states or the *meso* form lying higher in energy by at least 7 kcal·mol⁻¹. The ligand-free complex may dimerize to give the experimentally observed HS state through ferromagnetic coupling. The latter process was not studied due to the complexity involved with ferromagnetic *versus* anti-ferromagnetic coupling of the many spin states that need to be considered. This was confirmed by a recent study using high-level *ab initio* methods that indeed found a singlet ground-state for these molecules.⁵⁰ In another recent study, “accurate” spin ground states for molecules **6** and **7** were found with the double hybrid B2PLYP functional, where an HS ground-state was obtained for molecule **6** with OPBE.⁵¹ Since the last result is in disagreement with the results of the present study, molecules **6** and **7** were re-optimized using the OPBE functional with the geometries from their paper⁵¹ as the starting point. The re-optimized structures resulted in spin state splittings that were in accordance with the previous study,⁵¹ however, the structures were highly distorted representing only a local minimum on the potential energy surface (and *ca.* 5–20 kcal·mol⁻¹ above the structures obtained here in Table III).

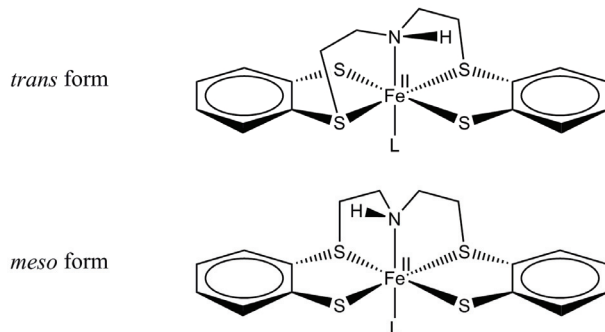


Fig. 2. Different forms of compounds **4–7**.

TABLE III. Spin state energies (kcal mol⁻¹) for labile (*meso*) complexes **6** and **7** using TZP basis, with OPBE and S12g functionals, in vacuum and COSMO

Geo. ^a	SP ^b	<i>meso</i> -(Fe(NH)S ₄)NH ₃ (6)			<i>meso</i> -(Fe(NH)S ₄)N ₂ H ₄ (7)		
		Singlet	Triplet	Quintet	Singlet	Triplet	Quintet
OPBE	OPBE	0	10.3	6.6	0	11.3	6.6
	OPBE cosmo	0	10.1	3.9	0	10.7	4.4
	S12g	0	7.7	2.6	0	8.5	2.5
	S12g cosmo	0	7.4	-0.1	0	7.9	0.3
OPBE	OPBE	0	10.6	7.2	0	11.5	7.1
cosmo	OPBE cosmo	0	9.9	3.5	0	10.1	3.8
	S12g	0	7.9	3.5	0	9.7	3.6
	S12g cosmo	0	7.0	-0.2	0	8.2	0.5

TABLE III. Continued

Geo. ^a	SP ^b	<i>meso</i> -(Fe(NH)S ₄)NH ₃ (6)			<i>meso</i> -(Fe(NH)S ₄)N ₂ H ₄ (7)		
		Singlet	Triplet	Quintet	Singlet	Triplet	Quintet
S12g	OPBE	0	10.1	7.5	0	11.1	7.6
	OPBE cosmo	0	10.7	5.7	0	11.0	6.8
	S12g	0	8.4	5.3	0	9.3	5.3
	S12g cosmo	0	8.7	3.4	0	9.2	4.6
S12g cosmo	OPBE	0	10.1	6.8	0	10.8	6.6
	OPBE cosmo	0	10.5	4.4	0	10.4	5.2
	S12g	0	8.7	4.9	0	9.4	4.6
	S12g cosmo	0	8.8	2.4	0	8.9	3.2

^aGeometry optimization with frozen core electrons; ^bsubsequent single point calculations with all-electron basis sets

As in the case of the previous investigated molecules **1–3**, after optimization with S12g, somewhat longer bond lengths were obtained in comparison with the OPBE geometries. Nevertheless, both of them are again in good agreement with the experimental data (Tables S-IV–S-VII). In contrast to the Fe(II) complexes **1–3**, the Fe(III) P450 model systems **4–7** are prone to the influence of solvent (COSMO calculations) on the spin state ordering, Tables II and III. Calculations with the COSMO solvation model revealed a tendency to favor the HS state for complexes **5–7**, and the LS state for complex **4**.

Iron porphyrin chloride and the porphyrazine analogue

The structures of FePCl (**8**) and FePzCl (**9**) were separately optimized in C_{4v} symmetry for each spin state. Similarly to previous results,^{30,52,53} it was found that the porphyrin core size increased when going from the LS to the HS state, while the Fe–Cl distance increased from the LS to the IS state, and then was slightly decreased in the HS state (Tables S-IX and S-X of the Supplementary material).

OPBE and S12g predicted the correct sextet spin ground state for both, FePCl and FePzCl (see Table IV). In the case of FePCl, a sextet ground state was predicted with the quartet higher in energy and *vice versa* for FePzCl, the quartet state was lower in energy. In both cases, the LS state was considerably higher in energy.

COSMO calculations revealed a clear and unambiguous solvent effect on the electronic structure, Table IV. Introduction of the solvent favored the LS state, and as such had small effects on the spin ground state of molecule **9** that has a quartet ground state and a sextet quartet state that is similar in energy. In contrast, for molecule **8**, that is in an HS state experimentally and has a low-lying quartet state, the quartet state is stabilized to the extent that it becomes the ground state within all COSMO calculations. Of course, it should be added that the spin-state splittings were investigated here through looking at the electronic energy and

hence, enthalpy and entropy effects were ignored. Both of these favor the high-spin states. Finally, S12g once again showed excellent agreement with the spin state energetics obtained at the OPBE level of theory.

TABLE IV. Spin state energy differences (kcal mol⁻¹, TZP basis) for FePCl (**8**) and FePzCl (**9**), with OPBE and S12g functionals, in vacuum and COSMO

Geo. ^a	SP ^b	FePCl			FePzCl		
		Doublet	Quartet	Sextet	Doublet	Quartet	Sextet
OPBE	OPBE	18.4	3.9	0	12.5	0	3.7
	OPBE cosmo	16.3	-1.0	0	15.6	0	7.6
	S12g	15.7	1.5	0	12.8	0	4.9
	S12g cosmo	13.8	-2.9	0	15.8	0	8.6
OPBE cosmo	OPBE	18.0	4.8	0	11.6	0	2.9
	OPBE cosmo	16.9	-1.7	0	16.6	0	8.2
	S12g	15.0	2.3	0	11.8	0	4.2
	S12g cosmo	14.1	-3.6	0	16.5	0	9.2
S12g	OPBE	18.6	4.0	0	12.7	0	3.7
	OPBE cosmo	16.3	-0.7	0	15.7	0	7.5
	S12g	15.4	1.5	0	12.6	0	5.0
	S12g cosmo	13.4	-2.8	0	15.4	0	8.6
S12g cosmo	OPBE	18.3	4.5	0	12.0	0	3.2
	OPBE cosmo	17.1	-1.6	0	16.8	0	8.1
	S12g	15.0	2.0	0	11.8	0	4.6
	S12g cosmo	14.0	-3.5	0	16.3	0	9.2

^aGeometry optimization with frozen core electrons; ^bsubsequent single point calculations with all-electron basis sets

CONCLUSIONS

Within this paper, an extension of previous validation¹⁴ of DFAs for a correct description of the spin states of Fe(II) and Fe(III) complexes is presented. In the present contribution, structure relaxation of the LS, IS and HS states of the iron compounds was allowed separately at the OPBE and S12g levels of theory and thereby, a more stringent test on the reliability of functionals for providing spin ground states of iron complexes was performed.

A detailed comparison with the already proven OPBE DFA for spin state energetics, and experimental findings, revealed that S12g performed remarkably well and thus, represents a very promising tool for studying spin states in complicated transition metal systems. Moreover, for all iron complexes under investigation, S12g gave a good match with experimental geometries and thus, could be considered as a good starting point for the investigation of transition metal compounds.

SUPPLEMENTARY MATERIAL

Selected bond lengths, OPBE/TZP ligand binding energies, as well as coordinates of optimized structures (as additional supplementary file), are available electronically from <http://www.shd.org.rs/JSCS/> or from the corresponding author on request.

Acknowledgments. The following organizations are thanked for financial support: the Ministerio de Ciencia e Innovación (MICINN, project CTQ2011-25086/BQU), the Ministerio de Economía y Competitividad (MINECO, project CTQ2014-59212/BQU) and the DIUE of the Generalitat de Catalunya (project 2014SGR1202, and Xarxa de Referència en Química Teòrica i Computacional). Financial support was provided by MICINN and the FEDER fund (European Fund for Regional Development) under grant UNGI10-4E-801, and the Serbian Ministry of Education, Science and Technological Development (Grant No. 172035). This work was performed within the framework of the COST action CM1305 “Explicit Control Over Spin-states in Technology and Biochemistry (ECOSTBio)” (STSM reference: ECOST-STSM-CM1305-27360). We would like to thank Dr. A. W. Ehlers and Prof. K. Lammertsma (VU Amsterdam, Netherlands) for help and fruitful discussions in the initial stages of this study.

ИЗВОД

РЕЛАКСАЦИЈА СПИНСКИХ СТАЊА КОД КОМПЛЕКСА ГВОЖЂА:
СЛУЧАЈ ЗА OPВЕ И S12g ФУНКЦИОНАЛЕМАЈА ГРУДЕН¹, СТЕПАН СТЕПАНОВИЋ² и MARCEL SWART^{3,4}

¹Хемијски факултет, Универзитет у Београду, Студентски бар 16, 11001 Београд, ²Центар за хемију, ИХТМ, Универзитет у Београду, Небошева 12, 11001 Београд, ³Institut de Química Computacional i Catalisi (IQCC) and Departament de Química, Universitat de Girona, Campus Montilivi, Facultat de Ciències, 17071 Girona, Spain и ⁴Institució Catalana de Recerca i Estudis Avançats (ICREA), Pg. Lluís Companys 23, 08010 Barcelona, Spain

Структуре девет комплекса гвожђа који показују разноврсност експериментално одређених основних спинских стања оптимизоване су теоријом функционала густине (DFT), а затим анализиране коришћењем различитих функционала. Извршена је обимна валидациона студија новог S12g функционала, са дискусијом о утицају окружења, геометрије, као и његових перформанси у односу на OPВЕ функционал који се већ показао као добар. OPВЕ и S12g тачно предвиђају основно спинско стање код свих испитиваних комплекса гвожђа. Како се S12g показао изузетно добро, он се може сматрати поузданим за проучавање енергетике спинских стања у компликованим системима прелазних метала.

(Примљено 11. јуна, ревидирано 14. јула, прихваћено 15. јула 2015)

REFERENCES

1. C. R. Jacob, M. Reiher, *Int. J. Quantum Chem.* **112** (2012) 3661
2. M. Swart, M. Güell, M. Solà, *Accurate Description of Spin States and its Implications for Catalysis*, in *Quantum Biochemistry*, C. F. Mattak, Ed., Wiley-VCH, Weinheim, 2010, p. 551
3. M. Swart, *Int. J. Quantum Chem.* **113** (2013) 2
4. M. Swart, *J. Chem. Theory Comput.* **4** (2008) 2057
5. M. Swart, *Chem. Phys. Lett.* **580** (2013) 166
6. R. Dreizler, E. Gross, *Density Functional Theory*, Plenum Press, New York, 1995
7. W. Koch, M. C. Holthausen, *A Chemist's Guide to Density Functional Theory*, Wiley-VCH, Weinheim, 2000
8. R. G. Parr, W. Yang, *Density functional theory of atoms and molecules*, Oxford University Press, New York, 1989
9. S. Matar, P. Guionneau, G. Chastanet, *Int. J. Mol. Sci.* **16** (2015) 4007

10. B. Pandey, A. Ansari, N. Vyas, G. Rajaraman, *J. Chem. Sci.* **127** (2015) 343
11. M. E. Pascualini, N. V. Di Russo, A. E. Thuijs, A. Ozarowski, S. A. Stoian, K. A. Abboud, G. Christou, A. S. Veige, *Chem. Sci.* **6** (2015) 608
12. M. Costas, J. N. Harvey, *Nature Chem.* **5** (2013) 7
13. M. Güell, J. M. Luis, M. Solà, M. Swart, *J. Phys. Chem., A* **112** (2008) 6384
14. M. Swart, A. R. Groenhof, A. W. Ehlers, K. Lammertsma, *J. Phys. Chem., A* **108** (2004) 5479
15. P. A. M. Dirac, *Proc. R. Soc. London, A* **123** (1931) 714
16. J. C. Slater, *Phys. Rev.* **81** (1951) 385
17. S. H. Vosko, L. Wilk, M. Nusair, *Can. J. Phys.* **58** (1980) 1200
18. J. P. Perdew, *Phys. Rev., B* **33** (1986) 8822
19. A. D. Becke, *Phys. Rev., A* **38** (1988) 3098
20. C. Lee, W. Yang, R. G. Parr, *Phys. Rev., B* **37** (1988) 785
21. J. P. Perdew, PW91, in *Electronic structure of Solids*, P. Ziesche, H. Eschrig, Eds., Akademie, Berlin, 1991, p. 11
22. J. P. Perdew, J. A. Chevary, S. H. Vosko, K. A. Jackson, M. R. Pederson, D. J. Singh, C. Fiolhais, *Phys. Rev., B* **46** (1992) 6671
23. A. D. Becke, *J. Chem. Phys.* **98** (1993) 5648
24. P. J. Stephens, F. J. Devlin, C. F. Chabalowski, M. J. Frisch, *J. Phys. Chem.* **45** (1994) 11623
25. C. Adamo, V. Barone, *J. Chem. Phys.* **110** (1999) 6158
26. Y. Zhao, D. G. Truhlar, *J. Chem. Phys.* **125** (2006) 194101
27. Y. Zhao, D. Truhlar, *Theor. Chem. Acc.* **120** (2008) 215
28. W. C. Isley III, S. Zarra, R. K. Carlson, R. A. Bilbeisi, T. K. Ronson, J. R. Nitschke, L. Gagliardi, C. J. Cramer, *Phys. Chem. Chem. Phys.* **16** (2014) 10620
29. N. C. Handy, A. J. Cohen, *Mol. Phys.* **99** (2001) 403
30. A. Ghosh, T. Vangberg, E. Gonzalez, P. Taylor, *J. Porphyrins Phthalocyanines* **5** (2001) 345
31. M. M. Conradie, J. Conradie, A. Ghosh, *J. Inorg. Biochem.* **105** (2011) 84
32. A. Ghosh, P. R. Taylor, *Curr. Opin. Chem. Biol.* **7** (2003) 113
33. ADF 2003.01, SCM, Amsterdam, 2003
34. G. te Velde, F. M. Bickelhaupt, E. J. Baerends, C. Fonseca Guerra, S. J. A. van Gisbergen, J. G. Snijders, T. Ziegler, *J. Comput. Chem.* **22** (2001) 931
35. E. van Lenthe, E. J. Baerends, *J. Comput. Chem.* **24** (2003) 1142
36. M. Swart, J. G. Snijders, *Theor. Chem. Acc.* **110** (2003) 34
37. A. Klamt, V. Jonas, *J. Chem. Phys.* **105** (1996) 9972
38. A. Klamt, *J. Chem. Phys.* **99** (1995) 2224
39. A. Klamt, G. Schuurmann, *J. Chem. Soc., Perkin Trans. 2* (1993) 799
40. M. Swart, F. M. Bickelhaupt, *J. Comput. Chem.* **29** (2008) 724
41. M. Swart, F. M. Bickelhaupt, *Int. J. Quantum Chem.* **106** (2006) 2536
42. A. J. Boone, C. H. Chang, S. N. Greene, T. Herz, N. G. J. Richards, *Coord. Chem. Rev.* **238–239** (2003) 291
43. J. C. Noveron, M. M. Olmstead, P. K. Mascharak, *Inorg. Chem.* **37** (1998) 1138
44. G. D. Fallon, B. M. Gatehouse, P. J. Minari, K. S. Murray, B. O. West, *J. Chem. Soc., Dalton Trans.* (1984) 2733
45. N. Govindaswamy, D. A. Quarless, S. A. Koch, *J. Am. Chem. Soc.* **117** (1995) 8468
46. D. Sellmann, T. Hofmann, F. Knoch, *Inorg. Chim. Acta* **224** (1994) 61
47. D. Sellmann, H. Kunstmann, F. Knoch, M. Moll, *Inorg. Chem.* **27** (1988) 4183

48. D. Sellmann, W. Soglowek, F. Knoch, G. Ritter, J. Dengler, *Inorg. Chem.* **31** (1992) 3711
49. D. Sellmann, J. Utz, N. Blum, F. W. Heinemann, *Coord. Chem. Rev.* **192** (1999) 607
50. M. Radoń, E. Broclawik, *J. Chem. Theory Comput.* **3** (2007) 728
51. S. Ye, F. Neese, *Inorg. Chem.* **49** (2010) 772
52. A. Ghosh, T. Vangberg, E. Gonzalez, P. Taylor, *J. Porphyr. Phthalocya.* **5** (2001) 345
53. A. Ghosh, B. J. Persson, P. R. Taylor, *J. Biol. Inorg. Chem.* **8** (2003) 507
54. M.-S. Liao, S. Scheiner, *J. Comput. Chem.* **23** (2002) 1391.



SUPPLEMENTARY MATERIAL TO
**Spin state relaxation of iron complexes:
The case for OPBE and S12g**

MAJA GRUDEN¹, STEPAN STEPANOVIĆ^{2#} and MARCEL SWART^{3,4*}

¹Faculty of Chemistry, University of Belgrade, Studentski Trg 12–16, 11001 Belgrade, Serbia,

²Center for Chemistry, ICTM, University of Belgrade, Njegoševa 12, 11001 Belgrade, Serbia,

³Institut de Química Computacional i Catalisi (IQCC) and Departament de Química,
Universitat de Girona, Campus Montilivi, Facultat de Ciències, 17071 Girona, Spain and

⁴Institució Catalana de Recerca i Estudis Avançats (ICREA),
Pg. Lluís Companys 23, 08010 Barcelona, Spain

J. Serb. Chem. Soc. 80 (11) (2015) 1399–1410

TABLE S-I. Selected bond lengths (Å) for compound **1** at the low (ground state), intermediate and high spin state

Data		Fe–N _{NCO}	Fe–N _{pyr}	Fe–S
X-Ray ^{a1}		1.954	2.000	2.230
OPBE	Doublet	1.947	1.980	2.195
	Quartet	2.150	2.051	2.262
	Sextet	2.160	2.243	2.342
OPBE cosmo	Doublet	1.945	1.981	2.203
	Quartet	2.140	2.022	2.279
	Sextet	2.133	2.208	2.378
S12g	Doublet	1.989	1.984	2.238
	Quartet	2.233	2.069	2.291
	Sextet	2.257	2.230	2.357
S12g cosmo	Doublet	1.986	1.984	2.249
	Quartet	2.240	2.054	2.303
	Sextet	2.259	2.196	2.378

^aCSD entry VACBOQ

TABLE S-II. Selected bond lengths (Å) for compound **2** at the low, intermediate (ground state) and high spin state

Data		Fe–Cl	Fe–S1	Fe–S2	Fe–N1	Fe–N2
X-Ray ^{a2}		2.336	2.195	2.187	1.979	2.031
OPBE	Doublet	2.277	2.203	2.203	1.947	1.947
	Quartet	2.418	2.232	2.232	1.988	1.988
	Sextet	2.286	2.365	2.365	2.140	2.140

*Corresponding author. E-mail: marcel.swart@icrea.cat

TABLE S-II. Continued

Data		Fe–Cl	Fe–S1	Fe–S2	Fe–N1	Fe–N2
OPBE cosmo	Doublet	2.184	2.157	2.157	1.908	1.908
	Quartet	2.264	2.213	2.213	1.971	1.971
	Sextet	2.213	2.342	2.342	2.154	2.154
S12g	Doublet	2.217	2.165	2.165	1.911	1.911
	Quartet	2.402	2.208	2.208	1.957	1.957
	Sextet	2.274	2.345	2.345	2.134	2.134
S12g cosmo	Doublet	2.226	2.194	2.194	1.937	1.937
	Quartet	2.287	2.239	2.239	2.002	2.002
	Sextet	2.232	2.368	2.368	2.161	2.161

^aCSD entry DABMUOTABLE S-III. Selected bond lengths (Å) for compound **3** at the low, intermediate and high spin state (ground state)

Data		Fe–N _{(CH₂)₃}	Fe–N _{imidazole}	Fe–S1	Fe–S2	Fe–S3
X-Ray ^{a3}		2.211	2.148	2.297	2.304	2.307
OPBE	Doublet	2.100	2.079	2.211	2.206	2.209
	Quartet	2.086	2.069	2.317	2.283	2.391
	Sextet	2.519	2.256	2.329	2.333	2.338
OPBE cosmo	Doublet	2.040	2.020	2.181	2.157	2.162
	Quartet	2.025	2.046	2.241	2.272	2.342
	Sextet	2.426	2.314	2.298	2.317	2.304
S12g	Doublet	2.045	2.030	2.179	2.156	2.167
	Quartet	2.028	2.031	2.276	2.369	2.246
	Sextet	2.430	2.244	2.324	2.310	2.319
S12g cosmo	Doublet	2.095	2.063	2.210	2.208	2.205
	Quartet	2.078	2.073	2.287	2.292	2.382
	Sextet	2.481	2.303	2.312	2.336	2.334

^aCSD entry ZAZNUJTABLE S-IV. Selected bond lengths (Å) for compound *trans*-**4** at the low (ground state), intermediate and high spin state

Data		Fe–S _b	Fe–S _{nb}	Fe–S _b	Fe–S _{nb}	Fe–CO	Fe–N _{ax}
X-Ray ^{a4}		2.241	2.304	2.241	2.304	1.749	2.074
OPBE	Singlet	2.187	2.262	2.185	2.272	1.713	2.087
	Triplet	2.492	2.235	2.464	2.267	1.744	2.168
	Quintet	2.484	2.395	2.463	2.430	1.955	2.350
OPBE cosmo	Singlet	2.196	2.267	2.194	2.274	1.700	2.082
	Triplet	2.521	2.265	2.447	2.290	1.727	2.138
	Quintet	2.474	2.425	2.457	2.458	1.956	2.292
S12g	Singlet	2.251	2.320	2.247	2.329	1.732	2.119
	Triplet	2.590	2.340	2.587	2.313	1.757	2.193
	Quintet	2.564	2.439	2.545	2.482	1.962	2.382
S12g cosmo	Singlet	2.262	2.328	2.259	2.336	1.719	2.115
	Triplet	2.563	2.421	2.559	2.380	1.736	2.148
	Quintet	2.546	2.476	2.537	2.521	1.964	2.314

^aCSD entry VADPEV

TABLE S-V. Selected bond lengths (\AA) for compound *trans*-**5** at the low (ground state), intermediate and high spin state

Data		Fe–S _{nb}	Fe–S _b	Fe–S _b	Fe–S _{nb}	Fe–PMe ₃	Fe–N _{ax}
X-Ray ^{a5}		2.308	2.230	2.230	2.308	2.216	2.066
OPBE	Singlet	2.252	2.171	2.163	2.262	2.201	2.082
	Triplet	2.221	2.219	2.219	2.230	2.466	2.461
	Quintet	2.396	2.430	2.544	2.402	2.578	2.366
OPBE cosmo	Singlet	2.252	2.176	2.167	2.260	2.209	2.077
	Triplet	2.232	2.216	2.212	2.244	2.545	2.398
	Quintet	2.389	2.441	2.528	2.406	2.673	2.319
S12g	Singlet	2.310	2.231	2.220	2.326	2.243	2.109
	Triplet	2.287	2.486	2.613	2.287	2.305	2.227
	Quintet	2.474	2.531	2.562	2.468	2.492	2.394
S12g cosmo	Singlet	2.311	2.237	2.226	2.329	2.256	2.108
	Triplet	2.310	2.512	2.627	2.305	2.319	2.193
	Quintet	2.485	2.499	2.586	2.490	2.564	2.347

^aCSD entry HEYNIITABLE S-VI. Selected bond lengths (\AA) for compound *meso*-**6** at the low, intermediate and high spin state (ground state)

Data		Fe–S _{nb}	Fe–S _b	Fe–S _b	Fe–S _{nb}	Fe–N _{ax}	Fe–NH ₃
X-Ray ^{a6}		2.587	2.395	2.395	2.587	2.189	2.395
OPBE	Singlet	2.255	2.174	2.174	2.255	2.017	2.025
	Triplet	2.235	2.249	2.249	2.235	2.334	2.503
	Quintet	2.322	2.565	2.565	2.322	2.326	2.296
OPBE cosmo	Singlet	2.254	2.174	2.174	2.254	2.032	2.028
	Triplet	2.242	2.252	2.252	2.242	2.402	2.414
	Quintet	2.354	2.536	2.536	2.354	2.349	2.271
S12g	Singlet	2.305	2.231	2.231	2.305	2.057	2.065
	Triplet	2.278	2.308	2.308	2.278	2.351	2.411
	Quintet	2.353	2.674	2.674	2.353	2.312	2.260
S12g cosmo	Singlet	2.305	2.233	2.233	2.305	2.069	2.069
	Triplet	2.285	2.311	2.311	2.285	2.354	2.414
	Quintet	2.388	2.625	2.625	2.388	2.310	2.247

^aCSD entry YAJLEATABLE S-VII. Selected bond lengths (\AA) for compound *meso*-**7** at the low, intermediate and high spin state (ground state)

Data		Fe–N ₂ H ₄	Fe–S _{nb}	Fe–S _b	Fe–S _{nb}	Fe–S _b	Fe–N _{ax}
X-Ray ^{a6}		2.193	2.602	2.392	2.602	2.392	2.254
OPBE	Singlet	2.048	2.256	2.175	2.256	2.175	2.036
	Triplet	2.467	2.237	2.250	2.237	2.250	2.384
	Quintet	2.263	2.323	2.578	2.323	2.578	2.341
OPBE cosmo	Singlet	2.053	2.254	2.179	2.254	2.179	2.043
	Triplet	2.528	2.237	2.251	2.237	2.251	2.386
	Quintet	2.270	2.349	2.548	2.349	2.548	2.331

TABLE S-VII. Continued

Data		Fe–N ₂ H ₄	Fe–S _{nb}	Fe–S _b	Fe–S _{nb}	Fe–S _b	Fe–N _{ax}
S12g	Singlet	2.093	2.314	2.229	2.314	2.229	2.072
	Triplet	2.425	2.286	2.303	2.286	2.303	2.377
	Quintet	2.237	2.361	2.682	2.361	2.682	2.353
S12g cosmo	Singlet	2.098	2.312	2.234	2.312	2.234	2.076
	Triplet	2.469	2.286	2.307	2.286	2.307	2.355
	Quintet	2.251	2.384	2.634	2.384	2.634	2.296

^aCSD entry YAJKUPTABLE S-VIII. OPBE/TZP ligand binding energy (kcal mol⁻¹) for *trans/meso*-(Fe(NH)S₄)L with respect to energy of infinitely separated *trans*-Fe(NH)S₄ (triplet ground state) and ligand (in parentheses corrected for basis set superposition error)

ligand L	Singlet	Triplet	Quintet
<i>trans</i>			
CO (4)	-32.0 (-29.8)	-8.6 (-6.9)	2.7 (3.8)
PM ₃ (5)	-15.3 (-11.6)	1.0 (3.9)	4.7 (7.1)
NH ₃ (6)	-3.1 (-1.6)	4.6 (5.5)	5.3 (6.3)
N ₂ H ₄ (7)	-3.5 (-1.8)	-1.9 (-1.5)	5.2 (6.1)
<i>meso</i>			
CO (4)	-29.2 (-27.0)	4.2 (5.8)	9.6 (11.1)
PM ₃ (5)	-12.2 (-8.5)	7.5 (10.3)	5.4 (7.8)
NH ₃ (6)	-0.6 (0.9)	9.7 (10.7)	6.0 (6.9)
N ₂ H ₄ (7)	-1.0 (0.8)	9.3 (10.3)	6.6 (7.7)

TABLE S-IX. Selected bond lengths (Å) for compound **8** at the low, intermediate and high spin state (ground state)

Data		Fe–Cl	Fe–N
X-Ray ^{a7}		2.203	2.015
OPBE	Doublet	2.223	1.994
	Quartet	2.387	2.011
	Sextet	2.289	2.090
OPBE cosmo	Doublet	2.134	1.987
	Quartet	2.240	2.019
	Sextet	2.197	2.107
S12g	Doublet	2.185	1.985
	Quartet	2.386	2.005
	Sextet	2.277	2.093
S12g cosmo	Doublet	2.168	1.995
	Quartet	2.251	2.026
	Sextet	2.207	2.107

^aCSD entry QEFWUV

TABLE S-X. Selected bond lengths (\AA) for compound **9** at the low, intermediate (ground state) and high spin state

Data		Fe–Cl	Fe–N
X-Ray ^{a8}		2.326	1.931
OPBE	Doublet	2.197	1.915
	Quartet	2.366	1.936
	Sextet	2.256	2.029
OPBE cosmo	Doublet	2.130	1.904
	Quartet	2.242	1.936
	Sextet	2.188	2.041
S12g	Doublet	2.161	1.904
	Quartet	2.364	1.927
	Sextet	2.244	2.031
S12g cosmo	Doublet	2.163	1.916
	Quartet	2.254	1.947
	Sextet	2.198	2.044

^aCSD entry NEGJIT

REFERENCES

1. J. C. Noveron, M. M. Olmstead, P. K. Mascharak, *Inorg. Chem.* **37** (1998) 1138
2. G. D. Fallon, B. M. Gatehouse, P. J. Minari, K. S. Murray, B. O. West, *J. Chem. Soc. Dalton Trans.* (1984) 2733
3. N. Govindaswamy, D. A. Quarless, S. A. Koch, *J. Am. Chem. Soc.* **117** (1995) 8468
4. D. Sellmann, H. Kunstmänn, F. Knoch, M. Moll, *Inorg. Chem.* **27** (1988) 4183
5. D. Sellmann, T. Hofmann, F. Knoch, *Inorg. Chim. Acta* **224** (1994) 61
6. D. Sellmann, W. Soglowek, F. Knoch, G. Ritter, J. Dengler, *Inorg. Chem.* **31** (1992) 3711
7. W. Morris, B. Voloskiy, S. Demir, F. Gándara, P. L. McGrier, H. Furukawa, D. Cascio, J. F. Stoddart, O. M. Yaghi, *Inorg. Chem.* **51** (2012) 6443
8. T. Goslinski, C. Zhong, M. J. Fuchter, C. L. Stern, A. J. P. White, A. G. M. Barrett, B. M. Hoffman, *Inorg. Chem.* **45** (2006) 3686.



Light-induced oxidative transformation of diphenylamine on ZrO₂. Synergism by ZnO and ZnS

CHOCKALINGAM KARUNAKARAN*, SWAMINATHAN KARUTHAPANDIAN**
and PAZHAMILAI VINAYAGAMOORTHY

Department of Chemistry, Annamalai University, Annamalainagar 608002, Tamilnadu, India

(Received 24 August, revised 13 December, accepted 15 December 2014)

Abstract: Diphenylamine (DPA) in ethanol on the surface of ZrO₂ undergoes photoinduced oxidative transformation yielding *N*-phenyl-*p*-benzoquinonimine (PBQI). The light-induced transformation on ZrO₂ enhanced with DPA concentration, ZrO₂-loading, airflow rate and photon flux. The formation of PBQI on ZrO₂ is larger on illumination at 254 nm than at 365 nm. The ZrO₂ is reusable without any treatment. The mechanism of light-induced oxidative transformation of DPA on ZrO₂ is discussed with an appropriate kinetic law. ZnO and ZnS enhance the UV light-induced transformation of DPA on ZrO₂, indicating synergism.

Keywords: photooxidation; wide band gap; sub-band gap illumination; photocatalysis.

INTRODUCTION

Semiconductor-photocatalyzed selective organic oxidative transformations have gained interest because of their environmental benign nature and the reviews by Lang *et al.*,¹ Palmisano *et al.*² and Shiraishi and Hirai³ present the different kinds of organic transformations performed photocatalytically. TiO₂-based materials are widely used as photocatalysts for organic synthesis.^{1–3} Like TiO₂, ZrO₂ is a nontoxic and photostable IV–VI semiconductor but with a larger band gap energy (\approx 5 eV). However, this large band gap enables the photocatalytic splitting of water⁴ and reduction of CO₂.^{5,6} The band gap of combustion synthesized ZrO₂ is not large (3.5 eV) and Madras and coworkers⁷ reported degradation of dyes with illumination at 365 nm; defects in the crystal lattice are the likely reason for the decreased band gap. Here, for the first time, the photo-induced oxidative transformation of diphenylamine (DPA) on untreated ZrO₂,

* Corresponding author. E-mail: karunakaranc@rediffmail.com

** Present address: Department of Chemistry, VHNSN College, Virudhunagar 626001, Tamilnadu, India.

doi: 10.2298/JSC140824122K

which is reusable, is reported. DPA is used in post-harvest treatment of apple and pear⁸ and the photosensitized oxidation of DPA is known; cyanoanthracenes⁹ and benzophenone¹⁰ are some of the photosensitizers used. The unsensitized photo-oxidation of DPA to *N*-phenyl-*p*-benzoquinonimine (PBQI) is slow.¹¹ The chemical transformation of DPA was studied in the absence and presence of ZrO₂ and the difference in the rates provides the rate of PBQI formation on ZrO₂. The oxidative transformation on ZrO₂ surface was investigated under UV light and under natural sunlight at different experimental conditions to obtain the kinetic law and to elucidate the reaction mechanism. ZnO is a promising II–VI semiconductor photocatalyst with a band gap of 3.2 eV and large excitonic binding energy (60 meV) at room temperature. Although the band gap energy of ZnO is not different from that of TiO₂ and the conduction band (CB) energy levels of the two semiconductors do not differ significantly and so are the valence band (VB) edges, there are reports that ZnO is a better photocatalyst than TiO₂.¹² ZnS is also a II–VI semiconductor but with a wide band gap (\approx 3.6 eV). Semiconductor mixtures are reported to enhance photocatalytic mineralization of organic molecules^{13,14} and here the photoconversion of DPA to PBQI on ZrO₂ was enhanced on mixing ZnO or ZnS with ZrO₂.

EXPERIMENTAL

Materials and measurements

ZrO₂, ZnS and ZnO (Merck) were used as received and their specific surface areas, obtained by BET method, were 15.1, 7.7 and 12.2 m² g⁻¹, respectively.¹⁵ The mean particle sizes (*t*) of ZrO₂, ZnS and ZnO, obtained using the formula $t = 6/\rho S$, where ρ is the material density and *S* is the specific surface area, are 68, 190 and 87 nm, respectively. The UV–visible diffuse reflectance spectra (DRS) of the semiconductors were obtained using a Shimadzu UV-2600 spectrophotometer with an ISR-2600 integrating sphere attachment. The Kubelka–Munk (KM) plots provide the band gaps of ZnS and ZnO as 3.57 and 3.15 eV, respectively. Potassium tris(oxalato)ferrate(III), K₃[Fe(C₂O₄)₃]·3H₂O, was prepared using a standard procedure.¹⁶ DPA, AR (Merck) was used as received. The infrared spectra were recorded on a Nicolet iS5 FT-IR spectrometer. Commercial ethanol was purified by distillation with calcium oxide.

UV light-driven transformation

The UV light-driven transformation on ZrO₂ was performed in a multilamp photoreactor equipped with eight 8 W mercury UV lamps (Sankyo Denki, Japan) emitting at 365 nm. The lamps were shielded by a highly polished anodized aluminum reflector. Four cooling fans mounted at the bottom of the reactor dissipated the generated heat. A borosilicate glass tube of 15-mm inner diameter was used as the reaction vessel and was placed at the center of the photoreactor. The UV light-induced reaction was also studied with a micro-photoreactor fixed with a 6 W 254 nm low-pressure mercury lamp and a 6 W 365 nm mercury lamp. Quartz and borosilicate glass tubes were employed as reaction vessels for 254 and 365 nm lamps, respectively. The light intensity (*I*) was measured by ferrioxalate actinometry. The volume of the reaction solution was always maintained as 25 mL in the multilamp photoreactor and 10 mL in the micro-photoreactor. Air was bubbled through the solution at a flow rate measured by

the soap bubble method. The UV–Visible spectra were obtained with a Hitachi U-2001 UV–Vis spectrophotometer. The solution was diluted 5-times to lower the absorbance to the Beer–Lambert law limit. The PBQI formed was estimated from its absorbance at 450 nm.

Sunlight-driven transformation

The sunlight-induced transformation on ZrO_2 was performed under clear sky in summer (March–July) at 11.30 am–12.30 pm. The solar irradiance (440 W m^{-2}) was measured using a Global pyranometer, supplied by Industrial Meters, Bombay, India. Ethanolic solutions of DPA of the required concentration were prepared afresh and taken in wide cylindrical glass vessels of uniform diameter. The entire bottom of the vessel was covered with ZrO_2 powder. Air was bubbled using a micro-pump without disturbing the ZrO_2 bed. The volume of DPA solution was 25 mL and the loss of solvent because of evaporation was compensated periodically. The formed PBQI was estimated spectrophotometrically.

RESULTS AND DISCUSSION

UV light-induced oxidative transformation on ZrO_2

The UV light-promoted oxidative transformation of DPA in ethanol on ZrO_2 surface was realized by bubbling air in a multilamp photoreactor fixed with UV lamps emitting at 365 nm. The UV-visible spectra of the DPA solution recorded at different illumination times show the formation of PBQI ($\lambda_{\max} = 450 \text{ nm}$). The time spectra are displayed in Fig. 1. The illuminated solution is EPR silent showing the absence of the formation of diphenylnitroxide. In addition, a thin layer chromatographic experiment revealed the formation of a single product. The illuminated DPA solution was evaporated to dryness after recovery of the particulate ZrO_2 and the solid was dissolved in chloroform to develop the chromatogram on a silica gel G-coated plate using benzene as eluent. The PBQI formed was estimated from its absorbance at 450 nm using the reported molar absorptivity.^{17,18} The linear increase of the concentration of PBQI with illumination time, as seen in the inset to Fig. 1, provides the PBQI formation rate and the

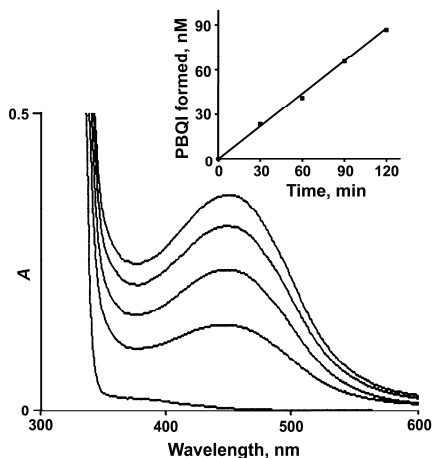


Fig. 1. UV light-induced PBQI formation with ZrO_2 in ethanol: the UV-visible spectra of reaction solution (5-times diluted) at 0, 30, 60, 90 and 120 min (increasing A); $[DPA] = 20 \text{ mM}$, ZrO_2 -loading = 1.0 g, airflow rate = 7.8 mL s^{-1} , $I = 13.7 \times 10^{-24} \text{ J L}^{-1} \text{ s}^{-1}$, volume of reaction solution = 25 mL; inset: Linear increase of formed PBQI with illumination time.

rates were reproducible to $\pm 6\%$. The photoformation of PBQI by direct photo-oxidation of DAP in the absence of ZrO_2 was slow¹¹ and the rate of PBQI formation on ZrO_2 was obtained by measuring the rates of PBQI formation in the presence and absence of ZrO_2 . The enhancement of PBQI formation on ZrO_2 with concentration of DPA is displayed in Fig. 2. The observed enhancement conforms to Langmuir–Hinshelwood (LH) kinetics with respect to the DPA concentration. The rate of surface reaction increased with ZrO_2 loading in the DPA solution and the rate reached a limit at a high ZrO_2 -loading, as could be seen in Fig. 3. A study of PBQI formation on ZrO_2 as a function of the airflow rate showed enhancement of the surface reaction by oxygen and the rate dependence on the airflow rate conformed to the LH kinetic law, as could be seen in Fig. 4.

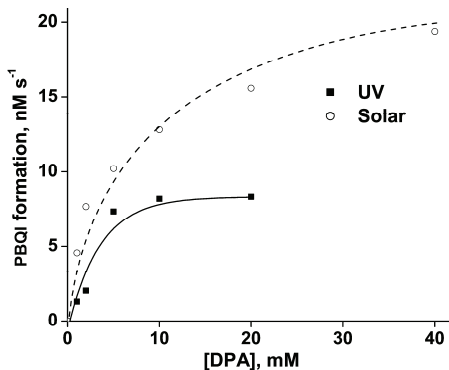


Fig. 2. Light-induced PBQI formation on ZrO_2 as a function of DPA concentration; ZrO_2 -loading = 1.0 g, volume of reaction solution = 25 mL; UV: $\lambda = 365$ nm, $I = 13.7 \times 10^{-24}$ J L $^{-1}$ s $^{-1}$, airflow rate = 7.8 mL s $^{-1}$; Solar: bed area = 11.36 cm 2 , airflow rate = 4.6 mL s $^{-1}$.

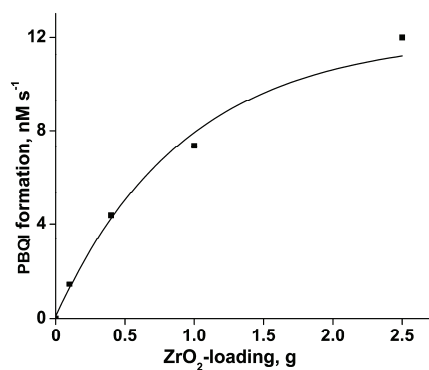


Fig. 3. Photoinduced PBQI formation on ZrO_2 at different ZrO_2 -loading; [DPA] = 5.0 mM, airflow rate = 7.8 mL s $^{-1}$, $\lambda = 365$ nm, $I = 13.7 \times 10^{-24}$ J L $^{-1}$ s $^{-1}$, volume of reaction solution = 25 mL.

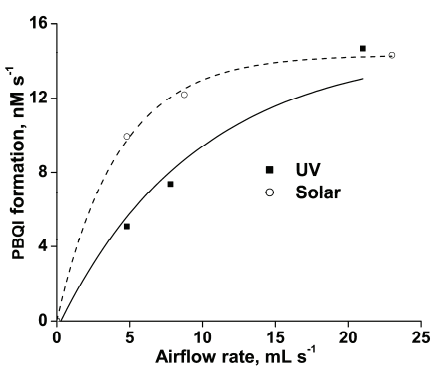


Fig. 4. Photoformation of PBQI on ZrO_2 as a function of airflow rate; [DPA] = 5.0 mM, ZrO_2 -loading = 1.0 g, volume of reaction solution = 25 mL; UV: $\lambda = 365$ nm, $I = 13.7 \times 10^{-24}$ J L $^{-1}$ s $^{-1}$; solar: bed area = 11.36 cm 2 .

The formation of PBQI on ZrO_2 was also determined without bubbling air but the solution was not deoxygenated. The dissolved oxygen itself enabled the light-induced surface reaction, but the reaction was slow. PBQI formation on ZrO_2 was studied at different intensities of illumination. The chemical transformation was studied with two, four and eight lamps and the angles sustained by adjacent lamps were 180, 90 and 45°, respectively. The dependence of the surface reaction rate on photon flux is displayed in Fig. 5. PBQI was not formed in the absence of illumination. A study of PBQI formation on ZrO_2 under UV-A and UV-C light, using a 6 W 365 nm mercury lamp ($I = 10.0 \times 10^{-24} \text{ J L}^{-1} \text{ s}^{-1}$) and a 6 W 254 nm low-pressure mercury lamp ($I = 4.09 \times 10^{-24} \text{ J L}^{-1} \text{ s}^{-1}$), separately in a micro-photoreactor under identical conditions showed that UV-C light was more efficient than UV-A light in inducing the organic transformation on ZrO_2 . The rate of PBQI formation with UV-A and UV-C light were 9.2 and 20.6 nM s^{-1} , respectively ([DPA] = 5.0 mM, ZrO_2 suspended: 1.0 g, airflow rate = 7.8 mL s^{-1}). The ZrO_2 retained its activity on usage. Reuse of ZrO_2 showed sustainable light-induced PBQI formation. The azide ion (5 mM), a singlet oxygen quencher, failed to suppress PBQI formation, showing the absence of an involvement of singlet oxygen in the light-induced organic transformation on ZrO_2 . This finds literature support; Fox and Chen¹⁹ ruled out the possibility of singlet oxygen in the TiO_2 -photocatalyzed olefin-to-carbonyl oxidative cleavage.

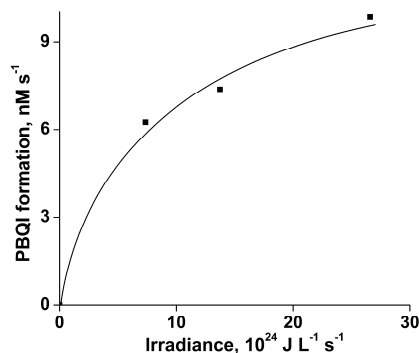


Fig. 5. Influence of photon flux on ZrO_2 -promoted PBQI formation; [DPA] = 5.0 mM, ZrO_2 -loading = 1.0 g, airflow rate = 7.8 mL s^{-1} , $\lambda = 365 \text{ nm}$, volume of reaction solution = 25 mL.

Sunlight-induced oxidative transformation on ZrO_2

The ZrO_2 -mediated oxidative transformation of DPA into PBQI also occurs under natural sunlight. The UV-visible spectrum of sun-shined DPA solution in ethanol in the presence of ZrO_2 and air was similar to that with UV light ($\lambda_{\text{max}} = 450 \text{ nm}$). Furthermore, the sun-shined solution was EPR silent revealing the absence of diphenylnitroxide. In addition, TLC analysis shows the formation of a single product. Determination of the solar irradiance (W m^{-2}) showed fluctuation of the sunlight intensity during the experiment, even under a clear sky. Hence, the solar experiments under different reaction conditions were performed in a set

to maintain the quantum of sunlight incident on a unit area the same. This enabled comparison of the solar results. A pair of solar experiments performed simultaneously under identical reaction conditions yielded results within $\pm 6\%$, which was also the case on different days. The effect of the operational parameters on the solar-promoted oxidative transformation was studied by performing the given set of experiments simultaneously and the results displayed in each figure represent identical solar irradiance. The rate of PBQI formation was obtained by shining the DPA solution on ZrO_2 bed for 60 min. The dependence of PBQI formation rate on the concentration of DPA is shown in Fig. 2. The observed increase of PBQI formation with DPA concentration is characteristic of the LH kinetic law. The double reciprocal plot of the PBQI formation rate *versus* DPA concentration was a straight line with a positive *y*-intercept (figure not shown), which confirmed the LH kinetic model. The rates of PBQI formation on ZrO_2 at different airflow rates are shown in Fig. 4. The observed enhancement of the PBQI formation by oxygen revealed that the surface reaction also conformed to LH kinetics with respect to oxygen. The double reciprocal plot of reaction rate *versus* airflow rate was linear with a finite *y*-intercept (figure not presented). The PBQI formation on ZrO_2 was measured without bubbling air but the solution was not deoxygenated. The dissolved oxygen was sufficient to effect the chemical transformation on ZrO_2 during the experimental period. However, the transformation was slow. The PBQI formation on ZrO_2 increased linearly with the apparent area of the ZrO_2 -bed, as could be seen in Fig. 6. The oxidative transformation did not occur in the absence of sunlight. ZrO_2 does not lose its activity on usage. Reuse of ZrO_2 showed sustainable activity.

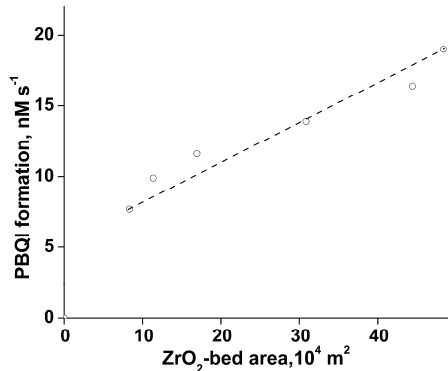


Fig. 6. Dependence of sunlight-driven PBQI formation rate on ZrO_2 -bed area; [DPA] = 5.0 mM, ZrO_2 -loading = 1.0 g, airflow rate = 4.6 mL s^{-1} , volume of reaction solution = 25 mL.

Mechanism

The DRS of ZrO_2 is presented in Fig. 7, from which it could be observed that the absorption edge of the employed pristine ZrO_2 was 320 nm. Illumination of ZrO_2 with light of wavelength 365 nm is energetically unviable to bring about

band gap excitation and hence the operation of the usual semiconductor-photocatalysis mechanism is ruled out. DPA is likely to be adsorbed on the surface of ZrO_2 . The FT-IR spectra of DPA and DPA adsorbed on ZrO_2 are displayed in Fig. 8. The shift of the $>\text{N}-\text{H}$ stretching vibrational frequency from 3408 to 3404 cm^{-1} and bending vibrational frequency from 1595 to 1591 cm^{-1} indicate binding of DPA with ZrO_2 through the amine hydrogen. The DRS of DPA-adsorbed ZrO_2 shows a shift of the absorption edge to the visible region (413 nm; Fig. 7). This absorption is likely due to electronic excitation of the adsorbed DPA. The excited electron may move to Zr^{4+} resulting in the formation of the radical cation Ph_2NH^+ . The reduced form of Zr^{4+} (*i.e.*, Zr^{3+}) may lose an electron to the adsorbed molecular oxygen yielding superoxide radical ion ($\text{O}_2^{\bullet-}$). The reaction of the formed radical cation with the superoxide radical ion may yield the product PBQI.

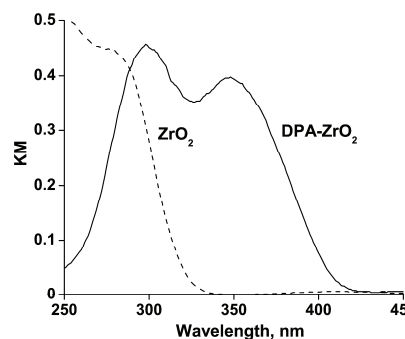


Fig. 7. DRS of bare ZrO_2 and DPA-adsorbed ZrO_2 .

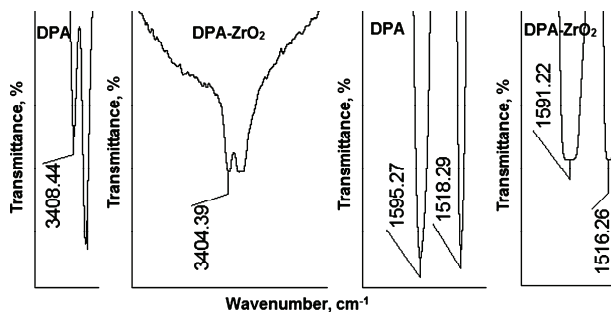


Fig. 8. FT-IR spectra of DPA and DPA-adsorbed ZrO_2 .

Ali *et al.*²⁰ studied the photodegradation of methylene blue on ZnO films, deposited on glass slides by either the hydrothermal method or the magnetron sputtering technique, with UV-C light and the results conformed to the LH kinetic law. Leaching of zinc due to photocatalysis was reported under oxygen limited conditions but the ZnO films were observed to be more stable under oxygen-rich conditions. It was suggested that the oxygen from the ZnO lattice

was removed and used in the radical initiation and propagation phases of the photocatalysis under oxygen-limited conditions. That is, the observed deformation of the ZnO lattice over time was ascribed to the use of lattice oxygen in the photocatalytic process. Oxygen-rich conditions either minimize the release of or replace the last ZnO lattice oxygen and the authors proposed the operation of a Mars Van Krevelen (MVK) type mechanism in the photocatalytic degradation of methylene blue under oxygen-limited conditions. In a similar study with UV-A and UV-C light, the same authors suggested the predominance of the MVK mechanism under UV-C illumination.²¹ However, Delmon²² stated that the re-oxidation step in the MVK mechanism is often too slow and consequently the catalysts become reduced in the corresponding reduction–oxidation cycle. That is, the photocatalytic activity is decreased remarkably on reuse. Furthermore, irrespective of the operative mechanism, leaching of zinc or a small decrease in the photocatalytic activity of ZnO on repeated reuse is well known.^{23,24} However, ZrO₂ is chemically unreactive and hence operation of a MVK type mechanism in the present study is unlikely. In addition, the fact that ZrO₂ shows sustainable photocatalytic activity (PBQI formation rate was not lowered on reuse of ZrO₂) does not support the operation of a MVK type mechanism in the title reaction. Serpone and co-workers^{25–28} stated that both the LH and Eley–Rideal (ER) models are applicable for semiconductor photocatalytic reactions. The LH model presents the adsorption of both the reactant molecules on the surface²⁹ while the ER model represents adsorption of one of the reactants on the surface; the other reactant molecule interacts with adsorbed reactant molecule to form the product. The LH model requires saturation kinetics with respect to both the reactants whereas the ER model demands saturation kinetics with respect to one of the reactants and first order dependence of the reaction rate with respect to the other reactant. The studied photocatalyzed reaction on ZrO₂ surface shows saturation kinetics with respect to DPA as well as oxygen (Figs. 2 and 4) and hence operation of the ER reaction mechanism is ruled out. Although Bansal and Sidhu³⁰ stated that singlet oxygen is the oxidant in dye-sensitized photooxidation of DPA, this has been ruled out in the present photocatalytic transformation as azide ion does not suppress the formation of PBQI (*vide supra*); de Lasa *et al.*³¹ also proposed the formation of reactive species superoxide radical anion in semiconductor photocatalyzed reactions.

Kinetic law

The heterogeneous photoinduced reaction occurring in a continuously stirred tank reactor (CSTR) conforms to the kinetic law:³²

$$\text{Rate of PBQI formation on ZrO}_2 = \frac{kK_1K_2SIC[\text{DPA}]\gamma}{(1+K_1[\text{DPA}]) \cdot (1+K_2\gamma)} \quad (1)$$

where K_1 and K_2 are the adsorption coefficients of DPA and O_2 on the illuminated ZrO_2 surface, k is the specific rate of oxidation of DPA on the ZrO_2 surface, γ is the airflow rate, S is the specific surface area of ZrO_2 , C is the amount of ZrO_2 suspended per liter and I is the light intensity. The data-fit to the LH kinetic curve, drawn using a computer program,³² confirmed the kinetic law (Figs. 2 and 4). The linear double reciprocal plots of surface reaction rate *versus* the DPA concentration and the airflow rate supports the LH kinetic law. The data-fit provides the adsorption coefficients K_1 and K_2 as 76 L mol^{-1} and $0.039 \text{ mL}^{-1} \text{ s}$, respectively, and the specific reaction rate k as $2.75 \times 10^9 \text{ mol L m}^{-2} \text{ J}^{-1}$. However, the rate of PBQI formation on ZrO_2 surface fails to increase linearly with ZrO_2 -loading. This is because of the high ZrO_2 loading. At high ZrO_2 loadings, the surface area of the ZrO_2 exposed to illumination does not correspond to the weight of ZrO_2 . The quantity of ZrO_2 used is beyond the critical amount corresponding to the volume of the reaction solution and reaction vessel; the whole quantity of ZrO_2 is not exposed to light. The photoinduced transformation lacks linear dependence on the illumination intensity; a lower than first power dependence of a surface-photoreaction rate on the light intensity at high photon flux is well known.³³

Synergism by ZnO and ZnS

Vectorial transfer of electrons and holes from one semiconductor to another is possible in semiconductor mixtures under band gap-illumination. This charge separation enhances the photocatalytic activity.^{13,14} However, what was observed in this study was enhanced phototransformation due to the presence of the semiconductor ZnO or ZnS nanoparticles with ZrO_2 nanoparticles; the wavelength of illumination could effect the band gap excitation of ZnO and ZnS but not ZrO_2 . The enhanced formation of PBQI with ZrO_2 mixed with ZnO or ZnS is displayed in Fig. 9; the two nanoparticles were kept under suspension and under continuous motion by bubbling air through the illuminated solution. Aggregation of nanoparticles under suspension is known.³⁴ The particle size distribution of ZrO_2 , ZnO and ZnS under suspension, determined by the light scattering method, are presented in Fig. 10. Examination of Fig. 10 along with the size of the particles obtained from the XRD and BET methods revealed aggregation of the nanoparticles. As observed in the individual ZrO_2 , ZnO and ZnS suspensions, aggregation in the ZrO_2 – ZnO and ZrO_2 – ZnS mixtures under suspension is likely, and both ZrO_2 and ZnO or ZnS nanoparticles are likely to be present in the aggregate. This may lead to transfer of the generated hole from the illuminated ZnO or ZnS to the DPA molecule adsorbed on ZrO_2 surface, resulting in enhanced photooxidation. The densities and particle sizes of ZrO_2 , ZnO and ZnS are different and this may be a reason for not observing maximum enhanced photo-oxidation at 50 % composition.

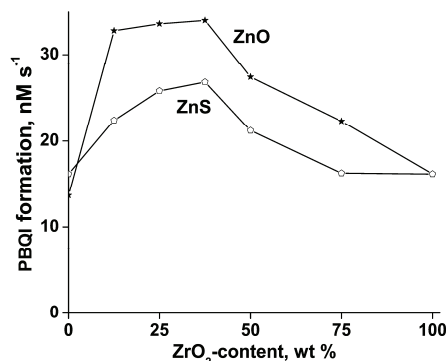


Fig. 9. Enhanced PBQI formation on mixing ZrO₂ with ZnO or ZnS; [DPA] = 5.0 mM, nanoparticles-loading = 1.0 g, airflow rate = 7.8 mL s⁻¹, λ = 365 nm, $I = 13.7 \times 10^{-24}$ J L⁻¹ s⁻¹, illumination time = 30 min, volume of reaction solution = 25 mL.

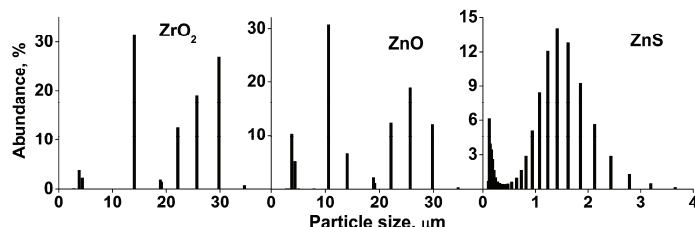


Fig. 10. Particles aggregation.

CONCLUSIONS

ZrO₂ mediates photoinduced oxidative transformation of DPA to PBQI. The formation of PBQI on ZrO₂ enhances with DPA concentration, airflow rate and photon flux and conforms to the Langmuir–Hinshelwood kinetic law. The PBQI formation on ZrO₂ is greater with UV-C light than with UV-A light. ZrO₂ mixed with ZnO or ZnS affords more PBQI than the individual nanoparticles due to synergism.

Acknowledgements. Prof. C. Karunakaran is thankful to the Council of Scientific and Industrial Research (CSIR), New Delhi for the Emeritus Scientist Scheme (21(0887)/12/EMR-II).

И З В О Д
ФОТО-ИНДУКОВАНА ОКСИДАТИВНА ТРАНСФОРМАЦИЈА ДИФЕНИЛАМИНА НА
ZrO₂ СИНЕРГИЗАМ ZnO И ZnS

C. KARUNAKARAN, S. KARUTHAPANDIAN И Р. VINAYAGAMOORTHY

Department of Chemistry, Annamalai University, Annamalainagar 608002, Tamilnadu, India

Дифениламин (DPA) у етанолу на површини ZrO₂ подлеже фото-индукованој оксидативној трансформацији дајући *N*-фенил-*p*-бензохинонимин (PBQI). Фото-индукована трансформација на ZrO₂ се повећава са порастом [DPA], количине ZrO₂, брзине протока ваздуха и флукаса фотона. Стварање PBQI на ZrO₂ је веће при озрачивању на 254 nm него на 365 nm. ZrO₂ се може поново користити без икаквог третмана. Механизам фото-индуковане оксидативне трансформације DPA на ZrO₂ је разматран применом одговарајућих метода.

рајућег кинетичког закона. ZnO и ZnS повећавају UV foto-индуковану трансформацију DPA на ZrO_2 указујући на синергизам.

(Примљено 24. августа, ревидирано 13. децембра, прихваћено 15. децембра 2014)

REFERENCES

1. X. Lang, X. Chen, J. Zhao, *Chem. Soc. Rev.* **43** (2014) 473
2. G. Palmisano, E. Garcia-Lopez, G. Marci, V. Loddo, S. Yurdakal, V. Augugliaro, L. Palmisano, *Chem. Commun.* **46** (2010) 7074
3. Y. Shiraishi, T. Hirai, *J. Photochem. Photobiol., C* **9** (2008) 157
4. M. J. Poston, A. B. Aleksandrov, D. E. Sabo, Z. J. Zhang, T. M. Orlando, *J. Phys. Chem., C* **118** (2014) 12789
5. S. Yoshida, Y. Kohno, *Catal. Surv. Jpn.* **4** (2000) 107
6. Y. Kohno, T. Tanaka, T. Funabiki, S. Yoshida, *Chem. Commun.* (1997) 841
7. S. Polisetty, P. A. Deshpande, G. Madras, *Ind. Eng. Chem. Res.* **50** (2011) 12915
8. A. Zanella, *Postharvest Biol. Technol.* **27** (2003) 69
9. Y. C. Chang, P. W. Chang, C. M. Wang, *J. Phys. Chem., B* **107** (2003) 1628
10. T. S. Lin, J. Retsky, *J. Phys. Chem.* **90** (1986) 2687
11. C. Karunakaran, S. Karuthapandian, *Sol. Energy Mater. Sol. Cells* **90** (2006) 1928
12. Y. Li, W. Xie, X. Hu, G. Shen, X. Zhou, Y. Xiang, X. Zhao, P. Fang, *Langmuir* **26** (2010) 591
13. C. Karunakaran, R. Dhanalakshmi, P. Gomathisankar, *Int. J. Chem. Kinet.* **41** (2009) 716
14. C. Karunakaran, R. Dhanalakshmi, P. Gomathisankar, G. Manikandan, *J. Hazard. Mater.* **176** (2010) 799
15. C. Karunakaran, R. Dhanalakshmi, P. Gomathisankar, *Spectrochim. Acta A* **92** (2012) 201
16. D. M. Adams, J. B. Raynor, *Advanced Practical Inorganic Chemistry*, Wiley, New York, USA, 1965, p. 54
17. S. Puri, W. R. Bansal, K. S. Sidhu, *Indian J. Chem.* **11** (1973) 828
18. W. R. Bansal, N. Ram, K. S. Sidhu, *Indian J. Chem., B* **14** (1976) 123
19. M. A. Fox, C. C. Chen, *J. Am. Chem. Soc.* **103** (1981) 6757
20. A. M. Ali, E. A. C. Emanuelsson, D. A. Patterson, *Appl. Catal., B* **91** (2010) 168
21. A. M. Ali, E. A. C. Emanuelsson, D. A. Patterson, *Appl. Catal., B* **106** (2011) 323
22. B. Delmon, *Catal. Today* **117** (2006) 69
23. W. Xie, Y. Li, W. Sun, J. Huang, H. Xie, X. Zhao, *J. Photochem. Photobiol., A* **216** (2010) 149
24. C. Karunakaran, P. Vinayagamoorthy, J. Jayabharathi, *Langmuir* **30** (2014) 15031
25. A. V. Emeline, V. K. Ryabchuk, N. Serpone, *Catal. Today* **122** (2007) 91
26. N. Serpone, A. Salinaro, A. Emeline, V. Ryabchuk, *J. Photochem. Photobiol., A* **130** (2000) 83
27. A. V. Emeline, V. Ryabchuk, N. Serpone, *J. Photochem. Photobiol., A* **133** (2000) 89
28. S. E. Braslavsky, A. M. Braun, A. E. Cassano, A. V. Emeline, M. I. Litter, L. Palmisano, V. N. Parmon, N. Serpone, *Pure Appl. Chem.* **83** (2011) 931
29. V. K. Sharma, C. R. Burnett, W. Rivera, V. N. Joshi, *Langmuir* **17** (2001) 4598
30. W. R. Bansal, K. S. Sidhu, *J. Photochem.* **5** (1976) 156
31. H. de Lasa, B. Serrano, M. Salaices, *Photocatalytic Reaction Engineering*, Springer, New York, 2005, p. 2
32. C. Karunakaran, S. Senthilvelan, *Curr. Sci.* **88** (2005) 962
33. L. Vincze, T. J. Kemp, *J. Photochem. Photobiol., A* **87** (1995) 257
34. M. Li, M. E. Noriega-Trevino, N. Nino-Martinez, C. Marambio-Jones, J. Wang, R. Damoiseause, F. Ruiz, E. M. V. Hock, *Environ. Sci. Technol.* **45** (2011) 8989.



Modeling of density and calculations of derived volumetric properties for *n*-hexane, toluene and dichloromethane at pressures 0.1–60 MPa and temperatures 288.15–413.15 K

GORICA R. IVANIĆ[#], ALEKSANDAR Ž. TASIĆ, IVONA R. RADOVIĆ[#], BOJAN D. DJORDJEVIĆ[#], SLOBODAN P. ŠERBANOVIĆ[#] and MIRJANA LJ. KIJEVČANIN^{**#}

Faculty of Technology and Metallurgy, University of Belgrade, Karnegijeva 4,
11120 Belgrade, Serbia

(Received 18 March, revised 30 June, accepted 1 July 2015)

Abstract: Densities data of *n*-hexane, toluene and dichloromethane at temperatures 288.15–413.15 K and at pressures 0.1–60 MPa, determined in a previous article, were fitted to the modified Tait equation of state. The fitted temperature-pressure dependent density data were used to calculate the following derived properties: the isothermal compressibility, the isobaric thermal expansivity, the difference between specific heat capacity at constant pressure and at constant volume and the internal pressure, over the entire temperature and pressure intervals specified above. In order to assess the proposed modeling procedure, the obtained values for the isothermal compressibility and the isobaric thermal expansivity were compared with the corresponding literature data. The average absolute percentage deviations for the isothermal compressibility were for *n*-hexane 2.01–3.64 %, for toluene 0.64–2.48 % and for dichloromethane 1.81–3.20 %, and for the isobaric thermal expansivity, they were for *n*-hexane 1.31–4.17 %, for toluene 0.71–2.45 % and for dichloromethane 1.16–1.61 %. By comparing the obtained deviations values with those found in the literature, it could be concluded that the presented results agree well with the literature data.

Keywords: high pressure; isobaric thermal expansivity; isothermal compressibility; *n*-hexane; toluene; dichloromethane.

INTRODUCTION

In a previous article,¹ the experimental densities of compressed liquid *n*-hexane, toluene and dichloromethane, determined using a set-up based on a density measuring cell AP DMA HP coupled with a DMA 5000 vibrating tube densimeter, were reported. The measurements were performed over the temperature

* Corresponding author. E-mail: mirjana@tmf.bg.ac.rs

[#] Serbian Chemical Society member.

doi: 10.2298/JSC150318062I

and pressure ranges: 288.15–413.15 K and 0.1–60 MPa, respectively. It was shown that the obtained data are in good and acceptable agreement with the corresponding literature values.

This paper, as well as the previous one related to the density measurements for the same pure compounds-solvents, is a part of the systematic investigation of crucial thermodynamic properties of important solvents, used in both industry and the laboratory.

Correlation of the volumetric information mentioned above allows the evaluation of temperature and pressure effects on various thermomechanical properties,² such as isothermal compressibility, κ_T , and isobaric thermal expansivity, α_p ; based on these properties, the internal pressure p_{int} and the difference of the isobaric and isochoric heat capacities, $C_p - C_V$, can also be determined. By coupling the mentioned isothermal and isobaric properties κ_T and α_p , and using the isentropic compressibility, κ_S , which is related to the thermodynamic speed of sound, some additional properties can be calculated; in this respect, the isobaric heat capacity, C_p , and isochoric heat capacity, C_V , could be mentioned.

Various methods, dealing with the correlation of measured densities as a function of temperature and pressure, have been established in the literature. In the present work, a Tait-like equation was applied. The obtained correlation was used to compute the aforementioned parameters.

CALCULATIONS

The experimental density data presented in a previous paper¹ were fitted to the Tait-like equation:

$$\rho(T, p) = \frac{\rho^{\text{ref}}(T)}{1 - C(T) \ln \left(\frac{B(T) + p}{B(T) + p^{\text{ref}}} \right)} \quad (1)$$

where, T and p refer to temperature and pressure, respectively, and $C(T)$ and $B(T)$ are parameters that were assumed to be temperature dependent and can be calculated from the second order polynomials:

$$B(T) = \sum_{i=0}^2 b_i T^i \quad (2)$$

$$C(T) = \sum_{i=0}^2 c_i T^i \quad (3)$$

ρ^{ref} is the density at the reference pressure, p^{ref} , and it can be calculated from the second order polynomial:

$$\rho^{\text{ref}}(T) = \sum_{i=0}^2 a_i T^i \quad (4)$$

In Eqs. (2)–(4), a_i , b_i and c_i are adjustable parameters.

As stated previously, a number of derived properties exist that can be calculated from density data.

The isothermal compressibility, κ_T , represents a measure of the sensitivity of density to a pressure change at constant temperature and it depends on the fluid structure. It can be expressed as:

$$\kappa_T = \frac{1}{\rho} \left(\frac{\partial \rho}{\partial p} \right)_T \quad (5)$$

Coupling Eqs. (1) and (5) leads to the expression for the calculation of κ_T :

$$\kappa_T = \frac{C(T)}{(B(T) + p) \left(1 - C(T) \ln \frac{B(T) + p}{B(T) + p^{\text{ref}}} \right)} \quad (6)$$

The isobaric thermal expansivity, α_p , is a measure of the relative fluid density change in response to a temperature change at constant pressure:

$$\alpha_p = \frac{1}{\rho} \left(\frac{\partial p}{\partial T} \right)_\rho \left(\frac{\partial \rho}{\partial p} \right)_T^{-1} = -\frac{1}{\rho} \left(\frac{\partial \rho}{\partial T} \right)_p \quad (7)$$

When Eq. (1) is included into Eq. (7), an expression for the calculation of the isobaric thermal expansivity is obtained:

$$\alpha_p = \frac{-\rho^{\text{ref}'}(T)}{\rho^{\text{ref}}(T)} - \frac{C(T) \frac{B'(T)(p^{\text{ref}} - p)}{(B(T) + p)(B(T) + p^{\text{ref}})} + C'(T) \ln \frac{B(T) + p}{B(T) + p^{\text{ref}}}}{\left(1 - C(T) \ln \frac{B(T) + p}{B(T) + p^{\text{ref}}} \right)} \quad (8)$$

where $\rho^{\text{ref}'}(T)$, $B'(T)$ and $C'(T)$ stay for the derivatives of the parameters ρ^{ref} , $B(T)$ and $C(T)$ of Eq. (1), respectively:

$$\rho^{\text{ref}'} = \sum_{i=0}^2 i a_i T^{i-1} \quad (9)$$

$$B' = \sum_{i=0}^2 i b_i T^{i-1} \quad (10)$$

$$C' = \sum_{i=0}^2 i c_i T^{i-1} \quad (11)$$

Another thermodynamic property that can be calculated from the aforementioned equations is the ratio of the isobaric thermal expansivity to the isothermal compressibility, *i.e.*, the thermal pressure coefficient, γ :

$$\gamma = \frac{\alpha_p}{\kappa_T} \quad (12)$$

The thermal pressure coefficient is associated with the internal pressure, p_{int} , which represents the change of the internal energy of a sample when it isothermally expands or

contracts, thus describing intermolecular interactions. It is easy to calculate the internal pressure when the isobaric thermal expansivity and the isothermal compressibility are known:

$$p_{\text{int}} = \left(\frac{\partial U}{\partial V} \right)_T = T \left(\frac{\partial p}{\partial T} \right)_\rho - p = T\gamma - p = \frac{T\alpha_p}{\kappa_T} p \quad (13)$$

where, U denotes the internal energy of a sample and V is its volume.

An important thermodynamic property that can be calculated from the quantities defined above is the difference between specific heat capacity at constant pressure, C_p , and specific heat capacity at constant volume, C_V :

$$C_p - C_V = T \frac{\left(\frac{\partial p}{\partial T} \right)_\rho^2}{\rho^2 \left(\frac{\partial p}{\partial \rho} \right)_T} \quad (14)$$

Linking Eqs. (5) and (7) with Eq. (14) gives the expression:

$$C_p - C_V = \frac{\alpha_p^2 T}{\rho \kappa_T} \quad (15)$$

The relation given by Eq. (15) is significant because it can be used to calculate the heat capacity at constant volume instead of its experimental determination. Heat capacity at constant pressure can be measured or calculated from speed of sound data and the above-defined coefficients by combining Eqs. (16)–(18).

Isentropic compressibility, κ_S , is defined as:

$$\kappa_S = \frac{1}{\rho} \left(\frac{\partial \rho}{\partial p} \right)_S \quad (16)$$

and can be calculated as follows:

$$\kappa_S = \frac{1}{\rho u^2} \quad (17)$$

where, u is the speed of sound waves spreading through the sample.

Further, the specific heat capacity at constant pressure can be obtained from the equation:

$$C_p = \frac{\alpha_p^2 T}{\rho(\kappa_T - \kappa_S)} \quad (18)$$

RESULTS AND DISCUSSION

The criteria used to assess the quality of fitting were the absolute average percentage deviation, AAD , the percentage maximum deviation, MD , the average percentage deviation, $Bias$, and standard deviation, σ :

$$AAD = \frac{100}{N} \sum_{i=1}^N \left| \frac{\rho_i^{\text{exp}} - \rho_i^{\text{cal}}}{\rho_i^{\text{exp}}} \right| \quad (19)$$

$$MD = \max \left(100 \left| \frac{\rho_i^{\text{exp}} - \rho_i^{\text{cal}}}{\rho_i^{\text{exp}}} \right| \right), i=1,N \quad (20)$$

$$Bias = \frac{100}{N} \sum_{i=1}^N \frac{\rho_i^{\text{exp}} - \rho_i^{\text{cal}}}{\rho_i^{\text{exp}}} \quad (21)$$

$$\sigma = \sqrt{\frac{\sum_{i=1}^N (\rho_i^{\text{exp}} - \rho_i^{\text{cal}})^2}{N-m}} \quad (22)$$

where, ρ^{exp} is the experimentally determined density, ρ^{cal} denotes the density value obtained from Eq. (1), N is the number of experimental data and m represents the number of parameters included in the correlation of the Tait-like equation.

The reference pressure in Eq. (1) was chosen to be 1 MPa. Hence, the density data of a sample at 1 MPa were first used for the optimization of the a_i parameters. Then, all the density data, presented for the studied compounds in a previous work¹ were employed for the determination of the b_i and c_i parameters. All the parameters were obtained applying the Marquardt algorithm for the minimization of the objective function, *i.e.*, the standard deviation.

The obtained parameters of Eqs. (2)–(4) and the corresponding deviations are given in Table I.

TABLE I. Fitting parameters of Eqs. (2)–(4)

Parameter	<i>n</i> -Hexane	Toluene	Dichloromethane
$a_0 / \text{kg m}^{-3}$	791.280	1082.499	1599.209
$a_1 / \text{kg m}^{-3} \text{ K}^{-1}$	-0.035271	-0.55689	-0.10023
$a_2 / \text{kg m}^{-3} \text{ K}^{-2}$	-0.14039×10 ⁻²	-0.60343×10 ⁻³	-0.28367×10 ⁻²
b_0 / MPa	349.513	504.019	654.433
$b_1 / \text{MPa K}^{-1}$	-1.46894	-1.96093	-2.80478
$b_2 / \text{MPa K}^{-2}$	0.15855×10 ⁻²	0.20102×10 ⁻²	0.30968×10 ⁻²
c_0	0.18450	0.15696	0.29779
c_1 / K^{-1}	-0.58799×10 ⁻³	-0.39307×10 ⁻³	-0.11415×10 ⁻²
c_2 / K^{-2}	0.87278×10 ⁻⁶	0.54981×10 ⁻⁶	0.15929×10 ⁻⁵
$AAD / \%$	0.023	0.008	0.019
$MD / \%$	0.191	0.028	0.128
$Bias / \%$	0.002	0.003	0.001
$\sigma / \text{kg m}^{-3}$	0.209	0.090	0.332

From the presented deviation values, it could be concluded that the proposed Eqs.(1)–(4) fit well the densities of the selected substances.

The isothermal compressibility, the isobaric thermal expansivity, the difference between the specific heat capacities at constant pressure and constant volume and the internal pressure for all three examined compounds, at temperatures 288.15–413.15 K and pressures 0.1–60 MPa, are presented in Tables S-I–S-III of the Supplementary material to this paper.

In order to verify the accuracy of the density data modeling and the procedure of calculating the derived properties listed in the previous section, the obtained values of the isothermal compressibility and isobaric thermal expansivity were compared to those found in the literature. The criteria for the evaluation of the agreement were the same as in a previous paper:¹ the absolute average percentage deviation (*AAD*), the percentage maximum deviation (*MD*) and the average percentage deviation (*Bias*), but here, instead of density, the corresponding values of the isothermal compressibility and the isobaric thermal were used.

n-Hexane

Data on *n*-hexane density were modeled and the calculated values of the isothermal compressibility, given in Table S-I, were compared to those published by Daridon *et al.*³ The comparison was performed at temperatures 293.15–373.15 K and at pressures 0.1–60 MPa; the obtained deviations were: *AAD* = 3.64 %, *MD* = 5.67 % and *Bias* = −3.64 % (Fig. 1a).

Aiming at assessing the accuracy of the presented density modeling, the isentropic compressibility was compared. Values of the speed of sound were retrieved from the literature³ and the isentropic compressibility was calculated using Eq. (17); the obtained values were compared to the literature data³ at temperatures 293.15–373.15 K and pressures 5–60 MPa. The corresponding deviations were *AAD* = 0.10 %, *MD* = 0.29 % and *Bias* = 0.01 %; these deviations represent one more proof that the modeling procedure was properly selected.

The calculated isothermal compressibility data were compared to those given by Rendzio *et al.*⁴ at several temperatures in the range 313.15–363.15 K and at pressures 0.1–60 MPa. Values of the criteria were *AAD* = 2.63 %, *MD* = 4.73 % and *Bias* = −2.56 %.

Rendzio *et al.*⁴ also reported equations for the calculation of isobaric thermal expansivity. Hence, their data with those reported in Table S-I were compared at temperatures 288.15–393.15 K and at pressures 0.1–60 MPa. The obtained deviations were *AAD* = 0.99 %, *MD* = 3.73 % and *Bias* = −0.68 %, indicating very good agreement (shown in Fig. 1b).

Tronkosko *et al.*⁵ gave the isothermal compressibility of *n*-hexane in the somewhat narrower ranges of pressure and temperature than did the aforementioned authors, and hence the comparison is realized at temperatures 293.15–

–413.15 K and at pressures 0.1–40 MPa. The deviations were $AAD = 2.01\%$, $MD = 3.31\%$ and $Bias = -2.01\%$.

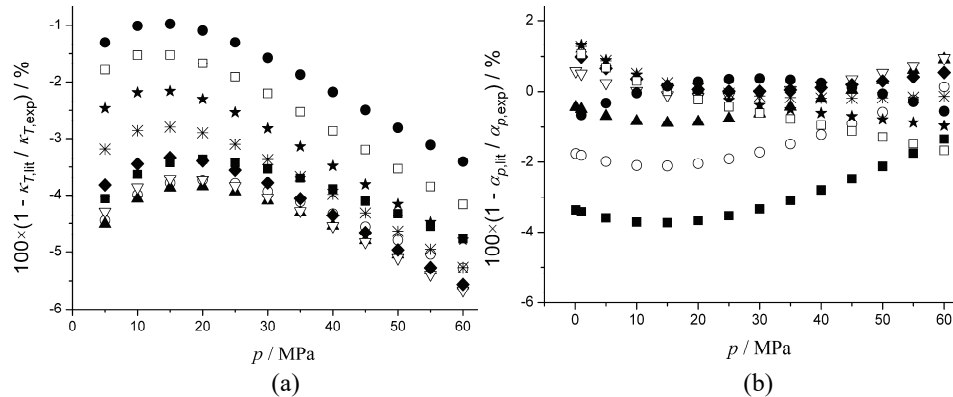


Fig. 1. Comparisons of the calculated derived properties with literature data for *n*-hexane: a) the isothermal compressibility with Daridon *et al.*³ at (■) 293.15, (○) 303.15, (▲) 313.15, (▽) 323.15, (◆) 323.15, (※) 343.15, (★) 353.15, (□) 363.15 and (●) 373.15 K; b) the isobaric thermal expansivity with Rendzio *et al.*⁴ at (■) 288.15, (○) 303.15, (▲) 318.15, (▽) 333.15, (◆) 343.15, (※) 353.15, (★) 363.15, (□) 373.15 and (●) 393.15 K.

The values of the isobaric thermal expansivity presented in this work were compared to those reported by Zhou *et al.*⁶ at temperatures 293.15–413.15 K and at pressures 0.1–40 MPa and the obtained deviation criteria were: $AAD = 4.17\%$, $MD = 6.08\%$ and $Bias = -3.86\%$.

Cardeirine *et al.*⁷ gave the isobaric thermal expansivities at atmospheric pressure and at temperatures 293.15–333.5 K. The results of the comparison of those data and the present ones were $AAD = 2.06\%$, $MD = 3.71\%$ and $Bias = -1.69\%$.

Considering the values of the deviations that the cited authors reported in their papers, it could be concluded that the agreement of the present results with those found in the literature was acceptable.

Toluene

The isothermal compressibility data of toluene, given in Table S-II, were compared to those reported by Chorazewski *et al.*⁸ The comparison was performed at temperatures 303.15–373.15 K and pressures 0.1–60 MPa and the obtained results were: $AAD = 1.19\%$, $MD = 1.97\%$ and $Bias = -1.18\%$ (Fig. 2a).

Chorazewski *et al.*⁸ gave equations for the determination of the isobaric thermal expansivities of toluene and hence, the data presented in Table S-II were compared to these values over wide ranges of temperature and pressure, 288.15–413.15 K and 0.1–60 MPa, respectively. The obtained deviations were $AAD = 2.45\%$, $MD = 5.18\%$ and $Bias = -2.29\%$ (Fig. 2a).

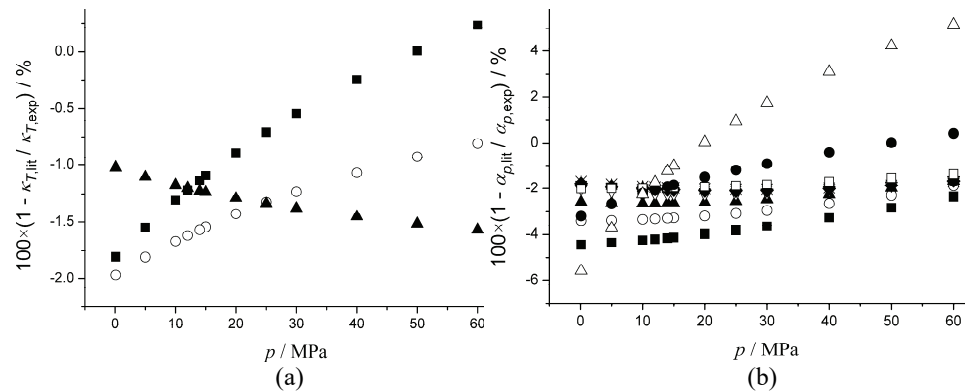


Fig. 2. Comparisons of the calculated derived properties with literature data for toluene: a) the isothermal compressibility with Chorazewski *et al.*⁸ at (■) 303.15, (○) 323.15 and (▲) 373.15 K, and b) the isobaric thermal expansivity with Chorazewski *et al.*⁸ at (■) 288.15, (○) 303.15, (▲) 318.15, (▽) 333.15, (◆) 343.15, (★) 353.15, (☆) 363.15, (□) 373.15, (●) 393.15 and (△) 413.15 K.

The values of the isothermal compressibility obtained in this paper were also compared to those given by Zéberg-Mikkelsen *et al.*⁹ at temperatures 303.15–333.15 K and at pressures 0.1–30 MPa. The deviations were rather low: *AAD* = 0.64 %, *MD* = 1.48 % and *Bias* = −0.20 %.

In addition, Zéberg-Mikkelsen *et al.*⁹ reported the isobaric thermal expansivities of toluene at the same temperatures and pressures as they did for the isothermal compressibility. For this property, the values of the appropriate criteria were *AAD* = 0.71 %, *MD* = 2.39 % and *Bias* = −0.17 %.

Easteal *et al.*¹⁰ presented the values for the isothermal compressibility and the isobaric thermal expansivity of toluene under the same conditions. The comparison was performed at temperatures 288.15–323.15 K and pressures 0.1–50 MPa and the attained results were: for the isothermal compressibility *AAD* = 2.48 %, *MD* = 4.01 % and *Bias* = −2.38 % and for the isobaric thermal expansivity *AAD* = 1.29 %, *MD* = 2.63 % and *Bias* = −0.21 %.

The values of the deviation criteria obtained for the isothermal compressibility and the isobaric thermal expansivity of toluene were sufficiently low for it to be concluded that the results calculated in this work agree well with the literature data.

Dichloromethane

Gonçalves *et al.*¹¹ recently presented results for the isothermal compressibility and the isobaric thermal expansivity for dichloromethane at temperatures 300–400 K and pressures 0.1–100 MPa. The application of Eqs. (1)–(11) enabled the calculation of the values for the mentioned properties at the same temperatures and at pressures up to 60 MPa. A comparison of the calculated data with

literature results¹¹ resulted in the following: for the isothermal compressibility *AAD* was 1.81 %, *MD* was 5.04 % and *Bias* was 0.38 % (Fig. 3a) and for the isobaric thermal expansivity *AAD* = 1.16 %, *MD* = 3.53 % and *Bias* = 0.19 % (Fig. 3b).

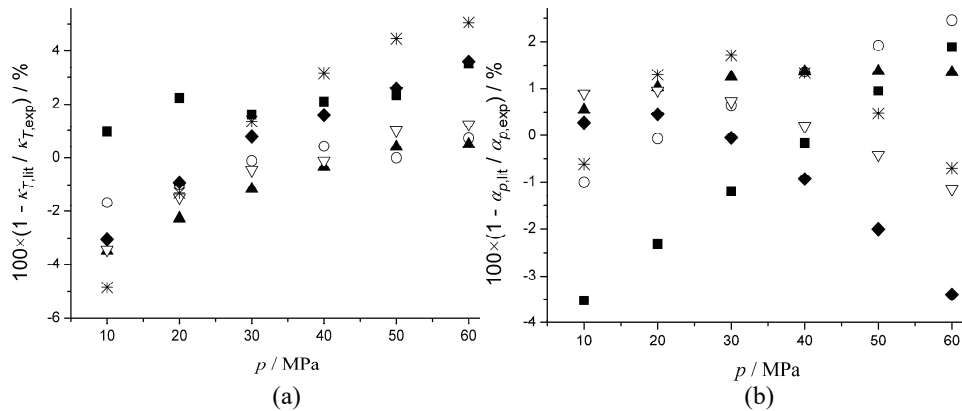


Fig. 3. Comparisons of the calculated derived properties with literature data for dichloromethane: a) the isothermal compressibility with Ferreira *et al.*¹¹ at (■) 300, (○) 320, (▲) 340, (▽) 360, (◆) 380 and (*) 400 K, and b) the isobaric thermal expansivity with Ferreira *et al.*¹¹ at (■) 300, (○) 320, (▲) 340, (▽) 360, (◆) 380 and (*) 400 K.

Easteal *et al.*¹⁰ gave the values of the isothermal compressibility and the isobaric thermal expansivity of dichloromethane at two temperatures, 288.15 and 298.15 K, and at pressures 0.1–50 MPa. The isothermal values presented in Table S-III agree with those taken from literature¹⁰ with: *AAD* of 3.20 %, *MD* of 3.56 % and *Bias* of 3.20 %. When comparing the isobaric thermal expansivities from Table S-III, the following deviations were obtained: *AAD* = 1.61 %, *MD* = 3.33% and *Bias* = −1.43 %.

Although the mentioned values of the criteria for the comparison of both properties for dichloromethane were slightly higher than those for toluene, they could still be considered as good.

CONCLUSIONS

The density data of *n*-hexane, toluene and dichloromethane, reported in a previous paper,¹ were fitted to a Tait-like equation; the obtained parameters, and the results of assessment of the modeling, by the comparison with literature information, are given in this work. The calculated values of the isothermal compressibility, the isobaric thermal expansivity, the difference between specific heat capacity at constant pressure and at constant volume as well as the internal pressure for each of three investigated compounds, at temperatures 288.15–413.15 K and at pressures 0.1–60 MPa, are also presented herein. In order to assess the proposed modeling procedure, the obtained values of the isothermal compres-

sibility and the isobaric thermal expansivity were compared to corresponding literature data, and the good agreement was achieved.

SUPPLEMENTARY MATERIAL

The calculated values of the isothermal compressibility, κ_T , the isobaric thermal expansivity, α_p , the difference between the specific heat capacities at constant pressure and constant volume, $C_p - C_V$, and the internal pressure, p_{int} , for *n*-hexane, toluene and dichloromethane, at temperatures 288.15–413.15 K and pressures 0.1–60 MPa, are available electronically from <http://www.shd.org.rs/JSCS/>, or from the corresponding author on request.

Acknowledgements. The authors gratefully acknowledge the financial support received from the Research Fund of Ministry of Education, Science and Technological Development (Project No. 172063) of the Republic of Serbia, and the Faculty of Technology and Metallurgy, University of Belgrade.

ИЗВОД

МОДЕЛОВАЊЕ ГУСТИНЕ И ПРОРАЧУН ИЗВЕДЕНИХ ВОЛУМЕТРИЈСКИХ СВОЈСТАВА НА ПРИТИСЦИМА ОД 0,1 ДО 60 МПА И НА ТЕМПЕРАТУРАМА ОД 288,15 ДО 413,15 К

ГОРИЦА Р. ИВАНИШ, АЛЕКСАНДАР Ж. ТАСИЋ, ИВОНА Р. РАДОВИЋ, БОЈАН Д. ЂОРЂЕВИЋ,
СЛОБОДАН П. ШЕРБАНОВИЋ И МИРЈАНА Љ. КИЈЕВЧАНИН

Технолошко-мешавински факултет, Универзитет у Београду, Карнеијева 4, 11120 Београд

Густине *n*-хексана, толуена и дихлорметана на температурама 288,15–413,15 K и притисцима 0,1–60 MPa су моделоване прилагођеном Тејтовом једначином. У овом раду су наведене одговарајуће једначине за рачунање изотермске стишљивости, изобарске топлотне експанзивности, разлике између специфичног топлотног капацитета при сталном притиску и оног при сталној запремини и унутрашњег притиска у читавом поменутом опсегу притисака и температура, као и вредности наведених изведенih величина. У циљу процене предложене методе моделовања поређене су добијене вредности коефицијента изотермске стишљивости и коефицијента изобарског топлотног ширења са онима из литературе. Просечно апсолутно процентуално одступање за изотермску стишљивост је било: за *n*-хексан 2,01–3,64 %, за толуен 0,64–2,48 % и за дихлорметан 1,81–3,20 %; а за изобарско топлотну експанзивност: за *n*-хексан 1,31–4,17 %, за толуен 0,71–2,45 % и за дихлорметан 1,16–1,61 %. Поређењем добијених одступања са оним која се могу наћи у литератури долази се до закључка да се представљени резултати добро слажу са литературним.

(Примљено 18. марта, ревидирано 30. јуна, прихваћено 1. јула 2015)

REFERENCES

1. G. R. Ivaniš, A. Ž. Tasić, I. R. Radović, B. D. Djordjević, S. P. Šerbanović, M. Lj. Kijevčanin, *J. Serb. Chem. Soc.* **80** (2015) 1073
2. J. Safarov, F. Millero, R. Feistel, A. Heintz, E. Hassel, *Ocean Sci.* **5** (2009) 235
3. J. L. Daridon, B. Lagourette, J.-P. E. Grolier, *Int. J. Thermophys.* **19** (1998) 145
4. S. L. Randzio, J.-P. E. Grolier, J. R. Quint, D. J. Eatough, E. A. Lewis, L. D. Hansen, *Int. J. Thermophys.* **15** (1994) 415
5. J. Troncoso, D. Bessières, C. A. Cerdeiriña, E. Carballo, L. Romaní, *Fluid Phase Equilib.* **208** (2003) 141
6. J. Zhou, R. Zhu, H. Xu, Y. Tian, *J. Chem. Thermodyn.* **42** (2010) 1429

7. C. A. Cerdeiriña, C. A. Tovar, D. González-Salgado, E. Carballo, L. Romaní, *Phys. Chem. Chem. Phys.* **3** (2001) 5230
8. M. Chorażewski, J.-P. E. Grolier, S. L. Randzio, *J. Chem. Eng. Data* **55** (2010) 5489
9. C. K. Zéberg-Mikkelsen, S. I. Andersen, *J. Chem. Eng. Data* **50** (2005) 524
10. A. J. Eastal, L. A. Woolf, *Int. J. Thermophys.* **6** (1985) 331
11. F. A. M. M. Gonçalves, C. S. M. F. Costa, J. C. S. Bernardo, I. Johnson, I. M. A. Fonseca, A. G. M. Ferreira, *J. Chem. Thermodyn.* **43** (2011) 105.



SUPPLEMENTARY MATERIAL TO

Modeling of density and calculations of derived volumetric properties for *n*-hexane, toluene and dichloromethane at pressures 0.1–60 MPa and temperatures 288.15–413.15 K

GORICA R. IVANIŠ[#], ALEKSANDAR Ž. TASIĆ, IVONA R. RADOVIĆ[#], BOJAN D. DJORDJEVIĆ[#], SLOBODAN P. ŠERBANOVIĆ[#] and MIRJANA LJ. KIJEVČANIN^{*#}

*Faculty of Technology and Metallurgy, University of Belgrade, Kariđegijeva 4,
11120 Belgrade, Serbia*

J. Serb. Chem. Soc. 80 (11) (2015) 1423–1433

TABLE S-I. Calculated derived volumetric properties of *n*-hexane at different temperatures (288.15–413.15 K) and pressures (0.1–60 MPa)

p / MPa	κ_T GPa ⁻¹	$\alpha_p \times 10^3$ K ⁻¹	$C_p - C_V$ kJ kg ⁻¹ K ⁻¹	p_{int} MPa	κ_T GPa ⁻¹	$\alpha_p \times 10^3$ K ⁻¹	$C_p - C_V$ kJ kg ⁻¹ K ⁻¹	p_{int} MPa
0.1	1.5076	1.2820	0.4731	244.9	1.5748	1.3124	0.4861	244.2
1	1.4865	1.2705	0.4706	245.3	1.5518	1.3000	0.4833	244.6
5	1.4000	1.2234	0.4606	246.8	1.4573	1.2493	0.4725	246.3
10	1.3057	1.1720	0.4502	248.6	1.3550	1.1943	0.4612	248.4
15	1.2238	1.1275	0.4417	250.5	1.2666	1.1470	0.4520	250.5
20	1.1521	1.0885	0.4348	252.3	1.1896	1.1057	0.4445	252.5
25	1.0887	1.0541	0.4292	254.0	1.1219	1.0694	0.4384	254.4
30	1.0322	1.0236	0.4246	255.8	1.0618	1.0372	0.4334	256.4
35	0.9815	0.9962	0.4208	257.5	1.0081	1.0084	0.4293	258.2
40	0.9359	0.9716	0.4179	259.2	0.9598	0.9826	0.4261	260.1
45	0.8945	0.9493	0.4155	260.8	0.9162	0.9592	0.4234	261.9
50	0.8568	0.9291	0.4137	262.5	0.8766	0.9380	0.4214	263.7
55	0.8223	0.9106	0.4123	264.1	0.8404	0.9187	0.4198	265.5
60	0.7906	0.8936	0.4113	265.7	0.8072	0.9010	0.4185	267.2
298.15 K								
0.1	1.6475	1.3433	0.4985	243.0	1.7259	1.3749	0.5104	241.4
1	1.6221	1.3300	0.4956	243.4	1.6981	1.3605	0.5072	241.9
5	1.5188	1.2754	0.4837	245.4	1.5847	1.3018	0.4943	244.0
10	1.4075	1.2166	0.4715	247.7	1.4636	1.2389	0.4811	246.6
15	1.3121	1.1662	0.4616	250.0	1.3604	1.1852	0.4703	249.1
20	1.2294	1.1225	0.4535	252.2	1.2714	1.1388	0.4615	251.5
25	1.1569	1.0841	0.4468	254.4	1.1939	1.0983	0.4544	253.9
303.15 K								

*Corresponding author. E-mail: mirjana@tmf.bg.ac.rs

TABLE S-I. Continued

p / MPa	κ_T GPa ⁻¹	$\alpha_p \times 10^3$ K ⁻¹	$c_p - c_v$ kJ kg ⁻¹ K ⁻¹	P_{int} MPa	κ_T GPa ⁻¹	$\alpha_p \times 10^3$ K ⁻¹	$c_p - c_v$ kJ kg ⁻¹ K ⁻¹	P_{int} MPa
298.15 K					303.15 K			
30	1.0930	1.0502	0.4414	256.5	1.1257	1.0626	0.4485	256.1
35	1.0360	1.0200	0.4370	258.5	1.0653	1.0309	0.4436	258.4
40	0.9849	0.9929	0.4333	260.6	1.0112	1.0025	0.4397	260.5
45	0.9389	0.9684	0.4304	262.5	0.9627	0.9769	0.4364	262.6
50	0.8972	0.9463	0.4281	264.4	0.9188	0.9537	0.4338	264.6
55	0.8593	0.9261	0.4262	266.3	0.8790	0.9326	0.4316	266.6
60	0.8245	0.9076	0.4248	268.2	0.8426	0.9133	0.4299	268.6
308.15 K					313.15 K			
0.1	1.8108	1.4072	0.5217	239.4	1.9028	1.4401	0.5323	236.9
1	1.7801	1.3916	0.5182	239.9	1.8687	1.4232	0.5284	237.5
5	1.6555	1.3283	0.5042	242.2	1.7316	1.3551	0.5132	240.1
10	1.5234	1.2610	0.4898	245.1	1.5873	1.2829	0.4977	243.1
15	1.4117	1.2038	0.4782	247.8	1.4661	1.2221	0.4852	246.0
20	1.3159	1.1547	0.4687	250.4	1.3629	1.1700	0.4750	248.8
25	1.2329	1.1119	0.4610	252.9	1.2740	1.1249	0.4666	251.5
30	1.1602	1.0743	0.4546	255.3	1.1964	1.0854	0.4597	254.1
35	1.0960	1.0410	0.4493	257.7	1.1281	1.0504	0.4540	256.6
40	1.0388	1.0113	0.4450	260.0	1.0676	1.0193	0.4493	259.0
45	0.9876	0.9845	0.4414	262.2	1.0136	0.9913	0.4453	261.3
50	0.9414	0.9603	0.4384	264.3	0.9650	0.9660	0.4420	263.5
55	0.8996	0.9383	0.4360	266.4	0.9211	0.9431	0.4392	265.6
60	0.8615	0.9182	0.4340	268.4	0.8811	0.9221	0.4369	267.7
318.15 K					323.15 K			
0.1	2.0024	1.4738	0.5422	234.1	2.1105	1.5083	0.5513	230.8
1	1.9646	1.4555	0.5380	234.7	2.0685	1.4885	0.5468	231.5
5	1.8134	1.3820	0.5215	237.5	1.9013	1.4091	0.5289	234.5
10	1.6555	1.3047	0.5047	240.7	1.7282	1.3263	0.5108	238.0
15	1.5239	1.2400	0.4913	243.9	1.5853	1.2574	0.4963	241.3
20	1.4127	1.1848	0.4803	246.8	1.4652	1.1991	0.4846	244.5
25	1.3172	1.1372	0.4713	249.7	1.3627	1.1489	0.4749	247.4
30	1.2344	1.0957	0.4639	252.4	1.2743	1.1052	0.4669	250.3
35	1.1619	1.0590	0.4577	255.0	1.1972	1.0668	0.4602	253.0
40	1.0978	1.0264	0.4525	257.5	1.1293	1.0327	0.4546	255.5
45	1.0407	0.9972	0.4481	259.9	1.0690	1.0022	0.4498	258.0
50	0.9895	0.9708	0.4444	262.1	1.0151	0.9747	0.4457	260.3
55	0.9434	0.9469	0.4413	264.3	0.9667	0.9498	0.4421	262.5
60	0.9016	0.9251	0.4386	266.4	0.9229	0.9271	0.4391	264.6
328.15 K					333.15 K			
0.1	2.2279	1.5436	0.5597	227.3	2.3555	1.5797	0.5672	223.3
1	2.1811	1.5220	0.5547	228.0	2.3032	1.5563	0.5618	224.1
5	1.9958	1.4363	0.5354	231.2	2.0974	1.4637	0.5410	227.5
10	1.8059	1.3477	0.5160	234.9	1.8887	1.3688	0.5201	231.4
15	1.6504	1.2744	0.5005	238.4	1.7194	1.2909	0.5035	235.1
20	1.5206	1.2126	0.4879	241.7	1.5791	1.2256	0.4901	238.6

TABLE S-I. Continued

p / MPa	κ_T GPa $^{-1}$	$\alpha_p \times 10^3$ K $^{-1}$	$c_p - c_v$ kJ kg $^{-1}$ K $^{-1}$	p_{int} MPa	κ_T GPa $^{-1}$	$\alpha_p \times 10^3$ K $^{-1}$	$c_p - c_v$ kJ kg $^{-1}$ K $^{-1}$	p_{int} MPa
328.15 K					333.15 K			
25	1.4106	1.1598	0.4775	244.8	1.4610	1.1699	0.4791	241.8
30	1.3162	1.1139	0.4689	247.7	1.3600	1.1218	0.4698	244.8
35	1.2341	1.0737	0.4617	250.5	1.2727	1.0798	0.4621	247.6
40	1.1622	1.0381	0.4556	253.1	1.1965	1.0426	0.4555	250.3
45	1.0985	1.0063	0.4503	255.6	1.1293	1.0094	0.4498	252.8
50	1.0418	0.9776	0.4458	257.9	1.0696	0.9796	0.4448	255.1
55	0.9909	0.9517	0.4419	260.2	1.0161	0.9527	0.4404	257.3
60	0.9451	0.9281	0.4384	262.3	0.9681	0.9281	0.4365	259.4
343.15 K					353.15 K			
0.1	—	—	—	—	—	—	—	—
1	2.5795	1.6270	0.5737	215.4	2.9053	1.7008	0.5824	205.7
5	2.3243	1.5189	0.5496	219.2	2.5865	1.5747	0.5547	210.0
10	2.0712	1.4102	0.5258	223.6	2.2780	1.4504	0.5279	214.8
15	1.8698	1.3223	0.5070	227.7	2.0380	1.3517	0.5069	219.2
20	1.7057	1.2495	0.4918	231.4	1.8457	1.2710	0.4901	223.2
25	1.5692	1.1881	0.4793	234.8	1.6880	1.2035	0.4762	226.8
30	1.4539	1.1353	0.4689	238.0	1.5563	1.1460	0.4646	230.0
35	1.3551	1.0894	0.4600	240.9	1.4445	1.0962	0.4546	233.0
40	1.2695	1.0491	0.4523	243.6	1.3485	1.0526	0.4460	235.7
45	1.1945	1.0132	0.4457	246.0	1.2649	1.0139	0.4383	238.1
50	1.1284	0.9810	0.4397	248.3	1.1917	0.9794	0.4314	240.2
55	1.0695	0.9519	0.4344	250.4	1.1268	0.9482	0.4250	242.2
60	1.0167	0.9255	0.4296	252.4	1.0690	0.9199	0.4191	243.9
363.15 K					373.15 K			
0.1	—	—	—	—	—	—	—	—
1	3.2895	1.7780	0.5880	195.3	3.7416	1.8588	0.5908	184.4
5	2.8887	1.6312	0.5569	200.1	3.2350	1.6889	0.5567	189.8
10	2.5115	1.4899	0.5272	205.4	2.7730	1.5294	0.5248	195.8
15	2.2250	1.3797	0.5043	210.2	2.4311	1.4075	0.5004	201.0
20	1.9996	1.2908	0.4860	214.4	2.1674	1.3106	0.4810	205.6
25	1.8175	1.2172	0.4709	218.2	1.9576	1.2310	0.4650	209.6
30	1.6672	1.1549	0.4581	221.6	1.7866	1.1641	0.4515	213.1
35	1.5410	1.1013	0.4472	224.5	1.6443	1.1068	0.4397	216.2
40	1.4333	1.0544	0.4376	227.2	1.5240	1.0569	0.4293	218.8
45	1.3405	1.0131	0.4289	229.5	1.4209	1.0129	0.4199	221.0
50	1.2594	0.9761	0.4211	231.5	1.3316	0.9737	0.4112	222.9
55	1.1881	0.9428	0.4139	233.2	1.2534	0.9384	0.4031	224.4
60	1.1249	0.9126	0.4070	234.6	1.1843	0.9064	0.3954	225.6
393.15 K					413.15 K			
0.1	—	—	—	—	—	—	—	—
1	4.8826	2.0327	0.5933	162.7	6.3497	2.2256	0.6007	143.8
5	4.0695	1.8125	0.5565	170.1	5.0723	1.9659	0.5741	155.1
10	3.3798	1.6174	0.5238	178.1	4.0732	1.7491	0.5529	167.4
15	2.8978	1.4744	0.4995	185.0	3.4155	1.5959	0.5382	178.0

TABLE S-I. Continued

p / MPa	κ_T GPa ⁻¹	$\alpha_p \times 10^3$ K ⁻¹	$C_p - C_V$ kJ kg ⁻¹ K ⁻¹	P_{int} MPa	κ_T GPa ⁻¹	$\alpha_p \times 10^3$ K ⁻¹	$C_p - C_V$ kJ kg ⁻¹ K ⁻¹	P_{int} MPa
393.15 K					413.15 K			
20	2.5412	1.3635	0.4805	190.9	2.9484	1.4795	0.5270	187.3
25	2.2662	1.2740	0.4648	196.0	2.5988	1.3866	0.5177	195.4
30	2.0474	1.1997	0.4514	200.4	2.3269	1.3097	0.5097	202.6
35	1.8690	1.1365	0.4395	204.1	2.1090	1.2445	0.5023	208.8
40	1.7206	1.0816	0.4288	207.2	1.9304	1.1878	0.4953	214.2
45	1.5951	1.0334	0.4189	209.7	1.7811	1.1379	0.4883	219.0
50	1.4876	0.9905	0.4094	211.8	1.6545	1.0933	0.4812	223.0
55	1.3944	0.9518	0.4003	213.3	1.5456	1.0530	0.4738	226.5
60	1.3128	0.9166	0.3914	214.5	1.4509	1.0163	0.4660	229.4

TABLE S-II. Calculated derived volumetric properties of toluene at different temperatures (288.15–413.15 K) and pressures (0.1–60 MPa)

p / MPa	κ_T GPa ⁻¹	$\alpha_p \times 10^3$ K ⁻¹	$C_p - C_V$ kJ kg ⁻¹ K ⁻¹	P_{int} MPa	κ_T GPa ⁻¹	$\alpha_p \times 10^3$ K ⁻¹	$C_p - C_V$ kJ kg ⁻¹ K ⁻¹	P_{int} MPa
288.15 K					293.15 K			
0.1	0.8424	1.0426	0.4267	356.5	0.8715	1.0553	0.4321	354.9
1	0.8359	1.0375	0.4255	356.7	0.8645	1.0499	0.4309	355.0
5	0.8084	1.0161	0.4206	357.2	0.8350	1.0272	0.4256	355.6
10	0.7766	0.9913	0.4151	357.8	0.8010	1.0011	0.4197	356.4
15	0.7473	0.9685	0.4102	358.4	0.7697	0.9771	0.4145	357.1
20	0.7203	0.9474	0.4058	359.0	0.7410	0.9551	0.4098	357.9
25	0.6952	0.9280	0.4019	359.6	0.7144	0.9347	0.4056	358.6
30	0.6719	0.9099	0.3985	360.2	0.6897	0.9158	0.4019	359.3
35	0.6502	0.8931	0.3954	360.8	0.6668	0.8983	0.3986	359.9
40	0.6300	0.8775	0.3927	361.4	0.6454	0.8820	0.3957	360.6
45	0.6110	0.8628	0.3902	361.9	0.6254	0.8667	0.3931	361.3
50	0.5932	0.8491	0.3881	362.5	0.6067	0.8525	0.3908	361.9
55	0.5764	0.8362	0.3863	363.0	0.5891	0.8391	0.3887	362.5
60	0.5606	0.8241	0.3846	363.6	0.5726	0.8265	0.3870	363.1
298.15 K					303.15 K			
0.1	0.9023	1.0681	0.4373	352.9	0.9349	1.0812	0.4420	350.5
1	0.8948	1.0625	0.4359	353.0	0.9268	1.0752	0.4406	350.7
5	0.8631	1.0385	0.4303	353.7	0.8927	1.0498	0.4346	351.5
10	0.8266	1.0109	0.4240	354.6	0.8537	1.0208	0.4278	352.5
15	0.7933	0.9857	0.4183	355.5	0.8180	0.9943	0.4218	353.5
20	0.7626	0.9626	0.4133	356.3	0.7854	0.9700	0.4164	354.4
25	0.7344	0.9413	0.4089	357.1	0.7554	0.9477	0.4117	355.3
30	0.7083	0.9216	0.4049	357.9	0.7277	0.9271	0.4074	356.2
35	0.6840	0.9033	0.4014	358.7	0.7020	0.9080	0.4037	357.1
40	0.6615	0.8863	0.3982	359.5	0.6782	0.8903	0.4003	358.0
45	0.6405	0.8704	0.3954	360.2	0.6561	0.8738	0.3973	358.8
50	0.6208	0.8556	0.3930	360.9	0.6354	0.8585	0.3947	359.6
55	0.6023	0.8417	0.3908	361.6	0.6160	0.8441	0.3923	360.4
60	0.5850	0.8287	0.3889	362.3	0.5979	0.8305	0.3903	361.1

TABLE S-II. Continued

TABLE S-II. Continued

p / MPa	κ_T GPa $^{-1}$	$\alpha_p \times 10^3$ K $^{-1}$	$c_p - c_v$ kJ kg $^{-1}$ K $^{-1}$	p_{int} MPa	κ_T GPa $^{-1}$	$\alpha_p \times 10^3$ K $^{-1}$	$c_p - c_v$ kJ kg $^{-1}$ K $^{-1}$	p_{int} MPa
343.15 K					353.15 K			
0.1	1.2766	1.1932	0.4671	320.6	1.3897	1.2235	0.4698	310.8
1	1.2613	1.1837	0.4647	321.0	1.3716	1.2128	0.4672	311.3
5	1.1979	1.1441	0.4549	322.7	1.2969	1.1687	0.4564	313.2
10	1.1275	1.0999	0.4441	324.8	1.2147	1.1199	0.4446	315.6
15	1.0652	1.0607	0.4347	326.7	1.1428	1.0769	0.4344	317.8
20	1.0098	1.0256	0.4265	328.5	1.0793	1.0386	0.4255	319.8
25	0.9601	0.9939	0.4192	330.2	1.0228	1.0043	0.4177	321.8
30	0.9154	0.9652	0.4127	331.8	0.9721	0.9734	0.4107	323.6
35	0.8748	0.9390	0.4070	333.4	0.9265	0.9453	0.4045	325.3
40	0.8378	0.9151	0.4018	334.8	0.8852	0.9197	0.3990	326.9
45	0.8039	0.8931	0.3972	336.2	0.8476	0.8962	0.3940	328.4
50	0.7729	0.8727	0.3930	337.5	0.8132	0.8746	0.3895	329.8
55	0.7442	0.8539	0.3892	338.7	0.7816	0.8547	0.3854	331.2
60	0.7177	0.8363	0.3857	339.9	0.7525	0.8361	0.3816	332.4
363.15 K					373.15 K			
0.1	1.5165	1.2548	0.4715	300.4	1.6579	1.2871	0.4724	289.6
1	1.4950	1.2429	0.4686	300.9	1.6323	1.2739	0.4691	290.2
5	1.4067	1.1939	0.4569	303.2	1.5278	1.2197	0.4566	292.9
10	1.3106	1.1401	0.4442	305.9	1.4153	1.1608	0.4432	296.1
15	1.2273	1.0931	0.4333	308.4	1.3190	1.1099	0.4317	299.0
20	1.1545	1.0517	0.4238	310.8	1.2355	1.0652	0.4219	301.7
25	1.0902	1.0147	0.4155	313.0	1.1624	1.0257	0.4132	304.2
30	1.0330	0.9816	0.4082	315.1	1.0979	0.9904	0.4057	306.6
35	0.9818	0.9516	0.4016	317.0	1.0405	0.9586	0.3989	308.8
40	0.9357	0.9244	0.3958	318.8	0.9891	0.9299	0.3929	310.8
45	0.8939	0.8995	0.3905	320.4	0.9428	0.9037	0.3875	312.7
50	0.8559	0.8767	0.3857	322.0	0.9008	0.8797	0.3825	314.4
55	0.8211	0.8557	0.3814	323.4	0.8625	0.8577	0.3780	316.0
60	0.7892	0.8362	0.3773	324.8	0.8276	0.8373	0.3738	317.5
393.15 K					413.15 K			
0.1	—	—	—	—	—	—	—	—
1	1.9514	1.3389	0.4688	268.8	2.3272	1.4084	0.4700	249.0
5	1.8049	1.2743	0.4557	272.6	2.1243	1.3352	0.4587	254.7
10	1.6513	1.2055	0.4419	277.0	1.9175	1.2589	0.4472	261.2
15	1.5229	1.1470	0.4304	281.1	1.7491	1.1954	0.4379	267.4
20	1.4139	1.0965	0.4206	284.9	1.6090	1.1413	0.4303	273.1
25	1.3201	1.0524	0.4122	288.4	1.4907	1.0947	0.4239	278.4
30	1.2385	1.0135	0.4048	291.7	1.3894	1.0538	0.4185	283.3
35	1.1669	0.9788	0.3983	294.8	1.3017	1.0176	0.4138	288.0
40	1.1035	0.9475	0.3926	297.6	1.2248	0.9852	0.4096	292.3
45	1.0470	0.9192	0.3874	300.2	1.1570	0.9560	0.4059	296.4
50	0.9963	0.8935	0.3826	302.6	1.0967	0.9295	0.4025	300.2
55	0.9505	0.8698	0.3783	304.8	1.0426	0.9052	0.3994	303.7
60	0.9089	0.8481	0.3742	306.8	0.9939	0.8829	0.3965	307.0

TABLE S-III. Calculated derived volumetric properties of dichloromethane at different temperatures (288.15–413.15 K) and pressures (0.1–60 MPa)

p / MPa	κ_T GPa $^{-1}$	$\alpha_p \times 10^3$ K $^{-1}$	$C_p - C_V$ kJ kg $^{-1}$ K $^{-1}$	p_{int} MPa	κ_T GPa $^{-1}$	$\alpha_p \times 10^3$ K $^{-1}$	$C_p - C_V$ kJ kg $^{-1}$ K $^{-1}$	p_{int} MPa
288.15 K					293.15 K			
0.1	0.9766	1.3065	0.3774	385.4	1.0154	1.3370	0.3894	385.9
1	0.9690	1.2999	0.3762	385.5	1.0071	1.3298	0.3881	386.1
5	0.9368	1.2717	0.3711	386.2	0.9720	1.2993	0.3824	386.9
10	0.8996	1.2394	0.3654	387.0	0.9316	1.2645	0.3761	387.9
15	0.8654	1.2099	0.3604	387.9	0.8945	1.2329	0.3706	389.0
20	0.8339	1.1830	0.3561	388.8	0.8605	1.2040	0.3659	390.2
25	0.8047	1.1583	0.3523	389.8	0.8291	1.1776	0.3617	391.4
30	0.7776	1.1356	0.3491	390.9	0.8001	1.1534	0.3581	392.6
35	0.7523	1.1147	0.3463	391.9	0.7731	1.1311	0.3550	393.9
40	0.7288	1.0954	0.3439	393.1	0.7480	1.1105	0.3523	395.2
45	0.7068	1.0774	0.3419	394.3	0.7246	1.0914	0.3501	396.6
50	0.6861	1.0608	0.3402	395.5	0.7027	1.0737	0.3482	398.0
55	0.6667	1.0453	0.3389	396.8	0.6821	1.0573	0.3466	399.4
60	0.6484	1.0308	0.3378	398.1	0.6628	1.0420	0.3453	400.9
298.15 K					303.15 K			
0.1	1.0575	1.3681	0.4010	385.6	1.1033	1.3999	0.4121	384.6
1	1.0485	1.3603	0.3995	385.8	1.0933	1.3914	0.4104	384.8
5	1.0100	1.3273	0.3932	386.8	1.0511	1.3557	0.4035	386.0
10	0.9660	1.2898	0.3863	388.1	1.0031	1.3151	0.3959	387.5
15	0.9258	1.2557	0.3803	389.4	0.9594	1.2785	0.3893	389.0
20	0.8890	1.2248	0.3750	390.7	0.9196	1.2453	0.3835	390.5
25	0.8552	1.1965	0.3704	392.1	0.8832	1.2151	0.3784	392.1
30	0.8241	1.1707	0.3664	393.6	0.8497	1.1875	0.3741	393.7
35	0.7952	1.1469	0.3630	395.0	0.8187	1.1621	0.3702	395.3
40	0.7684	1.1250	0.3600	396.5	0.7901	1.1388	0.3669	396.9
45	0.7435	1.1047	0.3575	398.0	0.7635	1.1173	0.3641	398.6
50	0.7202	1.0860	0.3553	399.6	0.7388	1.0974	0.3616	400.3
55	0.6984	1.0685	0.3535	401.2	0.7157	1.0790	0.3596	402.0
60	0.6780	1.0523	0.3520	402.8	0.6941	1.0618	0.3579	403.8
308.15 K					313.15 K			
0.1	1.1529	1.4323	0.4226	382.7	1.2069	1.4654	0.4326	380.1
1	1.1419	1.4231	0.4208	383.0	1.1948	1.4553	0.4306	380.4
5	1.0956	1.3843	0.4132	384.4	1.1437	1.4133	0.4222	382.0
10	1.0430	1.3405	0.4049	386.0	1.0861	1.3660	0.4131	383.9
15	0.9955	1.3011	0.3976	387.8	1.0343	1.3236	0.4051	385.8
20	0.9524	1.2655	0.3912	389.5	0.9874	1.2855	0.3981	387.7
25	0.9130	1.2332	0.3857	391.2	0.9449	1.2509	0.3921	389.6
30	0.8770	1.2038	0.3808	393.0	0.9060	1.2194	0.3868	391.5
35	0.8438	1.1768	0.3766	394.8	0.8704	1.1907	0.3822	393.4
40	0.8132	1.1520	0.3730	396.5	0.8377	1.1644	0.3781	395.3
45	0.7848	1.1292	0.3698	398.3	0.8074	1.1402	0.3746	397.2
50	0.7585	1.1081	0.3670	400.2	0.7794	1.1178	0.3715	399.1
55	0.7340	1.0885	0.3647	402.0	0.7534	1.0972	0.3688	401.0

TABLE S-III. Continued

p / MPa	κ_T GPa ⁻¹	$\alpha_p \times 10^3$ K ⁻¹	$c_p - c_v$ kJ kg ⁻¹ K ⁻¹	P_{int} MPa	κ_T GPa ⁻¹	$\alpha_p \times 10^3$ K ⁻¹	$c_p - c_v$ kJ kg ⁻¹ K ⁻¹	P_{int} MPa
308.15 K								
60	0.7111	1.0704	0.3627	403.8	0.7291	1.0780	0.3665	403.0
318.15 K								
0.1	—	—	—	—	—	—	—	—
1	1.2522	1.4882	0.4398	377.1	1.3147	1.5218	0.4482	373.1
5	1.1959	1.4427	0.4306	378.8	1.2523	1.4723	0.4382	374.9
10	1.1325	1.3915	0.4205	380.9	1.1826	1.4171	0.4272	377.2
15	1.0759	1.3459	0.4118	383.0	1.1206	1.3680	0.4177	379.5
20	1.0250	1.3050	0.4042	385.1	1.0652	1.3241	0.4094	381.7
25	0.9789	1.2680	0.3976	387.1	1.0152	1.2846	0.4022	383.9
30	0.9370	1.2345	0.3918	389.2	0.9700	1.2489	0.3959	386.1
35	0.8988	1.2040	0.3868	391.2	0.9288	1.2164	0.3904	388.2
40	0.8637	1.1760	0.3823	393.2	0.8912	1.1868	0.3855	390.3
45	0.8314	1.1503	0.3784	395.2	0.8567	1.1596	0.3812	392.4
50	0.8015	1.1267	0.3750	397.2	0.8249	1.1346	0.3774	394.5
55	0.7739	1.1048	0.3719	399.2	0.7955	1.1115	0.3740	396.5
60	0.7482	1.0845	0.3693	401.2	0.7682	1.0901	0.3710	398.5
328.15 K								
0.1	—	—	—	—	—	—	—	—
1	1.3827	1.5561	0.4559	368.3	1.4567	1.5910	0.4629	362.9
5	1.3135	1.5023	0.4450	370.3	1.3797	1.5327	0.4510	365.1
10	1.2366	1.4426	0.4330	372.8	1.2948	1.4681	0.4380	367.8
15	1.1687	1.3898	0.4227	375.3	1.2202	1.4114	0.4268	370.4
20	1.1082	1.3428	0.4137	377.6	1.1542	1.3610	0.4171	372.9
25	1.0540	1.3006	0.4059	379.9	1.0953	1.3160	0.4086	375.3
30	1.0051	1.2626	0.3990	382.2	1.0424	1.2756	0.4012	377.7
35	0.9608	1.2281	0.3930	384.5	0.9947	1.2390	0.3947	380.0
40	0.9204	1.1967	0.3877	386.6	0.9513	1.2057	0.3888	382.2
45	0.8835	1.1679	0.3829	388.8	0.9118	1.1753	0.3837	384.4
50	0.8496	1.1415	0.3787	390.9	0.8756	1.1474	0.3791	386.5
55	0.8183	1.1171	0.3750	393.0	0.8424	1.1217	0.3749	388.6
60	0.7894	1.0945	0.3716	395.0	0.8117	1.0979	0.3712	390.6
343.15 K								
0.1	—	—	—	—	—	—	—	—
1	1.6251	1.6632	0.4746	350.2	1.8248	1.7386	0.4834	335.5
5	1.5292	1.5944	0.4606	352.8	1.7044	1.6576	0.4671	338.4
10	1.4250	1.5191	0.4454	355.8	1.5756	1.5701	0.4497	341.9
15	1.3347	1.4537	0.4325	358.7	1.4657	1.4950	0.4349	345.2
20	1.2557	1.3961	0.4212	361.5	1.3710	1.4295	0.4221	348.2
25	1.1860	1.3450	0.4114	364.2	1.2883	1.3719	0.4110	351.1
30	1.1240	1.2994	0.4028	366.7	1.2155	1.3208	0.4013	353.7
35	1.0685	1.2583	0.3952	369.1	1.1509	1.2750	0.3926	356.2
40	1.0185	1.2212	0.3884	371.4	1.0932	1.2338	0.3849	358.6
45	0.9732	1.1873	0.3823	373.6	1.0413	1.1963	0.3779	360.7
50	0.9320	1.1564	0.3769	375.7	0.9943	1.1622	0.3716	362.8

TABLE S-III. Continued

p / MPa	κ_T GPa ⁻¹	$\alpha_p \times 10^3$ K ⁻¹	$c_p - c_v$ kJ kg ⁻¹ K ⁻¹	P_{int} MPa	κ_T GPa ⁻¹	$\alpha_p \times 10^3$ K ⁻¹	$c_p - c_v$ kJ kg ⁻¹ K ⁻¹	P_{int} MPa
343.15 K								
55	0.8944	1.1279	0.3719	377.8	0.9517	1.1309	0.3658	364.7
60	0.8598	1.1016	0.3674	379.7	0.9127	1.1021	0.3605	366.4
363.15 K								
0.1	—	—	—	—	—	—	—	—
1	2.0610	1.8176	0.4894	319.2	2.3389	1.9003	0.4935	302.2
5	1.9088	1.7226	0.4710	322.7	2.1456	1.7899	0.4731	306.3
10	1.7489	1.6216	0.4515	326.7	1.9466	1.6745	0.4518	311.0
15	1.6149	1.5359	0.4350	330.4	1.7830	1.5779	0.4340	315.2
20	1.5009	1.4621	0.4208	333.8	1.6460	1.4956	0.4187	319.1
25	1.4028	1.3977	0.4085	336.8	1.5296	1.4244	0.4055	322.5
30	1.3173	1.3409	0.3977	339.7	1.4293	1.3621	0.3939	325.6
35	1.2421	1.2903	0.3880	342.2	1.3421	1.3069	0.3836	328.4
40	1.1755	1.2449	0.3794	344.6	1.2654	1.2575	0.3743	330.8
45	1.1160	1.2039	0.3716	346.7	1.1974	1.2130	0.3658	333.0
50	1.0626	1.1666	0.3645	348.7	1.1368	1.1726	0.3580	334.9
55	1.0144	1.1325	0.3579	350.4	1.0824	1.1358	0.3508	336.6
60	0.9705	1.1011	0.3519	352.0	1.0332	1.1019	0.3440	338.0
393.15 K								
0.1	—	—	—	—	—	—	—	—
1	3.0323	2.0785	0.4989	268.5	3.8848	2.2767	0.5141	241.1
5	2.7208	1.9369	0.4776	274.9	3.4026	2.1181	0.5007	252.2
10	2.4148	1.7940	0.4559	282.1	2.9522	1.9630	0.4877	264.7
15	2.1736	1.6778	0.4380	288.5	2.6121	1.8400	0.4774	276.0
20	1.9784	1.5810	0.4229	294.2	2.3458	1.7389	0.4687	286.3
25	1.8170	1.4985	0.4098	299.2	2.1313	1.6536	0.4613	295.6
30	1.6812	1.4271	0.3982	303.7	1.9547	1.5802	0.4545	304.0
35	1.5653	1.3644	0.3878	307.7	1.8066	1.5159	0.4484	311.7
40	1.4652	1.3087	0.3784	311.1	1.6806	1.4588	0.4426	318.6
45	1.3778	1.2587	0.3697	314.2	1.5720	1.4075	0.4370	324.9
50	1.3008	1.2135	0.3615	316.8	1.4773	1.3610	0.4315	330.6
55	1.2324	1.1722	0.3538	318.9	1.3941	1.3185	0.4261	335.7
60	1.1713	1.1344	0.3465	320.8	1.3203	1.2794	0.4205	340.3



Preparation and characterization of a new polyaniline salt with good conductivity and great solubility in dimethyl sulphoxide

HICHEM ZEGHIOUD^{1*}, SAAD LAMOURI¹, YASMINE MAHMOUD¹
and TARIK HADJ-ALI²

¹Laboratoire de Chimie Macromoléculaire, Ecole Militaire Polytechnique, BP 17,
Bordj El Bahri, Alger, Algeria and ²Laboratoire des systèmes électroniques et
optroniques, Ecole Militaire Polytechnique, BP 17, Bordj El Bahri, Alger, Algeria

(Received 5 March, revised 2 June, accepted 18 June 2015)

Abstract: In this study, a novel conducting and soluble polyaniline salt prepared by chemical polymerization in the presence of a new doping agent (IAs) is proposed. This doping agent was prepared by the sulphonation of itaconic acid (IA) with concentrated sulphuric acid in tetrahydrofuran (THF). The obtained doped polyaniline (PANI-IAs) was extremely soluble in dimethyl sulphoxide (DMSO) at room temperature, in which the solubility reached 44 mg mL⁻¹. The conductivity measurement of doped polyaniline powder precipitated in THF as dispersing medium gave a value of 0.13 S cm⁻¹ when the emeraldine base form of polyaniline was fully protonated. The polyaniline salt sample was characterized by thermogravimetry (TG), differential scanning calorimetry (DSC), X-ray diffraction and UV–Vis and FTIR spectroscopy.

Keywords: conducting polymer; PANI; itaconic acid; sulphonation; solubility.

INTRODUCTION

Intrinsically conducting polymers (ICPs) have attracted important attention in many advanced applications. Among ICPs, polyaniline (PANI) is one of the essential conductive polymer for its wide use in many domains, such as organic lightweight batteries,¹ electro-chromic display devices,^{2,3} photo-electronic devices,⁴ chemical sensors^{5,6} and hydrogen storage.⁷ Polyaniline has been considered as one of the most promising electrode materials due to its simple synthesis, environmental stability, unique electronic properties, and simple acid–base doping/dedoping chemistry.^{8,9} On the other hand, the intractable solubility of PANI in common organic solvents has limited its practical applications in many fields. It is therefore a very important challenge to design doped polyaniline and its derivatives in forms that are easily processable and applicable. In

*Corresponding author. E-mail: hicheming@yahoo.fr
doi: 10.2298/JSC150305064Z

recent years, a number of studies were focused on the improvement of PANI solubility, a variety of methods were proposed that consisted in doping PANI emeraldine base (PANI-EB) by extended organic alkyls of sulphonic acids (DBSA and CSA)^{10–12} or with polymeric acids.^{13–16}

In 2009, Peng studied an emulsion polymerization process that had been developed for the direct synthesis of organo-soluble polyaniline (PANI) with oleic acid (OA) as a surfactant and dopant.¹⁷ Gribkova *et al.*, reported the chemical synthesis of polyaniline in the presence of polymeric acids (such as poly(amidosulphonic acids)), which contain sulphonic groups in the chemical structure. They found that the matrix polymerization of aniline resulted in the formation of water-soluble interpolymer complexes of PANI with polyacid.¹⁸ In 2015, Zeghioud *et al.* prepared soluble polyaniline salts doped with poly(itaconic acid); they found that the solubility reaches 4 mg mL^{−1} in an optimized mixture of THF/water at room temperature.¹⁹

Wang *et al.* prepared polyaniline nanorods by chemical oxidation polymerization using itaconic acid as dopant. The obtained polyaniline salt, compared to the undoped form, possesses high productivity, conductivity and excellent solubility in organic solvents (*N*-methylpyrrolidone, NMP, tetrahydrofuran, THF, and dimethyl formamide, DMF), which reached 19 mg mL^{−1}.²⁰

In this work, a new and low-cost sulphonic dopant was prepared from itaconic acid (a platform chemical produced from renewable resources) by a simple chemical reaction. Therefore, the development of a new polyaniline salt with simultaneously very good solubility (in common solvents) and good electrical conductivity is a challenge and it was the aim of the present study. The structure, spectroscopic properties, thermal stability and conductivity of the obtained polyaniline were also investigated.

EXPERIMENTAL

Materials

Aniline (ANI, 99b% pure) was purchased from Fluka. The other employed materials were hydrochloric acid (35.37 %) from Organics Stinnes Chemicals, methanol (99.5 %) and ammonium peroxodisulphate (APS, 99 %) from Prolabo, acetone (99 %) from Acros Organics. While ammonia (25 % solution), *N*-methylpyrrolidone (NMP, 99.5 %) and tetrahydrofuran (99 %) were from Merck. Itaconic acid (IA, 99 %) was from Aldrich, dimethyl sulfoxide (DMSO, 100 %) and dimethyl formamide (DMF, 100 %) from Sigma-Aldrich. All these products were used without further purification.

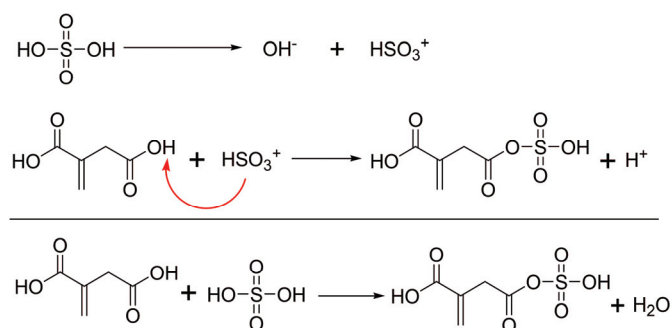
Synthesis of PANI

Polyaniline powder in the emeraldine salt form was synthesized as follows: 4.8 g of aniline (4.75 mL) and 15 mL of HCl were dispersed in 50 mL of deionised water under vigorous stirring at room temperature for 2 h, to obtain a uniform solution. An aqueous solution of APS (11.8 g of APS + 50 mL of deionised water) was slowly added to the above mixture with mole ratio equal to one (APS/ANI = 1). The resulting solution was stirred for 30 min to ensure complete mixing. Then, the reaction was followed by continuous stirring at 2 °C

for about 4 h. Finally, the formed precipitate was filtered, washed successively with distilled water followed by methanol (to remove oligomers and other by-products) until the filtrate was colourless, and then dried at 60 °C for 48 h. The polyaniline salt (PANI–HCl) was converted to base form (PANI–EB) by treatment with aqueous NH₄OH solution for 72 h, followed by washing with distilled water and methanol; the base form of PANI was obtained as a blue powder. The polymerization yield was 80 %.

Synthesis of the dopant

Itaconic acid sulphonated (IAs) was prepared by chemical reaction between itaconic acid (IA) and a concentrated sulfuric acid as follows: 3 g of IA was dissolved in 10 ml of THF under continuous stirring in round-bottom flask (triple-neck type); the system was placed in a thermostatic bath at 40 °C. A small quantity of sulfuric acid was added drop by drop to the above solution with the help of dropping funnel to a mole ratio equal to one. The solution was left under constant stirring for 3 days. Subsequently, the product (IAs) was separated by drying for 5 days at 70 °C. The possible reaction mechanism is presented in Scheme 1.



Scheme 1. Plausible mechanism of the sulphonation reaction.

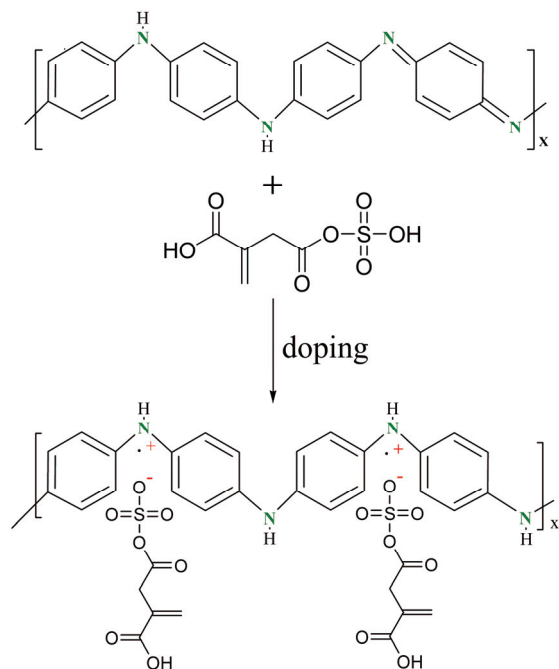
Doping

For the preparation of sulphonated acid doped polyaniline, undoped PANI solution in THF (or another organic solvent) was mixed with IAs in mole ratio equal to two between IAs and tetrameric repeat unit of PANI–EB. The mixture was transferred to an ultrasound bath for 2 h, followed by constant agitation for 6 h. A dark green colour was obtained. The PANI–IAs dispersion (in THF or NMP) was filtered using polytetrafluoroethylene (PTFE) filters, washed and dried at 60 °C for 24 h. The reaction mechanism is shown in Scheme 2. The obtained apparent viscometric average molar mass of the sulphonated itaconic acid-doped polyaniline (PANI–IAs) was $\bar{M}_v = 4430 \text{ g mol}^{-1}$.

Characterization

Fourier transform infrared (FTIR) spectra were recorded between 400 and 4000 cm⁻¹ from KBr pellets on an infrared Fourier transform spectrometer (Shimadzu type 8400 S). UV–Vis spectra of all samples dissolved in different solvents were recorded using a Shimadzu UV-2401PC UV–Vis spectrometer with a resolution of 2 nm, in the wavelength range of 300–900 nm. X-Ray powder diffraction patterns were recorded on a PANalytical X'Pert PRO diffractometer fitted with CuK α radiation ($\lambda = 1.5404 \text{ nm}$) at 40 kV and 40 mA in the 4–60° 2θ region. Thermogravimetry (TG) was performed using Setaram an MTB thermogravimetric instrument at a sensitivity of “10⁻⁸”, operating at a heating rate of 10 °C min⁻¹, from room

temperature up to 450 °C under an air atmosphere. The sample mass ranged between 3 and 6 mg. The differential scanning calorimetry (DSC) measurements were realised on a Netzsch DSC 204 F1 at a scanning rate of 10 °C min⁻¹ from room temperature up to 400 °C under an inert atmosphere.



Scheme 2. Mechanism of PANI doping with IAs.

RESULTS AND DISCUSSION

Conductivity measurements

The conductivity measurements on compressed pellets of various forms of PANI powder prepared by chemical polymerization were made by the conventional four-point probe technique at room temperature. For IAs-doped polyaniline, the powder was obtained by filtration and drying of the precipitate formed in the dispersion of THF and NMP.

The band gap in eV was calculated by the equation:²¹

$$E_g = \frac{1237.5}{\lambda} \quad (1)$$

where λ represents the maximum wavelength (nm) in the band attributed to $\pi-\pi^*$ (Band 1) transitions. The measured values of conductivity are given in Table I; PANI-HCl has better conductivity (4.6 S cm⁻¹) than PANI-IAs. This was confirmed by the smaller band gap of PANI-HCl, around 3.2 eV, compared with that of PANI-IAs (3.62 eV). However, the conductivity value of the latter depended

strongly on the dispersion medium during synthesis, whereby the highest value (0.13 S cm^{-1}) was obtained in THF.

TABLE I. Conductivities and energy band gap of different forms of PANI

Sample (dispersion medium)	UV-Vis band, nm		Conductivity S cm^{-1}	Band gap energy eV
	1	2		
PANI-HCl	387	467	4.60	3.20
PANI-EB	331	626	8.14×10^{-10}	—
PANI-IAs (THF)	—	—	0.13	3.62
PANI-IAs (NMP)	—	—	0.01	—
PANI-IAs (DMSO)	342	417	—	—

UV-Vis spectroscopy

The UV-Vis spectrum of undoped polyaniline included two absorption bands at 331 and 626 nm due to the excitation of the benzoid and quinoid segments in the polyaniline chain, respectively,²² (Fig. 1, curve (a)).

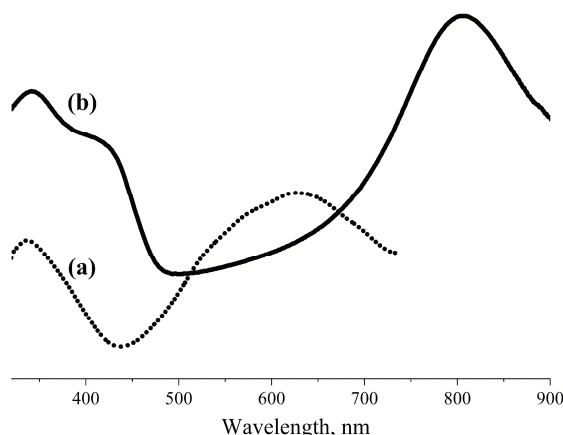


Fig. 1. UV-Vis spectra of: a) PANI-EB and b) PANI-IAs recorded in DMSO solvent.

Curve (b) in Fig. 1 illustrates the UV-Vis spectrum after IAs had been added to the DMSO containing PANI-EB. Thus, the absorption band at 626 nm disappeared. However, the characteristic polaron band would appear at 807 nm. The characteristic absorption bands in the spectrum of PANI-IAs are clearly observed at about 807 and 417 nm, which are attributed to the transitions from the π band to the polaron band and from the polaron band to the π^* band of the alternating benzoid-quinoid structures, respectively.²³ The band around 342 nm is referred to the transition from the π band to the π^* band centred on the benzoid rings associated with the extended π orbitals on polymer backbone (band gap excitation).²⁴

Fourier transform infrared spectroscopy (FTIR)

The FTIR spectra of IA and IAs samples are shown in Fig. 2. The spectrum of IA and IAs presented a broad band centred at 2926 cm^{-1} , which is attributed to O–H stretching vibrations. The spectrum of IA (curve a) showed peaks around 1718 , 1430 , and 1190 cm^{-1} , indicating the stretching C=O (carboxylic acid), C–O–H in the plane and C–O, respectively.^{25,26}

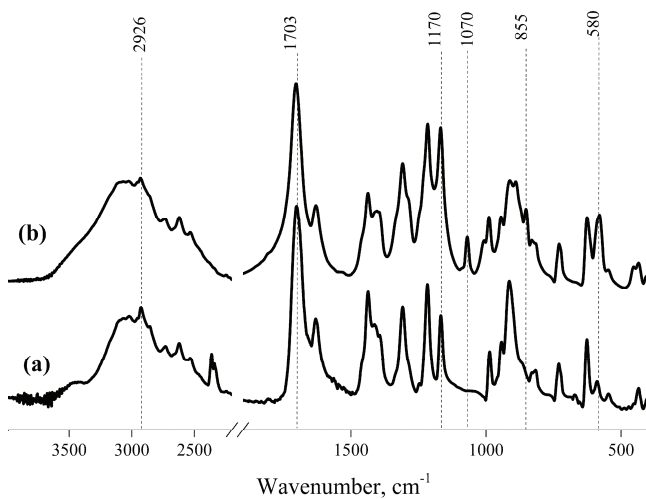


Fig. 2. FTIR spectra of: a) IA and b) IAs.

The spectrum of IA obtained after sulphonation (curve b) showed the characteristic absorption band for the acid carbonylic groups at 1703 cm^{-1} .²⁷ The peaks around 1400 and 1170 cm^{-1} were assigned to the stretching vibrations of C–O–H of carboxylic acid and asymmetrical stretching of SO_2 , respectively. New peaks appeared at 1070 and 855 cm^{-1} , which are attributed to the stretching vibration of symmetrical SO_2 and the bending of O–S, respectively.^{27–29} The non-disappearance of the C=C peak at 1629 cm^{-1} confirmed the sulphonation of IA by sulphuric acid according to the mechanism proposed in the Scheme 1.

Figure 3 shows the FTIR spectra of PANI–EB and PANI–IAs. In the spectrum of PANI–EB (curve a), the characteristic absorption peaks at 1583^{30} and 1494^{31} cm^{-1} could be assigned to the C=C stretching mode for the quinoid rings and the C=C stretching mode for the benzoid rings, respectively. The absorption peak at 1303 cm^{-1} corresponds to the C–N stretching mode. The in-plane bending of C–H is reflected in the 1160 cm^{-1} peak, and the out-of-plane bending vibration of C–H occurred at 508 cm^{-1} .^{31–33} In the spectrum of PANI–IAs (curve c), the characteristic peaks at 1562^{27} and 1470^{28} cm^{-1} could be assigned to the C=C stretching mode for the quinoid rings and the C=C stretching mode for the benzoid rings, respectively. Two absorption peaks at 1303 and 1240 cm^{-1} corres-

pond to the C–N stretching³³ and C–N stretching of protonated mode,³⁰ respectively. The in-plane bending of C–H was reflected in the 1121 cm⁻¹ peak, and the out-of-plane bending vibration of C–H occurred at 508 cm⁻¹.²⁷ The shift of the characteristic peaks of PANI indicated strong interaction between PANI–EB and the dopant.

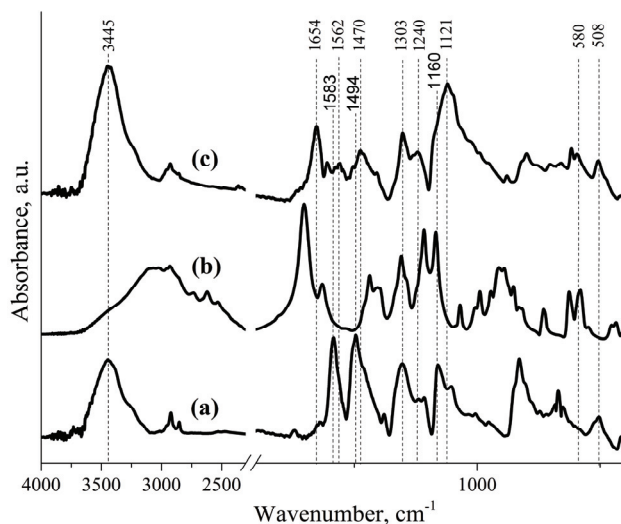


Fig. 3. FTIR spectra of: a) PANI–EB, b) IAs and c) PANI–IAs.

Solubility determination

The PANI–IAs was synthesized in different polar solvents, such as NMP, DMSO, THF and DMF (Fig. 4). The obtained dispersions (in THF and NMP) were filtered using 0.45-μm PTFE filters, washed and dried to recover the PANI–IAs powder.

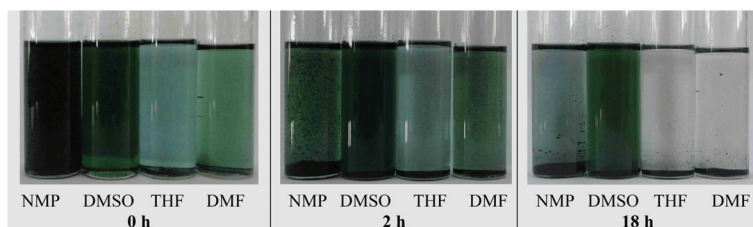


Fig. 4. PANI–IAs dispersions in different solvents.

Figure 4 shows the very good solubility in NMP and DMSO just after doping. After 2 h, strong interactions between the polymers chains were clearly detected in all dispersion media except for the PANI–IAs/DMSO solution. After filtration and UV–Vis analysis of the resulting solutions, DMSO was found to be

the only solvent capable of dissolving the PANI-IAs chains at room temperature. The maximum solubility was determined by calculation of the difference between the densities of PANI-IAs/DMSO solution and pure DMSO; it was found that the solubility could reach 44 mg mL^{-1} . From this, it was concluded that DMSO is a very good solvent for PANI-IAs, which is confirmed by Fig. 5.



Fig. 5. Digital photos of solutions of: a) concentrated and b) dilute solution of PANI-IAs in DMSO solvent.

Polyaniline is soluble only in DMSO because the interactions between the PANI chains and DMSO are more important than the interactions between the polyaniline chains that increases the distance between the molecular chains and gives a relatively extended conformation to these chains. Thus, the solubility of polyaniline is primarily controlled by the molecular structures of the polymer chain (including the doping agent) and the solvent properties (polarity, number of carboxylic groups and molecular size).

X-Ray diffraction pattern (XRD)

The X-ray diffraction pattern of the PANI-EB and PANI-IAs powder are presented in Fig. 6. The crystalline region presented by the peak and the amorphous region presented by the remainder of diffractogramme were both integ-

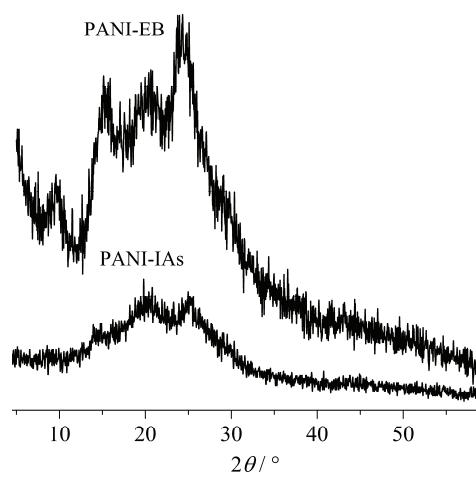


Fig. 6. XRD Patterns of PANI-EB and PANI-IAs.

rated in 2θ space. From these integrated peaks areas (I_c, I_a), the ratio X_c/X_a can be calculated from $X_c/X_a = 1.8(I_c/I_a)$. A Ryland factor of 1.8 is commonly used for semi-crystalline polymers.³⁴ The percentage crystallinity X_c (%) was obtained from Eq. (2):³⁴

$$X_c (\%) = 100 - \frac{100}{(1 + X_c / X_a)} \quad (2)$$

The XRD profile of PANI-EB showed a number of narrow sharp reflection peaks at 2θ 9.54, 15.22, 20.75 and 24.29°, representing the (001), (011), (100) and (110) crystal planes, respectively (Table II). The peak centred at $2\theta \sim 20^\circ$ may be ascribed to periodicity parallel to the polymer chain, while the peak at $2\theta \sim 25^\circ$ may be caused by periodicity perpendicular to the polymer chain.³⁵

TABLE II. The 2θ values, intensity and indexation (hkl) of PANI-EB and PANI-IAs

Sample	$2\theta / ^\circ$	$d / \text{\AA}$	hkl	Ref.	$X_c / \%$
PANI-EB	09.57	09.23	001	36	9.64
	15.22	05.82	011	27	
	20.75	04.28	100	37	
	24.29	03.66	110	38	
PANI-IAs	08.63	10.23	001	37	8.70
	14.20	06.23	011	39	
	19.73	04.49	100	36	
	25.19	03.54	110	38	

After conversion of PANI-EB into PANI-IAs, broad diffuse peaks centred at 2θ 8.63 (001) and 14.2° (011) appeared, and two small peaks at 2θ 19.73 (100) and 25.19° (110) were observed. Compared to PANI-EB, the intensities of the two last peaks (2θ 19.73 and 25.19°) were strongly reduced.⁴⁰ This was proved by the decrease in the degree of crystallinity (X_c) from 9.64 % for PANI-EB to 8.70 % for PANI-IAs.

Thermogravimetry (TG)

The thermal stability of the PANI-IAs was evaluated using TG. Polyaniline salt powder (PANI-IAs) showed poor thermal stability. As seen in Fig. 7, the degradation occurred in three stages; the first mass loss was assigned to the evaporation of water and residual solvents,^{41,42} in the second temperature region (200–270 °C), the degradation was due to the start of loss of the sulphonic and carboxylic groups of itaconic acid.⁴³ This was followed by a broad loss of mass starting from 270 °C. This mass loss was probably due to the dehydration and the decomposition of the chemical structure of the short PANI chains.⁴⁴

It is important to notice that more than 50% of the initial mass was conserved for temperatures up to 500 °C. This residual mass was related to the existence of reticule polymer, which is formed at high temperatures.⁴⁵

DSC thermal analysis

The DSC curve for PANI–IAs (Fig. 8) showed two endothermic peaks around 35–184 °C and 200–350 °C. The first endothermic transition is related to the excess water existing in the PANI lattice that influences the conductivity and crystal structure of PANI.⁴⁶ The second thermal transition, which was centred at 290 °C, involved the beginning of PANI–IAs degradation (decarboxylation) and the detachment of doping agent. In Fig. 9, there was an absence of dopant carboxylic groups after DSC analysis, which confirmed that complete decarboxylation had occurred.

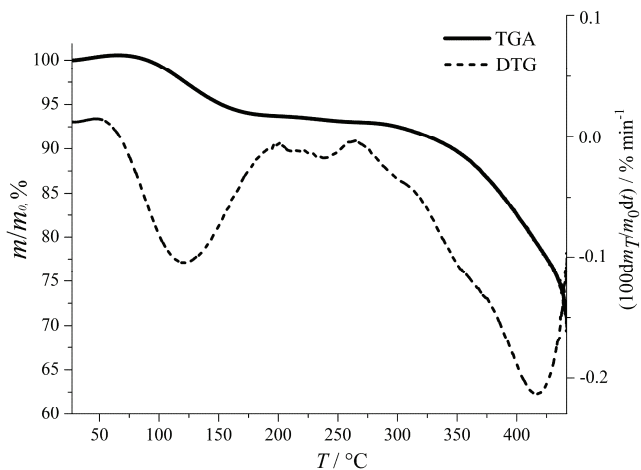


Fig. 7. Thermogravimetric analysis of PANI–IAs.

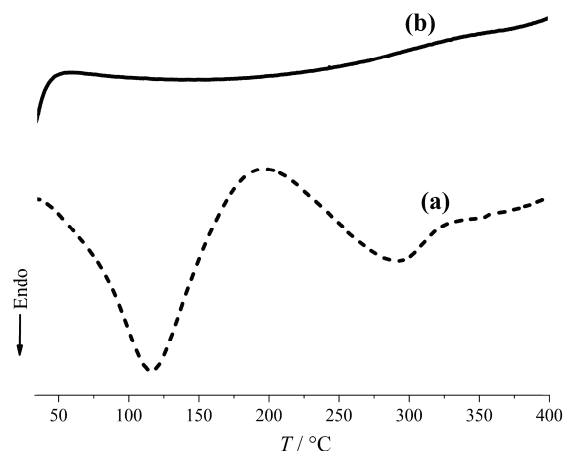


Fig. 8. DSC thermal analysis curves of the PANI–IAs powder under a nitrogen atmosphere: a) first run and b) second run (heating rate: 10 °C min⁻¹).

The curve b shown in Fig. 8 represents the second scan DSC thermogram of the same PANI–IAs sample. There are no significant endothermic or exothermic

peaks on this curve. This is because almost all the moisture had evaporated from the PANI-IAs sample during the first thermal treatment run. Moreover, a cross-linking reaction may have occurred during the first thermal analysis run and may have resulted in a 3D chemical structure. This crosslinking reaction, illustrated in Scheme 3,⁴⁷ was the result of the coupling of two neighbouring $-N=Q=N-$ groups.

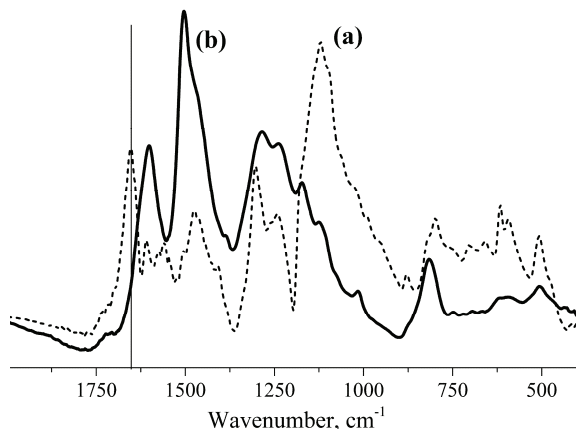
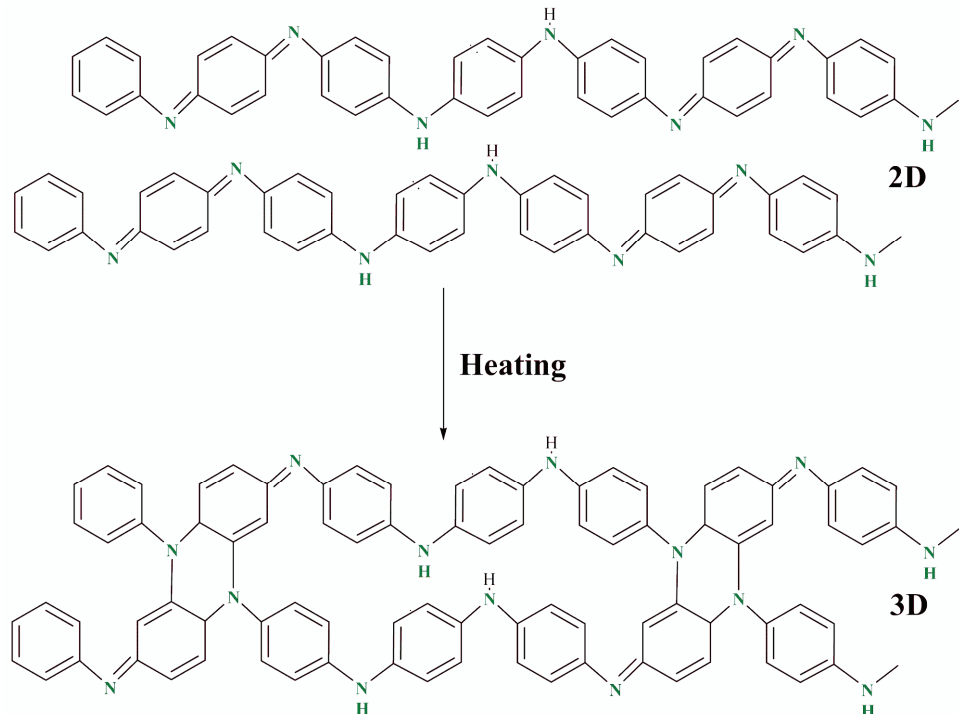


Fig. 9. FTIR spectra of PANI-IAs:
a) before and b) after DSC analysis.



Scheme 3. Thermal crosslinking reaction between the PANI molecular chains.

CONCLUSIONS

The sulphonation of itaconic acid was successfully performed in a simple chemical reaction. The doping of PANI-EB by the synthesised dopant (IAs) was effectively realised. The results of this study provide further that the use of IAs as a novel sulphonic dopant for polyaniline delivers a significant improvement in the solubility of the polyaniline salt compared to those reported previously. The maximum solubility reached 44 mg mL^{-1} in pure DMSO as polar organic solvent at room temperature. It was shown that a conducting form of PANI that is thermally stable up to 200°C could be prepared. The characterization of the PANI-IAs confirmed the success in obtaining good conductivity that reaches 0.13 S cm^{-1} for fully doped PANI-EB. A low degree of crystallinity was found for the conducting form of PANI compared to the non-doped one.

ИЗВОД

СИНТЕЗА И КАРАКТЕРИЗАЦИЈА НОВЕ ПРОВОДНЕ И У ДИМЕТИЛСУЛФОКСИДУ
ВЕОМА РАСТВОРНЕ СОЛИ ПОЛИАНИЛИНАHICHEM ZEGHIOUD¹, SAAD LAMOURI¹, YASMINE MAHMOUD¹ и TARIK HADJ-ALI²¹Laboratoire de Chimie Macromoléculaire, Ecole Militaire Polytechnique, BP 17, Bordj El Bahri, Alger, Algeria и ²Laboratoire des systèmes électroniques et optroniques, Ecole Militaire Polytechnique, BP 17, Bordj El Bahri, Alger, Algeria

У раду је приказана синтеза нове растворне и проводне соли полианилина оксидативном полимеризацијом у присуству новог агенса за допирање. Агенс за допирање (IAs) је синтетисан сулфоновањем итаконске киселине (IA) концентрованом сумпорном киселином у тетрахидрофурану (THF). Со допиреног полианилина (PANI-IAs) је веома растворна у диметилсулфоксиду (DMSO) на собној температури, при чему се достиже растворљивост од 44 mg mL^{-1} . Мерења проводљивости допиреног полианилина, добијеног таложењем у THF, показала су да се максимална проводљивост од 0.13 S cm^{-1} достиже у при потпуном протоновању полианилина у облику емералдинске базе. Поред тога, узорци соли полианилина су карактерисани термогравиметријском анализом (TGA), диференцијалном сканирајућом спектроскопијом (DSC), дифракцијом X-зрака (XRD), као и UV-Vis и FTIR спектроскопијом.

(Примљено 5. марта, ревидирано 2. јуна, прихваћено 18. јуна 2015)

REFERENCES

1. R. Garjonte, A. Malinauskas, *Biosens. Bioelectronics* **15** (2000) 445
2. L. B. Hu, G. Gruner, D. Li, R. B. Kaner, J. Cech, *J. Appl. Phys.* **101** (2007) 016102
3. P. Camurlu, A. Cirpan, L. Toppare, *Mater. Chem. Phys.* **92** (2005) 413
4. T. Yamamoto, Y. Umemura, M. Nakagawa, T. Iyoda, Y. Einaga, *Thin Solid Films* **515** (2007) 5476
5. H. L. Tai, Y. D. Jiang, G. Z. Xie, K. Q. Yu, X. Chen, Z. H. Ying, *Sensors Actuators, B* **129** (2008) 319
6. H. Bai, L. Zhao, C. H. Lu, C. Li, G. Q. Shi, *Polymer* **50** (2009) 3292
7. J. Germain, J. M. J. Frechet, F. Svec, *J. Mat. Chem.* **17** (2007) 4989
8. X. Lu, W. Zhang, C. Wang, T. C. Wen, Y. Wei, *Prog. Polym. Sci.* **36** (2011) 671
9. D. Li, J. Huang, R. B. Kaner, *Acc. Chem. Res.* **42** (2009) 135

10. H. Xie, Y. Ma, D. Feng, *Eur. Polym J.* **36** (2000) 2201
11. J. Kim, S. Kwon, D. Ihm, *Curr. Appl. Phys.* **7** (2007) 205
12. E. Ruckenstein, W. Yin, *J. Appl. Polym. Sci.* **79** (2001) 80
13. K. Shannon, J. E. Fernandez, *J. Chem. Soc. Chem. Commun.* (1994) 643
14. L. Sun, H. Liu, R. Clark, S. C. Yang, *Synth. Met.* **85** (1997) 67
15. Y. Guo-Li, K. Noriyuki, S. Shi-Jian, *Synth. Met.* **129** (2002) 173
16. J. Tarver, J. E. Yoo, T. J. Dennes, J. Schwartz, Y. L. Loo, *Chem. Mater.* **21** (2009) 280
17. L. Peng, *Synth. Met.* **159** (2009) 148
18. O. L. Gribkova, A. A. Nekrasov, M. Trchova, V. F. Ivanov, V. I. Sazikov, A. B. Razova, V. A. Tverskoy, A. V. Vannikov, *Polymer* **52** (2011) 2474
19. H. Zeghioud, S. Lamouri, Z. Safidine, M. Belbachir, *J. Serb. Chem. Soc.* **80** (2015) 917
20. Y. Wang, H. Zheng, L. Jia, H. Li, T. Li, K. Chen, Y. Gu, J. Ding, *J. Macromol. Sci., A* **51** (2014) 577
21. F. C. Tsai, C. C. Chang, C. L. Liu, W. C. Chen, S. A. Jenekhe, *Macromolecules* **38** (2005) 1958
22. Y. Chunmirtg, F. Zheng, Z. Pingn, *J. Cent. South Univ. Technol.* **6** (1999)
23. J. Chen, B. J. Winther, Y. Pornputtkul, K. West, L. M. Kane, G. G. Wallace, *Electrochem. Solid State Lett.* **9** (2006) 11
24. I. Sasaki, J. Janata, M. Josowicz, *Polym. Degrad. Stab.* **92** (2007) 1408
25. B. H. Stuart, *Infrared spectroscopy: fundamentals and applications*, Wiley, Chichester, 2004, p. 71
26. B. D. Mistry, *A Handbook of Spectroscopic Data Chemistry (UV, IR, PMR, ¹³CNMR and Mass Spectroscopy)*, Oxford Book Co., Jaipur, 2009, p. 26
27. L. Xin, W. Meixiang, L. Xiaoning, Z. Guoliang, *Polymer* **50** (2009) 4529
28. C. Yin-Ju, D. D. Nguyen, L. Yu-An, Y. Ming-Chuen, H. Wen-Kuang, T. Nyan-Hwa, *Diam. Relat. Mater.* **20** (2011) 1183
29. I. Shoji, M. Kazuhiko, T. Seiichi, A. Ryuji, A. Yoshinobu, T. Kohshin, M. H. Brian, *Synth. Met.* **96** (1998) 161
30. X. Peipei, T. Qunwei, C. Haiyan, H. Benlin, *Electrochim. Acta* **125** (2014) 163
31. B. Kutlu, A. Leuteritz, R. Boldt, J. Dieter, U. Wagenknecht, G. Heinrich, *Appl. Clay Sci.* **72** (2013) 91
32. M. Hasik, A. Drelinkiewicz, E. Wenda, C. Paluszkiewicz, S. Quillard, *J. Mol. Struct.* **596** (2001) 89
33. H. Xiaoyun, G. Ligang, J. Haihui, Z. Lichun, L. Hong, Z. Wei, *Synth. Met.* **171** (2013) 1
34. P. J. Rae, D. M. Dattelbaum, *Polymer* **45** (2004) 7615
35. T. Abdiryim, Z. Xiao-Gang, R. Jamal, *Mater. Chem. Phys.* **90** (2005) 367
36. P. Rannou, M. Nechtschein, J. P. Travers, D. Bernera, A. Walter, D. Djurado, *Synth. Met.* **101** (1999) 734
37. D. Yuping, W. Guangli, L. Xiaogang, J. Zhijiang, L. Shunhua, L. Weiping, *Solid State Sci.* **12** (2010) 1374
38. K. H. Lee, B. J. Park, D. H. Song, I. J. Chin, H. J. Choi, *Polymer* **50** (2009) 4372
39. D. Gui, C. Liu, F. Chen, J. Liu, *Appl. Surf. Sci.* **307** (2014) 172
40. D. Tsotcheva, T. Tsanov, L. Terlemezyan, S. Vassilev, *J. Therm. Anal. Calorim.* **63** (2001) 133
41. L. Shao, J. Qiu, L. Lei, X. Wu, *Synth. Met.* **162** (2012) 2322
42. Z. Durmus, A. Baykal, H. Kavas, H. Sozeri, *Phys., B* **406** (2011) 1114
43. B. Somboonsub, S. Srisawan, M. A. Invernale, S. Thongyai, P. Praserthdam, D. A. Scola, G. A. Sotzing, *Polymer* **51** (2010) 4472

44. L. Shao, J. Qiu, L. Lei, X. Wu, *Synth. Met.* **162** (2012) 2322
45. N. Naar, S. Lamouri, B. Belaabed, T. Kouroughli, N. Gabouze, *Polym. J.* **41** (2009) 432
46. I. Dumitrescu, C. A. Nicolae, A. M. Mocioiu, R. A. Gabor, M. Grigorescu, M. Mihailescu, *U.P.B. Sci. Bull., Series A* **71** (2009) 63
47. C. Cheng-Ho, *J. Polym. Res.* **9** (2002) 195.



The influence of interlayer interactions on the mechanical properties of polymeric nanocomposites

MEHRDAD JABBARZADEH^{1*} and AMIR REZA GOLKARIAN²

¹*Department of Mechanical Engineering, Mashhad Branch, Islamic Azad University, Mashhad, Iran and ²Department of Mechanical Engineering, Science and Research Branch, Islamic Azad University, Tehran, Iran*

(Received 25 October 2014, revised 10 March, accepted 18 June 2015)

Abstract: In this study, the influence of the type of interlayer interactions on the elastic modules of multilayer graphene sheets (GS) and nanocomposites was investigated. The modeling and investigation of mechanical properties of graphite layers were performed using the molecular mechanics (MM) method. Initially, for improving the model and decreasing the amount of computations, three types of elements, *i.e.*, a beam, a linear spring and a nonlinear spring, were used. Continuing, the mechanical properties of multilayers and nanocomposites were compared using three types of interlayer interactions. Initially, a nonlinear spring defined by the Leonard Jones potential was used to define the interlayer interactions (ordinary case). Then, a linear spring with a certain stiffness, to obtain an equal linear spring and to investigate the ultimate capacity of interlayer interactions in the translation of force, by increasing the stiffness of linear springs, was employed (chemical change). Then, by omitting all Van der Waals interactions and the creation of defects in the graphite layers, covalent interlayer interactions (using the Morse potential) were created. Finally, Van der Waals and covalent interlayer interactions were created spontaneously to study the properties of multilayers and nanocomposites (functionalization). The results were compared with other available literature data in order to validate the modeling.

Keywords: structural mechanics approach; graphene sheet; elastic modules; vacancy defect; functionalization.

INTRODUCTION

Graphene sheets (GS) and carbon nanotubes (CNT) have attracted the attention of many researchers and scientists due to their wonderful properties and abundant applications in industry, medicine, martial science and other fields.^{1–6} Besides their unique mechanical, thermal and electrical properties, their significant capabilities in other fields have attracted further attention. Among these

*Corresponding author. E-mail: jabbarzadeh@mshdiau.ac.ir
doi: 10.2298/JSC141025054J

properties, their potential to be used as a reinforcement agent in polymeric composites and producing nanocomposites with exclusive properties could be mentioned. High tensile strength beside the lightening and high flexibility of these products is one of their extraordinary mechanical properties that make them unique. Besides the mentioned benefits, weak interlayer interactions, which persuade researchers to demonstrate the functionalization idea or chemical changes,^{7–12} should be noticed.

Modeling approaches for these nanomaterials are needed, due to their small scales and expensive equipment in this field. One of the most attractive methods in this field is the molecular mechanic (MM) method, which was introduced for the first time by Li and Chou¹³ who used linear beam elements to simulate CNTs. Subsequently, many researchers devoted their time to improving this field by working on the type and quality of the employed elements. Among the studies performed in this field, one by Meo and Rossi,¹⁴ who introduced spring elements as a suitable replacement for beam elements, could be mentioned. Afterwards, Georgantzinos *et al.*¹⁵ presented the idea of using fully nonlinear spring-based models, which were then improved further by other researchers.^{16–20}

To date, nonlinear spring elements were commonly used to simulate interlayer interactions in nanocomposites.^{21–23} Rafiee *et al.*²⁴ studied the idea of functionalization of CNT nanocomposites using linear beam elements (introduced by the AMBER potential) as covalent interlayer interactions and reported that this action decreased the elastic modulus of CNTs and reinforced nanocomposites. The focus of this study was the important problem that the connector between the base material and the reinforcement (CNT) agent are weak Van der Waals interactions, which cannot translate the maximum power of the reinforcement to the base.

Therefore, in this study, the effect of using different types of interlayer interactions was investigated. The most important goals were the calculation of the maximum limit of load transferring and the study of the influence of different types of functionalization (introduced by many researchers).^{7–12} The most important objectives investigated were:

- The influence of different types of mechanical elements used to simulate monolayer GS.
- The influence of four different types of interlayer interactions on the mechanical properties of multilayer GSs and nanocomposites, *i.e.*: a) van der Waals interlayer interactions using nonlinear spring elements defined by the Leonard–Jones potential (ordinary case), b) linear spring elements, whose the stiffness of which increased at each step to obtain the ultimate value of translating force (chemical change), c) covalent interlayer interaction using a linear spring element defined by the Morse potential energy and d) a combination of Van der Waals and covalent bonds.

– A comparison between the reinforcing effect of monolayer and multilayer GSs in nanocomposites.

CONSIDERED MODELS

Considered models, theoretical background and calculations are described in Supplementary material to this paper.

RESULTS AND DISCUSSION

Monolayer GS

The results related to the elastic module of a monolayer GS for different types of mechanical elements are given in Table I. With change in the mechanical element from linear beam to linear spring, the influence of the defined cross section area could be obtained. By replacing a nonlinear spring with a linear spring, the influence of the definition of the nonlinear behavior for the employed elements could be computed. It was observed that by replacing a linear beam with a linear spring, the elastic module in model I increased by 11 % and in model II increased by 17 %. This shows that by assuming a cross section area for the element, a significant change was observed in the elastic module. In addition, in this step, the time of the computations for both cases was the same. To continue, by replacing a nonlinear spring with a linear spring, the elastic module of both models increased by about 3 %. This showed that by defining nonlinear behavior for the elements, the results did not show significant changes but the time of the computations was very long, which further increased on increasing the dimensions of the sheets. Therefore, a linear spring element could be introduced as a suitable element to simulate interatomic interactions of GSs, because they make less error and require shorter computation times.

TABLE I. Variation of the elastic module of a GS in dependence on the type of the mechanical element

Type of the mechanical element	Elastic module, TPa	
Linear beam	Model I:	1.096
	Model II:	1.078
	Lit. ²⁵ :	1.025
Linear spring	Model I:	1.217
	Model II:	1.269
	Lit. ²⁶ :	1.367
Nonlinear spring	Model I:	1.255
	Model II:	1.308
	Lit. ¹⁸ :	1.245

Double-layer GSs

Interlayer interaction: type I. GS used at this step is perfect and its elastic module is about 1.2175 TPa. By defining a second layer at a distance of 0.34 nm

from the first one and the creation of Van der Waals interaction between the layers with a cut-off distance of 0.38 nm, the elastic module increased to 1.2275 TPa. This result is in good agreement with the results reported by other researchers (Table II).

TABLE II. A comparison of the results related to the elastic module of double-layer GSs with Van der Waals interlayer interactions

Study	Elastic module of a monolayer, TPa	Elastic module of a double-layer, TPa
Present study	1.2175	1.2275
Golkarian and Jabbarzadeh ¹⁸	1.2447	1.2537
Li and Chou ¹³	1.025	1.035
Bao <i>et al.</i> ²⁷	1.030	1.032

Interlayer interaction: type II. The results obtained at this step (Table III) showed that at a stiffness of 300 nN nm⁻¹, the elastic module is about 1.2263 TPa, which is in good agreement with the value 1.2257 TPa related to the previous step and showed that this stiffness is a good replacement for nonlinear Van der Waals interactions. It was observed that at a stiffness of about 10⁸ nN nm⁻¹ (330000 times stronger than 300 nN nm⁻¹ equal to the van der Waals forces), the elastic module of double-layer GS increased to 1.59 TPa, showing a 30 % increase. It could be deduced that if the maximum increase of 30 % was satisfactory and the complication of working on the power of interlayer interactions was possible, chemical work on the interlayer interactions could be helpful.

TABLE III. Variation of the elastic module of double-layer GSs from the stiffness of linear springs as interlayer interactions

Stiffness, nN nm ⁻¹	Elastic module, TPa
0	1.2175
1	1.2176
10	1.2178
100	1.2205
300	1.2263
10 ³	1.2452
10 ⁴	1.5513
10 ⁶	1.5905
10 ⁸	1.5954
10 ¹⁰	1.5955
10 ¹²	1.5955

Interlayer interaction: type III. In the third step, by defining a defect in each layer, the elastic module of each layer was reduced to 1.1979 TPa; this negligible decrease is in the range of results reported by other researchers (Table IV). By defining van der Waals forces between two layers, the elastic module of the

layers increased to 1.2060 TPa. If the layers were linked together by covalent bonds, the elastic module increased to 1.1988 TPa and when a combination of van der Waals and covalent bonds was used, the elastic module increased to 1.2067 TPa, which shows a 0.7 % increase in comparison to defective monolayers and 0.9 % reduction if compared to the perfect ones.

TABLE IV. Variation of elastic module of a monolayer GS caused by defining a defect

Study	Perfect elastic module, TPa	Defective elastic module, TPa
Present study	1.2175	1.1979
Rafiee & Pourazizi ²⁴	1.032	0.990
Ansari <i>et al.</i> ²⁸	0.79	0.77
Scalante <i>et al.</i> ²⁹	1.042	1.036

The results showed that by defining a defect in the layers, the elastic module showed a 1.6 % reduction and that the reduction after functionalization by defining covalent and van der Waals forces was 1.5 %, which is a negligible difference. From these results, it could be deduced that functionalization in order to repair existing defects or after defining the defects in the model, to form covalent interlayer interactions cannot improve the mechanical properties of the model. Therefore, other ways, such as a change in the type of interlayer interaction, should be considered.

Nanocomposite

Monolayer reinforcement. Interlayer interaction: type I. In this step, a GS with an elastic module of 1.2175 TPa was imported into a polymeric base with an elastic module of 3.5 GPa and they were coupled with Van der Waals forces. The elastic module of nanocomposite at this step was 63.7 GPa, which is in good agreement with the result of 64.2 GPa obtained from ROM. In a same research performed by Rafii-Tabar and Montazeri²¹ for a polymeric base with an elastic module of 3.5 GPa, the elastic module of nanocomposite was reported to be about 59.536 GPa, which is in suitable agreement with the results obtained in this study. Moreover, the elastic module of the polymeric base (3.5 GPa) in this step was found to be 3.67 GPa, which was a 4.8 % increase.

Interlayer interaction: type II. By using linear springs instead of Van der Waals forces and increasing its stiffness, no significant change was observed in the translate ratio from reinforced to polymeric base (Table V). It could be seen that the maximum elastic module of the nanocomposite in a stiffness of 300 nN nm⁻¹ (the same as when van der Waals forces existed) was obtained, which was equal to the 63.68 GPa. The maximum value for the elastic module of polymeric base was about 3.678 GPa, *i.e.*, a 1.5 % increase.

Interlayer interaction: type III. By omitting all van der Waals forces, defining a defect and creating three covalent bonds, the elastic module of the nanocomposite and the polymeric base were about 62.69 GPa and 3.5 GPa, respect-

ively. By defining, a second defect and the next three covalent bonds (bidirectional), the elastic module of the nanocomposite and of the polymeric base were 61.69 and 3.5 GPa, respectively. By defining van der Waals forces (together with bidirectional covalent bonds), the elastic modules reached 61.71 and 3.6 GPa, respectively. From these results, it can be deduced that the functionalization of nanocomposites reinforced by monolayer GS does not lead to an improvement of the elastic module of the nanocomposite.

TABLE V. Variation of elastic module of polymeric base according to the stiffness of a linear spring as an interlayer interaction (monolayer reinforcement)

Stiffness, nN nm ⁻¹	Elastic module of polymeric base, GPa
0	3.5
0.1	3.557
10	3.67
300	3.677
1000	3.678
10 ⁴	3.678

Double-layer reinforcement. Interlayer interaction: type I. By importing a double-layer GS in polymeric base, the elastic module of nanocomposite increased to 64.11 GPa, which is a 0.7 % increase. In this step, the elastic module of polymeric base decreased to 3.6 from 3.67 GPa for a monolayer reinforcement. This showed that increasing the number of layers in the presence of van der Waals forces as interlayer interactions was inefficient.

From the results of this step and the previous steps (related to the functionalization by using monolayer reinforcement), it can be deduced that the functionalization of double-layer GS would be inefficient, because the increase in the number of layers did not improve the elastic module of the nanocomposite and also defect creation (in order to make covalent bonds) decreased the elastic module of the nanocomposite.

Interlayer interaction: type II. By increasing the stiffness of all interlayer interactions including the interactions GS–GS and GS–polymeric base, the elastic module of the nanocomposite increased to 82.5 GPa, *i.e.*, a 30 % increase (in a stiffness of 1 nN nm⁻¹) (Table VI), which is equal to the time that the elastic module of double-layer GS reached its maximum value. In addition, the elastic module of the polymeric base decreased to 3.605 GPa (in stiffness of 100 nN nm⁻¹) from 3.67 GPa related to the use of monolayer reinforcement (Table VII). This shows that increasing the number of layers and the stiffness of interlayer interactions cannot improve the elastic module of the polymeric base.

Some of the important points that can be deduced from the results are:

1. Making a defect in the graphene layer for replacing three carbon–carbon covalent bonds instead of three weak van der Waals interlayer interactions to inc-

TABLE VI. Variation of elastic module of nanocomposite according to the stiffness of the linear spring element as an interlayer interaction (double layer reinforcement)

Stiffness, nN nm ⁻¹	Elastic module of nanocomposite, GPa
0	63.7
1	63.68
10	63.69
100	63.74
1000	64.18
10 ⁴	67.39
10 ⁵	76.72
10 ⁶	81.68
10 ⁷	82.41
10 ⁸	82.48
10 ⁹	82.5

rease the elastic module of nanocomposite or multilayers is a useless operation. This is because the decreasing effect of making a defect in a layer on the elastic module more than decreases the effect of this type of functionalization.

TABLE VII. Variation of the elastic module of the polymeric base in dependence on the stiffness of the linear spring elements as interlayer interaction (double-layer reinforcement)

Stiffness, nN nm ⁻¹	Elastic module of the polymeric base, GPa
0	3.5
1	3.585
10	3.602
100	3.605
1000	3.605

2. By increasing the strength of interlayer interactions (which includes each type of functionalization or chemical changes), a maximum increasing effect of 30 % in the elastic module of nanocomposites reinforced by multilayer graphene sheets is estimated. Of course, this results may have some changes in experimental studies because, in this case, the influence of many graphene layers as a multilayer GS was only investigated and the influence of some important parameters, such as the contribution, dispersion, local density, direction of the layers and some other parameters that could not be considered in the atomic mechanical modeling and appear only in real, experimental investigations.

3. This increasing effect is when the employment of multilayer graphene layers (in the experimental works most of the employed graphene layers are also multilayers, because monolayers are rarely available) and increasing the strength of interlayer interactions between a monolayer graphene sheet and a polymeric base does not lead to a significant increasing effect in the elastic module of the nanocomposite.

Among theoretical studies performed in this case, the study performed recently by Rafiee and Rourazizi²⁴ could be mentioned, in which they used the molecular mechanic modeling method and reinforced a polymeric cylindrical matrix with monolayer carbon nanotube and investigated the influence of this type of functionalization (making defect and replacing C–C covalent bonds instead of van der Waals interlayer interactions) and reported the same results.

They reported the decreasing effect of this type of functionalization on the elastic module of a cylindrical polymeric base reinforced by single layer carbon nanotube and they explained that the effect of functionalization cannot be observed on the micro scale but its improving effect may appear on the meso or macro scale.

Therefore, in the present study, time was devoted to investigate the effect of each type of functionalization (by increasing the strength of interlayer interactions up to its highest level) for both mono and multilayer graphene sheets. It was found that in the case of multilayers, an up to 30 % increase in the elastic module of the nanocomposite was possible by increasing the effect but in the case of monolayer reinforcements, no increase was observed in the case of graphene sheet, but not with carbon nanotubes

As a general result, it could be deduced that, maybe, more attention should be paid to the interactions between the graphene layers than those between the graphene layer and the polymeric base. However, this objective cannot be strongly emphasized because, as explained previously, there are some crucial parameters that cannot be considered using this modeling approach.

CONCLUSIONS

In this paper the influences of three types of interlayer interactions on the elastic module of multilayer GSs and nanocomposites reinforced by monolayer and double-layer GS were studied. The following important cases were considered in this investigation:

The influence of type of element used for simulating of GSs on the elastic module and the amount of computations.

The influence of type of element used for simulating interlayer interactions in double-layer GSs and nanocomposites reinforced by monolayer and double-layer GS.

Using four types of interlayer interactions:

- van der Waals interlayer interaction using nonlinear spring element defined by the Leonard–Jones potential to validate the modeling method,
- linear spring elements, the stiffness of which was increased at each step to find the ultimate value of the possible force translation ratio,
- omitting all van der Waals forces, defining defects in the layers and make three covalent interlayer interactions by defining each defect and

– combination of van der Waals and covalent interlayer interactions.

The influence of an increase in the number of layers on the reinforcement of the nanocomposites.

The maximum amount of possible force translation ratio from reinforcement to polymeric base (chemical changes).

Some of the important results are:

– The linear spring element is in best agreement with other results and requires the lowest computations time.

– Making defects and replacing van der Waals interlayer interactions with C–C covalent bonds cannot improve the elastic module of multilayer GSs and nanocomposites. This means that the decreasing effect of making defects is more than the increasing effect of the replacement by covalent interlayer interactions.

– Chemical changes (functionalization) in interlayer interactions under the best conditions can lead to an increase of about 30 % in the elastic module of multilayer GSs and nanocomposites reinforced by multilayer GSs.

– Improving the elastic modules of nanocomposites due to the functionalization (reported by experimental works) is the consequence of functionalization of interlayer interactions between graphene layers not between graphene layer and polymeric base.

– Improving the quality of interlayer interactions cannot help to improve the elastic module of polymeric base.

Consequently, it could be deduced that by using multilayer GSs and improving the strength of the interlayer interactions, significant increases in the elastic module of double-layer GSs and also nanocomposites reinforced by multilayer GSs of up to 30 % could be expected. In addition, improving the strength of the interlayer interactions or increasing the number of layers does not lead to an improvement in the elastic module of the polymeric base.

SUPPLEMENTARY MATERIAL

Details of the considered models, their theoretical background and method of calculations are available electronically from <http://www.shd.org.rs/JSCS/>, or from the corresponding author on request.

Acknowledgement. The authors wish to thank the Islamic Azad University of Mashhad for financing the project “The influence of quality of interlayer interactions on the mechanical properties of polymeric nanocomposites”.

ИЗВОД

УТИЦАЈ ИНТЕРАКЦИЈА МЕЂУСЛОЈА НА МЕХАНИЧКА СВОЈСТВА ПОЛИМЕРНИХ
НАНОКОМПОЗИТА

MEHRDAD JABBARZADEH и AMIR REZA GOLKARIAN

Department of Mechanical Engineering, Mashhad Branch, Islamic Azad University, Mashhad, Iran

Проучаван је утицај типова интеракције међуслоја на еластичне модуле вишеслојног графена (GS) и нанокомпозита. Моделовање и испитивање механичких својстава графитних слојева изведено је методом молекулске механике (MM). Најпре су, због побољшања модела и смањења обима израчунавања, коришћена три елемента: зрак, линеарна и нелинеарна опруга, а у наставку су упоређена механичка својства вишеструктурних слојева и нанокомпозита применом три типа интеракције међуслоја. Прво је коришћена нелинеарна опруга дефинисана Leonard–Jones потенцијалом да би се дефинисале интеракције међуслоја (ординарни случај). Затим је примењена донекле пригушена линеарна опруга (еквивалентна линеарна опруга) и повећавањем пригушености линеарних опруга испитао крајњи капацитет интеракције међуслоја у трансляцији силе (хемијска промена). Уз то су, у једном случају занемарене све van der Waals интеракције и настајање дефеката у графитним слојевима, те је оно доводило до ковалентних интеракција међуслоја (Morse потенцијал), а у другом, van der Waals и ковалентне интеракције међуслоја креиране су спонтано да би се проучила својства вишеструктурних слојева и нанокомпозита (функционализација). Резултати су поређени са подацима из литературе ради валидизације моделовања.

(Примиљено 25. октобра 2014, ревидирано 10. марта, прихваћено 18. јуна 2015)

REFERENCES

1. M. Paradise, T. Goswami, *Mater. Design* **28** (2007) 1477
2. C. P. Firme, P. R. Bandaru, *Nanomedicine* **6** (2010) 245
3. D. A. Gomez-Gualdrón, J. C. Burgos, J. Yu, P. B. Balbuena, *Prog. Mol. Biol. Transl. Sci.* **104** (2011) 175
4. R. Orinakova, A. Orinak, *Fuel* **90** (2011) 3123
5. V. K. K. Upadhyayula, S. Deng, M. C. Mitchell, G. B. Smith, *Sci. Total Environ.* **408** (2009) 1
6. V. N. Popov, *Mater. Sci. Eng. R* **43** (2004) 61
7. J. L. Bahr, J. M. Tour, *J. Mater. Chem.* **12** (2002) 1952
8. S. J. V. Frankland, A. Caglar, D. W. Brenner, M. Griebel, *J. Phys. Chem.* **106** (2002) 3046
9. M. L. Shofner, V. N. Khabashesku, E. V. Barrera, *Chem. Mater.* **18** (2006) 906
10. F. Buffa, G. A. Abraham, B. P. Grady, D. Resasco, *J. Polym. Sci. B Polym. Phys.* **45** (2007) 490
11. C. A. Cooper, S. R. Cohen, A. H. Barber, H. D. Wagner, *Appl. Phys. Lett.* **81** (2002) 3873
12. A. H. Barber, S. R. Cohen, H. D. Wagner, *Appl. Phys. Lett.* **82** (2003) 4140
13. C. Li, T.-W. Chou, *Int. J. Solids Struct.* **40** (2003) 2487
14. M. Meo, M. Rossi, *Compos. Sci. Technol.* **66** (2006) 1597
15. S. K. Georgantzinos, D. E. Katsareas, *Physica E* **43** (2011) 1833
16. V. Parvaneh, M. Shariati, H. Torabi, *Comp. Mater. Sci.* **50** (2011) 2051
17. R. Rafiee, M. Heidarhaei, *Compos. Struct.* **94** (2012) 2460
18. A. R. Golkarian, M. Jabbarzadeh, *Comp. Mater. Sci.* **74** (2013) 138
19. A. R. Golkarian, M. Jabbarzadeh, *J. Solid Mechanics* **4** (2012) 106

20. A. A. Shariati, A. R. Golkarian, M. Jabbarzadeh, *J. Solid Mechanics* **6** (2014) 255
21. A. Montazeri, H. Rafii-Tabar, *Phys. Lett. A* **375** (2011) 4034
22. M. M. Shokrieh, R. Rafiee, *Compos. Struct.* **92** (2010) 2415
23. K. I. Tserpes, A. Chanteli, *Compos. Struct.* **99** (2013) 366
24. R. Rafiee, R. Pourazizi, *Comp. Mater. Sci.* **93** (2015) 576
25. C. Li, T. W. Chou, *Int. J. Solids Struct.* **40** (2003) 2487
26. S. K. Georgantzinos, G. I. Giannopoulos, N. K. Anifantis, *Mater. Design* **31** (2010) 4646
27. B. Wen Xing, Z. Chang Chun, C. Wan Zhao, *Physica, B* **352** (2004) 156
28. R. Ansari, S. Ajori, B. Motevalli, *Superlattice. Microst.* **51** (2012) 274
29. A. Tapia, R. Peon-Escalante, C. Villanueva, F. Avilés, *Comp. Mater. Sci.* **55** (2012) 255.



SUPPLEMENTARY MATERIAL TO
**The influence of interlayer interactions on the mechanical
properties of polymeric nanocomposites**

MEHRDAD JABBARZADEH^{1*} and AMIR REZA GOLKARIAN²

¹*Department of Mechanical Engineering, Mashhad Branch, Islamic Azad University,
Mashhad, Iran and ²Department of Mechanical Engineering, Science and Research Branch,
Islamic Azad University, Tehran, Iran*

J. Serb. Chem. Soc. 80 (11) (2015) 1449–1459

CONSIDERED MODELS, THEIR THEORETICAL BACKGROUND AND THE METHOD
OF CALCULATIONS

In the MM method, which was introduced for the first time by Li and Chou,¹ CNTs and GSs were simulated using mechanical elements, *i.e.*, beams, rods and springs.

In this method, the use each element has some benefits or problems. For example, a linear beam element requires the cross section area be defined, which causes some errors but defining such elements is simple and the amount of computations is very low. Using a linear spring element decreases the errors, is simply defined and the amount of computation for this step is the same as for linear beam elements. The only probable error in this step is the linear behavior of the elements. Using nonlinear spring elements increases the accuracy of the computations but increases drastically the amount of computations necessary and defining such elements is problematic.

In this study, all three elements were initially used and the most suitable element with minimum amount of computations and errors was introduced.

Therefore, paying attention to the location and arrangement of carbon atoms in GSs, a program was prepared using MATLAB software to calculate the location of the nodes (carbon atoms) and then between each two neighboring atoms, a mechanical element was introduced. For defining, a model based on linear beam elements, the same model as introduced by Li and Chou¹ was employed. The cross section area of the elements was 0.147 nm, the elastic module was 5.49 TPa and the shear module was 0.871 TPa with a length of 0.1421 nm (Fig. S-1). To define a linear spring, the same strategy as employed by Giannopoulos *et al.*² was used, which includes two types of elements A and B responsible for the stretching and bending of bonds (Fig. S-1). The stiffness of spring type A was equal to $K_{rA} = 6.52 \times 10^7 \text{ N nm}^{-1}$ and of type B, it was $K_{rB} = 1.735 \times 10^7 \text{ N nm}^{-1}$. In the third model, which was the same model as used previously^{3–5} and by Rafiee and Heidarhaei⁶ and Shariati *et al.*,⁷ two types of nonlinear spring elements (types A and B, Fig. S-1) were used. The nonlinear behavior of spring group A obeyed the following equation:⁸

*Corresponding author. E-mail: jabbarzadeh@mshdiau.ac.ir

$$F(\Delta r) = 2\beta D_e (1 - e^{\beta \Delta r}) e^{\beta \Delta r} \quad (1)$$

where $D_e = 6.03105 \times 10^{10} \text{ N m}$, $\beta = 26.26 \text{ nm}^{-1}$ and Δr is the amount of deviation of the length of the bond length from its equilibrium distance ($r_0 = 0.1421 \text{ nm}$). The nonlinear behavior of spring type "B" was defined using the following equation:

$$F(\Delta R) = \frac{4}{r_0^2} k_\theta \Delta R [1 + \frac{48}{r_0^4} k_{\text{sextic}} (\Delta R)^4] \quad (2)$$

with $K_\theta = 0.9 \times 10^{-18} \text{ N m rad}^{-2}$, $K_{\text{sextic}} = 0.754 \text{ rad}^{-4}$ and ΔR is the deviation of bond's length from its equilibrium value ($R_0 = \sqrt{3} r_0$).

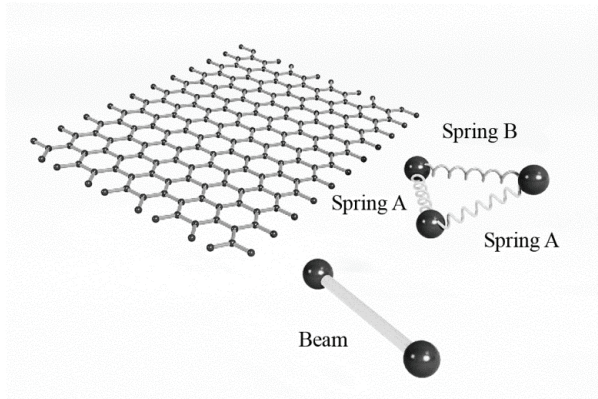


Fig. S-1. Definition of the mechanical elements.

To continue, after defining the mentioned elements, the model was imported into ABAQUS software, one side of the model was restricted and a stretching force was applied to the other side. In this study, initially, two sheets with dimension of $2.21 \text{ nm} \times 2 \text{ nm}$ (model I) and $3.69 \text{ nm} \times 3.26 \text{ nm}$ (model II) in the armchair direction were stretched and the related elastic module was calculated. The polymeric base employed in this study had an elastic module equal to 3.5 GPa and the volume fraction of the reinforcement agent in all cases was 5% . The dimension of the polymeric base was calculated with attention being paid to the volume fraction of the reinforcement agent.

Models

Generalities. To define weak Van der Waals interlayer interactions in multilayers and nanocomposites, usually nonlinear spring elements defined by Leonard–Jones (L–J) potential are used,^{6,9,10} although using these elements, especially in the models with large dimensions, increases the amount of computations intensively. On the other hand, stronger interlayer interactions are needed in nanocomposites. Therefore, some researchers presented the idea of functionalization or chemical changes in the GSs,^{11–16} which induces them to make covalent bond with other layers (or the composite base) or using other stronger chains of molecules as a link between them.

In this study, an attempt was made to investigate the effect of different types of interlayer interactions for both double layer GSs and nanocomposites reinforced with mono and multilayer GSs.

Interlayer interaction: type I. Initially using nonlinear spring elements defined by the Leonard–Jones potential, the same as was employed by other researchers,^{6,9,10} the interlayer interactions were simulated and the following equation shows their nonlinear behavior:

$$F(r) = 24 \frac{\varepsilon}{\sigma} \left(2 \left(\frac{\sigma}{r} \right)^{13} - \left(\frac{\sigma}{r} \right)^7 \right) \quad (3)$$

where r is the distance between interacting atoms and ε and σ are the L–J parameters, which are $\varepsilon = 0.38655 \times 10^{-3}$ nN nm and $\sigma = 0.34$ nm for carbon atoms. In this step, the results related to the elastic module could be compared with the results of other studies to validate the models. It should be mentioned that in this step, each atom makes a bond with an atom from another layer or the composite base, the distance of which from each other is less than 0.85 nm (cut-off distance, Fig. S-2). In this study, the thickness of the GSs was assumed 0.34 nm and the distance between the graphene layers or GS and the composite base was 0.17 nm. To reduce the amount of computations, the cut-off distance was assumed 0.38 nm. The chirality of all models is armchair and Fig. S-3 shows the model created for double layer GS and Fig. S-4 is a schematic view of a nanocomposite reinforced by a monolayer GS.

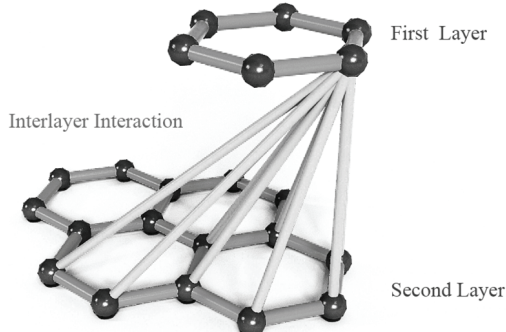


Fig. S-2. Definition of interlayer interactions by nonlinear spring elements.

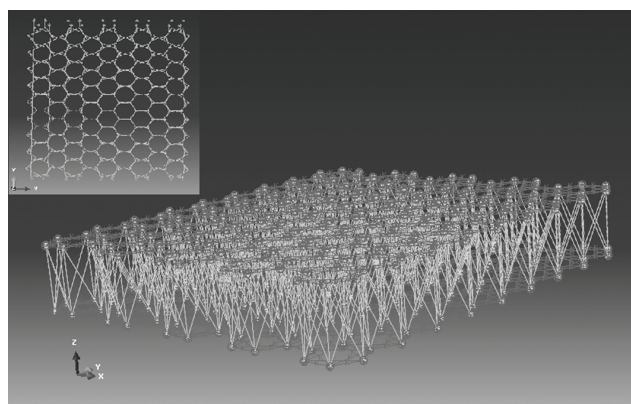


Fig. S-3. Two views of double-layer GSs coupled by Van der Waals forces.

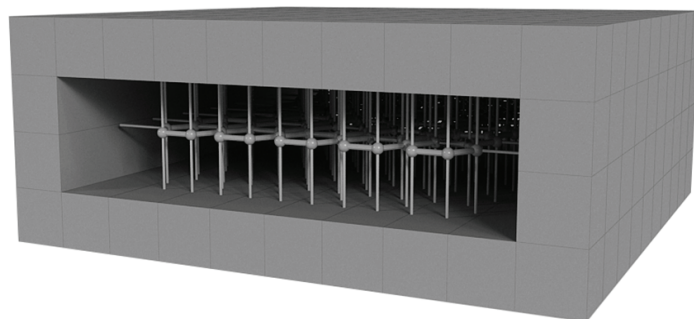


Fig. S-4. Graphic view of a nanocomposite reinforced by a monolayer GS coupled by Van der Waals forces.

Interlayer interaction: type II. In this step using a linear spring element (Fig. S-5) and change in its stiffness, an attempt was made to calculate the ultimate force-translating ratio from the reinforcement agent to the polymeric base. For this purpose, initially a spring with zero stiffness was located between two atoms from different layers and then its stiffness was increased systematically.

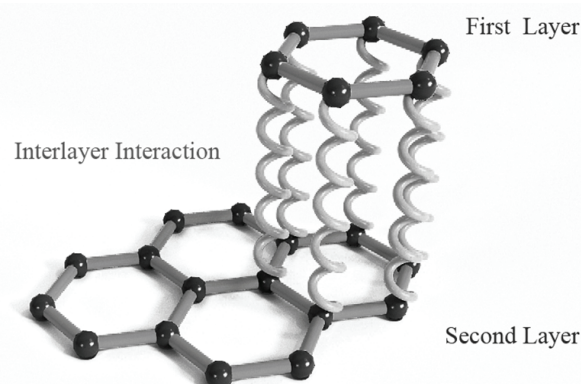


Fig. S-5. Definition of interlayer interactions by linear spring elements.

Interlayer interaction: type III. All the van der Waals forces were eliminated in this step and a vacancy defect was introduced into each layer (one atom is diminished), so three atoms obtain one empty orbital and they can make covalent atoms by three atoms from another layer or the polymeric base (Fig. S-6). For this step, the interlayer thickness was assumed to be 0.1421 nm and the interlayer covalent bonds were made using a linear spring element type A ($K_{rA} = 6.52 \times 10^7 \text{ N nm}^{-1}$).⁶ Here, initially, van der Waals forces with a cut-off distance of 0.38 nm and the next time, a combination of covalent and van der Waals interlayer interactions were used to have a better comparison between the base and the functionalized level. To better understanding the effect of functionalization, atoms that should make a covalent bond with each other were chosen from different layers and are not *vis-à-vis* (Figs. S-7 and S-8).

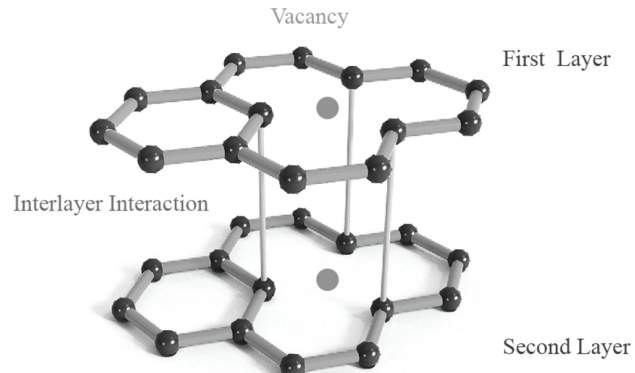


Fig. S-6. Definition of covalent interlayer interactions.

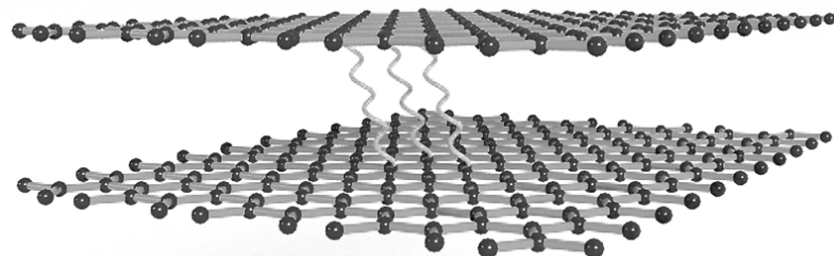


Fig. S-7. Graphic view of GSs coupled by covalent bonds.

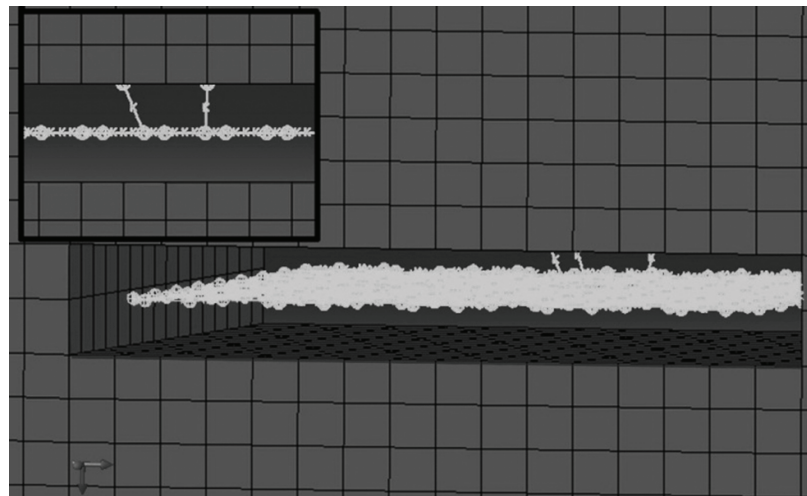


Fig. S-8. Nanocomposite reinforced by a monolayer GS and covalent bonds as interlayer interactions.

In addition, to study further the effect of covalent interlayer bonds, second defects, bidirectional covalent interlayer interactions are created (Fig. S-9). All the mentioned steps were repeated for importing monolayer and double-layer GS into the polymeric base (Fig. S-10).

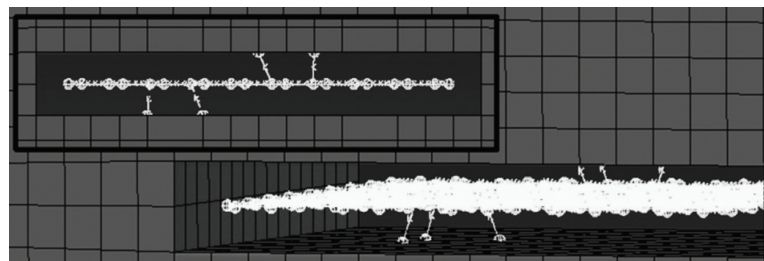


Fig. S-9. Nanocomposite reinforced by a monolayer GS and bidirectional covalent bonds as interlayer interactions.

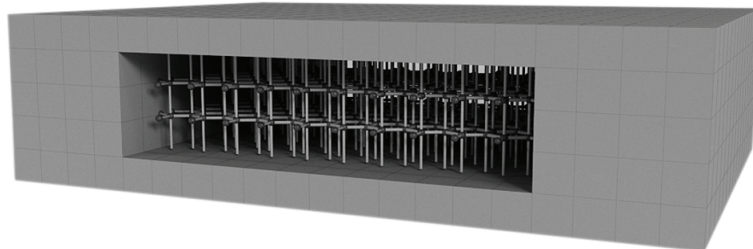


Fig. S-10. Graphic view of a nanocomposite reinforced by double-layer GSs.

To validate the results in the case of nanocomposites, the rule of mixture (ROM) was employed:

$$E_t = v_G E_G + v_Z E_Z \quad (4)$$

where E_t is the total elastic module of a nanocomposite, E_G is the GS elastic module, E_Z is the polymeric base elastic module, v_G is the GS volume fractions and v_Z is the polymeric base volume fraction.

REFERENCES

1. C. Li, T.-W. Chou, *Int. J. Solids Struct.* **40** (2003) 2487
2. G. I. Giannopoulos, P. A. Kakavas, N. K. Anifantis, *Comp. Mater. Sci.* **41** (2008) 561
3. A. R. Golkarian, M. Jabbarzadeh, *Comp. Mater. Sci.* **74** (2013) 138
4. A. R. Golkarian, M. Jabbarzadeh, *Journal of Solid Mechanics* **4** (2012) 106
5. A. A. Shariati, A. R. Golkarian, M. Jabbarzadeh, *Journal of Solid Mechanics* **6** (2014) 255
6. A. Montazeri, H. Rafii-Tabar, *Phys. Lett. A* **375** (2011) 4034
7. V. Parvaneh, M. Shariati, H. Torabi, *Comp. Mater. Sci.* **50** (2011) 2051
8. K. Machida, Principles of molecular mechanics, Wiley and Kodansha, 1999
9. M. M. Shokrieh, R. Rafiee, *Compos. Struct.* **92** (2010) 2415
10. K. I. Tsierpes, A. Chanteli, *Compos. Struct.* **99** (2013) 366
11. J. L. Bahr, J. M. Tour, *J. Mater. Chem.* **12** (2002) 1952

12. S. J. V. Frankland, A. Caglar, D. W. Brenner, M. Griebel, *J. Phys. Chem.* **106** (2002) 3046
13. M. L. Shofner, V. N. Khabashesku, E. V. Barrera, *Chem. Mater.* **18** (2006) 906
14. F. Buffa, G. A. Abraham, B. P. Grady, D. Resasco, *J. Polym. Sci. B Polym. Phys.* **45** (2007) 490
15. C. A. Cooper, S. R. Cohen, A. H. Barber, H. D. Wagner, *Appl. Phys. Lett.* **81** (2002) 3873
16. A. H. Barber, S. R. Cohen, H. D. Wagner, *Appl. Phys. Lett.* **82** (2003) 4140.